This is to certify that the
dissertation entitled

ESTIMATING FOREST CANOPY ATTRIBUTES VIA AIRBORNE, HIGH-RESOLUTION, MULTISPECTRAL IMAGERY IN MIDWEST FOREST TYPES

presented by

DEMETRIOS GATZIOLIS

has been accepted towards fulfillment
of the requirements for the

Ph.D. degree in Forestry

Larry A. Leefers
Major Professor's Signature

September 2, 2003
Date

# ESTIMATING FOREST CANOPY ATTRIBUTES VIA AIRBORNE, HIGH-RESOLUTION, MULTISPECTRAL IMAGERY IN MIDWEST FOREST TYPES

By

Demetrios Gatziolis

A DISSERTATION

Submitted to
Michigan State University
in partial fulfillment of the requirements
for the degree of

DOCTOR OF PHILOSOPHY

Department of Forestry

2003

EST

ABSTRACT

ESTIMATING FOREST CANOPY ATTRIBUTES VIA AIRBORNE, HIGH-RESOLUTION, MULTISPECTRAL IMAGERY IN MIDWEST FOREST TYPES

By

Demetrios Gatziolis

*An investigation of the utility of high spatial resolution (sub-meter), 16-bit, multispectral, airborne digital imagery for forest land cover mapping in the heterogeneous and structurally complex forested landscapes of northern Michigan is presented. Imagery frame registration and georeferencing issues are presented and a novel approach for bi-directional reflectance distribution function (BRDF) effects correction and between-frame brightness normalization is introduced. Maximum likelihood classification of five cover type classes is performed over various geographic aggregates of 34 plots established in the study area that were designed according to the Forest Inventory and Analysis protocol. Classification accuracy estimates show that although band registration and BRDF corrections and brightness normalization provide an approximately 5% improvement over the raw imagery data, overall classification accuracy remains relatively low, barely exceeding 50%. Computed kappa coefficients reveal no statistical differences among classification trials. Classification results appear to be independent of geographic aggregations of sampling plots.*

*Estimation of forest stand canopy parameter parameters (stem density, canopy closure, and mean crown diameter) is based on quantifying the spatial autocorrelation among pixel digital numbers (DN) using variogram analysis and slope break analysis, an*

*alternative non-parametric approach. Parameter estimation and cover type classification proceed from the identification of tree apexes. Parameter accuracy assessment is evaluated via value comparison with a spatially precise set of field observations. In general, slope-break-based parameter estimates are superior to those obtained using variograms. Estimated root mean square errors at the plot level for the former average 6.5% for stem density, 3.5% for canopy closure and 2.5% for mean crown diameter, which are less than or equal to error rates obtained via traditional forest stand cruising by experienced personnel. The employed methodology entails parsimonious parameterization and is supportive of automation. Overall cover type classification accuracy increases from approximately 70% when using original imagery DNs to over 85% when band registration problems are corrected and variable brightness regimes among imagery frames are normalized. Limiting cover type classification to pixels identified as tree apexes is found to improve traditional classification approaches that use all pixels by 35%.*

*Image-texture analysis based on intensity co-occurrence provides a quantitative evaluation of second order image texture features that carry discriminatory potential for forest cover type classification purposes. Procedure development and evaluation is based on two independent data sets. Classification accuracies exceeding 60% can potentially be achieved by using only image texture information. In its current level of development, procedure applicability may be limited because of substantial computational cost, absence of computer software for automation, and the complexity of methodologies integral to the feature selection process.*

To my sweetheart and fiancée Evagelia Baros with all my love

Dr. Larry A.

Dr. David P.

thro

Dr. Hagop Q

tea

Dr. Steven K

in h

Dr. Jeremy

Frank Sapo

coll

Mark Zwe

The late Dr

dev

The late Dr

My friends

My parents

ACKNOWLEGEMENTS

Dr. Larry A. Leefers, my major professor, for his guidance and support;

Dr. David P. Lusch, my academic adviser, for stimulating my interest in remote sensing through his charismatic teaching;

Dr. Jiaguo Qi, for sharing his invaluable insights on analysis methodologies and techniques;

Dr. Steven K. Friedman, for providing working space and access to computing resources in his laboratory;

Dr. Jeremy S. Fried, for his long-term commitment to my academic progress;

Frank Sapio, for providing access to the imagery and financially supporting the field data collection;

Mark Zweifler, for the encouragement and help with research logistics;

The late Dr. Carl W. Ramm, for his mentoring and his contribution towards the development of critical thinking;

The late Dr. George Bouyoucos, whose fellowship enabled my graduate studies;

My friends, Gem, Joe, and Marcelo, for their encouragement; and

My parents, Georgios and Styliani Gatziolis, for their emotional support and love.

## TABLE OF CONTENTS

Table 2.1.

Table 2.2.
calculate
the NIR
centered

Table 2.3.
overlapp
before a
only the
coefficie
optimal

Table 2.4a.
assessm
signatur

Table 2.4b.
assessm
original

Table 2.4c.
assessm
original

Table 2.4d.
assessm
original

Table 2.4e.
assessm
original

Table 2.4f.
assessm
brightn

Table 2.4g.
assessm
post-by

## LIST OF TABLES

Table 2.4h. M
assessment
post-bright

Table 2.4i. M
assessment
post-bright

Table 2.4j. M
assessmen
post-bright

Table 2.5. Z
validation
respective

Table 2.6.
after brig

Table 2.7.
(deciduo
validatio

Table 3.1.
stem den
techniqu

Table 3.2.
density
measure
parenth
stem de

Table 3.3.
canopy
process
canopy

Table 3.4.
predic
crown
closure
percen

Table 3.5. Pa
crown diam
analysis to
image crow
crown delin

Table 3.6. R
predictions
using varia
using direc
subplots, a
Values in p
mean of m

Table 3.7a. C
associated
developed
break met

Table 3.7b. C
associated
developed
(slope bre

Table 3.7c. C
associated
developed
slope bre

Table 3.7d.
associated
developed
(slope bre

Table 3.7e.
associate
developed
(slope br

Table 3.7f.
associate
developed
break me

Table 3.7g. Cro
associated ac
developed fr
slope breal
pixel DNs...

Table 3.7h. Cr
associated a
developed f
slope breal
pixel DNs.

Table 3.7i. C
associated
developed
slope brea
pixel DNs

Table 3.7j. C
associated
developed
slope bre
pixel DNs

Table 3.8.
cross-val
differenc
in bold a
significa
identifie

Table 3.9.
decidua
validatio
using su
performa

Table 3.10.
after br

Table 3.1. Z-
cross-valid
differences
parentheses
scenarios e
pixels corre
imagery L

Table 4.1. C

Table 4.2. F
assessmen
classifier
homogene
independe

Table 4.3. S
accuracy
maximum
standard

Table A.1.

Table A.2.
deciduou

Table A.3.

Figure 2.1. St

Figure 2.3. Re
and each of
calculated u
colors corre

Figure 2.4. P
Site II (bot

Figure 3.1.
and corres
northern h

Figure 3.2.
and pixel
transect in

Figure 3.3.
cover type
NIR-band
condition
estimates
are symbo

Figure 3.4.
using loc
variogram

Figure 3.5.
types. Ca
crown ap
(LMF) w
(b) mean
LMF tec

## LIST OF FIGURES

Figure 3.6.
forest cove
delineation
maximum
variogram
coded wh

Figure 3.7.
forest cov
range of v
simplot in

Figure 3.8.
oak subp
performed
origin is a

Figure 3.9.
imposed
of cover t
of classif
slope bre
only.

Figure 4.1.
Correspo
Between-
for distan

Figure 4.2.
Weightin
weightin
shades in

Figure 4.3.
statistic
Angular

Figure 4.4.
decrease
from 1-D
Gaussian
expresse

Figure 4.5.
and quadr
Object cla

Figure 4.6.
subplot pa
d, and val

Figure 4.7.
for five su
area, usin

Figure 4.8.
discrimin
Level Co-
pixel disp

Figure A.1.

Figure A.2.

Figure A.3.
(24B). Cr
represent

Figure A.4.
associated
perspectiv

Figure A.5.
ground of
Dashed li
quadrants
segments
produced
ratio, $R_v$ =

Figure A.6.
(24B). Cr
represent

Figure A.7.
a 10 incre
occupying

Figure B.1.
indices of
empirical v
translation
numbers a
imaginary
normaliza

Figure B.2.
computed
processing
superimpo
plot denot

Figure B.3.
imagery d

# CHAPTER 1

## INTRODUCTION

## 1.1. Back

Remo

evolution of

American So

the measure

phenomenon

object or phe

be gleaned fr

frequently us

extracted fro

managers m

analysis are

of digital im

Toda

unicately In

incompatibi

ever increasi

multifaceted

spatial and te

non-spatial d

management

Remo

It is rather th

## 1.1. Background

Remote sensing has been synoptically defined as the detection, recognition, or evaluation of objects by means of distant sensing or recording devices. Formally, the American Society for Photogrammetry and Remote Sensing defined remote sensing as "the measurement or acquisition of information of some property of an object or phenomenon, by a recording device that is not in physical or immediate contact with the object or phenomenon under study" (Colwell, 1983). In forestry, the information that can be gleaned from visual interpretation of analog aerial photographs is well-understood, frequently used, and routinely integrated in forest planning and management. Information extracted from digital remote sensing data, however, is less commonly used. Many forest managers maintain that the majority of digital remotely sensed data and the methods of analysis are too complex to be of adequate utility to them. Furthermore, the effective use of digital imagery often requires substantial investment in technological infrastructure.

Today, more than ever, forest management challenges are multiscale and intricately linked to society's need to measure, preserve, and manage for multiple, often incompatible, values. Population growth and climate change are likely to catalyze these ever increasing pressures on forests. The forest ecosystem itself is complex and multifaceted. Understanding its functional structure requires information at a range of spatial and temporal scales. Remote sensing information, integrated with other spatial and non-spatial data sets, could form the information base upon which sound forest management decisions can be made.

Remotely sensed imagery on its own is probably of little value to forest managers. It is rather the interpretation of information extracted from those data that is used to

address management challenges. Converting data to information is not a straightforward task. It requires an understanding of the laws of physics and principles that govern the formulation of remote sensing data and expertise in selecting the appropriate data analysis methodology. It is often assumed that if an element of interest can be "seen" in a digital remote sensing image, there would shortly be an automated procedure capable of translating that visual impression into a usable piece of information. Practice has shown that such optimism if frequently unfounded.

Forestry remote sensing began with manual methods of analysis applied to analog aerial photographs (Silva, 1978). Relative to information content, analog aerial photographs are inexpensive and easy to use (Caylor, 2000). Comprehensibility and economic considerations make airphotos the most common form of remote sensing in forestry. As new types of imagery and analyses emerge, digital remote sensing will become increasingly useful for forest managers (Wynne et al., 2000). Clearly, the onus is on the remote sensing community to provide forest managers with examples of applications that are cost-effective and easily implemented. These considerations are the primary motivation for this dissertation. Using remote sensing data carrying some of the most advanced characteristics currently available, a series of methodologies were developed or refined that translated these data into information needed in operational forest management. The chapter begins with an outline of the dissertation's objectives. Then forest attributes retrievable by remote sensing are discussed, and characteristics of imagery acquisition systems are presented. A brief overview of the current and projected operational remote sensing applications follows. Finally, image processing and analysis

methods emphasizing the extraction of forest canopy characteristics and inventory variables are introduced.

## 1.2. Dissertation Objectives

The goal of this study was to evaluate the utility of airborne, high resolution, multispectral digital imagery for forest management decision-making in the structurally complex forested landscapes of the upper Midwest. To ensure that the findings would be representative, all dominant cover types in the region were included in the investigation. Development and testing of methodologies was based on detailed and precise field observations. The potential for automation, where promising, guided the methodology choices.

The three objectives of this dissertation were:

- Evaluate the influence of airborne image acquisition characteristics/idiosyncrasies on traditional, spectrally-based forest classification efforts.
- Assess the ability of image spatial analysis to reveal the horizontal structure of the forest canopy and to enhance classification accuracies.
- Evaluate the role image texture can have in stand classification.

## 1.3. Formation and Characteristics of Remote Sensing Data

A basic understanding of the characteristics of remote sensing data is essential when considering its relevance to providing forest information products. In an ideal world, a remote sensing image would be formed only from the energy reflected from a target, and received by a perfect sensor. In practice, image formation is a rather

complicated process. Gerstl (1990), Richard and Jia (1999), and Jensen (2000) offer a summary of the principles that govern the interaction of light energy with forests, as those are manifested in digital imagery. Other sources such as the energy reflected by objects in the vicinity of the target and the contribution from atmospheric constituents are exogenous to target radiance. The image formation process is also affected by the spectral (wavelength-range specific) reflectance characteristics of the target, viewing geometry (which describes the position of the sensor relative to the target), and illumination geometry (which for optical remote sensing describes the position of the sun in relation to the target). To complicate the process further, spectral target reflectance, and viewing and illumination geometry factors are not independent. Rather, they operate synergistically and regulate target reflectance in a spatial pattern referred to as the bi-directional reflectance distribution function (BRDF). Forests in particular, because of their complicated structure, cause a strongly directional reflectance. Accounting for the effects of illumination geometry, atmosphere, and BRDF, would help the interpretation of remote sensing image in forest applications.

Remotely sensed data are typically presented to the user in the form of digital numbers (DN). Digital numbers are the quantification of energy recorded by the sensor via an analog-to-digital converter. Because DNs are consistent within the imagery, in the sense that higher DNs correspond to a higher amount of energy or density of photons intercepted in unit time, they can be used in image analysis without further processing (Franklin and Giles, 1995). The assumption made is that analog-to-digital converters translate photon density to DNs monotonically. A more rigorous assumption is that photon density and DNs are related linearly. The coefficient that describes the

relationship is commonly known as the gain of the sensor. Knowing the gain coefficient facilitates imagery comparisons acquired using the same or different sensors at different times, and the comparison between satellite, airborne and field-based sensor measurements. Most satellite sensors provide calibration information embedded in the header of the imagery. Digital airborne imagery acquired by commercial vendors often completely lacks information on sensor calibration thereby depriving the user of the opportunity to fully explore the information content of the imagery. The implications might be more serious for multispectral array scanners, which are in essence a collection of theoretically identical detectors arranged on a grid. Many array scanners currently in use, including those employed in the acquisition of the imagery used in this dissertation, are equipped with a million or more such detectors across the matrix and the assumption that all of them are operationally identical is undoubtedly improbable. Calibrating detector is practically infeasible though, and image analysis usually proceeds assuming that sensitivity and gain differences among detectors are negligible.

Sensor resolution is a compound term comprising spectral, spatial, radiometric, and temporal dimensions. Spectral resolution denotes the number and width of specific wavelength intervals, known as bands or channels, of the electromagnetic spectrum to which the sensor is sensitive. Particular intervals, sometimes as narrow as 5nm, are optimal for uncovering certain biophysical information. Broadband multispectral sensors are designed to detect radiance across a 50 to 100nm, usually non-overlapping, intervals in a few different areas of the spectrum. Hyperspectral sensors detect radiance over very narrow intervals (e.g., 2 to 4 nm wide).

Spatial resolution is the projection of the detector element through the sensor optics onto the landscape forming the instantaneous field of view (IFOV). It corresponds to the smallest separation distance between objects that can be distinguished by the sensor. The higher the spatial resolution the smaller the objects that can be detected. The spatial resolution of airborne platforms is dependent on the flight altitude. Irrespective of altitude, the energy intercepted by a single detector, is represented, after its quantification to DN, as an image or picture element (pixel).

Frequently, remote sensing data are distinguished in terms of their spatial dimension as of L(ow)- or H(igh)-resolution (Strahler, 1986). This characterization is in reference to the size of the object(s) of interest. It is possible the same imagery set to be L-resolution for one application and H-resolution for another. In forestry remote sensing, typical satellite data are L-resolution ($\geq$20-30m pixels). In this case, the dominant scene objects (trees) are smaller than the pixel size and the sensor records the composite radiance emanating from a collection of trees within the pixel area. Airborne data are usually H-resolution ($\leq$2m pixels), with a single, average-sized tree crown being larger than the pixel size. Therefore, radiance measured for a given pixel location is likely to be directly related to the reflectance characteristics of an individual tree crown or portion of a crown.

Radiometric resolution is related to the sensor's ability to detect differences in the signal strength of intercepted energy in specific wavelengths. Greater radiometric resolution allows smaller differences in reflectance to be discriminated. Sensor radiometric resolution in expressed in bits ($2^n$) where the value of $n$ is usually between 8

and 16. Thus, a 16-bit sensor is theoretically capable of discriminating $2^{16}$ (= 65,536) radiance increments within its sensitivity range.

With the exception of temporal resolution (the ability to provide repeated coverage of a particular area), which can be considered as an independent dimension, there are certain trade-offs among the remaining three imagery resolution dimensions. An increase in the number of bands or channels is often accompanied by a decrease in spatial resolution. To acquire more or narrower bands, a sensor must view an area on the ground for a longer period of time, and therefore, the size of the area viewed increases from a constant altitude. If the radiometric resolution is increased so that smaller differences in radiance can be detected, then the spatial resolution, the number of bands, the narrowness of the bands, or all three, must be reduced. This is because the amount of energy that is reflected from the area viewed is fixed. If the amount of energy is divided into too many bands (spectral resolution) using many increments (radiometric resolution) over too small an area (spatial resolution), then the energy signal becomes unacceptably weak compared to the always-present system noise. In sensor design, it is the signal-to-noise ratio that should be maximized, rather than any of the spectral, spatial, or radiometric resolutions.

## 1.4. Remote Sensing Platforms

Digital remote sensing data of forests can be acquired from field-based, airborne, and satellite platforms and might comprise a variety of imagery types (Chen et al., 1991) or non-imaging spectroscopy measurements (Miller et al., 1976). Many types of ground platforms have been used in remote sensing of forest canopy spectral reflectance (Blackburn and Milton, 1997). Field spectroscopy can be used in remote sensing in at least three ways (Milton et al., 1995): 1) to provide data for developing and testing of

models of spectral reflectance, 2) to collect calibration information for airborne or satellite image acquisition (Wulder et al., 1996), and 3) as a remote sensing tool of its own (Blackburn, 2000).

A variety of free-flying airborne platforms have been used in collecting remote sensing observations. The ones most commonly used include low- and high-altitude flying aircrafts and satellites. Sensors on airborne platforms typically offer greatly enhanced spatial and spectral resolution over their satellite counterparts, coupled with the ability to more closely control experimental design during image acquisition. For example, they allow control over flight path azimuth or they can operate under clouds and at different altitudes from low and slow survey flights (McCreight et al., 1994) and to high-altitude reconnaissance flights (Moore and Pozlin, 1990). Airborne sensors usually exceed satellite system capabilities in terms of their combined spatial resolution, spectral resolution, and signal-to-noise ratio performance (Anger, 1999). As a result, satellite imagery cannot be expected to replace digital airborne imagery by providing the same type of forestry information (Roller, 2000). Basically, airborne data are of higher quality. Airborne sensors allow longer exposure or dwell times, they often offer a customizable sampling of the electromagnetic spectrum to fit the needs of the user, and their measurements can be calibrated and atmospherically corrected by simultaneous ground-based measurements over deployed reflectance targets. Compared to satellite imagery however, airborne digital imagery has higher acquisition cost per unit area covered, inferior sensor calibration, smaller area footprint, often ambiguous data documentation, and only rarely availability of imagery archives at frequencies higher than once in 5-10 years.

Much of the cost of remote sensing is embedded in the analysis of the imagery to produce information products. Generally, imagery quality is more important that the initial acquisition cost, particularly in applications where the final cost of the information product is critical (Agner, 1999). Often a better quality, and therefore more expensive, set of images can yield information more economically, simply because it requires less processing. The challenge is to optimize the choice of an imagery type to meet the needs of the user (King, 1995). Bergen et al., (2000) presented a list of criteria that can be used to assess the cost-effectiveness of information using the characteristics of the derived information and the cost of producing such information. In cases where remotely sensed information mandatory for the development of management plans can replace what is typically acquired with field visits, the cost savings can be very significant. Even if remote sensing information can only partially replace field-collected information, the use of remote sensing technology could still be economically prudent.

## 1.5. Imagery Calibration

Remote sensing data contain a series of distortions produced by sensor imperfections, atmospheric effects, viewing and illumination conditions, and topography. In general, in digital analysis, failure to normalize these radiometric and geometric distortions could lead to inaccurate remote sensing output products (Yang and Vidal, 1990), especially in the presence of significant relief (Sandmeier and Itten, 1997). Radiometric imagery correction can be a multi-stage process in which DNs are in succession converted to at-sensor radiances, at-sensor reflectances, and finally to target reflectances using atmosphere and illumination models (Sandmeier and Itten, 1997). All steps are not always necessary. Often, only internally consistent calibration to at-sensor

radiance

be an ac

of image

availabl

analyst.

T

direction

specific

same tim

BRDF e

radiolog

Scatter

correctio

images

provide

which is

between

T

In image

because

altitude,

Investme

using arra

radiances (Wilson et al., 1994; Wolter et al., 1995) is sufficient. In some cases there may be no need to perform any radiometric correction at all (Cohen et al., 1998). The number of image radiometric correction stages that should be implemented is a function of the availability of calibration information, analysis objectives, and the experience of the analyst.

The complexity of atmospheric and topographic effects increases by the strongly directional reflectance patterns of forest canopies. Because BRDF effects are target-specific, information on canopy characteristics is required prior to its correction. At the same time, extracting canopy information such as cover type requires atmospheric and BRDF effects to be normalized first, which gives rise to a tautology. To avoid the tautology, it is common practice to assume that canopies exhibit Lambertian behavior (Sandmeier and Itten, 1997), which in turn renders topographic and atmospheric corrections only marginally successful. Geometric distortions are related to sensor and imaging geometry and topography (Fogel and Tinney, 1996). Corrections can applied to provide locational accuracy (Burkholder, 1999), but they necessitate image resampling which is known to alter pixel spectral characteristics proportionally to the spatial relation between the input and output grids.

The forms of imagery distortions mentioned above are usually more pronounced in imagery acquired by airborne platforms, especially those flying at low altitudes, because of the large parallax present and the sometimes substantial variation in platform altitude, velocity, and attitude. Distortion correction requires a substantial effort investment by experienced analysts, especially for digital airborne imagery acquired using array scanners. Contrary to satellite imagery, where each image frame typically

encompasse

average

National Fo

imagery fra

varying targ

particular,

acility fre

ween betwe

brightness

the spectra

imitations

compone

imagery

to know

of BRDF

a handful

discussion

coarse re

concerned

methodo

allowing

encompasses tens of thousands of hectares, airborne digital imagery frames extend over an average of only 100 hectares. Hence, airborne imagery covering a watershed or a National Forest, usually comprises several hundred to thousand frames. Such large imagery frame sets have coordinate systems of variable orientation, are characterized by varying target reflectance and brightness regimes. In the forests of the upper Midwest in particular, which are characterized by intense fragmentation and cover type variability, and by frequent presence of swamps, wetlands, and lakes, such brightness variability even between image frames acquired in sequence is prominent. Although in theory brightness variability could be easily normalized across the entire imagery set by using the spectral gain factor effective during each image frame acquisition, practical limitations originating at the sensor's sensitivity adjustment at the analog system component (i.e. prior to signal conversion from analog to digital format), typically result in imagery sets for which the per-frame gain factor remains unknown. To date, there are no known examples of research investigations that attempted a simultaneous correction of BRDF effects, geometric distortions, and variable brightness regimes using more than a handful of array scanner imagery frames. Perhaps the difficulty in correcting those distortions has discouraged such efforts; or perhaps the preoccupation with the relatively coarse resolution spatial imagery obtained from satellite platforms has prevented a more concerted effort in the airborne arena. Those issues are addressed in this dissertation. A methodology was developed, capable of substantially reducing distortion magnitude and allowing for significant improvements in the quality of subsequent analysis products.

## 1.6. Current and Projected Operational Forestry Remote Sensing Applications

Remote sensing has the potential of playing a critical role in forest management in many different settings – operational forest cover mapping, forest structure and change analysis, and forest inventory assessment. A minimal list of probable, near-future operational forest remote sensing applications could include (Wynne and Carter, 1997): a. Forest cover type characterization, b. Determination of forest stand conditions and forest health, c. Site characterization, and d. Fire monitoring. If emphasis is shifted from applications to the fundamental concepts of digital remote sensing, additional applications in forestry could be considered operational (Cohen et al., 1996): e. Mapping forest cover, f. Measuring and monitoring structure, function, and composition of vegetation, and g. Detecting change in these conditions over time. An additional set of applications appears to be on the threshold of operational status: landscape structure modeling, defoliation monitoring, and biophysical forest inventory. It is expected that by 2008 a complete set of operational remote sensing applications in forestry, will become increasingly apparent, with major contributions primarily from analysis of high-resolution imagery (Wynne and Oderwald, 1998).

## 1.7. Analysis Methods of Remotely Sensed Data in Forestry

Most forestry remote sensing analysis methods are either experimental or normative. The former operate on the assumption that the control of variables influencing a phenomenon under investigation is feasible. In forest remote sensing applications the experimental method is used to improve our understanding of the relationship between a forest condition of interest and the information available about that condition extracted

from remote sensing data. In this context, the analysis can be viewed as an experiment where the remote sensing data are the dependent variables and the forest condition(s) of interest form the independent variables. If control could be exerted on all the independent variables, then it could be expected that a strong relationship be identified between the independent and dependent variables. The identified relationship could then be treated as a precise and accurate predictive model that, when inverted, could provide reliable estimates of the forest condition under investigation using only remote sensing data (Bracher and Murtha, 1994).

Controlling all confounding variables is perhaps feasible in a laboratory setting. In an actual image acquisition mission over a forested area though, it is impossible to know all the variables that influenced the remote sensing measurements. These influences cannot be uniquely determined, but can certainly overwhelm the signal from the condition of interest. Hence, the actual relationship between a forest condition and remotely sensed data is typically much less predictable than those obtained by standard experimental methods (Blackburn, 2000). Because of this limitation, the normative (Haring, 1992) method is often employed.

Under the normative approach there is typically a lack of control of the independent variables that influence the image characteristics. This makes the relationships found subject to caveats and constraints that must be carefully documented and described. Although the normative approach supports the development of relationships under less than ideal conditions, it suffers from the lack of generality that could lead to highly spurious local insights, especially where there is very little theoretical foundation in support of an identified relationship.

Both experimental and normative remote sensing analysis methodologies are, in essence, modeling efforts. A unique characteristic of the remote-sensing-based models is that, in their inverted mode, all their independent variables are derived from sensor measurements of energy reflected (or backscattered) from an object or condition. The models operate under the implicit assumption that object or condition variates cause a predictable variation on sensor measurements. In digital remote sensing over forested landscapes this assumption may not necessarily hold. For example, the energy reflected from a forest stand canopy in a leaf-on condition, is basically unaffected by the stand stem wood mass. If the objective were to estimate wood biomass using remote sensing, it would seem more reasonable to use one or more surrogate variables (e.g., crown diameter, tree height, species association) for which more accurate quantitative estimates can be derived using remote sensing data and then use these surrogate variables to predict stand woody biomass. Such considerations have raised concerns that perhaps the application of remote sensing technology to routine forest management is not feasible, at least in the short term (Battaglia and Sands, 1998). From a remote sensing analyst's perspective, it is frequently the absence of explicit and complete problem definition that has precluded wide acceptance of remote sensing as a forest management tool (English and Dale, 1999). Despite reservations by certain forest managers, there appears to be a general consensus that the synoptic and repetitive biophysical vegetation information requirements for large geographic areas over long periods of time can only be provided by remote sensing.

Several studies in the 1980s established that low-resolution satellite data can be classified for forest cover, stand age, and crown closure (Walsh, 1980; Horler and Ahern,

1986). In most studies since then, correlations to height, basal area, and biomass were good to moderate (e.g., Kovats, 1997; Shettigara and Sumerling, 1998); correlations to density, size diversity, mean diameter, and number of species were moderate (e.g., Roy et al., 1996; Cohen et al., 2001; Franco-Lopez, 2001); and correlations to understory measures such as number of seedlings, and understory cover were weak (e.g., Stenback and Congalton, 1990; Jakubauskas and Price, 1997; Hall et al., 2000). Even the better correlations though were usually too weak to allow them to be used in forest management and planning. The main problem is rooted in the fact that the optical sensor only detects reflectance from the top of the canopy (Holmgren and Thuresson, 1998) effectively precluding assessment of attributes that are physically demonstrable only beneath the canopy. In many forests, crown closure will reach a maximum while basal area and structural complexity will continue to increase, but the optical remotely sensed signal, particularly from low-resolution imagery, is not significantly affected by these changes (Franklin, 1986).

High spatial or spectal resolution digital imagery is subject to similar restrictions in terms of its beneath-canopy, forest-stand structure information content. However, it offers a much more detailed view of the horizontal structure of the canopy. In particular, it provides explicit information on the amount and spatial distribution of shadowing in the stand, which can exert a dominant influence on the stand's reflectance (St-Onge and Cavayas, 1995). A pixel in this type of imagery would characterize only a small part of the tree crown, shadow, or the understory. The spatial detail present in high-resolution imagery allows individual tree-crown delineation (Gougeon, 1995; Brandtberg, 1997), and could improve estimates of crown closure, stem density, and species composition by

exploring image texture (Gerylo et al., 1998). Identification of individual trees has been successful with images having spatial resolution of 0.6m or smaller, but conceivably will work well enough with 1m satellite data to justify more extensive use and development (Wulder, 1999). Most investigations of individual tree identification have been reported in pure or mixed conifer stands where the conical shape of crowns generates abrupt distinctions between sunlit and shadowed portions of crowns and facilitates accurate tree identification. In deciduous stands, tree crowns usually defy formal shape conventions, have multiple crown maxima and less distinct edges, making tree identification much more challenging (Warner et al., 1999). Although imagery with 1m or finer spatial resolution has been available from airborne platforms for decades, and is now becoming available from satellite platforms, there are very few examples of projects using this type of imagery for stand structure, species composition, and crown closure mapping.

In this dissertation the normative analysis approach was used. The concerns aforementioned and related to the ability of optical remotely sensed imagery to provide accurate and reliable information on forest structure, even in the presence of high resolution imagery, guided the early stages of dissertation objective formulation. In response to those concerns, analyses focused on canopy cover type classification and on quantifying canopy surface attributes including stem density, canopy closure, and crown size. Were other types of forest structure information to be pursued (e.g., tree height, composition of understory vegetation, basal area, etc.), non-optical remotely sensed imagery (microwave, lidar) would have been explored as more promising for delivering those types of information (Dubayah and Drake, 2000; Fransson et al., 2000). To improve the chances of regional methodology applicability, analyses techniques were based on

canopy morphological characteristics extracted from the imagery, rather than, for example, identified mathematical relationships.

## 1.8. Image Information Extraction by Spectral Analysis

The extraction of information from remotely sensed data is usually based on differentiating spectral response patterns in the landscape. The three more common types of information of interest in forest management applications are: a). Continuous forest variable estimation, b). Forest classification information, and c). Forest change or difference information. A plethora of image analysis techniques has been proposed for deriving such information, and each technique has spawned numerous options, that will likely continue to evolve. A common characteristic among analysis methods is that they are oriented towards providing information at the stand level, which should not come as a surprise given that most methodologies were developed for L-resolution imagery. Using essentially those same techniques with H-resolution imagery can potentially be imprudent, given that the information content in H- and L-resolution imagery is organized at different spatial levels. To confirm the hypothesis that indeed high spatial resolution imagery is a unique information source for forestry applications that requires the use of specific analysis methods, this research investigated the second type of forest applications mentioned above (forest classification) in a dual spatial scope: at the stand-level and at the individual tree level.

Continuous variable estimation occurs primarily by one of the few common forms of inversion modeling, including regression analysis, neural networks, reflectance modeling, or radiative transfer modeling. These approaches follow traditional, albeit sometimes unconventional, statistical probability design where two sets of variables, one

derived from the imagery and the second from field observations or ancillary information, are related. Because however, these methods do not account for the position of the pixels within the forest stand examined, and offer no theoretical justification for the form of the models produced, the accuracy of the continuous variables they estimate is largely dependent on the quality and comprehensiveness of the input training data (Salvador and Pons, 1998) and tends to drop substantially when used at stand conditions other than those used to developed the models. To improve the robustness of derived continuous variable estimates in this research, model formulation was spatially explicit, in the sense that the spatial relationships among adjacent pixels determined model output.

Positionally explicit information for model development and evaluation, however, is rather costly, especially at the individual tree level. Very few cases are known (Warner et al., 1999; Pouliot et al., 2002; Wulder et al., 2002) for which spatially explicit stem information was used, and all involved a single stand. Tree stem location information probably suffices for an evaluation of methods aiming at predicting stem density but is likely inadequate for models developed to estimate canopy structure variables, such as canopy closure and mean tree diameter. Those concerns led to an ambitious endeavor that by using survey equipment and methodology mapped precisely the horizontal canopy structure of plots installed in 34 stands, stratified across major cover types of the Midwest region. It was assumed that the detailed field observations could lead to interesting insights related to how canopy structure is manifested in high-resolution imagery and permit canopy structure model tuning to account for those insights. Whether the expenses associated with such an endeavor were justified, can be judged by observing associated

research findings, not only in terms of estimate accuracy obtained but also in regard to the value and generalized applicability of the methodologies employed.

A major trend in remotely sensed data analysis in forestry has been the emphasis on automation. However, it is still the case that most techniques, even when supported by software package routines, require substantial human intervention, judgment, and guidance in order to operate successfully, prerequisites that defy automation. The importance of automation is more pronounced in the analysis of high-resolution imagery in part because of the small footprint and therefore the large number of image frames that need to be processed. Possibly the only area in forestry remote sensing where automation and standardization has been achieved is the assessment of classification accuracy in the form of a contingency table or confusion matrix (Congalton and Green, 1999).

## 1.9. Beyond Spectral Analysis

Despite numerous achievements associated with information product extraction from digital imagery in forestry, the accuracy of product attributes are usually inferior to those achieved by experienced interpreters of analog aerial photographs. This might be, in part, because digital imagery rarely supports stereoscopic view of the forest but probably also because attribute value estimation is usually based strictly on the per-pixel spectral response of the forest. Photointerpreters, on the other hand, in addition to tonal characteristics, are accustomed to using a variety of textural, pattern, shape, object, shadow, and topographical evidence. Improvements in the use of these texture/context descriptors in digital remote sensing analysis may allow canopy structure parameter estimates obtained from digital imagery to rival the accuracy levels that manual photointerpretation achieves (Green, 2000). Development of such methodologies is

emphasized by the need for forest classification and inventory parameter product integration with other forms of digital information usually provided via Geographic Information Systems, and the steady decline in the number of experienced photointerpreters available to perform those tasks.

One of the most promising alternatives to spectrally-based analysis of digital imagery in forestry is to consider classification in a spatial context. The premise is that a pixel's most probable classification, when viewed in isolation, may change when viewed in some context (Haralick and Joo, 1986). The simplest context classifiers use neighboring pixels to decide, confirm, or change the classification or labeling of the pixel at the center of the neighborhood. Attempts to broaden context classifier algorithms have included incorporating the spatial correlation function between pixels (Khazanie and Crawford, 1990) and contextual parameters (Chen, 1999). These concepts are closely related to image texture analysis. Image texture is the quantification of the spatial variation of image tones, often referred to as gray levels, that defies precise definition because of its perceptual character (Hay et al., 1996).

Human vision possesses a powerful innate ability to recognize textural differences, although the complex neural and psychological processes by which this is accomplished have so far evaded detailed scientific explanation. The interest in quantifying texture in digital domains has led analysts to focus on the structural and statistical properties of textures (Haralick, 1986). It is expected that by combining per-pixel and area-based texture processing, more accurate classifications of remotely sensed imagery can be generated (Ryherd and Woodcock, 1997). Parallel to the use of texture in classification, interest has developed in texture itself as a variable in forest applications

(Coops and

aspects of f

al., 1996; S

Ima

in a variety

sensing, re

metrics. Th

Today, the

metrics ma

chapter of

type classi

co-occurre

the investig

methodolo

## 1.1

Th

study obje

formation,

detection,

customaril

that allows

among ima

impact of g

(Coops and Culvenor, 2000). Texture has been shown to be directly related to different aspects of forest stand structure, including age, density, and leaf area index (Wulder et al., 1996; St-Onge and Cavayas, 1997).

Image texture, however, is an abstract term. Its quantification has been attempted in a variety of disciplines including machine vision, pattern recognition, and remote sensing, resulting in a large number of approaches and an even larger number of texture metrics. Their value for forestry remote sensing applications is, at large, unknown. Today, there are few guidelines to help analysts decide which of these approaches and metrics may be better suited, if suited at all, for a particular forestry application. A chapter of this dissertation is devoted in providing such guidelines towards forest cover type classification using a branch of texture quantification methods known as gray level co-occurrence analysis. Instead of simply relaying analysis results for the metrics used in the investigation, as is the usual case, the chapter provides a detailed presentation of methodology options encountered at every step of the multistage procedure employed.

## 1.10. Dissertation Outline

The current chapter described the motivation behind the dissertation research, the study objectives, and a brief exposure to the factors that affect remote sensing imagery formation, calibration, and analysis used in forestry applications. Chapter 2 deals the detection, quantification, and correction of a series of imagery imperfections that are customarily encountered in a digital airborne imagery set. It presents a novel approach that allows for a simultaneous correction of BRDF and variable brightness regimes among imagery frames and a technique for reducing band registration problems. The impact of geometric and radiometric imperfections on the accuracy of forest cover type

classification based on the popular, maximum likelihood method is assessed by comparing classification results obtained using the original imagery set and one obtained after correction/ normalization of the imperfections. It is shown that although corrections do improve classification results, the classification accuracy even for the corrected set remains too low to be of any utility.

Chapter 3 describes a parametric method known as variogram analysis and the development of a non-parametric metric, both capable of quantifying pixel brightness autocorrelation and used for the identification of tree apexes, the number of which is subsequently converted to an estimate of stand density. Further investigations of canopy reflectance patterns based on identified tree apexes, yield estimates of canopy closure and mean crown diameter. Estimate accuracies were found to be comparable, if not superior, to those obtained with field observations, especially when tree apexes are identified using the non-parametric approach. The Chapter also describes cover type classification scenarios involving only pixels identified as tree apexes. It is shown that a remarkable accuracy improvement of more than 30 percentage points is achieved compared to the traditional, non-spatially explicit approach used in Chapter 2. Classification accuracies achieved using the corrected imagery (>85%) are found to approach operational status.

Chapter 4 describes the use of image texture for forest cover type classification purposes. It introduces a multistage procedure, which shows that the quantitative evaluation of texture-related cover type discrimination power associated with image bands, necessary image pre-processing choices, texture measures, and finally texture features can provide classification accuracies similar to those obtained using spectral classification of raw (uncorrected) imagery.

Chapter 5 provides a critique of analysis methods used in this dissertation and an evaluation of analysis results. It also describes a framework that can be used to combine spectral, textural, and canopy structural characteristics for potential improvements in cover type classification accuracy. Insights regarding field data collection methodologies and a projection of additional research investigations in the study area are also presented.

## Literature


Anger, C.D.
4th Int. S
Aeronau

Banaglia, M
applicata

Bergen, K.,
impleme

Byrne, G.S
videogra
Sensing

Blackburn,
using ai
Rem. Se

Blackburn,
concentr
237.

Brandtberg,
resolutio

Bracher, G.,
Douglas

Burkholder,
Model, S

Caylor, J. 20

Chen, J.M.,
for deter
Meteorol

Chen, J.M. 1
Rem. Sen

Cohen, W.B.
methods
USA. En

## Literature Cited


Anger, C.D. 1999. Airborne hyperspectral remote sensing in the future? In Vol I, *Proc. 4th Int. Symp. Airborne Rem. Sensing 21st Can. Symp. Rem. Sensing*, Canadian Aeronautics and Space Institute, Ottawa, Canada, pp. 1-5.

Battaglia, M., and P.J. Sands. 1998. Process-based forest productivity models and their application in forest management, *For. Ecol. Manage.*, 102:13-32.

Bergen, K., J. Colwell, and F. Sapio. 2000. Remote sensing and forestry: collaborative implementation for a new century of forest information solutions, *J. For.*, 98:5-9.

Biging, G.S., M. Dobbertin, and E.C. Murphy. 1995. A test of airborne multispectral videography for assessing the accuracy of wildlife habitat maps, *Can. J. Rem. Sensing*, 21:357-367.

Blackburn, G.A., and E.J. Milton. 1997. An ecological survey of deciduous woodlands using airborne remote sensing and geographical information systems (GIS), *Int. J. Rem. Sensing*, 18:1919-1935.

Blackburn, G.A. 2000. Relationships between spectral reflectance and pigment concentrations in stacks of deciduous broadleaves, *Rem. Sensing Environ.*, 70:224-237.

Brandtberg, T. 1997. Towards structure-based classification of tree crowns in high spatial resolution aerial images, *Scand. J. For. Res.*, 12:89-96.

Bracher, G., and P. Murtha. 1994. Estimation of foliar macro-nutrients and chlorophyll in Douglas-fir seedlings by leaf reflectance, *Can. J. Rem. Sensing*, 20:102-115.

Burkholder, E.F. 1999. Spatial data accuracy as defined by the Global Spatial Data Model, *Surv. Land Inf. Syst.*, 59:26-30.

Caylor, J. 2000. Aerial photography in the next decade, *J. For.*, 98: 12-18.

Chen, J.M., t.A. Black, and R.S. Adams. 1991. Evaluation of hemispherical photography for determining plant area index and geometry of a forest stand, Agric. For. Meteorol., 32:1656-1665.

Chen, J.M. 1999. Spatial scaling of a remotely sensed surface parameter by contexture, *Rem. Sensing Environ.*, 69:30-42.

Cohen, W.B., J.D. Kushla, W.J.Ripple, and S.L.Garman. 1996. An introduction to digital methods in remote sensing of forested ecosystems: focus on the Pacific Northwest, USA, *Environ. Manag.*, 20:421-435.

Cohen, W.B. M. Fiorella, J. Gray, E. Helmer, and K. Anderson. 1998. An efficient and accurate method for mapping forest clearcuts in the Pacific Northwest using Landsat imagery, *Photogramm. Eng. Rem. Sensing,* 64:293-300.

Cohen W.B., T.K. Maierspergers, T.A. Spies, and D.R. Oetter. 2001. Modelling forest cover attributes as continuous variables in a regional context with Thematic Mapper data, Int. J. Rem. Sensing, 22:2279-2310.

Colwell, R.N. 1984. *Manual of Remote Sensing*, 2nd Ed., Falls Church, VA, American Society of Photogrammetry.

Congalton, R.G., and K. Green. 1999. *Assessing the Accuracy of Remotely Sensed Data: Principles and Practice*, CRC Press, Boca Raton, Florida.

Coops, N.C., and D. Culvenor. 2000. Utilizing local variance of simulated high spatial detail imagery to predict spatial patterns of forests, *Rem. Sensing Environ.*, 71:208-260.

Dubayah, R.O., and J.B. Drake. 2000. Lidar remote sensing for forestry, *J. For.*, 98:44-46.

English, M.R., and V.H. Dale. 1999. Next steps for tools to aid environmental decision making. In V.H. Dale and M.R. English, Eds. *Tools to Aid Environmental Decision Makers*, Springer-Verlag, New York.

Fogel D.N., and L.R. Tinney. 1996. *Image registration using multiquadratic function, the finite element method, bivariat mapping polynomials and the thin place spline*, NCGIA Tech. Rep. 96-1. University of California, Santa Barbara.

Franco-Lopez H., A.R Ek, and M.E. Bauer. 2001. Estimation and mapping of forest stand density, volume, and cover type using the k-nearest neighbors method, *Rem. Sensing Environ.*, 77:251-274.

Franklin, S.E. 1986. Thematic Mapper analysis of conifer forest structure and composition, *Int. J. Rem. Sensing*, 7:1287-1301.

Franklin, S.E., and P.T. Giles. 1995. Radiometric processing of aerial and satellite remote sensing imagery, *Comput. Geosci.*, 21:413-425.

Fransson, J.E.S., F. Walter, and L.M.H. Ulander. 2000. Estimation of forest parameters using CARABAS-II VHF SAR data, *IEEE Trans. Geosci. Rem. Sensing*, 38:720-727.

Gerstl, S.A.W. 1990. Physics concepts of optical and radara reflectance signatures, *Int. J. Rem. Sensing*, 11:1109-1117.

Gerylo, G
image
form

Gougeon,
indiv
21:27

Green, K

Hall R.J.
mixe
For

Haralick
Han

Haralick
24:9

Hanng,
Geo

Hay, G.
anal

Holmgr
revi

Horler,
data

Jakubau
spe
Sen

Jensen,
Pre

Khazar
con

King, I
rev

Gerylo, G., R.J. Hall, S.E. Franklin, A. Roberts, and E.J. Milton. 1998. Hierarchical image classification and extraction of forest species composition and crown closure form airborne multispectral images, *Can. J. Rem. Sensing*, 24:219-232.

Gougeon, F. 1995. A crown-following approach to the automatic delineation of individual tree crowns in high spatial resolution aerial images, *Can. J. Rem. Sensing*, 21:274-284.

Green, K. 2000. Selecting and interpreting high-resolution images, *J. For.*, 98:37-39.

Hall R.J., D.R. Peddle, and D.L. Klita. 2000. Mapping conifer understory within boreal mixedwoods from Landsat TM satellite imagery and forest inventory information, *For. Chron.*, 76:887-902.

Haralick, R.M. 1986. Statistical image texture analysis. In T.Y. Young and K.S. Fu, Eds. *Handbook of Pattern Recognition and Image Analysis*, Academic Press, New York.

Haralick R.M., and H. Joo. 1986. A context classifier, *IEEE Trans. Geosci. Rem. Sensing*, 24:997-1007.

Haring, L.L., J.F. Lounsbury, and J.W. Frazier. 1992. *Introduction to Scientific Geographic Research*, 4th ed. Wm. C. Brown Publishers, Dubuque, Iowa.

Hay, G.J., K.O. Niemann, and G.F. McLean. 1996. An object-specific image texture analysis of H-resolution forest imagery, *Rem. Sensing Environ.*, 55:108-122.

Holmgren, P., and T. Thuresson. 1998. Satelite remote sensing for forest planning – a review. *Scand. J. Rem. Sensing*, 13:90-110.

Horler, D.N.H., and F.J. Ahern. 1986. Forestry information content of Thematic Mapper data. *Int. J. Rem. Sensing*, 7:405-428.

Jakubauskas M.E., and K.P. Price. 1997. Empirical relationships between structural and spectral factors of yellowstone lodgepole pine forests, *Photogramm. Eng. Rem. Sensing*, 63:1375-1381.

Jensen, J.R. 2000. *Remote sensing of the environment, an earth resource perspective*, Prentice-Hall, Engelwood Cliffs, New Jersey.

Khazanie, N., and M.M. Crawford. 1990. Spatial-temporal autocorrelated model for contextual classification, *IEEE Trans. Geosci. Rem. Sensing*, 28:529-539.

King, D.J. 1995. Airborne multispectral digital camera and video sensors: a critical review of system designs and applications, *Can. J. Rem. Sensing*, 21: 245-273.

Kovats, M. 1997. A large-scale aerial photographic technique for measuring tree heights on long-term forest installations, *Photogramm. Eng. Rem. Sensing*, 63:741-747.

Li, X., and A. Strahler. 1985. Geometric-optical modeling of a conifer forest canopy. *IEEE Trans. Geosci. Rem. Sensing*, 23:705-721.

McCreight, R., C.F. Chen, and R.H. Waring. 1994. Airborne environmental analysis using ultralight aircraft, In Vol I *Proc. 1st Int. Airborne Rem. Sensing Conf.*, ERIM, Ann Arbor, Michigan, pp. 384-392.

Miller, L.D., R.L. Pearson, and C.J. Tucker. 1976. A mobile field spectrometer laboratory, *Photogramm. Eng. Rem. Sensing*, 42:569-572.

Milton, E.J., E.M. Rollin, and D.R. Emery. 1995. Advances in field spectroscopy, In F.M. Danson, and S.E. Plummer, Eds. *Advances in Environmental Remote Sensing*, John Wiley & Sons, London, pp 9-32.

Moore, W., and T. Polzin. 1990. ER-2 high altitude reconnaissance: a case study, *For. Chron.*, 66:480-486.

Pouliot, D.A., D.J. King, F.W. Bell, and D.G. Pitt. 2002. Automated tree crown delineation in high-resolution digital camera imagery of coniferous forest regeneration, *Rem. Sensing Environ.*, 82:322-334.

Richards J.A., and X. Jia. 1999. *Remote Sensing Digital Image Analysis. An introduction*, 3rd ed. Springer-Verlag, New York.

Roller, N. 2000. Intermediate multispecral satellite sensors, *J. For.*, 98:32-35.

Roy, P.S., K.P. Sharma, and A. Jain. 1996. Stratification of density in dry deciduous forest using satellite remote sensing digital data - an approach based on spectral indices, *J. Biosci.*, 21:723-734.

Ryherd, S., and C.E. Woodcock. 1997. Combining spectral and texture data in the segmentation of remotely sensed images, *Photogramm. Eng. Rem. Sensing*, 62:181-194.

Salvador R., and X. Pons. 1998. On the reliability of Landsat TM for estimating forest variables by regression techniques: a methodological analysis, *IEEE Trans. Geosci. Rem. Sensing*, 36:1888-1897.

Sandmeier, St., and K.I. Itten. 1997. A physically based model to correct atmospheric and illumination effects in optical remote sensing of rugged terrain, *IEEE Trans. Geosci. Rem. Sensing*, 35:708-717.

Shettigara V.K., and G.M. Sumerling. 1998. Height determination of extended objects using shadows in SPOT images, *Photogramm. Eng. Rem. Sensing*, 64:35-44.

Silva, L.F. 1978. Radiation and instrumentation in remote sensing. In P.H. Swain, and S.M. Davis, Eds. *Remote Sensing: The Quantitative Approach*. McGraw-Hill, New York, pp. 21-135.

St-Onge, B.A., and F. Cavayas. 1995. Estimating forest stand structure from high resolution imagery using the directional variogram, *Int. J. Rem. Sensing*, 16:1999-2021.

St-Onge, B.A., and F. Cavayas. 1997. Automated forest structure from high resolution imagery based on directional variogram estimates, *Rem. Sensing Environ.*, 61:82-95.

Stenback J.M., and R.G. Congalton R.G. 1990. Using Thematic Mapper imagery to examine forest understory, *Photogramm. Eng. Rem. Sensing*, 56:1285-1290.

Strahler A.H., C.E. Woodcock, and J.A. Smith. 1986. On the nature of models in remote sensing, *Rem. Sensing, Environ.*, 20:121-139.

Walsh, S.J. 1980. Coniferous tree species mapping using Landsat data. *Rem. Sensing Environ.*, 9:11-26.

Warner, T., J. Lee, and J. McGraw. 1999. Delineation and identification of individual trees in the eastern deciduous forest. In D.A. Hill, and D.G. Leckie, Eds. *Proc. Int. Forum Automated Interpretation High Spatial Resolution Ditigal Imagery Forestry.* Canadian Forest Service, Pacific Forestry Centre, Victoria, British Columbia, pp. 81-91.

Wilson, B.A., C.F. Ow, M. Heathcott, D. Milne, T. McCaffrey, G. Ghitter, and S.E. Franklin. 1994. Landsat MSS classification of fire fuel type in Wood Buffalo National Park, *Global Ecol. Biogeogr. Lett.*, 4:33-39.

Wolter, P.T., D.J. Mladenoff, G.E. Host, and T.R. Crow. 1995. Improved forest classification in the northern Lake States using multispectral Landsat imagery, *Photogramm. Eng. Rem. Sensing*, 61:1129-1143.

Wulder, M.A., S.E. Franklin, and M.B. Lavigne. 1996. High spatial resolution optical image texture for improved estimation of forest stand leaf area index, *Can. J. Rem. Sensing*, 22:441-449.

Wulder, M.A. 1999. Image spectral and spatial information in the assessment of forest structural and biophysical data. In D.A. Hill, and D.G. Leckie, Eds. *Proc. Int. Forum Automated Interpretation High Spatial Resolution Ditigal Imagery Forestry*, Canadian Forest Service, Pacific Forestry Centre, Victoria, British Columbia, pp. 267-281.

Wulder, M., K.O. Niemann, and D.G. Goodenough. 2002. Error reduction methods for local maximum filtering of high spatial resolution imagery for location trees, *Can. J. Rem. Sensing*, 28:621-628.

Wynne, R.H, and R.G. Oderwald. 1998. Forest inventory and assessment in the smallsat era. In *Proc. ASPRS Res. Technol. Inst. Annu. Meet.* American Society of Photogrammetry and Remote Sensing, Bethesda, MD, pp. 810-815.

Wynne, R.H., R.G. Oderwald, G.A. Reams, and J.A. Scrivani. 2000. Optical remote sensing for forest area estimation, *J. For.*, 98:31-36.

Yang C., and A. Vidal. 1990. Combination of digital elevation models with SPOT-1 HRN multispectral imagery for reflectance factor mapping, *Rem. Sensing Environ.*, 32:35-45.

# CHAPTER 2

## AN EVALUATION OF BAND REGISTRATION, BRIGHTNESS VARIABILITY, AND BI-DIRECTIONAL REFLECTANCE DISTRIBUTION FUNCTION EFFECTS ON FOREST COVER TYPE CLASSIFICATION USING HIGH SPATIAL RESOLUTION, MULTISPECTRAL IMAGERY

## Abstract

*An investigation of the utility of high spatial resolution (sub-meter), 16-bit, multispectral, airborne digital imagery for forest land cover mapping in the heterogeneous and structurally complex forested landscapes of northern Michigan is presented. The Chapter addresses imagery frame registration and georeferencing issues and introduces a novel approach for bi-directional reflectance distribution function (BRDF) effects correction and between-frame brightness normalization. Maximum likelihood classification of five cover type classes is performed over various geographic aggregates of 34 plots established in the study area that were designed according to the Forest Inventory and Analysis protocol. Classification accuracy estimates derived from confusion matrices show that although band registration and BRDF corrections and brightness normalization provide an approximately 5% improvement over the raw imagery data, overall classification accuracy remains relatively low, barely exceeding 50%. Computed kappa coefficients reveal no statistical differences among classification trials. Classification results appear to be independent of geographic aggregations of sampling plots. The low overall classification accuracies are attributed to the cover type-invariant spectral properties of crown portions in shadows.*

## 2.1. Introduction

The most common use of digital remote sensing data in forestry is for cover type classification of forested landscapes. Its importance is demonstrated by the fact that there are forest classification precedents in virtually all the major biomes of the world (Darvishsefat, 1995; Foody and Hill, 1996; Hansen et at. 2001). The purpose of the classification effort is often to allow contiguous areas covered with forests to be depicted

in their natural state, thus making a single classification scheme appropriate for these areas. Level II classification of Anderson et al. (1976) is an example of a generic scheme often imposed in such cases. In practice though, rarely would a general purpose classification serve specialized purposes equally well (Bailey, 1996), resulting in forest cover type classification challenges in certain areas of the world to be better understood than in others because of the extensive prior work performed there or the presence of long-term research initiatives (Shoshany, 2000).

Most remote sensing-based forest cover type classification efforts use L-resolution multispectral satellite imagery (Strahler et al., 1986), in part because of the reasonable cost and extensive archives many satellite platforms offer (White et al., 1995; Archard et al, 2001; Woodcock et al., 2001), and have traditionally been spectrally based. Pixel values in L-resolution imagery correspond to the composite reflectance of many objects and therefore mask the spatial arrangement of objects within the pixel and allow only broader spatial patterns to be identifiable, thereby limiting the utility of spatial and textural investigations to the stand level or beyond. On the other hand, operational forest management decisions are almost exclusively based on information extracted from analog infrared or color infrared aerial photographs (Wynne and Oderwald ,1998). The use of analog aerial photographs in forest classification, however, is subject to constraints, including availability of experienced photointerpreters, lack of photographic enhancement capabilities, and difficulty in photographic reproduction, mosaicing, and overlay with other forms of spatial data. The increasing popularity of digital airborne imagery over the last decade can be regarded as an attempt to combine the merits of satellite L-resolution imagery with the rich information content of large-scale

photogra

nformat

Stahler

Imaging

ptimism

and attri

economi

I

mappin

resolutio

2001) a

ypically

and one

large-sc

Little ju

tendenc

evaluati

errors a

account

are subj

spatial

within-

photography, and the flexibility of processing options characteristic of digital information. Recent technological advancements have allowed H-resolution imagery (Strahler et al., 1986) to be available even from satellite platforms (e.g. IKONOS-Space Imaging, QuickBird-Eurimage), at least at the panchromatic level, thus allowing growing optimism that improvements in our ability to extract enhanced information on the types and attributes of forests from airborne digital data could be directly applicable to future, economical satellite H-resolution data.

In contrast to the popularity of L-resolution satellite imagery for forest cover type mapping, there is only a handful of examples that have employed airborne, high-spatial-resolution, multispectral imagery for that purpose (Coulter et al., 2000; Lefsky et al., 2001) and none of them in the forests of the Midwest region. The few known examples typically involve a very limited number of cover type classes, often only one coniferous and one deciduous class, utilize a single image (frame), and use information derived from large-scale aerial photography for evaluating classification results (Biging et al., 1995). Little justification is usually offered, other than perhaps financial constraints, for the tendency to rely upon assessed information as opposed to direct observations when evaluating classification accuracy. Such practices are likely to foster propagation of errors and introduce uncertainty in information treated as "ground-truth" which is not accounted for in derived classification products.

Spectral classifications of airborne, high-spatial resolution, multispectral imagery are subject to the *H-resolution challenge* (Hay et al., 1996), which implies that as the spatial resolution of the sensor increases (i.e. the pixel size becomes smaller), so does the within-class spectral variability of surface features, resulting in a reduction of class

separability and a consequent reduction in classification accuracy. The latter is often attributed, in part, to the spectral properties of pixels that represent the shadowed portions of tree crowns (Woodcock and Strahler, 1987; Marceau et al., 1990). However, a few studies have argued that although shadows mutually cast between tree crowns reduce the spectral differences between cover types, shadow pixels maintain adequate information content that would permit cover type classification with reasonable accuracy levels, especially for 16-bit imagery (Gwinner and Schaale, 1997).

In forest classifications, the H-resolution challenge is further intensified because of similarities in the spectral reflectance characteristics among forest cover types relative to non-forested ones. An additional level of complexity is introduced by the strong, directionally anisotropic reflectance, known as the bi-directional reflectance distribution function (BRDF) effect, that forests exhibit due to their complex horizontal and vertical structure and by topographic effects where present. In contrast, Landsat scene (or frame) which encompasses millions of hectares, a very large number of digital airborne imagery frames are required to cover even a relatively small sample area, spanning an extensive range of solar illumination conditions. In geographic regions characterized by forest cover type variability, such as those typical in upper Midwest, airborne imagery frames are subject to considerable variation in scene brightness. H-resolution airborne digital imagery is often delivered to the analyst with substantial georeferencing errors introduced by imprecise aircraft internal navigation systems, inadequate camera calibration information, or with noticeable registration discrepancies between bands, especially when a multi-camera arrangement is used for imagery acquisition. All of these factors/characteristics of airborne digital imagery operate synergistically and the extent to

which they

subject to

Th

quantifyin

airborne, c

evaluate th

affect fore

effects, an

accurate a

types com

## 2.

### 2.

Th

Traverse

Michigan

are separa

and 12,62

owned an

study area

crops, rep

(4% ). Res

Geomorp

by using

which they affect forest cover type classification products is unknown, or at least it is subject to speculation.

The objectives of this study are to 1) develop a procedure for detecting, quantifying, and correcting the geometric and spectral distortions that are often present in airborne, digital imagery (multispectal and multiframe, high spatial resolution), and 2) evaluate the extent to which camera and sensor-related imperfections and idiosyncracies affect forest cover type classification while considering frame proximity issues, BRDF effects, and brightness variations among imagery frames. Evaluation is based on spatially accurate and precise field observations at the individual tree level for five forest cover types common in the Great Lakes region.

## 2.2. Methods

### 2.2.1. Site characteristics

The study area comprises two sites, the one in the south-central part of Grand Traverse County (Site I) and the other in the northern part of Wexford County (Site II), Michigan (Figure 2.1). Note that figures in this dissertation often contain color. The sites are separated by about 10km in the northwest-southeast direction and extend over 8,805 and 12,626 hectares of land, respectively. More than half (56%) of the study area is owned and managed by the Michigan Department of Natural Resources. Most of the study area consists of forests and wetlands (82%), while agricultural use, mainly row crops, represents 8%. Other land use classes include orchards (4%) and residential areas (4%). Residential development is concentrated in the northwestern part of site I. Geomorphic features include moraines and outwash plains. The average slope, calculated by using the finite differences algorithm on a 10m, 1:24,000 USGS Digital Elevation

Model available for the area is 3.5% and 2.7% for sites I and II respectively. Relief is more pronounced along the Manistee River, which crosses site II from northeast to southwest.

The study area is characterized by pronounced spatial heterogeneity of forest cover types. For that reason, it was selected in 1999 by the Michigan Department of Natural Resources (MDNR) as one of the pilot areas used for evaluating the utility of digital remote sensing data for monitoring and mapping state-owned forest resources. The associated effort is formally known as the Integrated Forest Mapping and Planning (IFMAP) project. The majority of the forest cover types extant in the northern Lower Peninsula of Michigan are present in the forested part of the study sites. The five cover types used in this study are listed in Table 2.1. The study area also contains cedar swamps dominated by Northern White Cedar (*Thuja occidentalis*).

The primary forest management objectives of the MDNR include timber production, wildlife habitat enhancement, recreation opportunities, and aspen preservation. Several private land owners offer seasonal horseback riding and snowmobiling opportunities.

### 2.2.2. Description of Imagery Set

The imagery data set used in this study was acquired on August 11, 1999, using the Digital Airborne Imaging System (DAIS [Space Imaging, 1999]), a sensor which provides imagery in four bands (three visible and one near infrared) via frame (digital array) cameras equipped with appropriate band-specific filters mounted in a 2x2 arrangement. Appendix 1, Table A.1 contains detailed information on the technical specifications of the system. The 394- frame imagery set was delivered by the vendor

georeferenced in TIFF uncompressed format and was accompanied by limited, per-frame metadata on flight direction, acquisition time, and flight height above the ground. The latter averaged 2,170m (st.dev = 25m) for site I and 2,195m (st.dev = 7m) for site II. Average frame endlap was 24.26% (st.dev = 0.74%) along flight lines, sidelap averaged 22.28% (st.dev = 1.41%) between flight lines. Flight line orientation and resulting spatial arrangement of frames in each of the two study sites are shown in Appendix 1, Figure A.1. Pixel size ranged from 0.893m to 0.949m (mean = 0.926m, st.dev = 0.018m). 36 frames contained clouds and/or cloud shadows. DAIS automatically adjusts the sensor sensitivity (sometimes known as sensor "gain") for each band immediately prior to image capture in order to prevent saturation or underexposure due to rapid changes in target reflectance. The system, however, does not record the spectral gain coefficients used for each frame.

### 2.2.3. Sampling Scheme

A total of 34 plots, 16 in site I and 18 in site II, were established stratified across the major forest cover types present in the study area with the exception of cedar swamps which were excluded due to difficult accessibility. Seven plots were installed in each of the northern hardwoods, aspen, red pine plantations, and natural pine cover types while 6 plots were located in the oak cover type. Plots were installed on level land, within homogeneous stands, and away from cover type ecotones. Stand homogeneity was evaluated by field inspections. A minimum 60% crown closure threshold was imposed by the MDNR as a selection criterion. Stands in the vicinity of image frame centers were given sampling priority. All plots were situated within the inner quarter area of the associated image frame, which resulted in a maximum view angle of 8.65° at plot-center.

### 2.2.4. Field Measurements

Field observations were obtained in a collaborative effort with the MDNR and the Forest Health Monitoring (FHM) program during the summer of 2000, exactly one year after image acquisition. Since its initiation in 1990, FHM has collected an expansive set of forest attributes (USDA FS, 1997) and it is since May 1998 integrated with the Forest Inventory and Analysis (FIA) program at the plot level. Adoption of the FIA/FHM field protocols ensured compatibility of data used in this study with a wealth of archived and soon-to-be-collected FIA data, greatly enhancing the potential for wide application of the study findings. Each plot in the FIA/FHM protocol consists of four subplots located at the center and vertices of an equilateral triangle with side length of 62.18m (Appendix 1, Figure A.2). The base of the triangle is oriented East-West. Although in the standard design subplots have a radius of 7.32m, recent protocol modifications have allowed for a large subplot, for example to increase the number of large trees sampled in oldgrowth stands. For this study, subplot diameters ranged from 10m to 15m but were consistent for all subplots belonging to any given plot.

Following the installation of a plot center, which coincides with the center of subplot 1, center points for subplots 2-4 were located using a theodolite and range finder. The center of subplot 1 served as the origin of a plot-specific coordinate system oriented to the cardinal directions. Direction was identified using a tripod-mounted survey compass adjusted for magnetic declination. Transects were subsequently used to link the subplot centers to the centroids of small reference objects that were clearly identifiable on the image frames. These reference points, usually small, short shrubs, had a horizontal footprint smaller that a pixel, contrasted well with surrounding vegetation, and were

selected so as to avoid confusion among reference and non-reference objects. Reference points were assigned plot coordinates using Euclidean geometry and distance/direction measurements (in three dimensions) between transect vertices. Subsequently, the plot coordinates associated with objects on each plot were translated into image frame coordinates by using these reference point coordinates. The Root Mean Square Error (RMSE) of plot-to-image coordinate translations calculated using subplot centers for each of the 34 plots had a mean of 18.2cm (st.dev = 5.3cm), or about 0.2 pixels. The precision of the theodolite and range finder measurements were evaluated by establishing, ten (two per cover type), closed transects of considerable total length (> 1km) with many vertices (>25) and comparing the positional discrepancy between the first and last vertex, which, in the absence of any measurement error, should coincide. The RMSE for the 10 trials was 4.2cm (st.dev = 2.9cm), or 0.045 pixels.

Spatial and attribute data were collected for all trees within each subplot having diameter at breast height (DBH) of at least 5cm. Spatial data included the azimuth and distance of the stem center from the subplot center, and the periphery of the visible-from-above tree crown projected to the ground. Crown portions of trees with stems outside the subplot were also recorded (Appendix 1, Figure A.3). The horizontal extent of a crown was projected to the ground using clinometers and measured as distance from the stem center using a tape. For regularly shaped crowns only four distance measurements along the cardinal directions were taken. Irregularly shaped crowns necessitated a larger number of angular and distance measurements. Attribute data included species, DBH, foliage vigor rating and presence or absence of tree membership in the canopy dominance/co-dominance class. For two trees in each subplot the total height was

measured. Spatial measurements were organized as polygon or point layers in a geographic information system (GIS) using plot coordinates. The methods used to delineate crowns from point measurements, and subsequently identify crown centroids and calculate crown diameters are described in Appendix 1. All GIS crown and tree stem layers, initially represented in plot coordinates were ultimately translated in image coordinates.

### 2.2.5. Image preprocessing

Examination of the spectral properties of pixels on line transects chosen randomly in image frames revealed imperfections in the geometric alignment (registration) of the bands. Further, overall brightness differences among image frames were very apparent. Depending on their magnitude, such image deficiencies could seriously degrade the quality of the subsequent image analysis products. The steps taken to correct band registration problems and normalize the spectral brightness among image frames are outlined below.

#### 2.2.5.1. Band Registration

Transparent materials such as atmospheric gases, refract wavelengths of electromagnetic radiation to different degrees, such that a point source in the image plane (i.e., the plane of the object) is recorded as multiple or almost-coalesced points in the focal plane (i.e., the plane at which the digital camera records the image), thereby producing band misregistrations. Band misregistration may also occur as the result of physical misalignment of cameras or their optical components at the focal plane. The traditional approach for correcting band registration problems is to identify areas of intense spectral gradient (i.e. edges), and attempt to align them (Tian and Huhns, 1986).

The proper displacement (or registration) vector is identified as the one that maximizes the correlation coefficient between the two bands processed. However, between-band correlation is strongly affected by the types of objects depicted in the imagery. It is indeed possible for two bands to be highly collinear for a given combination of surfaces and practically unrelated for another. Because the reflectance regimes of most natural objects and surfaces present in the blue, green, and red bands are highly collinear, correlation-based investigations are expected to reduce the magnitude of registration problems. Such optimism though cannot be extended to include the near infrared band, because the abrupt increase in the reflectance of healthy vegetation in that band is not accompanied by similar reflectance behavior in other types of surfaces.

Spectral correlation computations were restricted to include only the darkest pixels per frame band. The appropriate digital number (DN) threshold for classifying a pixel as 'dark' was identified by examining the DN histogram for the NIR band. For unimodal NIR histograms, the pixels with a DN smaller than the $2^{nd}$ percentile were selected. For bimodal histograms, characteristic of frames containing water features, first the DN corresponding to the trough between histogram modes was identified, and then the threshold was set to include the 2% of pixels in the frame with DN value larger than the trough DN (Figure 2.2b). This approach effectively masked all pixels not positioned in deep shadows or water (Figure 2.2c). Subsequently, with the NIR band kept stationary, all other bands in a frame were shifted up to 5 pixels, in whole pixel increments, around the center of an 11x11 window. Shorter (subpixel) intervals could be used for frame shifting, but subpixel intervals would have necessitated pixel interpolation, which is known to distort image features and spectral attributes. For each band shift, the

correlation coefficient with the 'dark' pixels in the NIR band was calculated. The optimal displacement offset, henceforward known as registration vector, was identified as the one that maximized this correlation. The NIR band was selected to remain stationary because of its lower sensitivity to atmospheric refraction of light in comparison to the visible bands. To evaluate the robustness of this registration vector identification method, the procedure was repeated for 20 frames, this time keeping the red band stationary.

It was discovered that the presence of large clusters of pixels identified as dark, might affect the ability of band correlation computations to reveal and correct registration problems. This can be particularly important in cases where the direction of the misregistration coincides with the main axis of elongated clusters of dark pixels, such as those occurring along stand edges or streams. Thus, prior to band shifting, dark pixel clusters containing more than 10 pixels where eliminated (2.2d). Cluster identification and membership calculations were performed using the connected components algorithm (Shapiro and Stockman, 2001) with the four-neighbor option. To investigate the potential presence of variable registration accuracy across a frame, spectral correlations were computed for every $1/16^{th}$ (128 x 128 pixels) of a frame, and, for frames containing a plot, for a 300 x 300 pixel window centered on each plot center.

#### 2.2.5.2. Normalization of spectral frame brightness

In the absence of 1) the sensor's spectral gain coefficients per frame and 2) the spectral reflectance of any targets, between-frame brightness normalization efforts explored alternative approaches. Preliminary investigations revealed that targets believed to have invariant reflectance during the course of image acquisition (such as ponds or unpaved roads on sandy soils), and therefore well suited to the normalization process,

were either only sporadically available in the study area (ponds) or had significant spectral variability (unpaved roads). Because of these limitations, normalization efforts focused on overlapping regions between adjacent frames. It was assumed that the difference in the mean DN value of pixels positioned in the overlapping region of a pair of adjacent frames would be representative of the overall spectral brightness difference between respective frames.

To determine the spatial extent of overlapping regions, adjacent frames needed to be properly georeferenced. To improve the poor registration accuracy of the imagery provided by the commercial vendor, often found to exceed 100m, image frames were georeferenced manually using leaf-on and leaf-off, 1:12,000-scale Digital Ortho Quadrangles (DOQs) available for the study area (Michigan Department of Natural Resources, 2001) and nearest neighbor pixel interpolation. Frame georeferencing using this method produced an RMSE of 1.9m or approximately two pixels.

Image portions close to the edge of frames are acquired with the largest view angles in an imagery set, and therefore are susceptible to stronger BRDF effects compared to other frame portions. Differences in DNs due to BRDF effects are likely to be further accentuated for overlapping frame regions, since in such circumstances the difference in relative viewing azimuth angles (Figure A.4, Appendix 1) for pixels in these regions approaches $180^{o}$. Failure to mitigate BRDF effects prior to calculating mean DN values for the overlapping region between frames would make successful brightness normalization unlikely.

A semi-empirical model applicable to heterogeneous surfaces, developed by Roujean et al. (1992), was used for BRDF correction of overlapping frame regions. It

considers the surface spectral reflectance to be the outcome of two main processes: a diffuse reflection component that accounts for the geometric structure of opaque reflectors on the surface of objects and scattering from the object's volume. Both components are represented in the model via three, surface-type-specific parameters, $k_0$, $k_1$, and $k_2$. BRDF correction coefficients are computed as the fraction of surface reflectance of standard over actual viewing and illumination geometry. Details on model structure, and an illustration of viewing and illumination geometry are in Appendix 1. BRDF corrections were computed for the portion of overlapping frame regions occupied by deciduous forest. It was assumed that the anisotropic reflectance of coniferous forests due to BRDF effects was similar to that of deciduous forests. The extent of deciduous forests was determined by spatial overlays of georeferenced image frames with a beta version of the IFMAP classification maps. Proper model parameter values were identified by using a simplistic optimization method to be discussed shortly. Other land use / land cover types available in the study area such as coniferous forest and grassland were not considered because they were present in fewer than half of the overlapping frame regions.

The optimization method entailed resolving band misregistration (if any) for each of the overlapping frame regions, correcting BRDF effects for deciduous forests at those regions, calculating the region's mean pixel DN values for the deciduous forest portion of each frame in an adjacent pair, computing the difference of the means for each frame pair, and finally summing the differences along a closed path that traversed many frames. The method operated under the assumption that BRDF differences among deciduous forest cover types were minimal. Since each of the paths originated and terminated at the same frame, and given that BRDF effects were considered normalized, the sum of mean

DN differences between adjacent frames along the path should be close to zero. Any discrepancies could be attributed to an improper combination of BRDF model parameter values. Ten closed paths were established, 5 per study site, each originating at different locations within the respective sites and traversing 15 to 20 frames. Established paths avoided frames with clouds or cloud shadows. Note that deciduous forests, unlike other forest cover and land use types, were present in each overlapping frame region along every path. Using published spectral model parameter values for deciduous forests as seed values (Table A.2, Appendix 1) a large number (> 1,200) of $k_0$, $k_1$, and $k_2$ value combinations were tested for each band, each resulting in pixel-specific spectral correction coefficients to be used for BRDF normalization. BRDF correction coefficients are defined as the ratio of model predictions for standard over actual illumination and viewing conditions (Table A.3, Appendix 1). Smaller increments in the values of $k_0$, $k_1$, and $k_2$ were examined as the model-parameter combinations being evaluated produced progressively smaller sums of DN differences along the paths. The combination that minimized the differences among all established paths while consistently providing spectral correction coefficients within the 0.7 to 1.3 range was identified as the one that provided the optimum BRDF correction and was subsequently used for brightness adjustment (Table A.2, Appendix 1). Spectral correction coefficients outside the 0.7 to 1.3 range were considered improbable. Brightness variation adjustment was also examined for individual paths. The optimum model coefficient values were used to determine the spectral brightness difference between a frame and its neighbors based on the brightness differences detected within the overlapping regions. The effectiveness of the method in correcting brightness variations among frames was evaluated by comparing

the DN difference sums along the established paths after the BRDF normalization to the DN difference sums obtained using the original DN values.

With the relative brightness difference among adjacent frames known, frame DN values for each band were adjusted relative to those of a frame in the middle of sites I and II respectively. Adjustments progressed radially away from the site centers. Subsequently, the mean per-band value for all frame portions occupied by forest was computed for each site. It was assumed that the ratio of spectral reflectance between deciduous and coniferous forests was constant. Finally, spectral DNs for the frames at site I were adjusted a second time so that their mean value over forested landscapes would match the mean DN value of forested landscapes in site II. All BRDF corrections and brightness normalization procedures were performed using Arc Macro Language (AML) scripts in ArcInfo (ESRI, 2001).

### 2.2.6. Image Classification

As mentioned earlier, all major cover types present in the study area, with the exception of Cedar swamps, were represented in the field data set. In the presence of a known forest cover type classification scheme, a supervised classification approach was selected. The maximum likelihood (ML) option was used primarily because of its parametric structure. Initial investigations of cover type spectral signatures, both with and without registration correction and BRDF/brightness normalization, showed that non-parametric classification options (e.g., parallelepiped) would result in significant signature overlaps and greater classification confusion rates.

Classification was conducted on the subplot level. Subplot pixel membership was determined via spatial overlays of image frames with vector subplot boundaries in image

coordinates. Pixels split by a boundary were considered to be subplot members if 50% or more of their area was within the subplot. In the ML classification process, pixels in each subplot were assigned to one of the five classes (Aspen, Northern Hardwoods, Oak, Red Pine Plantations, or Natural Pine). A cross-validation approach (Lachenbruch and Mickey, 1968) was undertaken for signature development involving two geographic extents: i) site-specific, and ii) global. A subplot Q2 (belonging to plot Q) in site I for example, was classified via three sets of spectral signatures developed: 1) using all pixels in the remaining subplots at site I except those in the related subplots (Q1, Q3, and Q4) and all the subplots in site II, 2) using the pixels in the remaining (unrelated) subplots of site I only, and 3) using all pixels in site II subplots but no pixels from site I subplots. Subplots in site II were classified in a similar fashion for a total of five classification products. Absent this cross-validation approach, it would be difficult to ensure that the potentially low spectral variability within a plot compared to the variability among plots of the same cover type would not inflate classification accuracy estimates. Subplot classification was applied to both raw DNs and to a dataset that had been corrected for between-band misregistration and normalized for BRDF/brightness variability, for a total of 10 classification trials (scenarios).

Classification outputs were post-processed with subplot-specific pixel majority filters that assigned a single class (cover type) to each subplot. Classification accuracy estimates were derived from confusion matrices and associated indicators (percent of subplots correctly classified and kappa coefficients) (Congalton, 1991) computed after the application of majority filters. Differences in the classification performance were evaluated using parametric statistical tests. Details on the tests and the computation of

confusion matrices and accuracy indicators are provided in Appendix 1. The power of each classification output was evaluated by imposing several different minimal probability thresholds (none, 0.1, 0.25, 0.50, 0.75) for class membership. Pixels with all class conditional probabilities below the imposed threshold remained unclassified.

## 2.3. Results

### 2.3.1. Band Registration

Between-band registrations errors (Figure 2.3a) identified by correlation-based investigations and quantified by using the length of calculated registration vectors revealed that, in general, the shorter the wavelength of the visible band the larger its registration discrepancy relative to the near infrared band (Table 2.2). For individual frames, spectral misregistration was practically random both in magnitude (vector length) and orientation (vector azimuth) (Figure 2.3b). The absence of any detectable pattern of misregistration among frames and bands remained even when the frames were arranged in acquisition time sequence. Spectral registration vectors computed for tiles arranged in a 4x4, non-overlapping formation within the frame (i.e. each tile covering a unique $1/16^{th}$ of the frame), revealed substantial within-frame vector variability and spatially correlated vector azimuth and length (Figure 2.4). Such variability in spectral registration cannot be attributed to varying atmospheric optical depth and spectral refraction rates, or to markedly different spectral reflectances among cover types, especially in the absence of significant topographic variations. It is, rather, an indication of imperfect alignment of the focal planes of the cameras used in the acquisition of imagery. The lack of consistent registration vector attributes (azimuth and length) between corresponding tiles in sequentially acquired frames could potentially be explained by an unstable mounting of

the camera set on the aircraft body, which would leave the alignment of the optical axes and focal planes of the cameras vulnerable to aircraft fuselage vibration and wind pressure.

Ranking of the band correlation coefficient values computed for different vectors, either for an entire frame or for a portion of it, revealed that, for many frames, a single vector would offer a correlation value clearly larger (by as much as 0.10) than any other vector. For many other frames, there were two vectors offering high correlation values, while the next best correlation values were substantially smaller than the two higher ones. In the latter case, vector length and relative azimuth difference was always one length unit and $45^0$ respectively thus providing a strong indication that registration discrepancy for the band pair tested for the frame in question was about half a pixel.

Comparisons of registration vectors computed with the NIR band stationary to those computed by keeping the red band stationary revealed that vector length and azimuth convergence for the two alternatives was achieved only when the DN band histogram threshold used to assign a pixel to the 'dark' class was appropriately low. Eliminating large clusters of 'dark' pixels allowed vector attribute convergence even when the DN histogram threshold was set to the $3^{rd}$ percentile. Maintaining large clusters had occasionally necessitated setting the DN threshold to the $1^{st}$ percentile.

### 2.3.2. Normalization of Frame Brightness

Brightness variations among frames in the original imagery were found to be significant. The sums of mean brightness differences (expressed in DNs) for overlapping regions along each the 10 close multi-frame paths established for testing varied between –6,315 and 4,989 DNs for the NIR band in the original imagery (Table 2.3). When scaled

to the number of frames present in the path, brightness variations among all established paths stretched from –421 to 301 DNs for a range of 722 and a mean of 285 DNs for the NIR band. The mean per frame brightness variation among paths for the blue, green, and red bands was 238, 319, and 255 DNs, respectively. The latter values could be considered as systematic errors that would accumulate in the process of adjusting frame spectral brightness starting from the frame in the center of each site and progressing to the frames on the periphery. Accordingly, the brightness adjustment for a frame positioned 10 frames from the center of each study site should be expected to sustain an average error of 2380, 3190, 2550, and 2850 DNs for the blue, green, red, and NIR bands. Those values correspond to approximately 12%, 15%, 13%, and 9% of the effective DN range for healthy forest vegetation and therefore should be considered substantial. It should be noted that these values correspond to the average per frame brightness correction error and errors in individual frame brightness adjustments could be larger.

Compared to the original imagery spectral DNs, post-normalization brightness variations calculated along the closed multi-frame paths, were on the average two orders of magnitude smaller (Table 2.3). For the NIR band, the mean per path brightness variation among the established paths had a range of 250 DNs or about $1/45^{th}$ of the same range without normalization. For the blue, green, and red bands, the reduction in along-path brightness variation achieved with the normalization process amounted to 93.9%, 93.7%, and 95.0% respectively; when expressed on a per-frame basis, post-adjustment mean brightness variations were practically absent. For pairs of adjacent frames, the mean DN difference of their overlapping regions occupied by deciduous forests was always less than 1% of the effective range for healthy forest vegetation after brightness

normalization. Note that if the normalization process involved individual paths, additional reductions in mean, per path brightness variation are attainable. However, the optimal BRDF correction coefficients computed for individual paths, would, generally, produce slightly larger brightness variations when applied to the other paths than those produced when optimizing simultaneously for all the paths. The differences in the site-specific, mean spectral brightness of forested land between the two sites ranged from $-175$ for the NIR band to 83 for the green band (Figure 2.5). These differences in the spectral means were used to adjust the frames of site I to those of site II. These discrepancies between site spectral means originated primarily from the mean brightness difference of the two frames at the respective site centers that were used for brightness adjustment. Brightness adjustment resulted in leptokurtic distributions of frame means with a range of about 1,000 DNs for the visible bands. For the NIR band, the distribution of frame means was approximately Gaussian with a range of 2,500 (Figure 2.5). It should be noted that some variability in spectral frame means was expected because of differences in the composition of forest types in each frame (deciduous vs. coniferous).

### 2.3.3. Image Classification

Classification accuracy estimates derived from computed confusion matrices were unacceptably low. Overall classification accuracies ranged from 43.1% to 48.4% when the original imagery was used and from 50.0% to 53.1% after brightness normalization (Table 2.4a-j). The average improvement in overall classification accuracy offered by brightness normalization was 5.66% with a coefficient of variation of 0.39, and was larger within each of the two sites (8.3% for site I and 6.3% for site II) than across them (6.9% for site I and 3.1% for site II). Overall kappa coefficients values followed a similar

trend, ranging from 0.29 to 0.36 for the original imagery and from 0.38 to 0.41 after brightness normalization (Table 2.4a-j). Correcting for brightness variations improved the overall classification kappas by an average of 0.070 with a 0.40 coefficient of variation. Again, the improvement was larger within sites (0.103 for site I and 0.077 for site II) than across sites (0.087 for site I and 0.037 for site II). Classification was significant at $\alpha$=0.01 ($Z_k$, Z-score of kappa, > 2.576) for all scenarios. However, all pair-wise comparisons of classification outcomes (overall, within and across sites, pre- and post-brightness normalization) based on the computation of standardized differences of respective kappa coefficients showed no statistical significance even at $\alpha$ = 0.10 (Table 2.5).

Class-conditional kappa coefficients computed before and after brightness normalization showed that correction of brightness variations generally resulted in increased coefficients (Table 2.6). Averaged across all five classification scenarios, the improvement was substantial for northern hardwoods subplots (0.150) and about half that amount for aspen (0.071), oak (0.065) and red pine plantations (0.066). This trend was absent in natural pine where brightness correction led to decreases in kappa coefficients for three of the five classification scenarios, however. Within-site brightness correction for natural pine increased the kappa coefficients. The largest coefficient increases observed included the classification scenarios of all northern hardwoods subplots from 0.29 to 0.51, of northern hardwoods in site I with signatures developed within the site from 0.23 to 0.40, of aspen in site I with signatures developed in site II from 0.24 to 0.40; and of oak in site I with signatures developed in site I from 0.14 to 0.30.

Class-conditional kappas computed prior to correcting for brightness variations among frames did not reveal any patterns related to whether the signatures for subplot

classification were developed within the subplot's site or not. In four scenarios (aspen and red pine plantations in site I, aspen and northern hardwoods in site II), within-site signatures yielded larger kappas, but in five others (northern hardwoods and oak in site I, and oak, red pine plantations and natural pine in site II) the kappas where higher for signatures from across sites. For one classification scenario (natural pine in site I), the kappa was the same within and across sites. After brightness normalization, in seven classification scenarios within and across sites signature development produced the same kappa. Once kappa was larger across sites (northern hardwoods in site I) and three times was larger within the site (natural pine in site I, and aspen and natural pine in site II).

Confusion matrices calculated for each of the classification scenarios (Table 2.4a-j) showed that there were substantial confusion rates among all five cover types. Confusion rates for aspen, northern hardwoods, and oak were higher within the deciduous cover type group (i.e. where a deciduous cover type subplot was assigned to a deciduous cover type other than the correct one) while red pine plantations and natural pine exhibited comparable error rates between themselves and the deciduous cover types (Table 2.7). This is an indication of overlapping signatures in the four dimensional feature space that is not limited to only coniferous or only deciduous cover types, as it is usually the case in traditional L-resolution imagery classification. Commission and omission errors calculated from the confusion matrices (Table 2.4a-j) suggested that signatures developed using all pixels in the training areas do a poor job of capturing the spectral identity of cover types or cover type groups known to be spectrally discernable in L-resolution imagery. Further, subplots assigned to the wrong cover type class in each classification scenario did not, in general, belong to the same plot. For most plots, one

and rarely two of its subplots were misclassified. Evidently, the classification errors observed cannot be solely attributed to the spectral variability between plots of the same cover type.

Interesting insights into the structure of the spectral signatures were gained by examining the percentage of pixels that are classified for various maximum likelihood thresholds (Table 2.4a-j). Even small (<= 0.10) probability thresholds left large percentages of pixels unclassified. The proportion of unclassified pixels was approximately 50% for a threshold of 0.25 and exceeded 80% when the threshold was set to 0.50. Hence, for the majority of pixels in a subplot, pixel assignment to a cover type was based on a weak association between the pixel's spectral profile and the structure of the signature of the assigned cover type class. A maximum likelihood threshold of 0.75 allowed only 2-5% of the pixels in a subplot to be classified, and these were always positioned approximately half way between the sunlit portion of the crown and the shadowed areas between crowns. Progressive threshold decreases resulted in a gradual expansion of classified pixel clusters positioned between the sunlit and shadowed areas; at very low thresholds, only the center of sunlit areas and deep shadows remained unclassified.

## 2.4. Discussion

### 2.4.1. Band Registration

The proposed method for correction of band registration errors is computationally efficient when the main cause of misregistration is imperfect alignment of the focal planes of cameras used in the acquisition of multispectral, low or medium altitude imagery. In the absence of significant topography, variation in image platform altitude

and overly heterogeneous conditions, focal plane misalignment can be expected to generate a consistent band misregistration among sequentially acquired frames. Under these circumstances, registration vectors identified for portions of one frame could be applied to all corresponding frame portions in the same flight path, thereby significantly reducing the computation load, while permitting reduction in registration errors for portions of frames in which spectral profiles do not support correlation optimization computations. When focal plan misalignment varies among frames or when image acquisition conditions result in variable registration accuracy regimes within frames, the presence of an adequate number of multispectrally 'dark' pixels in all frame regions is crucial if the correlation-based methodology employed in this study is to produce satisfactory corrections. The absence of 'dark' pixels in a portion of a frame occupied by forest, and for which registration correction is required, is common in stands with a smooth canopy surface and high canopy closure. In such cases, increasing the DN threshold that assigns a pixel to the 'dark' class and applying the correlation method would likely yield satisfactory correction of misregistration for the visible bands, but not for the infrared band.

Discrepancies in the magnitude and orientation of registration vectors that maximized band correlations for different choices of stationary bands and DN histogram thresholds used to identify 'dark' pixels emphasize the need for a careful DN threshold selection. The 2$^{nd}$ DN histogram percentile and the subsequent processing of 'dark' pixels with the connected components algorithm were found to be good choices for the imagery in this study. Very low DN histogram percentiles, for example 0.5%, would eliminate any dependencies of the method to differences in reflectance characteristics among objects in

a frame. However, they would also reduce the number of 'dark' pixels used in the computation of band correlation thereby increasing the susceptibility of the registration vectors to errors introduced by the variable, non-linear spectral gain effect that sensors exhibit at the lower range of their spectral sensitivity.

Because the method is designed to evaluate band registration only in whole-pixel increments along the axes of digital arrays, it is incapable of correcting misregistration caused by relative rotation between the arrays. Further, the proximity or coincidence of principal points in each spectral component in a frame could, in the presence of band rotation, lead to gross underestimates of misregistration magnitude because pixels positioned symmetrically away from the principal points would tend to produce local registration vectors of similar length but opposite orientation. Therefore, in the presence of band rotation, registration vectors would vary among different frame portions. The only realistic option for correcting or reducing such misregistration that does not involve frame resampling would be to restrict correction to each frame portion separately -- a less than ideal solution because of ensuing band registration discontinuities at frame partitioning boundaries. When applied properly, in terms of 'dark' pixel identification and frame portion extent, the method would eliminate any band registration errors larger than 0.5 pixels, while preserving the spectral profiles of objects of interest.

### 2.4.2. Normalization of Frame Brightness

BRDF model coefficients optimized during the brightness adjustment procedure are not necessarily appropriate for any deciduous forest. The Roujean's et al. (1992) model, as well as many others, is designed to standardize reflectance of an object for various illumination and viewing geometries. Without information on spectral gain

coefficients and radiometric field measurements, however, the only alternative is to base classification on DNs. In this study, thebrightness adjustment operated under the potentially unrealistic assumption that object reflectance could be approximated as a linear transformation of DNs intrinsic to the BRDF correction process, with the linearity assumption imposed by the kernel-based structure of the BRDF model. The fact that theBRDF model coefficient values converge to minimize brightness differences for the overlapping regions along frame paths and that the vast variations in brightness among frames for the original DNs are practically eliminated by the brightness adjustment are encouraging, albeit qualitative indications that these assumptions are valid. Coefficient generalization could be further restricted by the fact that optimization was based only on larger viewing zenith angles (i.e. those that corresponded to overlapping frame regions). Note that although only deciduous forests were used as a basis for the brightness adjustment, normalization was based on all forested land. In landscapes where coniferous stands are ubiquitous in the overlapping regions of frames, a separate, independent brightness adjustment could be derived, which would permit an assessment of the method's dependence on and ability to provide brightness normalization for another class of vegetation.

### 2.4.3. Image Classification

The classification approach used in this study, although conceptually similar, differs from traditional classifications of L-resolution imagery in the sense that the classification unit (a single pixel) corresponds to small portions of tree crowns rather than multiple crown aggregates. The differences in spatial scale between the imagery unit (pixel) and the classification unit (subplot) have important implications for classification

results because, unless a fuzzy classification scheme is employed, it necessitates elimination of the within-subplot pixel class variability. The classification accuracy estimates that were derived do not account for the fact that the confusion table entries are not assigned directly by the ML classifier on a pixel basis, but are in addition post-processed with a majority filter on the subplot level. As such, the classification accuracy estimates could be seriously overestimated. Concerns about accuracy estimate bias are accentuated by the low maximum likelihood probabilities of the most probable class determined by the classifier.

The observations made on the spatial allocation of classified pixels for various maximum likelihood thresholds, the variability of assigned classes for subplots in the same plot, and the analysis of the confusion matrices all suggest that the spectral signatures for each cover type class are 'contaminated' by the presence of a significant number of spectrally dark pixels with DNs that are not exclusively associated with any one class. The spectral signature for each of the five cover types classes could be regarded as approximating a hyperellipse in four-dimensional space in which the dark pixels that correspond to shadowed crown portions or small canopy openings occupy the volume around one of the ellipse's focus while the pixels for the sunlit portions of crowns are centered around the other focus. The signature mean, positioned approximately half way between the two foci, corresponds to crown portions located at the fringe of direct and diffuse illumination. Moreover, the dark foci of ellipses for different cover types tend to be proximal in four-dimensional space thereby indicating that there is little, if any, spectral separability between shadowed portions of the five cover types. By contrast, the bright foci for the five cover type signatures represented in this study tend to exhibit

mutual inhibition, thus causing a rotation of the main ellipse axis around its respective dark focus. Hence, when all cover types are simultaneously considered, only the brighter components of their ellipsoid volumes do not overlap. Because signature means are positioned much closer to dark foci rather than bright foci, the relative signature ellipse rotation produces smaller spectral separation between signature means than the distance between the bright foci thereby decreasing the accuracy of maximum likelihood classification, given that the latter is based on the spectral distance of a pixel from signature means (Appendix 1, Equation A.19).

While the presence of shadows and resulting spectrally dark pixels in high spatial resolution digital imagery over forested landscapes affects the means of spectral signatures, brightness variations and BRDF effects are primarily related to the structure of covariance matrices (Appendix 1, Equation A.19) and inflate the volume those signatures occupy in multi-dimensional space and hence the extent of overlap. The approximately 5% improvement in classification accuracy achieved after BRDF corrections and brightness adjustments is most likely the result of a reduction in the 4-dimensional volume of the cover type signatures involved.

The larger variability of classification accuracy estimates for individual cover type classes compared to the variability of estimates for the pooled subplot set can be partially attributed to differences in the number of subplots considered in each scenario, but also to differences in canopy roughness within cover types. Even with invariable canopy density, foliage composition and orientation of leaves or needle bundles, differences in canopy surface roughness occasionally present between and within plots of the same cover type will generate variability in the size and darkness of shadows cast

between crowns of adjacent trees and hence alter the degree to which dark pixels influence the composition of respective cover type signatures. Note that the significance of kappa coefficient differences between the various geographic extents of signature development and brightness correction alternatives cannot be evaluated at the cover type level because the kappa coefficient variance estimates necessary for the associated statistical testing are known to be unstable and biased when the sample size is relatively small.

## 2.5. Conclusion

The low overall accuracy of all classification products obtained using all subplot pixels, found to be considerably inferior to the accuracy traditionally obtained using L-resolution, mid-summer imagery for similar classification schemes, suggests that their value for cover type classification and support of forest management decisions is fairly limited. The spectral profiles of pixels corresponding to shadowed portions of forest stand canopies are instrumental in minimizing the spectral separability of signatures for the five forest cover types of this study. At the same time though, they emphasize the potential of signature development conditional to crown portions to offer significant improvements in their power to discern cover types. The merits of the latter approach are investigated in detail in Chapter 3. The approach used in this Chapter, however, is computationally more efficient and does not require a shift of classification focus from the subplot level to individual trees, nor does it necessitate identification of individual tree crowns.

Signature development based on variable geographic extents was found to have minimal impact on classification accuracy, but it should be kept in mind that there is only

marginal variability in the ecological gradients (edaphic, climatic, and topographic) that influence forest growth between the two sites used in this study. It was shown that the noticeable decline in classification accuracy that results from band misregistration and variable frame brightness conditions can be avoided, but the associated computation cost, analyst expertise and time investment, and ancillary information requirements necessary for error correction and brightness normalization could be prohibitive. Depending on the type of registration errors, absolute corrections may be impossible unless compromises related to the objects' spectral profiles are made (i.e. resampling). However, it should be expected that the process of correcting band misregistration could be simplified if technical problems such as camera focal plane alignment imperfections were to be eliminated. Similarly, simply recording the spectral gain coefficients used for the acquisition of each image frame would have permitted reflectance- rather than DN-based classification and would have allowed for theoretically sound BRDF correction rather than the empirical approximation used. It should be expected that as commercial vendors of airborne, multispectral, high resolution digital imagery gain experience, such technical problems would diminish, ultimately increasing the potential utilization of this type of imagery for forest land cover classification.

## Literature Cited


Anderson, J.R., E.E. Hardy, J.T. Roach, and R.E. Witmer. 1976. *A Land Use and Land Cover Classification System for Use with Remote Sensor Data*. U.S. Geological Survey Professional Paper 964. Washington, D.C.

Archard C., H. Eva, P. Mayaux. 2001. Tropical forest mapping from coarse spatial resolution satellite data: production and accuracy assessment issues. *Int. J. Rem. Sensing*, 2741-2762.

Bailey, R.G. 1996. Ecosystem Geography. Springer-Verlag, New York.

Biging, G.S., M. Dobbertin, and E.C. Murphy. 1995. A test of airborne multispectral videography for assessing the accuracy of wildlife habitat maps. *Can. J. Rem. Sensing*, 21:357-367.

Congalton, R. 1991. A review of assessing the accuracy of classifications of remotely sensed data. *Rem. Sensing of Environ.* 37, 35-46, 1991.

Coulter, L., D. Stow, A. Hope, J. O'Leary, D. Turner, P. Longmire, S. Peterson, and J. Kaiser. 2000. Comparison of high spatial resolution imagery for efficient generation of GIS vegetation layers. *Photogramm. Eng. Rem. Sensing*, 66:1329-1335.

Darvishsefat, A.A. 1995. *Einsatz und fusion von multisensoralen satellitendaten zur erfassung von waldinventuren*. Technical Report, University of Zurich, Department of Geography, Remote Sensing Series, Vol. 24.

ESRI. 2001. Arc Macro Language for ArcInfo 8.1. Redlands, California.

Foody, G.M. and G.M. Hill. 1996. Classification of tropical forest classes from Landsat TM data. *Int. J. Rem. Sensing*, 12:2353-2367.

Gwinner K., and M. Schaale. 1997. A Case Study on the Influence of Shadows and Shading on Multispectral Airborne Imaging Data. In *Proc. Third International Airborne Remote Sensing Conference and Exhibition*, Volume I, Kopenhagen, Denmark, pp. 409-416, 7-10 July 1997, Environmental Research Institute of Michigan (ERIM), Ann Arbor.

Hansen, M.J., S.E. Franklin, C. Woudsma, and M. Peterson. 2001. Forest structure classification in the north Columbia mountains using the Landsat TM tasseled cap wetness component. *Can. J. Rem. Sensing*, 27:20-32.

Hay, G.J., K.O. Niemann, and G.F. McLean. 1996. An object-specific image texture analysis of H-resolution forest imagery. *Rem. Sensing Environ.*, 55:108-122.

Lefsky, M.A., W.B. Cohen, and T.A. Spies. 2001. An evaluation of alternate remote sensing products for forest inventory, monitoring, and mapping, of Douglas-fir forests in western Oregon. *Can. J. For. Res.* 31:78-87.

Marceau, D.J., P.J. Howarth, J.M.M. Dubois, and D.J. Gratton. 1990. Evaluation of the grey-level co-occurrence matrix method for land-cover classification using SPOT imagery. *IEEE Trans. Geosci. Rem. Sensing*, 28:513-519.

May, Dennis M. 1998. The north central forest inventory and analysis timber product output database – a regional composite approach. Gen. Tech. Rep. NC-200. St. Paul, MN: U.S. Department of Agriculture, Forest Service, North Central Research Station. pp. 16.

Michigan Department of Natural Resources. 2001. Forestry, Mineral and Fire Management Division, Resource Mapping and Aerial Photography; *1992 Series USGS Digital Orthophoto Quadrangles*, http://www.mcgi.state.mi.us/mgdl/doqs_zip/DOQQ92_Map.htm

Roujean, J.L., M. Leroy, and P.Y. Deschamps. 1992. A bi-directional reflectance model on earth's surface for the correction of remote sensing data, *J. Geophys. Res.*, 97:455-468.

Shapiro, L.G., and G.C. Stockman. 2001. *Computer Vision*, Prentice Hall, Upper Saddle River, New Jersey.

Shoshany, M. 2000. Satellite remote sensing of natural Mediterranean vegetation: a review within an ecological context. *Prog. Phys. Geogr.*, 24:153-178.

Space Imaging Inc. 1999. DAIS: A Digital Airborne Imaging System. Space Imaging Corporation, Thornton, Colorado.

Strahler A.H., C.E. Woodcock, and J.A. Smith. 1986. On the nature of models in remote sensing, *Rem. Sensing, Environ.*, 20:121-139.

USDA Forest Service. 1997. Forest health monitoring field methods guide. Research Triangle Park, North Caroline, pp. 325.

Tian, Q., and M.N. Huhns. 1986. Algorithms for subpixel registration. *Comp. Vision, Graphics and Image Proc.*, 35:220-233.

White, J.D., G.C. Kroh, and J.E. Pinter. 1995. Forest mapping at Lassen Volcanic National Park, California, using Landsat TM Data and a Geographical Information System. *Photogramm. Eng. Rem. Sensing*, 61:299-305.

Woodcock, C.E., and A.H. Strahler. 1987. The factor of scale in remote sensing. *Rem. Sensing Environ.*, 21:311-332.

Woodcock C.E., S.A. Macomber, M. Pax-Lenney, and W.B. Cohen. 2001. Forest mapping with generalized classifier and Landsat TM data. *Rem. Sensing, Environ.*, 77:194-203.

Wynne, R.H., R.G. Oderwald. 1998. Forest inventory and assessment in the smallsat era. In *Proc. ASPRS Res. Technol. Inst. Annu. Meet.,* American Society of Photogrammetry and Remote Sensing, Bethesda, Maryland, pp. 810-815.

# Tables

**Table 2.1.** Cover types and their major species components in the study area.

| Cover Type | Major species present | |
|---|---|---|
| | Common name | Latin name |
| Aspen | Big Tooth Aspen<br>Quaking Aspen | (*Populus grandidentata*), and<br>(*Populus tremuloides*) |
| Northern hardwoods | Sugar Maple<br>Red Maple<br>American Beech<br>Black Cherry<br>Basswood<br>White Ash | (*Acer saccharum*),<br>(*Acer rubrum*),<br>(*Fagus americana*),<br>(*Prunus serotina*),<br>(*Tilia americana*), and<br>(*Fraxinus americana*) |
| Oak | White Oak<br>Red Oak | (*Quercus alba*), and<br>(*Quercus rubra*) |
| Red Pine Plantation | Red Pine | (*Pinus resinosa*) |
| Natural Pine | White Pine | (*Pinus strobes*) |

**Table 2.2.** Spectral registration vector components and length at plot centers calculated as those that maximized between-band correlation using dark pixels of the NIR band. Band correlation was evaluated within a 300 x 300 window centered at respective plot centers.

| | NIR-BLUE | | | NIR-GREEN | | | NIR-RED | | |
|---|---|---|---|---|---|---|---|---|---|
| | Vector component | | Vector length | Vector component | | Vector length | Vector component | | Vector length |
| Plot ID | Easting | Northing | | Easting | Northing | | Easting | Northing | |
| 1 | 0 | -1 | 1.00 | 0 | 0 | 0.00 | 0 | 0 | 0.00 |
| 2 | 0 | -1 | 1.00 | -1 | 0 | 1.00 | 0 | 0 | 0.00 |
| 3 | -2 | -1 | 2.24 | 0 | 0 | 0.00 | 0 | 0 | 0.00 |
| 4 | 0 | 1 | 1.00 | -1 | 0 | 1.00 | 0 | -1 | 1.00 |
| 5 | 0 | 0 | 0.00 | 0 | -2 | 2.00 | 1 | 1 | 1.41 |
| 6 | 0 | 0 | 0.00 | 1 | 0 | 1.00 | -1 | 0 | 1.00 |
| 7 | -1 | 0 | 1.00 | 2 | 1 | 2.24 | 0 | 0 | 0.00 |
| 8 | -1 | 1 | 1.41 | 0 | 0 | 0.00 | -1 | 0 | 1.00 |
| 9 | -2 | -1 | 2.24 | 1 | 1 | 1.41 | 1 | 1 | 1.41 |
| 10 | 0 | 1 | 1.00 | 1 | 0 | 1.00 | 1 | -1 | 1.41 |
| 11 | -1 | 0 | 1.00 | 0 | 1 | 1.00 | 0 | -1 | 1.00 |
| 12 | -1 | -1 | 1.41 | 0 | 1 | 1.00 | 0 | 0 | 0.00 |
| 13 | 1 | -1 | 1.41 | -2 | -1 | 2.24 | 1 | 1 | 1.41 |
| 14 | 0 | 0 | 0.00 | 0 | 1 | 1.00 | 0 | -1 | 1.00 |
| 15 | 0 | 0 | 0.00 | -1 | 0 | 1.00 | -1 | -1 | 1.41 |
| 16 | 1 | -1 | 1.41 | 0 | -1 | 1.00 | -1 | 0 | 1.00 |
| 17 | 0 | 0 | 0.00 | -1 | -1 | 1.41 | 1 | 1 | 1.41 |
| 18 | 1 | -1 | 1.41 | 1 | 0 | 1.00 | 0 | 0 | 0.00 |
| 19 | -1 | 0 | 1.00 | 0 | -1 | 1.00 | -1 | 0 | 1.00 |
| 20 | 0 | 1 | 1.00 | -1 | -2 | 2.24 | 0 | 1 | 1.00 |
| 21 | 0 | 1 | 1.00 | -1 | -1 | 1.41 | 1 | 1 | 1.41 |
| 22 | 0 | -1 | 1.00 | -1 | 0 | 1.00 | 0 | 0 | 0.00 |
| 23 | 0 | 0 | 0.00 | -1 | 1 | 1.41 | 0 | 0 | 0.00 |
| 24 | 0 | -2 | 2.00 | 0 | 0 | 0.00 | 1 | 0 | 1.00 |
| 25 | 2 | 0 | 2.00 | 0 | 0 | 0.00 | 0 | 1 | 1.00 |
| 26 | -1 | 1 | 1.41 | 2 | 0 | 2.00 | 0 | 0 | 0.00 |
| 27 | 2 | 1 | 2.24 | 0 | 1 | 1.00 | 1 | 0 | 1.00 |
| 28 | 1 | -1 | 1.41 | 0 | 1 | 1.00 | 0 | -1 | 1.00 |
| 29 | 1 | -1 | 1.41 | 1 | 0 | 1.00 | 1 | 0 | 1.00 |
| 30 | -2 | 1 | 2.24 | 0 | 0 | 0.00 | 0 | 0 | 0.00 |
| 31 | -2 | -2 | 2.83 | 0 | 1 | 1.00 | 0 | 0 | 0.00 |
| 32 | 0 | -1 | 1.00 | -1 | 0 | 1.00 | 1 | -1 | 1.41 |
| 33 | 0 | 2 | 2.00 | 1 | 1 | 1.41 | 1 | 0 | 1.00 |
| 34 | -1 | 2 | 2.24 | 1 | 0 | 1.00 | -1 | 0 | 1.00 |
| Total | | | 42.32 | | | 35.78 | | | 26.31 |

**Table 2.3.** Sums of spectral DN value differences between DN means of overlapping regions of adjacent frames along closed multi-frame paths calculated before and after BRDF/Brightness adjustment. DN means were computed using only the portion of overlapping regions occupied by deciduous forests. BRDF coefficients of the Roujean et al. model, integral to the normalization process and optimized to minimize spectral column sums, are shown.

| | | | Brightness Variability Within a Frame Path (DN) | | | | | | | |
|---|---|---|---|---|---|---|---|---|---|---|
| | | | Blue | | Green | | Red | | NIR | |
| Site | Path | Number of frames in path | Original | Normalized | Original | Normalized | Original | Normalized | Original | Normalized |
| I | 1 | 16 | 1279 | -44 | -2730 | 54 | 3460 | -98 | 4813 | 143 |
| I | 2 | 18 | -2384 | 130 | -1238 | 46 | 1107 | -38 | 3085 | -75 |
| I | 3 | 17 | 1137 | 182 | -3320 | 276 | 1729 | 212 | -4695 | -91 |
| I | 4 | 20 | -2259 | 24 | -169 | 30 | -3251 | 30 | 1926 | -28 |
| I | 5 | 20 | 3720 | -192 | -2829 | -112 | -2910 | -142 | -4166 | 52 |
| II | 6 | 18 | -1252 | -6 | 3774 | -56 | 3778 | 110 | 2865 | -107 |
| II | 7 | 15 | 1260 | -114 | 3549 | -174 | -2323 | 148 | 4185 | -104 |
| II | 8 | 15 | 3466 | 80 | 3542 | -24 | -508 | 72 | -6315 | 6 |
| II | 9 | 15 | -2092 | -38 | 2282 | 42 | 1466 | -128 | -975 | 83 |
| II | 10 | 20 | 886 | 44 | 1350 | 38 | 1298 | -62 | 4989 | 77 |
| Column Sum | | | 3761 | 66 | 4211 | 120 | 3846 | 104 | 5712 | -44 |
| Column Range | | | 6104 | 374 | 7094 | 450 | 7029 | 354 | 11304 | 250 |
| Mean (among paths) per frame brightness variability | | | 238 | 2 | 319 | 6 | 255 | 8 | 285 | -1 |
| Range (among paths) of per frame brightness variability | | | 370 | 21 | 432 | 28 | 379 | 21 | 722 | 16 |
| Optimized BRDF Coefficients | $k_0$ | | | 0.153 | | 0.183 | | 0.147 | | 0.281 |
| | $k_1$ | | | 0.115 | | 0.147 | | 0.099 | | 0.058 |
| | $k_2$ | | | 0.036 | | 0.052 | | 0.058 | | 0.301 |

**Table 2.4a.** Maximum Likelihood classification results and associated accuracy assessment parameters obtained with cross validation for all subplots with signatures developed from sites I and II using original DNs.

| | | Observed | | | | | |
|---|---|---|---|---|---|---|---|
| | | ASP | NH | Oak | RPP | NP | Row Total |
| Classified | Aspen (ASP) | 12 | 5 | 4 | 2 | 2 | 25 |
| | Northern Hardwoods (NH) | 7 | 13 | 4 | 3 | 3 | 30 |
| | Oak | 5 | 6 | 10 | 2 | 3 | 26 |
| | Red Pine Plantation (RPP) | 1 | 2 | 4 | 16 | 8 | 31 |
| | Natural Pine (NP) | 3 | 2 | 2 | 5 | 12 | 24 |
| | Column Total | 28 | 28 | 24 | 28 | 28 | 136 |

| | Accuracy (%) | | Errors (%) | |
|---|---|---|---|---|
| | Producer's | Consumer's | Commission | Omission |
| ASP | 42.86 | 48.00 | 46.43 | 57.14 |
| NH | 46.43 | 43.33 | 60.71 | 53.57 |
| Oak | 41.67 | 38.46 | 66.67 | 58.33 |
| RPP | 57.14 | 51.61 | 53.57 | 42.86 |
| NP | 42.86 | 50.00 | 42.86 | 57.14 |

| ML Probability Threshold | Unclassified Pixels (%) |
|---|---|
| 0.00 | 0.00 |
| 0.10 | 21.30 |
| 0.25 | 48.20 |
| 0.50 | 87.60 |
| 0.75 | 98.20 |

| Class | Conditional Kappa |
|---|---|
| ASP | 0.3452 |
| NH | 0.2864 |
| Oak | 0.2527 |
| RPP | 0.3907 |
| NP | 0.3704 |

| | |
|---|---|
| Overall Accuracy (%) | 0.4632 |
| Kappa Coefficient | 0.3288 |
| $s^2_k$ | 0.0019 |
| $Z_k$ | 7.5535* |

* Significant at $\alpha = 0.01$

**Table 2.4b.** Maximum Likelihood classification results and associated accuracy assessment parameters obtained with cross validation for subplots in site I using original DN site I signatures.

| | | Observed | | | | | |
|---|---|---|---|---|---|---|---|
| | | ASP | NH | Oak | RPP | NP | Row Total |
| Classified | Aspen (ASP) | 7 | 2 | 2 | 3 | 1 | 15 |
| | Northern Hardwoods (NH) | 4 | 5 | 3 | 0 | 2 | 14 |
| | Oak | 3 | 3 | 4 | 2 | 2 | 14 |
| | Red Pine Plantation (RPP) | 0 | 1 | 2 | 8 | 4 | 15 |
| | Natural Pine (NP) | 2 | 1 | 1 | 3 | 7 | 14 |
| | Column Total | 16 | 12 | 12 | 16 | 16 | 72 |

| | Accuracy (%) | | Errors (%) | |
|---|---|---|---|---|
| | Producer's | Consumer's | Commission | Omission |
| ASP | 43.75 | 46.67 | 56.25 | 50.00 |
| NH | 41.67 | 35.71 | 58.33 | 75.00 |
| Oak | 33.33 | 28.57 | 66.67 | 83.33 |
| RPP | 50.00 | 53.33 | 50.00 | 43.75 |
| NP | 43.75 | 50.00 | 56.25 | 43.75 |

| ML Probability Threshold | Unclassified Pixels (%) |
|---|---|
| 0.00 | 0.00 |
| 0.10 | 23.50 |
| 0.25 | 50.10 |
| 0.50 | 86.60 |
| 0.75 | 97.50 |

| Class | Conditional Kappa |
|---|---|
| ASP | 0.3143 |
| NH | 0.2286 |
| Oak | 0.1429 |
| RPP | 0.4000 |
| NP | 0.3571 |

| | |
|---|---|
| Overall Accuracy (%) | 0.4306 |
| Kappa Coefficient | 0.2876 |
| $s^2_k$ | 0.0035 |
| $Z_k$ | 4.8617* |

* Significant at $\alpha = 0.01$

**Table 2.4c.** Maximum Likelihood classification results and associated accuracy assessment parameters obtained with cross validation for subplots in site I using original DN site II signatures.

| | | Observed | | | | | |
|---|---|---|---|---|---|---|---|
| | | ASP | NH | Oak | RPP | NP | Row Total |
| Classified | Aspen (ASP) | 7 | 3 | 3 | 3 | 1 | 17 |
| | Northern Hardwoods (NH) | 4 | 5 | 2 | 0 | 1 | 12 |
| | Oak | 3 | 2 | 4 | 2 | 2 | 13 |
| | Red Pine Plantation (RPP) | 1 | 1 | 1 | 7 | 4 | 14 |
| | Natural Pine (NP) | 1 | 1 | 2 | 4 | 8 | 16 |
| | Column Total | 16 | 12 | 12 | 16 | 16 | 72 |

| | Accuracy (%) | | Errors (%) | |
|---|---|---|---|---|
| | Producer's | Consumer's | Commission | Omission |
| ASP | 43.75 | 41.18 | 56.25 | 62.50 |
| NH | 41.67 | 41.67 | 58.33 | 58.33 |
| Oak | 33.33 | 30.77 | 66.67 | 75.00 |
| RPP | 43.75 | 50.00 | 56.25 | 43.75 |
| NP | 50.00 | 50.00 | 50.00 | 50.00 |

| ML Probability Threshold | Unclassified Pixels (%) |
|---|---|
| 0.00 | 0.00 |
| 0.10 | 21.30 |
| 0.25 | 48.20 |
| 0.50 | 87.60 |
| 0.75 | 98.20 |

| Class | Conditional Kappa |
|---|---|
| ASP | 0.2437 |
| NH | 0.3000 |
| Oak | 0.1692 |
| RPP | 0.3571 |
| NP | 0.3571 |

| | |
|---|---|
| Overall Accuracy (%) | 0.4306 |
| Kappa Coefficient | 0.2856 |
| $S^2_k$ | 0.0035 |
| $Z_k$ | 4.8183* |

* Significant at $\alpha = 0.01$

**Table 2.4d.** Maximum Likelihood classification results and associated accuracy assessment parameters obtained with cross validation for subplots in site II using original DN site II signatures.

| | | Observed | | | | | |
|---|---|---|---|---|---|---|---|
| | | ASP | NH | Oak | RPP | NP | Row Total |
| Classified | Aspen (ASP) | 5 | 3 | 2 | 1 | 1 | 12 |
| | Northern Hardwoods (NH) | 2 | 7 | 3 | 0 | 0 | 12 |
| | Oak | 3 | 4 | 5 | 0 | 1 | 13 |
| | Red Pine Plantation (RPP) | 0 | 1 | 1 | 7 | 4 | 13 |
| | Natural Pine (NP) | 2 | 1 | 1 | 4 | 6 | 14 |
| | Column Total | 12 | 16 | 12 | 12 | 12 | 64 |

| | Accuracy (%) | | Errors (%) | |
|---|---|---|---|---|
| | Producer's | Consumer's | Commission | Omission |
| ASP | 41.67 | 41.67 | 58.33 | 58.33 |
| NH | 43.75 | 58.33 | 56.25 | 31.25 |
| Oak | 41.67 | 38.46 | 58.33 | 66.67 |
| RPP | 58.33 | 53.85 | 41.67 | 50.00 |
| NP | 50.00 | 42.86 | 50.00 | 66.67 |

| ML Probability Threshold | Unclassified Pixels (%) |
|---|---|
| 0.00 | 0.00 |
| 0.10 | 19.50 |
| 0.25 | 47.20 |
| 0.50 | 82.80 |
| 0.75 | 96.40 |

| Class | Conditional Kappa |
|---|---|
| ASP | 0.2821 |
| NH | 0.4444 |
| Oak | 0.2426 |
| RPP | 0.4320 |
| NP | 0.2967 |

| | |
|---|---|
| Overall Accuracy (%) | 0.4688 |
| Kappa Coefficient | 0.3366 |
| $s^2_k$ | 0.0040 |
| $Z_k$ | 5.2889* |

* Significant at $\alpha = 0.01$

**Table 2.4e.** Maximum Likelihood classification results and associated accuracy assessment parameters obtained with cross validation for subplots in site II using original DN site I signatures.

| | | Observed | | | | | |
|---|---|---|---|---|---|---|---|
| | | ASP | NH | Oak | RPP | NP | Row Total |
| Classified | Aspen (ASP) | 5 | 4 | 2 | 2 | 1 | 14 |
| | Northern Hardwoods (NH) | 2 | 6 | 3 | 0 | 0 | 11 |
| | Oak | 4 | 4 | 6 | 0 | 0 | 14 |
| | Red Pine Plantation (RPP) | 0 | 1 | 0 | 6 | 3 | 10 |
| | Natural Pine (NP) | 1 | 1 | 1 | 4 | 8 | 15 |
| | Column Total | 12 | 16 | 12 | 12 | 12 | 64 |

| | Accuracy (%) | | Errors (%) | |
|---|---|---|---|---|
| | Producer's | Consumer's | Commission | Omission |
| ASP | 41.67 | 35.71 | 58.33 | 75.00 |
| NH | 37.50 | 54.55 | 62.50 | 31.25 |
| Oak | 50.00 | 42.86 | 50.00 | 66.67 |
| RPP | 50.00 | 60.00 | 50.00 | 33.33 |
| NP | 66.67 | 53.33 | 33.33 | 58.33 |

| ML Probability Threshold | Unclassified Pixels (%) |
|---|---|
| 0.00 | 0.00 |
| 0.10 | 19.10 |
| 0.25 | 48.60 |
| 0.50 | 83.20 |
| 0.75 | 95.40 |

| Class | Conditional Kappa |
|---|---|
| ASP | 0.2088 |
| NH | 0.3939 |
| Oak | 0.2967 |
| RPP | 0.5077 |
| NP | 0.4256 |

| | |
|---|---|
| Overall Accuracy (%) | 0.4844 |
| Kappa Coefficient | 0.3569 |
| $s^2_k$ | 0.0041 |
| $Z_k$ | 5.5768* |

* Significant at $\alpha = 0.01$

**Table 2.4f.** Maximum Likelihood classification results and associated accuracy assessment parameters obtained with cross validation for all subplots using post-brightness normalization signatures from site I.

| | | Observed | | | | | |
|---|---|---|---|---|---|---|---|
| | | ASP | NH | Oak | RPP | NP | Row Total |
| Classified | Aspen (ASP) | 15 | 5 | 4 | 2 | 3 | 29 |
| | Northern Hardwoods (NH) | 5 | 14 | 2 | 1 | 1 | 23 |
| | Oak | 4 | 6 | 11 | 2 | 5 | 28 |
| | Red Pine Plantation (RPP) | 1 | 1 | 4 | 16 | 7 | 29 |
| | Natural Pine (NP) | 3 | 2 | 3 | 7 | 12 | 27 |
| | Column Total | 28 | 28 | 24 | 28 | 28 | 136 |

| | Accuracy (%) | | Errors (%) | |
|---|---|---|---|---|
| | Producer's | Consumer's | Commission | Omission |
| ASP | 53.57 | 51.72 | 46.43 | 50.00 |
| NH | 50.00 | 60.87 | 50.00 | 32.14 |
| Oak | 45.83 | 39.29 | 54.17 | 70.83 |
| RPP | 57.14 | 55.17 | 42.86 | 46.43 |
| NP | 42.86 | 44.44 | 57.14 | 53.57 |

| ML Probability Threshold | Unclassified Pixels (%) |
|---|---|
| 0.00 | 0.00 |
| 0.10 | 18.10 |
| 0.25 | 41.20 |
| 0.50 | 83.20 |
| 0.75 | 94.80 |

| Class | Conditional Kappa |
|---|---|
| ASP | 0.3921 |
| NH | 0.5072 |
| Oak | 0.2628 |
| RPP | 0.4355 |
| NP | 0.3004 |

| | |
|---|---|
| Overall Accuracy (%) | 0.5000 |
| Kappa Coefficient | 0.3751 |
| $s^2_k$ | 0.0019 |
| $Z_k$ | 8.5801* |

* Significant at $\alpha = 0.01$

**Table 2.4g.** Maximum Likelihood classification results and associated accuracy assessment parameters obtained with cross validation for subplots in site I using post-brightness normalization signatures from site I.

| | | Observed | | | | | |
|---|---|---|---|---|---|---|---|
| | | ASP | NH | Oak | RPP | NP | Row Total |
| Classified | Aspen (ASP) | 8 | 2 | 2 | 2 | 1 | 15 |
| | Northern Hardwoods (NH) | 3 | 7 | 3 | 0 | 1 | 14 |
| | Oak | 3 | 2 | 5 | 1 | 1 | 12 |
| | Red Pine Plantation (RPP) | 1 | 0 | 1 | 9 | 5 | 16 |
| | Natural Pine (NP) | 1 | 1 | 1 | 4 | 8 | 15 |
| | Column Total | 16 | 12 | 12 | 16 | 16 | 72 |

| | Accuracy (%) | | Errors (%) | |
|---|---|---|---|---|
| | Producer's | Consumer's | Commission | Omission |
| ASP | 50.00 | 53.33 | 50.00 | 43.75 |
| NH | 58.33 | 50.00 | 41.67 | 58.33 |
| Oak | 41.67 | 41.67 | 58.33 | 58.33 |
| RPP | 56.25 | 56.25 | 43.75 | 43.75 |
| NP | 50.00 | 53.33 | 50.00 | 43.75 |

| ML Probability Threshold | Unclassified Pixels (%) |
|---|---|
| 0.00 | 0.00 |
| 0.10 | 25.60 |
| 0.25 | 50.90 |
| 0.50 | 83.40 |
| 0.75 | 97.50 |

| Class | Conditional Kappa |
|---|---|
| ASP | 0.4000 |
| NH | 0.4000 |
| Oak | 0.3000 |
| RPP | 0.4375 |
| NP | 0.4000 |

| | |
|---|---|
| Overall Accuracy (%) | 0.5139 |
| Kappa Coefficient | 0.3907 |
| $s^2_k$ | 0.0036 |
| $Z_k$ | 6.5202* |

* Significant at $\alpha = 0.01$

**Table 2.4h.** Maximum Likelihood classification results and associated accuracy assessment parameters obtained with cross validation for subplots in site I using post-brightness normalization signatures from site II.

| | | Observed | | | | | |
|---|---|---|---|---|---|---|---|
| | | ASP | NH | Oak | RPP | NP | Row Total |
| Classified | Aspen (ASP) | 8 | 2 | 2 | 1 | 2 | 15 |
| | Northern Hardwoods (NH) | 2 | 7 | 3 | 0 | 1 | 13 |
| | Oak | 3 | 3 | 5 | 0 | 1 | 12 |
| | Red Pine Plantation (RPP) | 1 | 0 | 1 | 9 | 5 | 16 |
| | Natural Pine (NP) | 2 | 0 | 1 | 6 | 7 | 16 |
| | Column Total | 16 | 12 | 12 | 16 | 16 | 72 |

| | Accuracy (%) | | Errors (%) | |
|---|---|---|---|---|
| | Producer's | Consumer's | Commission | Omission |
| ASP | 50.00 | 53.33 | 50.00 | 43.75 |
| NH | 58.33 | 53.85 | 41.67 | 50.00 |
| Oak | 41.67 | 41.67 | 58.33 | 58.33 |
| RPP | 56.25 | 56.25 | 43.75 | 43.75 |
| NP | 43.75 | 43.75 | 56.25 | 56.25 |

| ML Probability Threshold | Unclassified Pixels (%) |
|---|---|
| 0.00 | 0.00 |
| 0.10 | 23.50 |
| 0.25 | 50.10 |
| 0.50 | 86.60 |
| 0.75 | 97.30 |

| Class | Conditional Kappa |
|---|---|
| ASP | 0.4000 |
| NH | 0.4462 |
| Oak | 0.3000 |
| RPP | 0.4375 |
| NP | 0.2768 |

| | |
|---|---|
| Overall Accuracy (%) | 0.5000 |
| Kappa Coefficient | 0.3727 |
| $s^2_k$ | 0.0036 |
| $Z_k$ | 6.1910* |

* Significant at $\alpha = 0.01$

**Table 2.**
assessm
brightne

| Classified | |
|---|---|
| | |

| | |
|---|---|
| ASP | |
| NH | |
| Oak | |
| RPP | |
| NP | |

| Clas |
|---|
| ASP |
| NH |
| Oak |
| RPP |
| NP |

**Table 2.4i.** Maximum Likelihood classification results and associated accuracy assessment parameters obtained with cross validation for subplots in site II using post-brightness normalization signatures from site II.

| | | Observed | | | | | |
|---|---|---|---|---|---|---|---|
| | | ASP | NH | Oak | RPP | NP | Row Total |
| Classified | Aspen (ASP) | 6 | 3 | 2 | 2 | 1 | 14 |
| | Northern Hardwoods (NH) | 2 | 9 | 3 | 0 | 0 | 14 |
| | Oak | 3 | 3 | 5 | 0 | 1 | 12 |
| | Red Pine Plantation (RPP) | 0 | 0 | 1 | 7 | 3 | 11 |
| | Natural Pine (NP) | 1 | 1 | 1 | 3 | 7 | 13 |
| | Column Total | 12 | 16 | 12 | 12 | 12 | 64 |

| | Accuracy (%) | | Errors (%) | |
|---|---|---|---|---|
| | Producer's | Consumer's | Commission | Omission |
| ASP | 50.00 | 42.86 | 50.00 | 66.67 |
| NH | 56.25 | 64.29 | 43.75 | 31.25 |
| Oak | 41.67 | 41.67 | 58.33 | 58.33 |
| RPP | 58.33 | 63.64 | 41.67 | 33.33 |
| NP | 58.33 | 53.85 | 41.67 | 50.00 |

| ML Probability Threshold | Unclassified Pixels (%) |
|---|---|
| 0.00 | 0.00 |
| 0.10 | 19.50 |
| 0.25 | 47.20 |
| 0.50 | 82.80 |
| 0.75 | 96.40 |

| Class | Conditional Kappa |
|---|---|
| ASP | 0.2967 |
| NH | 0.5238 |
| Oak | 0.2821 |
| RPP | 0.5524 |
| NP | 0.4320 |

| | |
|---|---|
| Overall Accuracy (%) | 0.5313 |
| Kappa Coefficient | 0.4132 |
| $s^2_k$ | 0.0040 |
| $Z_k$ | 6.5028* |

* Significant at $\alpha = 0.01$

**Table 2.4j.** Maximum Likelihood classification results and associated accuracy assessment parameters obtained with cross validation for subplots in site II using post-brightness normalization signatures form site I.

| | | Observed | | | | | |
|---|---|---|---|---|---|---|---|
| | | ASP | NH | Oak | RPP | NP | Row Total |
| Classified | Aspen (ASP) | 6 | 4 | 2 | 1 | 2 | 15 |
| | Northern Hardwoods (NH) | 2 | 9 | 3 | 0 | 0 | 14 |
| | Oak | 3 | 2 | 5 | 1 | 1 | 12 |
| | Red Pine Plantation (RPP) | 0 | 0 | 1 | 7 | 3 | 11 |
| | Natural Pine (NP) | 1 | 1 | 1 | 3 | 6 | 12 |
| | Column Total | 12 | 16 | 12 | 12 | 12 | 64 |

| | Accuracy (%) | | Errors (%) | |
|---|---|---|---|---|
| | Producer's | Consumer's | Commission | Omission |
| ASP | 50.00 | 40.00 | 50.00 | 75.00 |
| NH | 56.25 | 64.29 | 43.75 | 31.25 |
| Oak | 41.67 | 41.67 | 58.33 | 58.33 |
| RPP | 58.33 | 63.64 | 41.67 | 33.33 |
| NP | 50.00 | 50.00 | 50.00 | 50.00 |

| ML Probability Threshold | Unclassified Pixels (%) |
|---|---|
| 0.00 | 0.00 |
| 0.10 | 20.00 |
| 0.25 | 48.40 |
| 0.50 | 80.90 |
| 0.75 | 95.10 |

| Class | Conditional Kappa |
|---|---|
| ASP | 0.2615 |
| NH | 0.5238 |
| Oak | 0.2821 |
| RPP | 0.5524 |
| NP | 0.3846 |

| | |
|---|---|
| Overall Accuracy (%) | 0.5156 |
| Kappa Coefficient | 0.3936 |
| $s^2_k$ | 0.0041 |
| $Z_k$ | 6.1819* |

* Significant at $\alpha = 0.01$

**Table 2.5.** Z-scores of subplot classification results for combinations of cross-validation-based classification choices computed as standardized differences of respective kappa coefficients and associated p-values.

| | | Site I & II, original DNs | Site I,signatures from Site I, original DNs | Site I, signatures from Site II, original DNs | Site II, signatures from Site II, original DNs | Site II, signatures from Site I, original DNs | Site I & II, with brightness normalization | Site I, signatures from Site I with brightness normalization | Site I, signatures from Site II with brightness normalization | Site II, signatures from Site II with brightness normalization |
|---|---|---|---|---|---|---|---|---|---|---|
| Z-score | Site I, signatures from Site I, original DNs | -0.5067 (0.6124) | | | | | | | | |
| | Site I, signatures from Site II, original DNs | -0.5879 (0.5566) | -0.0239 (0.9809) | | | | | | | |
| | Site II, signatures from Site II, original DNs | 0.1015 (0.9192) | 0.5658 (0.5715) | -0.5889 (0.5559) | | | | | | |
| | Site II, signatures from Site I, original DNs | 0.3628 (0.7168) | 0.7949 (0.4267) | 0.8179 (0.4134) | 0.2256 (0.8215) | | | | | |
| | Site I & II, brightness normalization | 0.7511 (0.4526) | 1.1907 (0.2338) | 1.2179 (0.2233) | 0.5012 (0.6162) | 0.2350 (0.8142) | | | | |
| | Site I, signatures from Site I, brightness normalization | 0.8346 (0.4039) | 1.2236 (0.2211) | 1.2473 (0.2123) | 0.6206 (0.5349) | 0.3852 (0.7001) | 0.2104 (0.8334) | | | |
| | Site I, signatures form Site II, brightness normalization | 0.5919 (0.5539) | 1.0100 (0.3125) | 1.0337 (0.3013) | 0.4141 (0.6788) | 0.1801 (0.8571) | -0.0324 (0.9742) | -0.2121 (0.8320) | | |
| | Site II, signatures from Site II, brightness normalization | 1.1759 (0.2396) | 1.4503 (0.1470) | 1.4734 (0.1406) | 0.8564 (0.3918) | 0.6256 (0.5316) | 0.4960 (0.6199) | 0.2581 (0.7963) | 0.4646 (0.6422) | |
| | Site II, signatures form Site I, brightness normalization | 0.8366 (0.4028) | 1.2159 (0.2240) | 1.2388 (0.2154) | 0.6333 (0.5265) | 0.4053 (0.6853) | 0.2388 (0.8113) | 0.0330 (0.9737) | 0.2382 (0.8117) | -0.2178 (0.8276) |

**Table 2.6.** Change in class-conditional kappa coefficients computed before and after brightness normalization.

| | Cover Type | Original DNs | Brightness Corrected | ΔKappa |
|---|---|---|---|---|
| All subplots using signatures from site I and II | ASP | 0.3452 | 0.3921 | 0.0469 |
| | NH | 0.2864 | 0.5072 | 0.2208 |
| | Oak | 0.2527 | 0.2628 | 0.0101 |
| | RPP | 0.3907 | 0.4355 | 0.0448 |
| | NP | 0.3704 | 0.3004 | -0.0700 |
| Site I subplots using site I signatures | ASP | 0.3143 | 0.4000 | 0.0857 |
| | NH | 0.2286 | 0.4000 | 0.1714 |
| | Oak | 0.1429 | 0.3000 | 0.1571 |
| | RPP | 0.4000 | 0.4375 | 0.0375 |
| | NP | 0.3571 | 0.4000 | 0.0429 |
| Site II subplots using site II signatures | ASP | 0.2821 | 0.2967 | 0.0146 |
| | NH | 0.4444 | 0.5238 | 0.0794 |
| | Oak | 0.2426 | 0.2821 | 0.0395 |
| | RPP | 0.4320 | 0.5524 | 0.1204 |
| | NP | 0.2967 | 0.4320 | 0.1353 |
| Site I subplots using site II signatures | ASP | 0.2437 | 0.4000 | 0.1563 |
| | NH | 0.3000 | 0.4462 | 0.1462 |
| | Oak | 0.1692 | 0.3000 | 0.1308 |
| | RPP | 0.3571 | 0.4375 | 0.0804 |
| | NP | 0.3571 | 0.2768 | -0.0803 |
| Site II subplots using site I signatures | ASP | 0.2088 | 0.2615 | 0.0527 |
| | NH | 0.3939 | 0.5238 | 0.1299 |
| | Oak | 0.2967 | 0.2821 | -0.0146 |
| | RPP | 0.5072 | 0.5529 | 0.0452 |
| | NP | 0.4256 | 0.3846 | -0.0410 |
| Average across all five classification scenarios | ASP | | | 0.0712 |
| | NH | | | 0.1495 |
| | Oak | | | 0.0646 |
| | RPP | | | 0.0657 |
| | NP | | | -0.0026 |

**Table 2.7.** Classification error rates of subplots conditional upon cover type group (deciduous or coniferous) produced with maximum-likelihood based cross validation for all plots in the study area before and after brightness normalization.

| | | Aspen | Northern Hardwoods | Oak | Red Pine Plantation | Natural Pine |
|---|---|---|---|---|---|---|
| Original DNs | Deciduous | 12 (43%) | 11 (39%) | 8 (33%) | 7 (25%) | 8 (29%) |
| | Coniferous | 4 (14%) | 4 (14%) | 6 (25%) | 5 (18%) | 8 (29%) |
| Brightness normalization | Deciduous | 9 (32%) | 11 (39%) | 6 (25%) | 5 (18%) | 9 (32%) |
| | Coniferous | 4 (14%) | 3 (11%) | 7 (29%) | 7 (25%) | 7 (25%) |

## Figures

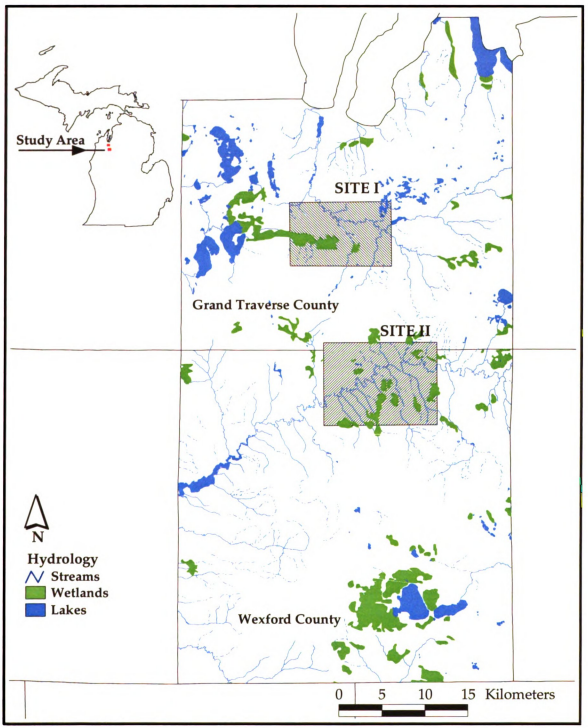


**Figure 2.1**. Study area map portraying hydrological features.

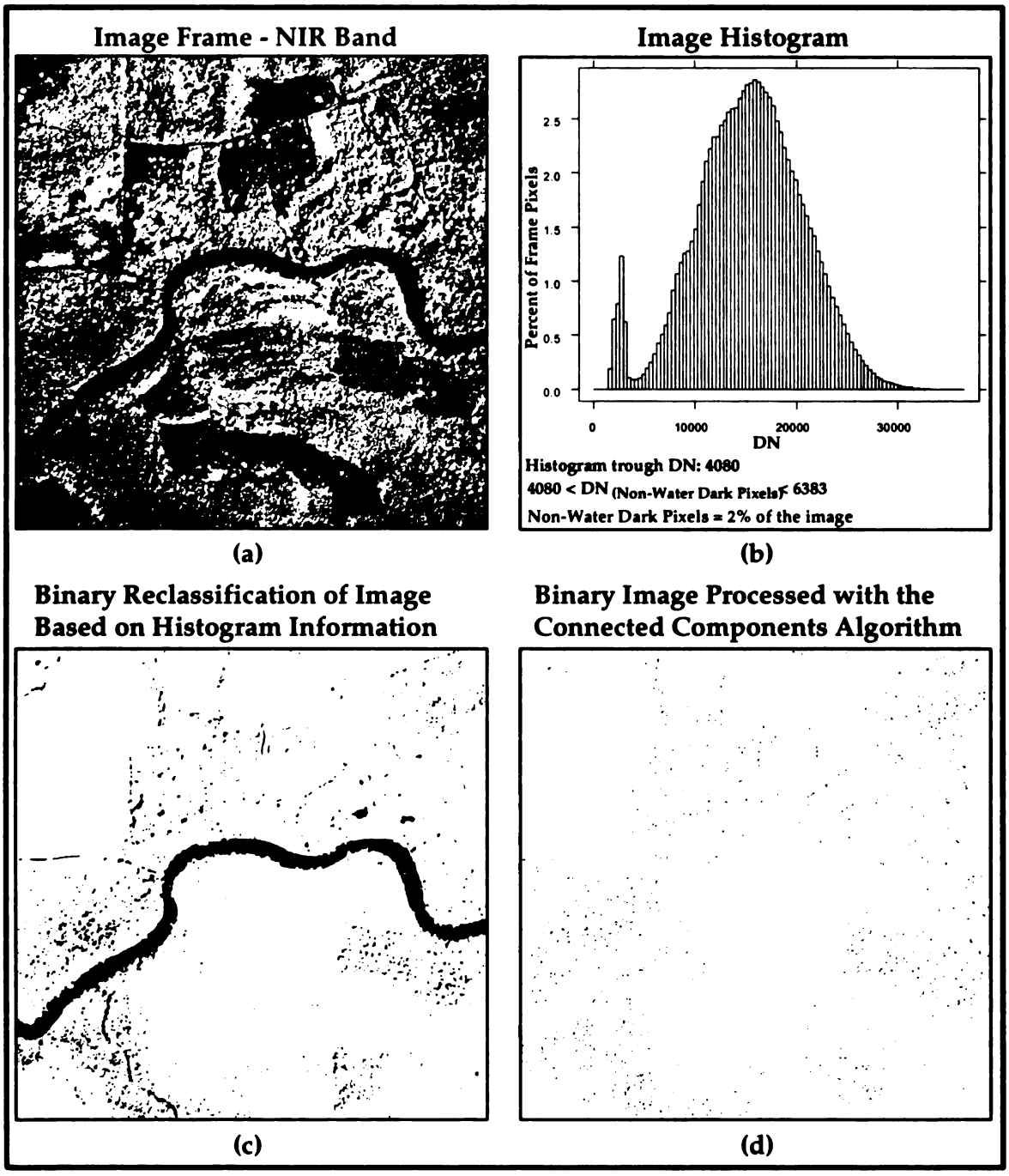


**Figure 2.2.** **a**. Original near infrared image frame, **b**. Image histogram with characteristic bimodal form, typical in the presence of water bodies, **c**. Binary reclassification of original image produced by using the upper dark pixel range DN as reclassification threshold, and **d**. Elimination of dark pixel clusters in the binary image with processing with the connected components algorithm for clusters with pixel membership exceeding 10.

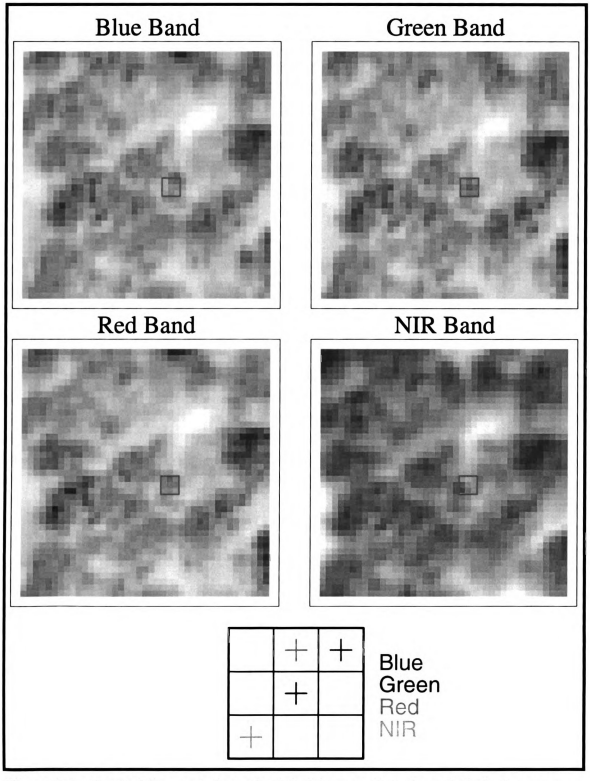


**Figure 2.3a**. Spectral frame portions of original imagery featuring a 3x3 pixels square window superimposed on each frame and corresponding to the same frame row and column indices. The 3x3 grid shows the location of the darkest pixel within the square window for each band.

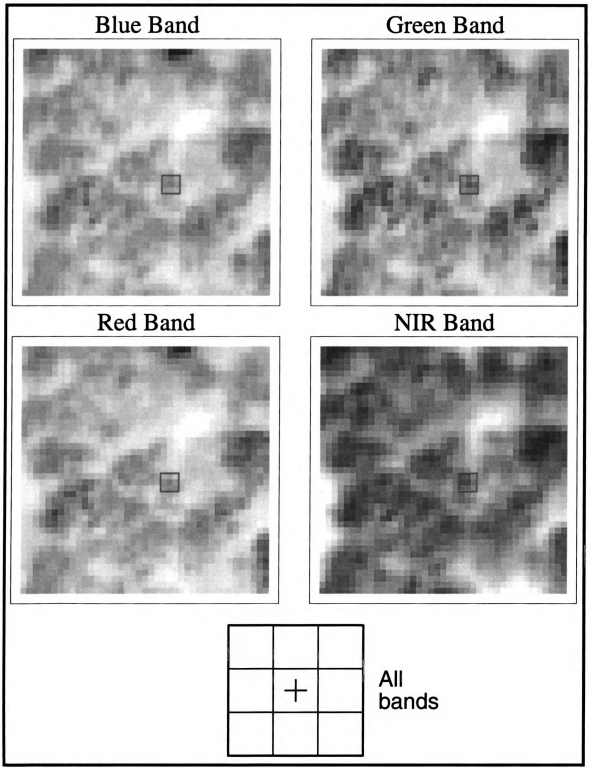


**Figure 2.3b**. Spectral frame portions of imagery corrected for registration errors featuring a 3x3 pixels square window superimposed on each frame and corresponding to the same frame row and column indices. The 3x3 grid shows the location of the darkest pixel within the square window.

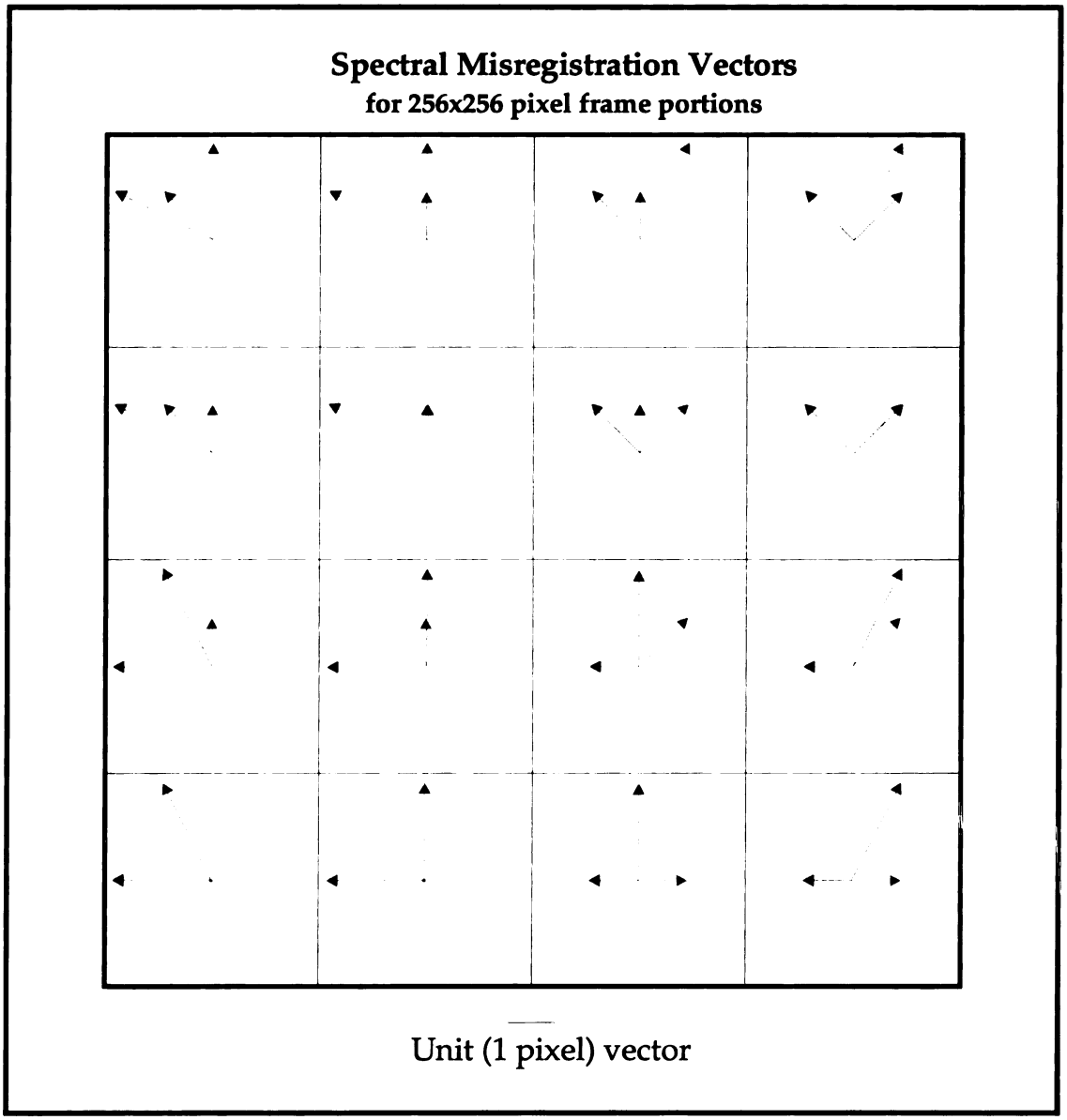


**Figure 2.4.** Registration vectors that maximized correlation between the NIR band and each of the visible bands for the image frame hosting plot 21. Correlation was calculated using the NIR band dark pixels for every $1/16^{th}$ frame portion. Vector colors correspond to respective bands.

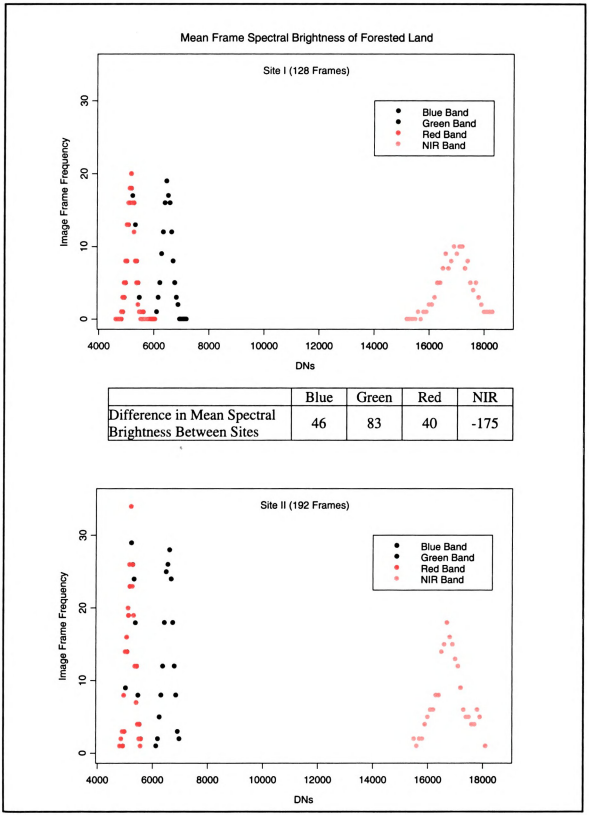


| | Blue | Green | Red | NIR |
|---|---|---|---|---|
| Difference in Mean Spectral Brightness Between Sites | 46 | 83 | 40 | -175 |




**Figure 2.5**. Post-brightness-adjustment mean spectral frame DNs for Site I (top) and Site II (bottom) and ensuing between-Site mean spectral brightness differences.

# CHAPTER 3

## FOREST STAND CANOPY STRUCTURE PARAMETER VALUE ESTIMATION AND COVER TYPE CLASSIFICATION VIA DIGITAL NUMBER AUTOCORRELATION TECHNIQUES IN HIGH-SPATIAL RESOLUTION MULTISPECTRAL DIGITAL AIRBORNE IMAGERY

## Abstract

*A study of forest stand canopy parameter assessment and cover type classification using digital, airborne, multispectral imagery is presented. The estimated parameters include stem density, canopy closure, and mean crown diameter. Parameter estimation is based on quantifying the spatial autocorrelation among pixel digital numbers (DN) using variogram analysis and an alternative, non-parametric approach known as slope-break analysis. Parameter estimation and cover type classification proceed from the identification of tree apexes. Parameter accuracy assessment is evaluated via value comparison with a spatially precise set of field observations over 34 plots installed in 5 cover types common in the Midwest region. Results show that, in general, slope-break-based parameter estimates are superior to those obtained using variograms. Estimated root mean square errors at the plot level for the former average 6.5% for stem density, 3.5% for canopy closure and 2.5% for mean crown diameter, which are less than or equal to error rates obtained via traditional forest stand cruising by experienced personnel. The employed methodology entails parsimonious parameterization and is supportive of automation. Overall cover type classification accuracy remains stable among classification scenarios across varying geographic extents and increases from approximately 70% when using original imagery DNs to over 85% when band registration problems are corrected and variable brightness regimes among imagery frames are normalized. Limiting cover type classification to pixels identified as tree apexes is found to improve traditional classification approaches that use all pixels by a remarkable 35%.*

## 3.1. Introduction

High spatial resolution digital imagery holds a promising potential for the extraction of forest inventory and canopy structure information including the delineation of individual tree crowns, canopy closure, stem density, stand species composition and crown classification (Franklin and McDermid, 1993; Gougeon, 1995a; Brandtberg, 1997; Dralle and Rudemo, 1997; Larsen, 1997; Gerylo et al., 1998; Larsen 1998; Quackenbush et al., 1999; Sheng et al, 2001). Traditionally, forest canopy structure parameters have been derived from aerial photographs (King, 2000; Wulder et al., 2002). A series of trials conducted by the Canadian Forest Management Institute three decades ago revealed that aerial photographs are rich in information content for individual-tree-based forest inventory purposes (Aldred and Kippen, 1967; Brun, 1972; Bonnor, 1977; Sayn-Wittgenstein, 1978). However, information extraction from aerial photographs is based on manual interpretation, a process known to be time consuming, labor intensive, and error-prone (Biging et al., 1991). Lately, due to increasing requirements on quantitative forest inventory information, a decrease in the popularity of aerial photographs for forest management decision-making has been observed (Hyyppä et al., 2000). *Digital*, high-spatial-resolution imagery, sometimes known as H-resolution imagery (Strahler et al., 1986), acquired from airborne platforms and recently available from satellites (QuickBird [Aplin et al., 1997] and IKONOS [Mangold, 1999]) is well suited to producing quantitative estimates of inventory variables and canopy structure attributes, and to process automation (Gong et al., 1999). Due to the large geographic extent of forests, automation is a practical prerequisite for full exploitation of the H-resolution digital

imagery in forest applications (Gougeon, 1995b; McGraw et al., 1998; Pouliot et al., 2002).

In high-spatial-resolution digital imagery of forested landscapes, each tree crown is represented by multiple pixels. Some of them correspond to the sunlit portion of the crowns while others represent crown portions in shadow. View and illumination angles, tree geometry, foliage orientation and bidirectional reflectance operate synergistically to create a variation of radiance, represented by pixel digital numbers (DN), at different locations within an individual crown (Leckie et al., 1992). Spectral DN values also vary as a function of the tree crown depth being greater near the tree center and lessening towards the crown edges (Li and Strahler, 1992). As a result, individual trees may be discerned as localized regions of high DN values. Individual tree identification based on high-DN-value digital image regions has been accomplished with a variety of techniques including valley following (Gougeon, 1995a), threshold-based clustering (Culvenor, 2002), template matching (Pollock, 1996; Larsen and Rudemo, 1997; Larsen, 1999), mathematical morphology (Walsworth and King, 1999), minimum cost route selection (Warner et al., 2000), maximum filtering (Brandtberg, 1997; Culvenor et al., 1999; Niemann et al., 1999; Pinz, 1999, Wulder et al., 2000), spatial autocorrelation (Treitz, 2001), or combinations of these approaches (Wulder et al., 2002).

Individual tree identification offers a potentially superior alternative to traditional per-pixel-based classification of forest cover types since it allows spectral signature construction using only the brightest pixels of a crown, or the average of the sunlit portion of a crown, or even the mean value within the identified crown (Gougeon, 1997). It has also been used for forest stand delineation and to provide estimates of forest stand

canopy st

(Gougeon

to forest

1997; Pe

et al., 19

l

having a

airborne

the H-re

techniq

stands v

(Gerylo

rough c

individ

confor

canopy

al., 19

classif

in fore

studies

operat

typica

canopy structure parameters such as crown size, stem density, and canopy closure (Gougeon, 1997; Gerylo, 1998). These canopy structure parameters are important inputs to forest models (Sprinz and Burkhart, 1987; Gering and May, 1995; Deutschman et al., 1997; Pereira et al., 1997; Trichon, 2001) and are critical in modeling forest fires (Keane et al., 1999).

Individual tree crown identification appears to work best with digital imagery having a spatial resolution less than 1m, but it is expected to work well enough with 1m airborne and satellite digital imagery to justify more extensive development and use of the H-resolution, digital remote sensing technology (Wulder, 1999). Most of the techniques mentioned above have been tested in pure or mixed coniferous stands, or stands with only simple combinations of one or two conifer and deciduous species (Gerylo et al., 1998). In such circumstances, the conical shape of crowns produces a rough canopy surface with distinct tree apexes and shadowed portions that facilitate individual crown delineation. Conversely, deciduous tree crowns typically defy conformal shapes, often have multiple maxima, usually exhibit a relatively smooth canopy surface and less distinct edges, and thus are more difficult to delineate (Warner et al., 1999).

Despite sporadic successes in utilizing H-resolution imagery in forest stand classification and canopy structure parameter estimation, "... this area of image analysis in forestry appears surprisingly poorly developed" (Franklin, 2001, p. 260). The few studies that have used this technology in forest inventory parameter estimation usually operated on a single image (frame) and a single forest stand, or a very small number of, typically coniferous, adjacent stands. Hence, little is known about whether high-spatial-

resolution imagery can reliably be used to predict forest inventory parameter values for stands of variable, deciduous forest cover types. Spatially extended investigations have been hindered by 1) frame geometric correction and registration requirements (Franklin, 2001, p.260); 2) logistic concerns related to the acquisition of necessary canopy parameter information in the field (Gong et al., 1999); 3) brightness variations among imagery frames (Mikkola and Pellikka, 2002; Chapter 2, this dissertation), and 4) a dearth of process automation paradigms (McGraw et al., 1998).

The objective of the research presented in this chapter is to investigate the utility of airborne, high-spatial-resolution, multispectral digital imagery for cover type classification and canopy structure parameter estimation while addressing all of the aforementioned factors known to hinder information extraction at the multiple stand scale. Two hypotheses are evaluated: 1) spectral classification of forest cover types based on signatures derived from selected tree crown portions improves classification accuracy obtained using spectral signatures of all pixels in a forest stand (the traditional approach), and 2) estimates of stand canopy structure parameters (stem density, average crown diameter, canopy closure) can be reliably obtained via pixel DN spatial autocorrelation structure analysis. These hypotheses were evaluated for five cover types common in the Midwest region using a detailed set of field observations obtained from multiple, non-adjacent stands.

## 3.2. Individual Tree Identification

At present, algorithms that detect individual trees in H-resolution imagery are based on the association of a tree apex with a local maximum in image brightness value. This spectral reflectance pattern of tree crowns constitutes the main structural element for

every forest stand canopy and when viewed in three dimensions it can be perceived as a convex shape. For coniferous species, the shape of individual crowns could be approximated by a cone. Hence, high-resolution imagery of a forest stand is composed of contiguous pixel regions, which represent trees or clusters of trees. The variety of techniques for processing individual trees from high-spatial-resolution imagery mentioned earlier, all attempt to capture the differing image spatial structure that emerges from the complex relationships between image spatial resolution and canopy structural characteristics. The ratio of crown size to resolution is sometimes used as an indicator capable of quantifying such relationships and thus for determining the image analysis technique best suited for individual crown identification (Pouliot et al., 2002). For example, at ratio values of 30 or larger the morphology of individual trees may be detected (Brandtberg, 1997). Ratio values between 8 and 30 appear to justify use of the valley following algorithm, while for ratio values in the range of 2 to 8 the most appropriate processing technique appears to be local maximum filtering (LMF) (Wulder, 1998). The latter case is typical of imagery sets acquired with a spatial resolution of 0.6-1.0m.

In medium to densely forested areas on high-spatial-resolution imagery, individual trees may be discerned as regions of high reflectance (i.e. high DNs). For conifers, the spatial structure of this reflectance pattern results in a single local maximum DN value found at or near the center of tree crowns (Wulder et al., 2000). Deciduous species, on the other hand, generally exhibit larger within-crown brightness variation due to the effect of branches, branch bundles, and branch shadow patterns on the spectral response of the crown, which is often characterized by multiple maxima and non-

monotonic change in brightness from the crown center to its periphery (Franklin et al., 1996). In the LMF approach for tree identification, a window is passed over all pixels of a forest stand to determine if a given pixel is of higher DN than all other pixels within the window (Dralle and Rudemo, 1997). Pixels identified as the largest DN within the window are noted as stem locations. However, when a window of fixed size is passed over a forest stand it does not account for the presence of trees with different crown sizes. Therefore a fixed sized window is incapable of accounting for the object-resolution relationship that exists between the trees (objects) and the image spatial resolution (Franklin, 1996). As a result, the presence of trees with a crown size larger than the fixed window would tend to inflate the number of trees identified and increase the tree commission error rate while trees with a crown size smaller than the fixed window would often be missed thus increasing the omission error rate. In fixed-size windows, a reduction in the one type of error typically results in an increase in the other error type (Wulder, 2002). In forest stands characterized by highly variable tree crown sizes, fixed-size windows were found to perform very poorly, often correctly identifying fewer than half of the total number of dominant and co-dominant trees present (Wulder, 2000). A simultaneous reduction in commission and omission error rates of identified trees is possible when the size of the window used in LMF is adjusted to reflect the brightness variability in the vicinity of the processed pixel (Pouliot et al., 2002). Such a pixel-specific conditioning of window size can be accomplished by examining the form of spatial autocorrelation among pixels. A quantification of spatial autocorrelation can be performed by several techniques and corresponding measures (Deutsch and Journel, 1992, p.40), including variogram analysis.

### 3.2.1. Parametric quantification of image autocorrelation

Variogram analysis is a well understood and frequently applied image-processing technique in remote sensing (Curran and Atkinson, 1998). It can be used to provide a quantitative assessment of spatial dependency for continuously varying phenomena (Varekamp et al., 1996). A variogram describes the magnitude, spatial scale and general form of the variation among spatially distributed, continuous variables (Matheron, 1963), but it can be modified to accommodate the analysis of spatial dependency for phenomena sampled at regular intervals, such as the spectral reflectance or brightness regimes in digital imagery (Curran and Atkinson, 1998). Variogram analysis entails the computation of relationships between pixel pairs. The relationship between pairs of pixels found $h$ pixels apart (the "lag" distance), is quantified as half the average square difference between pixel pair values and it is known as the semivariance for that lag. Hence the semivariogram, $\gamma(h)$, is a plot of semivariance as a function of lag and is computed (Curran, 1988) as

$$\gamma(h) = \frac{1}{2} E[Z(x) - Z(x-h)]^2 \tag{3.1}$$

where $Z$ denotes a pixel value at location $x$. When computed on digital imagery, $x$ is a two element vector of the pixel's row and column indices. The lag $h$ indexes the distance between pixel pairs for comparison. The prefix "semi" in semivariance denotes the fact that each pixel in a pair enters the computation of (1) twice, once as $Z(x)$ (head value) and once as $Z(x\text{-}h)$ (tail value). A division by two is necessary to adjust $\gamma(h)$ to its proper value. It should be noted that the terms variogram and semivariogram are treated as equivalent in the literature and are used interchangeably unless specifically mentioned

otherwise. When the semivariogram is computed for an imagery region $R$, its value for a given lag $h$ is an estimate of the semivariance for that lag and represents a measure of dissimilarity between spatially separated pixels (Jupp et al., 1988). The lag-specific semivariance estimate is computed as

$$\hat{\gamma}(h) = \frac{1}{2m(h)} \sum_{i=1}^{m(h)} [z(x_i) - z(x_i - h)]^2 \tag{3.2}$$

where $m(h)$ is the number of pixels within $R$ separated by $h$. In the presence of spatial structure, a semivariogram would reveal that semivariance rises with increasing $h$, until reaching an asymptote known as the "sill", which indicates the maximum variability between pixels. The "range" of the semivariogram is the number of lags, or distance to the sill (Curran and Atkinson, 1998). Within the range, spatial dependence is indicated; pixels separated by distances larger than the range are understood to be spatially independent (uncorrelated) (Levesque and King, 1996). The range of semivariograms computed on digital imagery represents the average size of the structural elements depicted in the imagery, which, in the case of medium- to high-density forests and H-resolution, equals the mean crown diameter (Cohen et al., 1990). Therefore, the range of the semivariogram computed for the neighborhood $R$ around individual pixels might be useful for determining the appropriate size of the window for identifying individual trees (Wulder et al., 2000).

Although conceptually, semivariogram range computation is associated with a number of logistical concerns and theoretical constraints (Daley et al., 1998). It assumes that the second-order spatial autocorrelation of pixels within $R$ is stationary, and first-order autocorrelation (trend) is absent. If a trend is indeed present and not accounted for,

unbounded or overestimated semivariogram ranges should be expected (Deutsch and Journel, 1992). Further, because solar illumination is strongly directional, mutual shadowing between adjacent crowns causes anisotropic reflectance autocorrelation patterns. Empirical semivariograms computed parallel to the solar plane over forest in H-resolution digital imagery tend to have shorter ranges than those computed across the solar plane. To avoid a systematic bias in range value computation, it is important to either identify the proper orientation for directional semivariogram computation or equally weight all possible directions, thus producing an omnidirectional semivariogram (Franklin et al., 1996). In addition, because the reliability of semivariance estimates is known to decrease with increasing lag (Curran and Atkinson, 1998), the size (largest dimension) of *R* around a processed pixel should be at least three times the maximum expected range value so that an adequate number of pixels pairs contribute to the computation of semivariance estimates for lag distances that approximate the expected range (Isaaks and Srivastava, 1989). Assuming a forest stand with dominant and co-dominant trees of maximum crown diameter of 8m, and with a 1m imagery spatial resolution, a reliable range estimation would necessitate a region of 24 x 24 = 576 pixels to be examined for each processed pixel, thereby resulting in substantial computational cost. A region of such size would allow pixels belonging to crowns non-adjacent to the crown in which the processed pixel belongs to influence the semivariogram range value computed for the latter pixel. Semivariograms, therefore, provide a quantification of autocorrelation that has a regional rather than local scope and may thus be a biased estimator of the appropriate window size for individual tree identification in stands characterized by variable crown sizes.

### 3.2.2 Non-parametric quantification of image autocorrelation

Alternative, local estimates of image autocorrelation can be obtained by relaxing the parametric structure of the variogram, sometimes known as *slope breaks* (Wulder et al., 2000). They are a simple means of measuring the region of dependence around a pixel and their use is based on the assumption that every pixel in the image may correspond to a local brightness or reflectance maximum and therefore a tree apex. For each pixel in the imagery an omnidirectional set of transects can be analyzed to assess the distance (in whole pixel increments) at which a minimum DN is encountered. Slope breaks may also be described as the first inflection point in the gradient of reflectance or brightness along a transect. Although a large number of transects can be considered, in practice slope breaks are computed along the 8 cardinal directions. The appropriate size of the window for LMF image processing is determined as the average distance from the center of the processed pixel to the inflection points along all transects. In addition to providing tree-specific estimates of autocorrelation, slope break computation offers substantial improvement in computation efficiency when compared to LMF window sizes estimated via variogram range. However, since fewer pixels are engaged in the computation of slope breaks it is likely that window size is more susceptible to bias introduced by random noise embedded in pixel DNs (Pouliot et al., 2002).

## 3.3 Individual Tree Classification

The variability in reflectance among portions of a single tree crown and, hence, in the DNs of pixels representing it in H-resolution imagery, has implications on the ability to accurately classify a particular crown to a cover type class. As demonstrated in Chapter 2, crown pixels in shadow reduce the separability of cover type signatures while

bright pixels located at or near the crown apex tend to improve it. Crown apexes identified with the LMF approach enable the partitioning of the, usually overlapping, cover type signatures to include only the brightest pixels, thus contributing to signature compactness and separability, and increasing the potential of improved classification accuracy. However, the reduction in the number of pixels that participate in signature development when only tree apexes are considered may enhance the influence of the geometric errors and spectral noise often present in H-resolution, digital, airborne imagery on the resulting classification accuracy.

When signature development is performed in the traditional approach, pixels contributing to signature development form clusters, each one of which extends over several trees and is sometimes as large as a forest stand. Even in the presence of substantial band registration errors, and assuming that the magnitude of the registration vectors is much smaller than the size of the pixel clusters used for signature development, there would be major spatial overlap of such clusters for each band in the imagery set. Therefore, even in the presence of misregistration, all tree crown portions would be represented equally well in signature development following the traditional approach. In tree-apex-based signature development, however, band misregistration of a single pixel could cause inclusion in the signature of pixels in one or more bands that actually represent crown parts other than the apex, particularly for coniferous species with conical crowns. Given that reflectance declines rapidly from the tree apex to the crown periphery, but at directionally variable rates (Pellikka et al., 2000), the classification accuracy of identified tree apexes in imagery characterized by different spectral registration vectors than those present at the signature training areas could be substantially inferior to one

obtained u

problems.

a tree ape

al., 1996;

hence, su

pixels ma

than the

current a

surface i

(Mikkol

the pote

classific

compar

of band

Traver

Michig

are sep

and 12

owned

area co

obtained using signatures generated and used in imagery free of band registration problems. In addition, for some crown shapes a pixel identified via the LMF approach as a tree apex, might in reality be the center of the sunlit portion of the crown (Franklin et al., 1996; Wulder et al., 2000). This problem is a function of illumination direction and, hence, subject to image acquisition timing. As a result, signatures developed from such pixels may have inherited BRDF effects related more to the morphology of the crown than the relation between illumination and viewing directions. It should be noted that current algorithms embedded in BRDF correction models do not account for target surface inclination and thus are incapable of normalizing BRDF effects within a crown (Mikkola and Pellikka, 2002). To date, the effect of imagery inferiorities and BRDF on the potential of tree-apex-based classification to provide improved cover type classification accuracy is speculative. This study attempts to quantify those effects by comparing tree-apex-based cover type classification results prior to and after elimination of band misregistration and normalization of variable brightness/BRDF regimes.

## 3.4 Methods

### 3.4.1 Study Site Characteristics and Description of Imagery Set

The study area comprises two sites, the one in the south-central part of Grand Traverse County (Site I) and the other in the northern part of Wexford County (Site II), Michigan (Figure 2.1). Note that figures in this dissertation often contain color. The sites are separated by about 10km in the northwest-southeast direction and extend over 8,805 and 12,626 hectares of land, respectively. More than half (56%) of the study area is owned and managed by the Michigan Department of Natural Resource. Most of the study area consists of forests and wetlands (82%), while agricultural use, mainly row crops,

represents 8%. Other land use classes include orchards (4%) and residential areas (4%). Residential development is concentrated in the northwestern part of site I. Geomorphic features include moraines and outwash. The average slope, calculated by using the finite differences algorithm on a 10m, 1:24,000 USGS Digital Elevation Model available for the area is 3.5% and 2.7% for sites I and II respectively. Relief is more prominent along the Manistee River, which crosses site II from northeast to southwest.

The study area is characterized by pronounced spatial heterogeneity of forest cover types. The majority of the forest cover types extant in the northern Lower Peninsula of Michigan are present in the forested part of the study sites. These include: 1. Aspen, consisting of Big Tooth (*Populus grandidentata*) and Quaking (*Populus tremuloides*) aspen; 2. Northern hardwoods, consisting primarily of Sugar Maple (*Acer saccharum*), Red Maple (*Acer rubrum*), American Beech (*Fagus americana*), Black Cherry (*Prunus serotina*), Basswood (*Tilia americana*) and White Ash (*Fraxinus americana*); 3. Oak, consisting of White (*Quercus alba*) and Red (*Quercus rubra*) oak; 4. Natural Pine, mainly White Pine (*Pinus strobus*); 5. Pine plantations consisting primarily of Red Pine (*Pinus resinosa*); and 6. Cedar swamps dominated by Northern White Cedar (*Thuja occidentalis*). The main forest management objectives of the MDNR include timber production, enhancement of wildlife habitat, recreation, preservation of aspen, and riparian best management practices. Several private land owners offer a network of tracts used seasonally for horseback riding and snowmobiling.

The imagery data set used in this study was acquired on August 11, 1999, using the Digital Airborne Imaging System (DAIS [Space Imaging, 1999]). It contains four bands, three in the visible and one near infrared that were acquired by frame (digital

array) cameras equipped with appropriate band-specific filters in a 2x2 arrangement. Appendix 1 contains detailed information on the technical specifications of the system (Table A.1), flight line orientation, and the spatial arrangement of frames in each study site (Figure A.1).

### 3.4.2. Field Measurements

A total of 34 plots, 16 in site I and 18 in site II, were established stratified across the major forest cover types present in the study area with the exception of cedar swamps that were excluded due to accessibility issues. Plots were allocated on level land, within homogeneous stands, and away from cover type ecotone zones. Stand homogeneity was evaluated with field inspections. A minimum 60% canopy closure threshold was imposed by the MDNR as a selection criterion. All plots were situated within the inner quarter area of the associated image frame, resulting in plot-center view angles less than $10^{o}$.

Field measurements were obtained in the summer of 2000, exactly a year after the acquisition of imagery, following the FIA/FHM field protocols (Appendix 1, Figure A.2). To ensure an adequate number of trees within a subplot, its radius was increased from the standard 7.32m, proportional to the size of trees present. Subplot diameter was kept equal within plots, but ranged from 10m to 15m between plots. Subsequent to plot center allocation, canopy structure parameters including the horizontal extent of individual tree crowns and stem locations were recorded using field survey techniques. All spatial and tabular data on tree crowns and stem locations were organized as geographic information system (GIS) layers translated into the image coordinate system. Details on the methodologies employed are available in Chapter 2.

### 3.4.3. Imagery Processing

Preliminary examinations of the 394-frame imagery set showed apparent variation in brightness, even among adjacent frames. Further investigations revealed imperfections in the geometric alignment (registration) of the frame bands and a non-stationary spatial distribution of registration vectors. In addition, BRDF effects were detected, principally along frame edges. A pair of novel techniques was developed to correct these imagery imperfections. The first was used to correct for band misregistration by using information extracted from spectral histograms of frames, and then by examining the magnitude of autocorrelation among the spectrally darkest pixels in a frame. The second technique, aimed at a simultaneous correction of BRDF effects and brightness variability, optimized the parameters of a popular BRDF model applied to the overlapping regions between adjacent frames. Both techniques are described in detail in Chapter 2.

### 3.4.4. Window Size Computation for LMF Imagery Processing

The computation of variable, locally adjusted window sizes for LMF processing of multispectral, H-resolution imagery and the subsequent identification of pixels believed to represent tree apexes are processes with many embedded parameters. In the interest of reducing the analysis load to manageable levels in this research, choices were made regarding the version of imagery to be used (original vs. corrected for band misregistration and variable brightness), and the bands to be considered.

Because window size computation is in essence an effort to quantify the extent of reflectance or DN autocorrelation, and hence of local, sub-frame scope, it is unlikely that it would be affected by BRDF effects or brightness variability, given that both of those phenomena are governed by processes with large, frame or multi-frame scope. It is

evident from a careful evaluation of equation (3.2) that the addition or subtraction of a constant (similar to the average brightness difference among two image frames) from each pixel DN value would not affect the shape, and therefore the range, of the computed empirical variograms. It can be shown (Appendix 2) that imagery processing with a kernel function similar to those employed in popular BRDF effect correction models (including the one by Roujean et al. (1992) used in Chapter 2), would not affect the range of variograms computed for the same image region before and after processing with the kernel. Window size computation via slope breaks, a spatial operation with even narrower spatial scope compared to the variogram, would be expected to produce the same window sizes regardless of the presence or absence of brightness variations and BRDF effects. However, to eliminate discrepancies in the position of identified tree apexes among different bands (later used in tree-apex cover type classification) due to registration problems, it was decided to proceed with the brightness/BRDF-normalized version of the imagery.

Visual inspection of empirical variograms computed for each of the four bands and every subplot revealed that the variogram ranges were often either unbounded (i.e. increased monotonically with lag distance, never reaching an asymptote) or were substantially larger than the mean tree crown diameter in corresponding subplots. Those observations were consistent with findings reported by Treitz (2001) using H-resolution, airborne, digital imagery of boreal forests in northern Ontario. Similar observations were made by Franklin and Wulder (1996) in British Columbia. They decided to truncate the range of unbounded variograms to a predefined maximum value in order to avoid unrealistically large window sizes. In addition, the assessed range of computed

variograms were found to occasionally differ among bands for the same subplot, although no patterns could be identified.

In the course of investigating the cause of unbounded variogram ranges and their apparent dependence on wavelength, imagery portions corresponding to subplots were examined for the presence of trend in pixel DNs. The procedure, sometimes known as trend surface analysis (Bailey and Gatrell, 1995, p. 168) and described in Appendix 2, regards pixel DNs as the product of a linear association between a function of image row and column indices known as the trend or first-order autocorrelation and a model of second-rder, or local, autocorrelation. In this study, the second order autocorrelation embedded as a component of the imagery DNs was assumed to represent the spatial pattern of reflectance formed by tree crowns. Imagery processing for the removal of potential trend would enable quantification of reflectance autocorrelation independent of non-tree-crown related influences. Post-trend-processed empirical variogram ranges were always bounded and of a magnitude within the range of dominant/co-dominant tree crown diameters present in the subplots (Appendix 2, Figure B.2). At the same time, trend removal eliminated differences in range magnitude among bands (Appendix 2, Figure B.3). Subsequent variogram analyses were performed strictly on imagery processed for trend using only the NIR band.

Variogram range computation of post-trend-processed imagery was automated by fitting a cubic spline (Hastie and Tibshirani, 1990) to the estimates of semivariance. The spline operated as a semivariance smoothing function, capable of eliminating sporadic non-monotonic fluctuations of semivariance estimates considered to be artifacts of a relatively small numbers of pixel pairs separated by short lag distances. The range was

subsequently calculated as the lag distance for which the slope of the corresponding spline segment was smaller than 5%. Reducing the length of lag increments to 1/3$^{rd}$ of the pixel size allowed for a more precise range calculation. Range values rounded to the closest integer were used as the proper window sizes for LMF imagery processing.

The appropriate window size for each subplot pixel was derived by modifying the standard slope break approach used by Wulder et al. (2000) to include a set of heuristic rules. Initial investigations had revealed that slope breaks computed as the first upward inflection point in DN value along a transect (the standard approach) were consistently overestimating crown, and hence window, size by extending slope break distances to the center of small canopy openings usually positioned in shadow. In the modified approach designed to correct for such bias, the processed pixel was placed in the middle, rather than at the origin, of a 30-pixel directional transect and a local regression (Cleveland and Devlin, 1988) was fitted to the DNs of the transect pixels. Placement of the processed pixel in the middle of the transect would eliminate transect-end-related biases in local regression predictions. The length of the diagonal transects (SW-NE and NW-SE) was set to 21 pixels to account for larger pixel spacing in those directions. The use of a local regression along each transect, in essence a DN smoothing function similar to the spline fitted on semivariance estimates mentioned previously, aimed at providing a monotonic decrease in DN from crown apex to crown periphery. It should be noted that fitting a spline instead of using local regression would be inappropriate due to the large variability in DNs of adjacent pixels along the transects.

The slope break value $sb_{Dir}$ for a transect centered at the processed pixel and oriented towards each of the 8 cardinal directions was computed as

$$sb_{D,r} = \begin{cases}$$

where $i$ c

local-reg

and $\tilde{D}_{TH}$

slope br

$sb$ = int

where i

the pres

gradien

dismiss

transec

Process

local re

from w

to 3 x 3

progra

$$sb_{Dir} = \begin{cases} \min(i) \text{ for which} & (\tilde{D}_{i-1} > \tilde{D}_i) \text{ and } (\tilde{D}_{i+1} > \tilde{D}_i) & (3.3a) & \\ & (\tilde{D}_{i-1} > \tilde{D}_i > \tilde{D}_{i+1}), \text{ and} & (3.3b) & \forall i \in [15,30] \mid Dir \in \{N, E, S, W\} \\ & \text{or } (\frac{\tilde{D}_{i-1}}{\tilde{D}_i} - 1) > 2(\frac{\tilde{D}_i}{\tilde{D}_{i+1}} - 1), \text{ and} & (3.3c) & \text{and } \forall i \in [11,21] \mid Dir \in \{NE, SE, SW, NW\} \\ & \tilde{D}_i > [\tilde{D}_{TR(\min)} + \frac{\tilde{D}_{TR(\max)} - \tilde{D}_{TR(\min)}}{2}] & (3.3d) & \end{cases}$$

where $i$ denotes the distance in pixel increments from the origin of the transect, $\tilde{D}_i$ the local-regression-fitted DN value for a pixel at distance $i$ from the origin of the transect, and $\tilde{D}_{TR(\min)}$ and $\tilde{D}_{TR(\max)}$ the minimum and maximum $\tilde{D}_i$ of all pixels in the transect. The slope break value for the processed pixel was subsequently computed as

$$sb = \text{int}(\frac{1}{8}\sum sb_{Dir}), \qquad \forall Dir \in \{N, NE, E, SE, S, SW, W, NW\} \tag{3.4}$$

where int() represents a function that rounds a real value to the closest integer.

The set of heuristic rules embedded in equations (3.3b) and (3.3c) shorten $sb_{Dir}$ in the presence of an abrupt reduction in the slope of the local, directional reflectance gradient often found to occur at the periphery of canopy openings. Equation (3.3d) dismisses $sb_{Dir}$ value shortening involving any of the brighter half of pixels on the transect. Equation (3.3a) represents the standard form of the slope break approach. Processed pixels with DN values smaller than the DNs of all of their 8 neighbors (i.e. local reflectance minima) were automatically assigned a 0 slope break and were excluded from window development. For all other pixels, the minimum size window was rescaled to 3 x 3. Window size computations were performed using scripts developed in the C programming language and optimized for computational efficiency. Empirical variogram

computation for each of the pixels in a subplot using custom developed scripts, was found to outperform, in terms of computation efficiency, commercially available software by a 1:10 margin.

### 3.4.5. Tree Apex Identification via LMF Imagery Processing

In the standard implementation of LMF, a pixel is characterized as a tree apex if and only if it carries the maximum reflectance value or DN for the window centered on it (Franklin et al., 1996; Wulder et al., 2000; Treitz, 2001). This implicitly assumes that the tree apex is located at the center of the crown and that the rate of reduction in reflectance or DNs from the tree apex to the crown periphery is isotropic (directionally independent). Those assumptions may be valid in coniferous species with conically shaped crowns, but they are potentially unrealistic for other coniferous and most deciduous species. Because the standard LMF approach considers as tree apex a pixel at the center of the window, it operates only with windows of side length equal to an odd number of pixels (henceforward referred to as 'odd-sized'). They require that the variogram range or slope break average computed at the previous analysis stage be rounded to the closest odd number, thereby introducing window sizes smaller or larger than the magnitude of the local imagery autocorrelation gradient. Preliminary investigations in several subplots showed large tree omission rates where tree identification was performed using the standard LMF approach, particularly in the presence of deciduous cover types.

To resolve the limitations mentioned above and to improve tree identification rates, a new approach is proposed here in which the window corresponding to each processed pixel 'votes' as tree apex the pixel having the highest DN within the window, regardless of where within the window the 'voted' pixel is located. When the appropriate

window is 'even-sized', it cannot be centered on the processed pixel because it has four central pixels instead of one. In such circumstances, the processed pixel is assigned to each of the four central pixels in the even-sized window and the voting process proceeds as before except that only a quarter vote is cast for each of the four window instances. Pixels with one half or more votes are labeled tree apex candidates. Candidate pixels are finally labeled tree apexes if their DN is larger that the DNs of all 8-neighboring pixels.

### 3.4.6. Computation of Canopy Structure Parameters

Identified tree apexes, variogram ranges, and directional slope breaks associated with the apexes were used to provide estimates of stem density, mean crown diameter, and canopy closure under the assumption that there existed a unique, one-to-one correspondence between identified tree apexes and stems. All estimates of the canopy structure parameter values were computed at the plot level to minimize estimate dependence on subplot boundary effects. Estimate aggregation at the plot level was encouraged by the fact that field observations revealed no apparent differences in forest canopy structure within the plots.

Stem density estimates were computed as the fraction of the total number of tree apexes identified (*i*) via the variogram range method and (*ii*) via the slope break approach employed in image LMF image processing within each subplot to the total plot area. Three mean plot crown diameter estimates were computed. The first estimate was obtained by (i) initially delineating circular crowns of diameter equal to the variogram range for each pixel identified as a tree apex via variogram LMF image processing, (ii) splitting the circular crown overlaps (if any) between adjacent trees, (iii) calculating the 'diameter' of the resulting non-overlapping crown shapes, and (iv) finally computing the

geometric mean of all 'diameters' in a plot. The second mean plot crown diameter estimate was obtained by (i) using pixels identified as tree apexes via slope break LMF image processing, (ii) delineating the corresponding tree crown using directional slope break length values $sb_{Dir}$ for each tree apex pixel, (iii) splitting potential crown overlaps, (iv) calculating the 'diameter' of resulting crown shapes, and (v) computing the geometric mean of all 'diameters' in a plot. The third mean plot crown diameter estimate was computed as the geometric mean of the variogram ranges derived for each subplot using all subplot pixels and thus it did not involve tree apex identification and crown delineation efforts. It should be noted that mean crown diameter estimates were in reference to the crown portion visible from above and not to the true horizontal extent of a crown. The methodology for computing a 'diameter' estimate for a crown shape is presented in detail in Appendix 1. The use of the geometric mean instead of the arithmetic mean aimed at reducing the influence of outliers in the distribution of crown diameter estimates on computed plot mean diameter values.

Canopy closure estimates were obtained by computing the ratio of the plot area occupied by crowns delineated for the derivation of the first two plot mean crown diameter estimates mentioned above. The portion of tree crowns with identified apexes outside the plot boundary was also considered in the computation of canopy closure estimates.

Computed stem density, mean crown diameter, and canopy closure estimates were compared to those obtained by field measurements. The methodologies for converting field measurements to canopy structure parameter values are discussed in Appendix 1. Predicted canopy closure parameter values were regressed against observed parameters

values. Regression parameter values were examined for statistical significance. Differences in the slope and mean of linear regression models pertaining to different methodologies used in canopy structure parameter derivation were also evaluated.

### 3.4.7. Cover Type Classification of Tree Apexes

In the presence of a pre-defined forest cover type scheme (Aspen, Northern Hardwoods, Oak, Red Pine Plantations, and Natural Pine), a supervised classification approach was selected. Among the many available options within the domain of supervised classification, the maximum likelihood (ML) option was selected because it would enable an evaluation of the statistical significance of classification results for signature development alternatives, while facilitating comparison of classification results obtained using only pixels corresponding to tree apexes and those obtained using all subplot pixels (Chapter 2).

All pixels identified as tree apexes and having their centers within the subplot boundary were used for signature development and classification performance evaluation. Pixel membership to a subplot was determined via spatial overlays of image frames with vector subplot boundaries in image coordinates. The subplot was selected as the classification unit. A cross-validation approach (Lachenbruch and Mickey, 1968) was undertaken for signature development involving two geographic extents: i) site -specific, and ii) global. A subplot Q2 (belonging to plot Q) in site I for example, was classified via three sets of spectral signatures developed: 1) using all pixels in the remaining subplots at site I except those in the related subplots (Q1, Q3, and Q4) and all the subplots in site II, 2) using the pixels in the remaining (unrelated) subplots of site I only, and 3) using all pixels in site II subplots but no pixels from site I subplots. Subplots in site II were

classified in a similar fashion for a total of five classification products. Absent this cross-validation approach, it would be difficult to ensure that the potentially low spectral variability within a plot compared to the variability among plots of the same cover type would not inflate classification accuracy estimates. Subplot classification was applied to both raw DNs and to a dataset that had been corrected for between-band misregistration and normalized for BRDF/brightness variability, for a total of 10 classification scenarios.

Classification results were processed with majority filters that assigned a single class (cover type) to each subplot. Classification accuracy estimates were derived from confusion matrices and associated indicators (percent of subplots correctly classified and kappa coefficients) (Congalton, 1991) computed after the application of the majority filters. Differences in the classification performance were evaluated using parametric statistical tests. Details on the tests and the computation of confusion matrices and accuracy indicators are provided in Appendix 1. The power of each classification result was evaluated by imposing five different ML probability thresholds (none, 0.1, 0.25, 0.50, 0.75) that pixel class-conditional probabilities had to exceed prior to their allocation to a class. Pixels with all class conditional probabilities below the imposed threshold remained unclassified.

## 3.5. Results

### 3.5.1. Local Maximum Filtering Methods

For the few (16/142 or 11%) subplots in which first-order DN autocorrelation was observed, subplot trend surface processing practically eliminated differences in computed variogram ranges among bands (Appendix 2, Figure B.3). All 16 trend occurrences were either in aspen or red pine plantation subplots characterized by high (> 80%) canopy

closure values. For the remaining 126 subplots, the difference of variogram ranges computed before and after trend surface processing for a given band was always equal to or less than 1/3$^{rd}$ of a pixel. Between bands, the mean difference of computed variogram ranges before and after processing was larger (0.39 pixels, standard deviation 0.09), but no pattern in the distribution of the difference magnitude could be identified.

Variogram ranges and mean, omnidirectional slope break estimates computed for a large number of subplot transects showed the former to vary substantially less than the latter (Figure 3.1). For 23 subplots (6 in northern hardwoods, 11 in aspen, and 6 in red pine plantations), the span of variogram ranges was smaller than 2/3$^{rds}$ of a pixel. For all subplots, the mean variogram range of subplot pixels exceeded corresponding mean slope break lengths. Often though, the variogram range for a particular pixel would be shorter than its slope break equivalent, particularly for pixels positioned at or near the center of the sunlit portion of a large crown. Conversion of mean slope break and variogram range estimates computed for subplot pixels into corresponding window sizes for LMF imagery processing resulted in similar conversion RMSE estimates (0.102 and 0.113 pixels, respectively). The fact that variogram range estimates were computed in 1/3$^{rd}$ of a pixel increments, while mean slope break estimates were unrestrained real numbers appeared to influence computed window sizes only minimally.

A comparison of variogram ranges computed using the automated method introduced in this study with variogram ranges determined manually via visual inspection for more than 50 circular imagery regions with a diameter of 30 pixels randomly distributed across cover types, canopy closure, and stem density conditions revealed that the automation process performed very well for most regions yielding an RMSE of 0.062

pixels. The method's performance was occasionally suboptimal for circular regions located within aspen and to a lesser extent red pine plantations and northern hardwood stands characterized by a smooth canopy surface, very high canopy closure values, and small variability in crown sizes. In such conditions, the empirical variograms exhibited a substantial semivariance fluctuation at the sill level potentially allowing for range overestimation. It should be noted that manual derivation of ranges via visual inspection of empirical variograms repeated at different times and in random region sequence produced a range variability twice as large as the one obtained from imagery regions characterized by rough canopy surfaces.

Local regressions fitted to subplot pixel DNs altered the value of the original DNs only slightly, generally maintaining the form of the DN profile along the transect (Figure 3.2). In the typical example shown in Figure 3.2, a zero-length directional slope break would be assigned and no window would be generated for the pixel at transect position 15 (middle of transect) regardless of whether the original or the local-regression-fit DNs were to be used, given that, in both cases, the preceding and following pixels along the transect had larger DNs. For a pixel at transect position 23, the directional slope break $sb_{Dir}$ would be 4 pixels when the heuristic rules described in equations 3.3a to 3.3d were applied but 5 pixels in their absence. The pixels at transect positions 6 to 8 and 27 to 30 correspond to shadowed canopy openings. As such, $sb_{Dir}$ truncation from 5 pixels to 4 would contribute to a window size reflecting that better matches the size of the tree crown at that location. Slope break lengths computed for transects parallel to the solar plane and extending through canopy openings were sometimes shorter for pixels situated on sunward crown portions than those for crown portions facing away from the sun. Such

instances occurred sporadically in northern hardwoods and oak subplots but rarely in the other cover types.

### 3.5.2. Stem Density

Strong linear relationships were found between predicted and observed plot stem densities (Figure 3.3) for both variogram and slope break methods. Slope break-derived density predictions, denoted as triangles in Figure 3.3, approximated observed densities (1:1 line) better than variogram-derived predictions (denoted as squares in Figure 3.3). Densities below approximately 350 stems/ha were generally slightly overestimated while those larger were increasingly underestimated. Discrepancies between predicted and observed stem densities increased at high and low density levels. Linear regression of predicted on observed stem densities using plots in all cover types (pooled regression) exhibited very high $R^2$ coefficients (Table 3.1). The pooled regression of slope break-derived density had a higher (0.864) and significantly different (at $\alpha$=0.01) slope that (0.741) of the pooled regression for variogram-derived density. Regression means were also significant at $\alpha$=0.01. Both pooled regressions had slopes significantly different than the slope of the 1:1 at $\alpha$=0.01. High $R^2$ coefficients (>0.947) were also present when individual cover types were considered, with the exception of the aspen plot stem densities computed using variogram ranges (Table 3.1). Regression slopes for individual cover types were higher for slope break-derived than for variogram-derived densities except for oak, but slope differences were not significant at $\alpha$=0.05 except for natural pine plots. Cover type-specific regression means, however, were significant between methods at $\alpha$=0.05 or $\alpha$=0.01 except for natural pine plots. Regression residual plots did not suggest the presence of any patterns or heteroskedasticity. Compared to observed

density, variogram-derived stem density exhibited root mean square errors (RMSE) approximately two times larger than those of the slope break-derived stem densities (Table 3.2). When expressed as percent of the cover type mean observed values, variogram-derived density errors ranged from a minimum of 6.1% for natural pine to a maximum of 12.5% for aspen; slope break-derived density errors ranged from a minimum of 3.6% for natural pine to a maximum of 7.4% for red pine plantations.

### 3.5.3. Tree apexes

Figure 3.4 is a typical example of tree apexes identified in a high density and crown closure aspen subplot. It is evident from the figure that in this aspen subplot there were no discrepancies in the position of pixels identified as tree apexes by the two methods, excluding cases with apex omission or commission errors. Positional discrepancies of correctly identified apexes were also rare in the remaining cover types. Where present, they involved two or fewer apexes per subplot and had a magnitude of a single pixel. For the subplot shown in Figure 3.4, the stem density obtained using field observations was 549 trees per hectare. Imagery LMF processing using variogram ranges correctly identified 22 apexes, missed 4, and had 2 false positives (commission errors), resulting in a predicted stem density of 507 trees per hectare and a prediction error of 8% (Figure 3.4a). Processing using slope breaks correctly identified 24 apexes, missed 2, and committed 1, resulting in a predicted stem density of 528 trees per hectare and a prediction error of 4% (Figure 3.4b).

It is evident from an examination of the NIR band image depicted in Figure 3.4 that the image portion with row indices approximately 20 to 40 contains larger tree crowns and would therefore yield larger variogram ranges than the remaining part of the

image. Influenced by the adjacent larger crowns, variogram ranges computed for subplot pixels in rows 15 to 20 would likely overestimate the appropriate window size used in apex identification, and increase the probability of omission errors for that image portion, particularly in the presence of high stem density. Because slope break lengths are calculated using a spatially limited (local) scope, they are independent of the crown sizes of trees not in the immediate vicinity of the processed pixels, and would therefore be less susceptible to apex omission errors. The tree apex at location [23,20], correctly identified using the slope break method, but missed when using the variogram method, demonstrates how differences between the two methods to adapt to local reflectance conditions influences the error rates of stem density predictions.

### 3.5.4. Canopy Closure

Plots of predicted vs. observed plot canopy closure showed strong linear relationships, but there was little evidence to support the superiority of either variograms or slope breaks (Figure 3.5). Variogram-derived canopy closure predictions appeared to envelope the 1:1 line in Figure 3.5 for the entire range of observed canopy closure values. Slope break-derived predictions behaved similarly at lower canopy closure conditions but appeared to slightly underestimate canopy closure at higher values. The pooled regression of variogram-derived prediction of observed canopy closure values yielded an $R^2$=0.941, while the pooled regression of slope break-derived canopy closure values produced an $R^2$=0.930. However, the two pooled regressions had significantly different slopes at $\alpha$=0.01. All individual cover type $R^2$ values exceeded 0.800 for both methods (Table 3.3), but exhibited substantial regression slope variability both across derivation methods and cover types. Differences in regression slope between methods were

significant at $\alpha$=0.01 or $\alpha$=0.05 for all cover types except oak. The RMSE of canopy-closure predictions were comparable for both derivation methods, with the exception of aspen for which slope break-derived prediction error was less than one third of variogram-derived prediction error for plot canopy closure (Table 3.4).

### 3.5.5. Crown Diameter

Plot mean crown diameter predictions derived using variogram ranges were found to overestimate diameter for smaller crowns and underestimate it for larger ones, while slope break predictions appeared to be unbiased except perhaps for crowns with mean diameters exceeding 7m (Figure 3.6). Linear models provided an adequate representation of the relationship between parameter derivation methods when simultaneously considering all cover types. Similar observations were made for plot crown diameters predicted via variogram ranges estimated with subplot scope (alternative variogram method) rather than the pixel-specific scope, the latter being the standard method used for predicting plot stem density and canopy closure. The former method overestimated the size of small crowns and exhibited heteroskedastic behavior with increasing crown size (Figure 3.7). Pooled regressions of variogram-, alternative variogram-, and slope break-derived predictions of observed mean crown diameter values had $R^2$ coefficients of 0.942, 0.921, and 0.990, respectively, and significantly different regression slopes at $\alpha$=0.01, except for the slope break – variogram regression pair (Table 3.5). Variability in cover type-specific regression slopes across crown diameter prediction methods was significant only for the oak plots. The RMSE of plot mean crown diameter predictions were comparable in magnitude for both the variogram and alternative variogram

parameter value derivation methods, but substantially larger than the prediction errors computed via the slope break method (Table 3.6).

### 3.5.6. Crown Delineation

Figure 3.8 portrays the delineation of crowns using either variogram ranges or directional slope break lengths for an oak subplot. Because variogram ranges and slope breaks performed identically in tree apex identification for this particular subplot, they rendered it a good demonstration case of the performance of slope breaks and variogram ranges for crown delineation, which in this research is a precursor to predicting canopy closure and mean crown diameter. Positional discrepancies between identified tree apexes and observed tree stems are apparent in both methods. The solar azimuth angle at the time of image acquisition for this oak subplot was 172° (measured from north). The angular components of the displacement vectors between actual stems and identified apexes were restricted to the 135° to 180° range. As such, it is likely that the pixels identified as tree apexes actually represent the middle of the sunlit portion of the crowns rather than the stem location. Such discrepancies occurred at, but were not limited to, coordinate locations [4, -7], [-6, -2], and [4, 2.5]. Non-conformal crown morphology, however, (i) often placed identified tree apexes elsewhere, as is evident in coordinate locations [-4, 1] and [-5.5, 7]; (ii) caused more than one apex to be identified for one observed stem, as in locations [0, 4] and [2,5]; or (iii) resulted in stem omission, as in location [8.5, 3]. Positional discrepancies between stem and identified tree apexes were smaller for coniferous than for deciduous cover types.

Variability in the spatial distribution of crown sizes appeared to influence canopy closure predictions when crowns were delineated with the variogram range method.

Larger crown sizes at the western half of the oak subplot shown in Figure 3.8, resulted in variogram ranges approximating the diameter of those crowns well. Crowns delineated for apexes at locations [-10, 1] and [-8, 7] in Figure 3.8a were in close agreement to observed crown boundaries. Variogram range-based delineation of smaller crowns adjacent to larger ones (location [6, -1] and [-2, -8]) caused substantial overestimation of crown extent for the former. Crown overestimation is represented in purple in Figure 3.8a. Smaller crown sizes east and south of the subplot resulted in variogram ranges shorter that the crown diameters present in the east half of the subplot, thus causing substantial crown underestimation, represented in yellow in Figure 3.8a. At the subplot level, however, crown underestimation for a few trees was nearly compensated by crown overestimation for others resulting in prediction error of only 2%. Crown delineation via slope breaks for this oak subplot appeared to be superior to the delineation produced using variogram ranges in the sense that the absolute crown under- and overestimation was more confined and showed no patterns in its spatial distribution (Figure 3.8b). Slope break delineation sometimes tended to overestimate crown extent towards canopy openings (location [2, -3], [-7, -4], [-10, -3], [-1, 9], etc.), resulting in an overall prediction error of 4%.

### 3.5.7. Cover Type Classification of Tree Apexes

Classification results obtained with signatures generated from pixels identified as tree apexes using variogram ranges, were practically identical to those obtained using slope breaks. Associated confusion matrices developed for each of the five geographic extents of signature development were found to have a maximum of 4/136 or 3/72 (pending on signature geographic extent) of subplots assigned to different cover type

classes between the two methods. Given these similarities, only slope break-related results are presented here.

Classification accuracy estimates and kappa coefficients derived from confusion matrices constructed using original DNs ranged among classification scenarios from 70.3% to 72.2% and 0.628 to 0.652 respectively (Table 3.7a-e). Use of brightness-normalized imagery resulted in classification accuracy and kappa coefficient estimates ranging from 84.4% to 87.5% and 0.804 to 0.844 (Table 3.7f-j). Brightness normalization improved classification accuracy among classification scenarios by an average of 14.6% with coefficient of variation 0.060; brightness normalization improved kappa coefficients by 0.182 (coefficient of variation 0.057). In all classification scenarios, results were significant at $\alpha$=0.01 (Table 3.7a-j). Pair-wise comparisons of classification outcomes based on the computation of standardized differences of respective kappa coefficients showed no statistical significance at $\alpha$=0.10 among classification scenarios using original DNs and among classification scenarios operating on brightness normalized imagery. All pair-wise comparisons involving a classification scenario using original DNs and a scenario operating on brightness normalized imagery were significant at $\alpha$=0.01 or $\alpha$=0.05 (Table 3.8).

In classification scenarios based on signature development from and testing on all subplots using original DNs, about one fourth of the total number of deciduous subplots (21/80) was assigned to a wrong deciduous class, but within the deciduous cover type group. About one fifth of the coniferous subplots (12/56) was assigned a wrong coniferous class but within the coniferous cover type group. Five subplots were assigned to the wrong cover type group (Table 3.7a). Brightness normalization reduced the numbe

of subplots assigned to the wrong class and correct group to 12 for deciduous and 5 for coniferous classes and eliminated all instances of subplots assigned to the wrong cover type group (3.7f). Classification error rates between cover type classes and cover type groups are shown in Table 3.9.

Brightness normalization dramatically improved class-conditional kappa coefficients for all classification scenarios (Table 3.10) and averaged 0.175 for aspen, 0.129 for northern hardwoods, and 0.164 for oak. The improvement was higher and less variable across scenarios for red pine plantations and natural pine, averaging 0.194 and 0.255 respectively. Class-conditional kappa improvement was practically uniform across classification scenarios and ranged from 0.175 to 0.196, but it was at least twice as variable for scenarios involving signature development and testing in the same site than scenarios involving signature development in one site and testing in the other.

The effect of frame brightness normalization on the structure of classification signatures can be assessed by examining the percentage of classified pixels for different maximum likelihood thresholds (Figure 3.9). For thresholds up to 0.25, there was little difference in the percentage of classified pixels before and after brightness normalization. A threshold of 0.50 classified approximately 50% of tree apex pixels in the original DN imagery and about 20% more for the set normalized for brightness. Even at high percentages, a substantial percentage (~ 25) of original DN, and approximately half of brightness-normalized pixels were still classified. Differences in the percent of classified pixels for different classification scenarios did not exceed 10% even for high maximum likelihood probability thresholds. It should be noted that the reference to classification results using DNs in Figure 3.9 implicitly assumed that LMF processing using original

DNs identifie

imagery set. A

would have be

for all subplot

(0.75) maximu

development t

compact and,

Using tree ape

(Table 3.11) in

classification

brightness nor

## 3.6.

Predic

crown surface

density predic

from the imag

yielded larger

and 3.6), part

despite the fa

Oak a

with crowns

several canop

subplots and

DNs identified the same pixels as tree apexes as those identified with the normalized imagery set. Although preliminary investigation had indicated that such an outcome would have been likely, LMF imagery processing using original DNs was not conducted for all subplots. The substantial amount of pixels that remained classified even for high (0.75) maximum likelihood probability thresholds indicated that constraining signature development to include only pixels identified as tree apexes results in signatures far more compact and, hence, likely more separable that those obtained using all subplot pixels. Using tree apex pixels instead of all pixels produced statistically significant increases (Table 3.11) in classification accuracies from approximately 45% to 70% for classification based on original DNs and from approximately 50% to 85% when brightness normalization was employed.

## 3.6. Discussion

Prediction of canopy structure parameters in this chapter was based on analysis of crown surface morphology. Identified tree apexes were used as a surrogate for stem density predictions while canopy closure and mean crown diameter were derived directly from the imagery. It should not therefore come as a surprise that stem density predictions yielded larger RMSE than canopy closure and crown diameter predictions (Table 3.2, 3.4, and 3.6), particularly when employing slope breaks for parameter value estimation, despite the fact that the latter two were based on the former.

Oak and northern hardwood subplots in this study contained large, mature trees with crowns of complex morphology and often two or more reflectance maxima, and several canopy openings, sometimes of similar size and uniform distribution within the subplots and sometimes of variable size and distribution. Further, stand structure

complexities were introduced by shorter co-dominant tree apexes positioned at the edge of larger adjacent crowns with which they formed composite crowns, whose tree-specific components were sometimes difficult to discern even with field inspection. In the presence of large-crown trees and uniform crown and canopy opening size distribution, the slope break-based and variogram-based methods performed equivalently in stem density prediction. By contrast, the presence of crown size variability or variable-sized canopy openings resulted in better accuracy for slope-break derived predictions of stem density, thereby corroborating that slope breaks are capable of adjusting well to local stand structure conditions. The minimal variability in canopy-opening and crown-size precluded a reliable assessment of canopy structure conditions on stem density predictions for the remaining three cover types.

Commission errors due to multiple tree maxima and corresponding tree apexes identified using variogram ranges in the presence of large northern hardwoods and oak trees produced mean crown diameter underestimation proportional to crown size, but appeared to only minimally affect the accuracy of canopy closure predictions. Note that it requires only 1 out of 10 trees with average crown diameter of 10m to be mistakenly identified as two separate stems in a subplot for an 8% reduction in subplot mean crown diameter value to occur. As a result, crown diameter predictions in large tree crown stands were more susceptible to errors of commission than of omission.

Stem density was underestimated for most of the natural pine and all of the red pine plantation and aspen subplots largely because the presence of small crows increased omission error rates. Errors of omission would often occur where most of the sun-facing crown portion of a co-dominant tree was in the shadow cast by adjacent dominant trees

(resulting in a lower brightness tree apex for that tree). Errors of omission occurred more frequently where pixels correctly identified as tree apexes were separated by distances smaller than half the variogram range or the slope break length calculated for those apex pixels. The second source of tree omission error could be potentially eliminated in such conditions by removing the LMF processing rule that necessitates all pixels identified as tree apexes to have DN larger that those of their 8 neighbors. Elimination of this LMF rule, however, would cause deterioration of stem density predictions obtained in stands of trees with larger crown sizes. LMF rule implementation conditional upon variogram range or slope break magnitude should be considered as a stem-density-prediction alternative worthy of investigation.

Stands exhibiting small crown size and high canopy closure were found to exhibit low tone or DN variability in digital imagery. Precise range estimation for variograms computed in those circumstances was challenging, even when performed manually, in part because of non-monotonic semivariance variability between consecutive lag distances and in part because semivariance often tended to increase slowly with lag distance and plateau (reach a sill) at distances larger than the diameter crowns present. Because such semivariance behavior persisted even after imagery processing for first-order autocorrelation removal, it was assumed that in smooth-canopy-surface stands, individual tree crowns may not necessarily be the main structural canopy element, and that perhaps parametric quantification of DN autocorrelation is susceptible to existing lower fractal dimensions of reflectance. Imagery spatial resolution was sufficiently fine to eliminate concerns of smooth canopy surface appearance originating from reflectance aggregation issues. LMF window size overestimation due to imprecise variogram

computation was considered the primary reason for larger stem density prediction RMSE than the one obtained with LMF window sizes conditioned upon slope break lengths.

A special case of variogram range-based stem density overestimation could arise in stands with systematic and anisotropic tree arrangements such as in red pine plantations where past thinning operations were performed along the rows. In such plantation stands, if sufficient time (>10 years) had elapsed between the thinning operation and the imagery acquisition, the trees will utilize the extra growing space and the variability in canopy reflectance along the rows will be reduced. In such conditions, the computed variogram range length could exceed the planting space between rows by 50% or more (particularly for rows oriented in the East-West direction) potentially causing tree omission errors. Such canopy structure conditions would also promote an overestimation of canopy closure and crown diameter, because the space actually occupied by the omitted trees would typically be assigned to adjacent trees along the rows during the crown delineation process, thus inflating crown diameter (i.e. a canopy opening would rarely be predicted). Systematic tree arrangements can also introduce a bias in the slope break-enabled crown delineation related to image resolution. This is especially the case where tree-spacing length is slightly less or more than 0.5 pixels the nearest pixel length multiple. For example, a 12ft (=3.66m) spacing would likely produce 4-m slope break lengths and cause crown size and canopy closure overestimation. Such bias is expected to cancel out among trees in natural stands.

The imposition of the heuristic rules on the slope break computations were undertaken to avoid substantial overestimation of LMF window sizes, and its negative impact on canopy closure and mean crown diameter predictions. Without the heuristics,

canopy openings between trees would occur only as sliver polygons between adjoined crowns or because of crown representation fidelity issues due to the limited number of directions analyzed around each identified tree apex. The implication of these limitations on the values of the canopy structure parameters would likely be negligible in high canopy closure stands, but substantial in the presence of canopy openings. The critical issue here is how to identify the appropriate value for the coefficient at the right side component of equation 3.3c, whose role is to inhibit directional slope break extension into canopy openings. The value used was the product of experimentation and, as shown in Figure 3.8b, did a good job in delineating crowns, while observing canopy openings, in all northern hardwoods, oak, and natural pine stands where openings were present. Coefficient values would likely need to be modified in the presence of large solar zenith angles, diffuse illumination, reduced foliage vigor and density, or finer imagery resolution. Coefficient adjustment for pixel size would be required in response to finer reflectance sampling, and the resulting finer reflectance value change utilized in equation 3.3c.

Applying the procedures presented in this chapter might not be advisable to derive stand-structure parameters for stands with medium or low canopy closure or where stand conditions permit direct illumination of the forest floor or background vegetation. In such conditions, grass, exposed sandy soil, or shrubs could easily be misidentified as tree apexes during LMF processing, and the variogram ranges would mistakenly represent the mean diameter of the canopy openings rather than the size of crowns. Note that the 60% minimum canopy closure threshold imposed as a prerequisite for plot installation precluded any occurrences of sunlit background in the plots. Although openings did exist

and were sometimes of sizes equivalent to those occupied by the dominant trees, the height of adjacent trees would place them in shadow. Preliminary imagery processing using band rationing could potentially reduce the effect of non-vegetated, sunlit stand backgrounds on the predicted canopy parameter values.

The pooled and individual cover type regression models of predicted vs. observed canopy structure parameter values for each cover type, presented in Tables 3.1, 3.3, and 3.6, are only intended to provide a preliminary understanding of the relationship between parameters and cover types. The small number of plots installed in each cover type and the often compressed range of observed values for the canopy structure parameters within each cover type suggest that the regression model parameter value might change if a larger number of plots in varying stand structure conditions were available in each cover type.

The classification results (Table 3.2, 3.4, and 3.6) indicate that the slope break-enabled stem density and mean crown diameter predictions are superior, not only to those obtained using variogram ranges, but also to those obtained during stand data cruising by experienced foresters in the Midwest region (Roger Meck and Larry Pedersen, MDNR analysts, personal communication). For canopy closure predictions, both methods exceed the accuracy typically obtained by stand cruising. Those observations suggest that automated imagery processing using the techniques of this chapter has a potential to become the standard approach for acquiring forest stand structure information, at least for stand conditions that approximate those in the plots used in this study. This potential is tempered by significant computational costs. Using 2003 vintage equipment, it would require several hours (~5) for the processing of one hectare of forest land using 0.9m

imagery. An exception to this is predicting mean crown diameter using the alternate variogram method, which is at least two orders of magnitude faster than the analytical variogram and slope break methods.

The classification results corroborate that brightness variability among imagery frames increases class covariance values in feature space and thus reduces class separability. In addition, the smaller variability in kappa coeffiecients or accuracy estimates obtained for different classification scenarios using tree apex pixels compared to those obtained using all pixels indicate that the brightest pixels in a crown manifest the cover type-specific reflectance characteristics better and with greater stability. Brightness normalization costs are warranted by the significant improvement in overall and class-specific classification accuracy. The fact that discrepancies in the number of pixels identified by each of the LMF processing methods hardly affected classification outcomes suggests that alternative, and likely computationally less costly, classification procedures based on bright pixel detection might be capable of delivering comparable classification products. Tree apex-based classification, however, offers the additional advantage of allowing for estimation of species composition within cover types. The presence of species with substantially different reflectance characteristics in the same cover type, for example white pine/aspen, often present in the Midwest region, could render the processing of classification results with majority filters inappropriate and cause a significant reduction in classification accuracy. In such cases, class-assignment of plots or forest stands could alternatively be based on heuristic rules. Reflectance variability only between big tooth and quaking aspen and absent among the species

present in each of the remaining cover types, at least when only tree apex pixels were considered, has precluded the development and evaluation of such alternatives.

## 3.7. Conclusion

The two methods of quantifying DN autocorrelation that were used in this study, the parametric variogram analysis and the non-parametricset of simple heuristic rules, have revealed the promising potential of high-spatial-resolution digital imagery as a source of reliable forest canopy structure information. The other known investigations that have attempted stem density predictions, primarily in coniferous forests, found prediction error rates that have rendered them and the methodologies employed of little utility for inventory or management purposes. In this study, the field acquisition of a detailed and positionally precise set of observations on stand structure distributed among five deciduous and coniferous cover types in northern Michigan, has provided a better understanding of the relationships between canopy characteristics and the reflectance regimes embedded in digital imagery. Methods were developed or modified that are capable of producing reliable predictions not only of forest stand density but also of canopy closure and mean crown diameter.

The methods that were developed support automation and entail parsimonious parameterization: 1) determination of the minimum slope between successive cubic spline segments fit to empirical variograms to determine the variogram's range; and 2) derivation of a coefficient used to hinder directional slope break extensions into canopy openings. Proper values for each parameter can be identified by visual inspections of empirical variograms generated over an area of interest and by examining pixel DN profiles traversing canopy openings. Because only stands with high canopy closure were

used to refine these methods and evaluate the results, the application of these techniques to medium or low canopy closure condition should be undertaken with caution.

The brightest crown pixels, identified automatically by the methods presented in this chapter, appear to be dominated by spectral information specific to the cover type they belong. Maximum likelihood classification of cover types based on those pixels is capable of delivering a high classification accuracy (> 85%) that remarkably improves (35% in this study) the accuracy obtained by traditional classification approaches that operate on all pixels in a forested area. Experimentation with scenarios that involved signature development and classification testing over varying geographic extents revealed that this classification performance was robust, thereby allowing optimism for regional applicability. Although computational loads currently restrict operational implementation of the methods presented, it is expected that continuous improvements in computational power would ultimately render the approaches investigated here useful for forest inventory and management purposes.

## Literature Cited


Aldred, A.H, and F.W. Kippen. 1967. *Tree Measurements on Large-Scale Oblique Photos*, Information Report FMR-X-4, Forest Management Institute, Ottawa, Ontario, Canada, pp. 14.

Aplin, P., P. Atkinson, and P. Curran. 1997. Fine spatial resolution satellite sensors for the next decade. *Int. J. Rem. Sensing*, 18:3873-3881.

Bailey, T.C., and A.C. Gatrell, Interactive spatial data analysis, Longman, Essex, U.K., 1995.

Biging, G.S., R.G. Congalton, and E.C. Murphy. 1991. A comparison of photointerpretation and ground measurements of forest structure, *Proc. of the 57th Annual Meeting of ASPRS*, Baltimore, Maryland, pp. 6-15.

Brandtberg, T. 1997. Towards structure-based classification of tree crowns in high spatial resolution aerial images. *Scand. J. For. Res.*, 12:89-96.

Bonnor, G.M. 1977. *Forest Inventories with Large-Scale Aerial Photographs: An Operational Trial in Nova Scotia*, Information Report FMR-X-96, Forest Management Institute, Ottawa, Ontario, Canada, pp. 21.

Brun, R. 1972. *A New Stereotype Digitizer System for Measuring and Processing Tree Data from Large-Scale Aerial Photographs*, Information Report FMR-X-41, Forest Management Institute Ottawa, Ontario, Canada, pp.35.

Cleveland, W.S., and S.J. Devlin, S.J. 1988. Locally-weighted regression: An approach to regression analysis by local fitting. *J. Am. Statist. Assoc.*, 83:596-610.

Cohen, W.B., T.A. Spies, and G.A. Bradshaw. 1990. Semivariogram of digital imagery for analysis of conifer canopy structure. *Rem. Sensing Environ.*, 34:167-178.

Curran, P.J. 1988. The semivariogram in remote sensing: an introduction. *Rem. Sensing Environ.*, 24:493-507.

Curran, P.J., and P. Atkinson. 1998. Geostatistics and remote sensing. *Prog. Phys. Geo.*, 22:61-78.

Culvenor, D.S., N. Coops, R. Preston, and K.G. Tolhurst. 1999. A spatial clustering approach to automated tree crown delineation. *Proc. International Workshop on Automated Interpretation of High Spatial Resolution Digital Imagery for Forestry*. D. Hill and D. Leckie (Eds). Natural Resources Canada, Canadian Forest Service, Pacific Forest Centre, Victoria British Columbia, Canada, pp. 67-80.

Culvenor, D. 2002. TIDA: An algorithm for the delineation of tree crowns in high spatial resolution imagery. *Computers & Geosciences*, 28:33-44.

Daley, N., C. Burnett, M. Wulder, K., Niemann, and D. Goodenough. 1998. Comparions of fixed-sized and variable-sized windows for the estimation of tree crown position. In *Proc. IGARSS '98*, Seattle, Washington, pp. 1323-1325.

Deutsch, C.V., and A.G. Journel. 1992. *GSLIB: Geostatistical Software Library and User's Guide*. Oxford University Press, New York, 340p.

Deutschman, D.M., A.L. Simon, C. Devine, and L.A. Buttel. 997. Scaling from trees to forest: Analysis of a complex simulation model, *Scienc*, 277:5332.

Dralle, K., and M. Rudemo. 1997. Stem number estimation by kernel smoothing of aerial photos. *Can. J. For. Res.*, 26:1228-1236.

Gering, L.R., and D.M. May. 1995. The relationship of diameter at breast height and crown diameter for four species groups in Hardin County, Tennessee. *South J. Appl. Forestry*, 19:177-181.

Franklin, S.E., and G. McDermid. 1993. Empirical relations between digital SPOT HRV and casi imagery and lodgepole pine (Pinus contorta) forest stand parameters. *Int. J. Rem. Sensing*, 14:2331-2348.

Franklin, S.E., M. Wulder, and M. Lavigne. 1996. Automated derivation of geographic windows for use in remote sensing digital analysis. *Comp. Geosci.*, 22:665-673.

Franklin, S.E. 2001. *Remote Sensing for Sustainable Forest Management*. Lewis Publishers, CRC Press, Boca Raton, Florida.

Gerylo, G., R.J. Hall, S.E. Franklin, A. Roberts, and E.J. Milton. 1998. Hierarchical image classification and extraction of forest species composition and crown closure from airborne multispectral images. *Can. J. Rem. Sensing*, 24:219-232.

Gong, P., G.S. Biging, S.M. Lee, X. Mei, Y. Sheng, R. Pu, B. Xu, K.P. Schwarz, and M. Mostafa. 1999. Photo-ecometrics for forest inventory, *Geogr. Inf. Sciences*, 5:9-14.

Gougeon, F. 1995a. A crown-following approach to automatic delineation of individual tree crowns in high spatial resolution aerial images. *Can. J. Rem. Sensing*, 21:274-284.

Gougeon, F. 1995b. Comparison of possible multispectral classification schemes for tree crowns individually delineated on high spatial resolution MEIS images. *Can. J. Rem. Sensing*, 21:1-9.

Gougeon, F. 1997. Recognizing the forest from the trees: individual tree crown delineation, classification and regrouping for inventory purposes. *Proc. 3rd International Airborne Remote Sensing Conference Exhibition*, Environmental Research Institute of Michigan, Ann Arbor, Michigan, Vol II, pp. 807-814.

Hastie, T.J., and R.J. Tibshirani. 1990. *Generalized Additive Models*. Chapman and Hall, London, U.K.

Hyyppä, J., H. Hyyppä, M. Inkinen, M. Engdahl, S. Linko, and Y. Zhu. 2000. Accuracy comparison of various remote sensing data sources in the retrieval of forest stand attributes. *Forest Ecology and Management*, 128:109-120.

Isaaks, E.H., and R.M. Srivastava. 1989. *An introduction to Applied Geostatistics*. Oxford University Press, New York.

Jupp, D., A. Strahler, and C. Woodcock. 1988. Autocorrelation and regularization in digital images: I. Basic theory, *IEEE Trans. Geosci. Rem. Sensing.*, 26:463-473.

Keane, R.E, S.A. Mincemoyer, K.M. Schmidt, J.P. Menakis, and J.L. Garner. 1999. Fuels and vegetation mapping for fire management on the Gila National Forest, New Mexico. *Proc. 1999 Annual Conference of the American Society or Photogrammetry and Remote Sensing*, Portland, Oregon (CD-ROM).

King, D.J. 2000. Airborne remote sensing in forestry: sensors, analysis and applications. *Forestry Chronicle*, 76:25-42.

Lachenbruch, P.A., and M.R. Mickey. 1968. Estimation of error rates in discriminant analysis, *Technometrics*, 10:1-11.

Larsen, M. 1997. Crown modeling to find tree top positions in aerial photographs, *Proc. International Airborne Remote Sensing Conference and Exhibition*, Copenhagen, Denmark, pp. 428-435.

Larsen, M., and M. Rudemo. 1997. Using ray-traced templates to find individual trees in aerial photos. *Proc. 10th Scandinavian Conference on Image Analysis*, Lappeenranta, Finland.

Larsen, M. 1998. Optimizing templates for finding trees in aerial photographs, *Pattern Recognition Letters*, 19:1153-1162.

Larsen, M. 1999. Finding an optimal match window for spruce top detection based on an optical tree model. *Proc. International Workshop on Automated Interpretation of High Spatial Resolution Digital Imagery for Forestry*. D. Hill and D. Leckie (Eds). Natural Resources Canada, Canadian Forest Service, Pacific Forest Centre, Victoria British Columbia, Canada, pp. 55-66.

Leckie, D., J
resolutio
basis. Re

Levesque, J.
airborne
*Canadia*

Li, X., and A
discrete
*Trans.* G

Mangold, R

Matheron,

McGraw,
remote
300-3

Mikkola,
photo
polle

Nieman
usin
*Inte*
Lec
Cer

Pellikk
dir
su
29

Perei
A
g

Pinz

Leckie, D., X. Yau, D. Ostaff, H. Piene, and D. McLean. 1992. Analysis of high spatial resolution MIES imagery for Spruce Budworm damage assessment on a single tree basis. *Rem. Sens. Env.*, 40:125-136.

Levesque, J., and D. King. 1996. Semivariance analysis of tree crown structure in airborne digital camera imagery. In *Proc. 26th Int. Symp. Rem. Sensing Environ./ 18th Canadian Symp. Rem. Sensing.*, Vancouver, British Columbia, Canada, pp. 275-278.

Li, X., and A. Strahler. 1992. Geometric-optical bidirectional reflectance modeling of the discrete crown vegetation canopy: effect of crown shape on mutual shadowing, *IEEE Trans. Geosc. Rem. Sensing*, 30:276-291.

Mangold, R. 1999. INONOS has arrived. *Earth Observation Magazine*, 8:7.

Matheron, G. 1963. Principles of geostatistics. *Econ. Geol.*, 58:1246-1266.

McGraw, J.B., T.A. Warner, T. Key, and W. Lamar, 1998. Advances in high resolution remote sensing for forest ecological studies. *Trends inEcology and Evolution* 13 (8): 300-301.

Mikkola, J., and P. Pellikka. 2002. Normalization of bi-directional effects in aerial CIR photographs to improve classification accuracy of boreal and subarctic vegetation for pollen-landscape calibration. *Int. J. Rem. Sensing*, 23:4719–4742.

Niemann, K.O., S. Adams, S., and G. Hay. 1999. Automated tree crown identification using digital orthophoto mosaics *Proc. International Workshop on Automated Interpretation of High Spatial Resolution Digital Imagery for Forestry.* D. Hill and D. Leckie (Eds). Natural Resources Canada, Canadian Forest Service, Pacific Forest Centre, Victoria British Columbia, Canada, pp. 105-113.

Pellikka, P., D.J. King, and S.G.Leblanc. 2000. Quantification and reduction of bi-directional effects in aerial CIR imagery of deciduous forest using two reference land surface types. *Rem. Sensing Rev.* M.M. Verstraete and B. Pinty, (Guest Eds), 19:259-291.

Pereira, J.M.C., M. Tome, J.M.B. Carreiras, J.A. Tome, J.S. Pereira, J.S; David, and A.M.D. Fabiao. 1997. Leaf area estimation from tree alometrics in Eucalyptus globulus plantations. *Can. J. For. Research*, 27:166-173.

Pinz, A. 1999. Tree isolation and species classification. *Proc. International Workshop on Automated Interpretation of High Spatial Resolution Digital Imagery for Forestry.* D. Hill and D. Leckie (Eds). Natural Resources Canada, Canadian Forest Service, Pacific Forest Centre, Victoria British Columbia, Canada, 127-140.

Pollock,
*fore*
Con

Pouliot,
deli
rege

Quacke
fron
*Am*
RO

Roujean
on e
468

Sayn-W
Info
Car

Sheng,
reco
67:

Space I
Cor

Sprinz,
cha
538

Strahle
sen

Treitz,
exa

Trichon
sca

Vareka
geo
*Sen*

Pollock, R. 1996. *The automatic recognition of individual trees in aerial images of forests based on a synthetic tree crown, image model.* Ph.D. thesis, Department of Computer Science, University of British Columbia, Vancouver, Canada.

Pouliot, D.A., D.J. King, F.W. Bell, and D.G. Pitt. 2002. Automated tree crown delineation in high-resolution digital camera imagery of coniferous forest regeneration. *Rem. Sensing Environ.*, 82:322-334.

Quackenbush, L.J., P.F. Hopkins, and G.J. Kinn. 1999. Developing derivative products from high resolution digital aerial imagery. *Proc. 1999 Annual Conference of the American Society for Photogrammetry and Remote Sensing*, Portland, Oregon (CD-ROM).

Roujean, J.L., M. Leroy, and P.Y. Deschamps. 1992. A bi-directional reflectance model on earth's surface for the correction of remote sensing data, *J. Geophys. Res.*, 97:455-468.

Sayn-Wittgenstein, L. 1978. *Recognition of Tree Species on Aerial Photographs,* Information Report FMR-X-118, Forest Management Institute, Ottawa, Ontario, Canada, pp. 97.

Sheng, Y., P. Gong, and G.S. Biging. 2001. Model-based conifer-crown surface reconstruction from high-resolution aerial images. *Photogr. Eng. Rem. Sensing*, 67:957-965.

Space Imaging Inc. 1999. DAIS: A Digital Airborne Imaging System. Space Imaging Corporation, Thornton, Colorado.

Sprinz, P.T. and H.E. Burkhart, 1987. Relationships between tree crown, stem, and stand characteristics in unthinned loblolly pine plantations. *Can. J. For. Research*, 17:534-538.

Strahler A.H., C.E. Woodcock, and J.A. Smith. 1986. On the nature of models in remote sensing, *Rem. Sensing Environ.*, 20:121-139.

Treitz, P.M. 2001. Variogram analysis of high spatial resolution remote sensing data: An examination of boreal forest ecosystems, *Int. J. Rem. Sensing*, 22:3895-3900.

Trichon, V. 2001. Crown typology and the identification of rain forest trees on large-scale aerial photographs, *Plant Ecology*, 153:301-312.

Varekamp, C., A.K. Skidmore, and P.A.B. Burrough. 1996. Using public domain geostatistical and GIS software for spatial interpolation, *Photogram. Eng. Rem. Sensing*, 62:845-854.

Walsworth, N., and D. King. 1999. Comparison of two tree apex delineation techniques, *Proc. International Workshop on Automated Interpretation of High Spatial Resolution Digital Imagery for Forestry*. D. Hill and D. Leckie (Eds). Natural Resources Canada, Canadian Forest Service, Pacific Forest Centre, Victoria British Columbia, Canada, pp. 93-104.

Warner, T., J. Lee, and J. McGraw. 1999. Delineation and identification of individual trees in the eastern deciduous forest. *Proc. International Workshop on Automated Interpretation of High Spatial Resolution Digital Imagery for Forestry*. D. Hill and D. Leckie (Eds). Natural Resources Canada, Canadian Forest Service, Pacific Forest Centre, Victoria British Columbia, Canada, pp. 81-91.

Warner T., J. McGraw, C. Dean, and R. Landenberger. 2000. Automatic Delineation of Individual Deciduous Trees in High Resolution Imagery. *Proc. 28th International Symposium on Remote Sensing of Environment*, Cape Town, South Africa.

Wulder, M. 1998. Optical remote sensing techniques for the assessment of forest inventory and biophysical parameters. *Prog. Phys. Geog.*, 22:449-476.

Wulder, M. 1999. Image spectral and spatial information in the assessment of forest structural and biophysical data, *Proc. International Workshop on Automated Interpretation of High Spatial Resolution Digital Imagery for Forestry*. D. Hill and D. Leckie (Eds). Natural Resources Canada, Canadian Forest Service, Pacific Forest Centre, Victoria British Columbia, Canada, pp. 267-281.

Wulder, M., K.O. Niemann, and D.G. Goodenough. 2000. Local maximum filtering for the extraction of tree locations and basal area from high spatial resolution imagery. *Rem. Sensing Environ.*, 73:103-114.

Wulder, M., K.O. Niemann, and D.G. Goodenough. 2002. Error reduction methods for local maximum filtering of high spatial resolution imagery for location trees. *Can. J. Rem. Sensing*, 28:621-628.

# Tables

**Table 3.1.** Parameter values of linear regression models obtained by fitting plot stem density values predicted via application of two image LMF processing techniques on field measurements of stem density.

| Cover Type | # of plots | LMF using Variogram Ranges | | | LMF using Slope Breaks | | | Regression parameter deviates between techniques | |
|---|---|---|---|---|---|---|---|---|---|
| | | $R^2$ | Slope Coefficient | Intercept Coefficient | $R^2$ | Slope Coefficient | Slope Coefficient | Slope | Mean |
| ASP | 7 | 0.744 | 0.773* | 59.3 | 0.935 | 0.802** | 76.4 | 0.030 | -34.14** |
| NH | 7 | 0.947 | 0.844** | 63.7* | 0.994 | 0.815** | 53.1** | -0.029 | 18.71** |
| Oak | 6 | 0.994 | 0.905** | 50.8** | 0.981 | 0.822** | 57.9* | -0.083 | 14.67* |
| RPP | 7 | 0.994 | 0.770** | 69.3** | 0.990 | 0.822** | 65.7* | 0.052 | -27.71** |
| NP | 7 | 0.997 | 0.826** | 71.1** | 0.996 | 0.906** | 34.4* | 0.091* | -8.14 |
| All | 34 | 0.986 | 0.741** | 91.8** | 0.996 | 0.864** | 44.7** | 0.117** | -6.94* |

* Significant at $\alpha = 0.05$
** Significant at $\alpha = 0.01$

**Table 3.2.** Root Mean Square Errors (RMSE) or discrepancies, between stem density values predicted via LMF image processing and corresponding field measurements. Stem density is expressed in trees per hectare. Values in parentheses represent percent absolute error from observed cover type mean of stem density.

| Cover Type | # of plots | RMSE Values (stems/ha) | | | |
|---|---|---|---|---|---|
| | | LMF using Variogram Ranges | | LMF using Slope Breaks | |
| ASP | 7 | 71.84 | (12.5) | 37.39 | (6.5) |
| NH | 7 | 24.00 | (8.5) | 10.78 | (3.8) |
| Oak | 6 | 26.97 | (10.2) | 18.45 | (7.0) |
| RPP | 7 | 72.07 | (11.9) | 44.53 | (7.4) |
| NP | 7 | 30.22 | (6.1) | 17.67 | (3.6) |
| All | 34 | 50.67 | (11.3) | 29.06 | (6.5) |

**Table 3.3.** Parameter values of linear regression models obtained by fitting plot canopy closure values predicted via tree apex identification using image LMF processing techniques and crown delineation algorithms on field measurements of canopy closure.

| Cover Type | # of plots | LMF using Variogram Ranges | | | LMF using Slope Breaks | | | Regression parameter deviates between techniques | |
|---|---|---|---|---|---|---|---|---|---|
| | | $R^2$ | Slope Coefficient | Intercept Coefficient | $R^2$ | Slope Coefficient | Slope Coefficient | Slope | Mean |
| ASP | 7 | 0.896 | 0.503** | 49.8** | 0.918 | 0.951** | 4.2 | 0.448* | 3.50** |
| NH | 7 | 0.802 | 1.010** | -2.7 | 0.864 | 0.527** | 40.9** | -0.483* | -0.31 |
| Oak | 6 | 0.927 | 0.734** | 17.5 | 0.981 | 0.811** | 17.0* | 0.077 | -5.22** |
| RPP | 7 | 0.989 | 1.161** | -11.1 | 0.969 | 0.861** | 8.5 | -0.300** | 4.90** |
| NP | 7 | 0.953 | 1.098** | -6.6 | 0.951 | 0.727** | 23.2* | -0.371* | -0.49 |
| All | 34 | 0.941 | 1.098** | -7.7** | 0.930 | 0.817** | 15.3** | -0.281** | 0.64 |

* Significant at $\alpha = 0.05$
** Significant at $\alpha = 0.01$

**Table 3.4.** Root Mean Square Errors (RMSE) between plot canopy closure predictions obtained using LMF image processing for tree apex identification and crown delineation algorithms and corresponding field measurements. Canopy closure is expressed in percent of plot area. Values in parentheses represent percent absolute error from observed cover type mean of canopy closure.

| Cover Type | # of plots | RMSE Values (stems/ha) | | | |
|---|---|---|---|---|---|
| | | LMF using Variogram Ranges | | LMF using slope breaks | |
| ASP | 7 | 3.51 | (3.7) | 0.99 | (1.1) |
| NH | 7 | 2.97 | (3.3) | 2.86 | (3.2) |
| Oak | 6 | 2.72 | (3.7) | 3.09 | (4.2) |
| RPP | 7 | 3.05 | (3.7) | 3.70 | (4.5) |
| NP | 7 | 2.62 | (2.1) | 3.28 | (2.6) |
| All | 34 | 3.00 | (3.6) | 2.93 | (3.5) |

**Table 3.5.** Parameter values of linear regression models obtained by fitting mean crown diameter value estimates obtained via variogram and image morphology analysis to corresponding diameter estimates derived from field observations. Image crown delineation was based on LMF processing techniques and associated crown delineation algorithms.

| Cover Type | # of plots | LMF using Variogram Ranges | | | LMF using Slope Breaks | | | Using mean variogram range of subplots | | |
|---|---|---|---|---|---|---|---|---|---|---|
| | | $R^2$ | Slope Coefficient | Intercept Coefficient | $R^2$ | Slope Coefficient | Slope Coefficient | $R^2$ | Slope Coefficient | Slope Coefficient |
| ASP | 7 | 0.706 | 0.952* | 0.65 | 0.868 | 1.213** | -0.87 | 0.426 | 0.928 | 0.73 |
| NH | 7 | 0.870 | 0.750** | 1.25 | 0.962 | 0.843** | 0.94 | 0.653 | 0.808* | 1.01 |
| Oak | 6 | 0.913 | 0.823** | 0.75 | 0.976 | 0.875** | 0.68 | 0.964 | 1.272** | -1.59 |
| RPP | 7 | 0.545 | 0.976* | 0.40 | 0.649 | 0.930* | 0.31 | 0.840 | 1.237** | -0.71 |
| NP | 7 | 0.935 | 0.758** | 1.20 | 0.974 | 0.974** | 0.21 | 0.919 | 0.837** | 0.85 |
| All | 34 | 0.942 | 0.700** | 1.58** | 0.990 | 0.921** | 0.42** | 0.921 | 0.847** | 0.91** |

| Cover Type | Regression Parameter Deviates between | | | | | |
|---|---|---|---|---|---|---|
| | LMF using Variogram Ranges and LMF using Slope Breaks | | LMF using Variogram Ranges and the Mean Variogram Range among Subplots | | LMF using Slope Breaks and the Mean Variogram Range among Subplots | |
| | Slope | Mean | Slope | Mean | Slope | Mean |
| ASP | 0.261 | 0.32** | -0.023 | 0.03 | 0.285 | 0.29** |
| NH | 0.092 | 0.28** | 0.057 | -0.13 | 0.035 | -0.15 |
| Oak | 0.052 | -0.24* | 0.449* | -0.41* | -0.398* | 0.17 |
| RPP | -0.046 | 0.28** | 0.261 | 0.03 | -0.307 | 0.25** |
| NP | 0.216 | 0.00 | 0.079 | -0.01 | 0.137 | 0.01 |
| All | 0.222** | 0.02 | 0.148** | -0.09 | 0.074 | 0.11* |

* Significant at $\alpha = 0.05$
** Significant at $\alpha = 0.01$

**Table**
predic
variog
direct
crown
repre

**Table 3.6.** Root Mean Square Error (RMSE) between plot mean crown diameter predictions obtained i) via crown delineation based on image LMF processing using variogram ranges, ii) via crown delineation based on image LMF processing using directional slope breaks, and iii) as the mean variogram range among subplots, and mean crown diameter estimates derived from field observations. Values in parentheses represent percent absolute error from observed cover type mean of mean crown diameter.

| Cover Type | # of plots | RMSE Values (%) | | | | | |
|---|---|---|---|---|---|---|---|
| | | LMF using Variogram Ranges | | LMF using Slope Breaks | | Mean Variogram Range among Subplots | |
| ASP | 7 | 0.43 | (9.5) | 0.33 | (7.3) | 0.42 | (9.2) |
| NH | 7 | 0.41 | (6.4) | 0.15 | (2.3) | 0.41 | (6.3) |
| Oak | 6 | 0.39 | (6.3) | 0.15 | (2.4) | 0.25 | (4.1) |
| RPP | 7 | 0.32 | (7.7) | 0.08 | (2.0) | 0.28 | (6.8) |
| NP | 7 | 0.18 | (3.9) | 0.12 | (2.6) | 0.18 | (3.8) |
| All | 34 | 0.36 | (6.9) | 0.13 | (2.5) | 0.32 | (6.3) |

**Table 3.7a.** Cross-validation-based Maximum Likelihood classification results and associated accuracy assessment parameters obtained by using spectral signatures developed from pixels identified as representing apexes of individual trees (slope break method) for subplots in sites I and II and original pixel DNs.

| | | Observed | | | | | |
|---|---|---|---|---|---|---|---|
| | | ASP | NH | Oak | RPP | NP | Row Total |
| Classified | Aspen (ASP) | 19 | 5 | 3 | 1 | 0 | 28 |
| | Northern Hardwoods (NH) | 5 | 20 | 3 | 0 | 0 | 28 |
| | Oak | 2 | 3 | 17 | 0 | 1 | 23 |
| | Red Pine Plantation (RPP) | 0 | 0 | 0 | 22 | 7 | 29 |
| | Natural Pine (NP) | 2 | 0 | 1 | 5 | 20 | 28 |
| | Column Total | 28 | 28 | 24 | 28 | 28 | 136 |

| | Accuracy (%) | | Errors (%) | |
|---|---|---|---|---|
| | Producer's | Consumer's | Commission | Omission |
| ASP | 67.86 | 67.86 | 32.14 | 32.14 |
| NH | 71.43 | 71.43 | 28.57 | 28.57 |
| Oak | 70.83 | 73.91 | 29.17 | 25.00 |
| RPP | 78.57 | 75.86 | 21.43 | 25.00 |
| NP | 71.43 | 71.43 | 28.57 | 28.57 |

| ML Probability Threshold | Classified Pixels (%) |
|---|---|
| 0.00 | 100.00 |
| 0.10 | 97.86 |
| 0.25 | 85.93 |
| 0.50 | 47.54 |
| 0.75 | 26.68 |

| Class | Conditional Kappa |
|---|---|
| ASP | 0.5952 |
| NH | 0.6402 |
| Oak | 0.6832 |
| RPP | 0.6960 |
| NP | 0.6402 |

| | |
|---|---|
| Overall Accuracy (%) | 0.7206 |
| Kappa Coefficient | 0.6503 |
| $s^2_k$ | 0.0015 |
| $Z_k$ | 16.5563* |

* Significant at $\alpha = 0.01$

**Table 3.7b.** Cross-validation-based Maximum Likelihood classification results and associated accuracy assessment parameters obtained by using spectral signatures developed from subplot pixels identified as representing apexes of individual trees (slope break method) in site I for subplots in site I and original DNs.

| | | Observed | | | | | |
|---|---|---|---|---|---|---|---|
| | | ASP | NH | Oak | RPP | NP | Row Total |
| Classified | Aspen (ASP) | 12 | 2 | 1 | 0 | 0 | 15 |
| | Northern Hardwoods (NH) | 3 | 9 | 2 | 0 | 0 | 14 |
| | Oak | 0 | 1 | 9 | 0 | 1 | 11 |
| | Red Pine Plantation (RPP) | 0 | 0 | 0 | 12 | 5 | 17 |
| | Natural Pine (NP) | 1 | 0 | 0 | 4 | 10 | 15 |
| | Column Total | 16 | 12 | 12 | 16 | 16 | 72 |

| | Accuracy (%) | | Errors (%) | |
|---|---|---|---|---|
| | Producer's | Consumer's | Commission | Omission |
| ASP | 75.00 | 80.00 | 25.00 | 18.75 |
| NH | 75.00 | 64.29 | 25.00 | 41.67 |
| Oak | 75.00 | 81.82 | 25.00 | 16.67 |
| RPP | 75.00 | 70.59 | 25.00 | 31.25 |
| NP | 62.50 | 66.67 | 37.50 | 31.25 |

| ML Probability Threshold | Classified Pixels (%) |
|---|---|
| 0.00 | 100.0 |
| 0.10 | 97.8 |
| 0.25 | 85.9 |
| 0.50 | 51.1 |
| 0.75 | 29.3 |

| Class | Conditional Kappa |
|---|---|
| ASP | 0.7429 |
| NH | 0.5714 |
| Oak | 0.7818 |
| RPP | 0.6218 |
| NP | 0.5714 |

| | |
|---|---|
| Overall Accuracy (%) | 0.7222 |
| Kappa Coefficient | 0.6515 |
| $s^2_k$ | 0.0029 |
| $Z_k$ | 12.0627* |

* Significant at $\alpha = 0.01$

**Table 3.7c.** Cross-validation-based Maximum Likelihood classification results and associated accuracy assessment parameters obtained by using spectral signatures developed from subplot pixels identified as representing apexes of individual trees (slope break method) in site II for subplots in site I and original DNs.

| | | Observed | | | | | |
|---|---|---|---|---|---|---|---|
| | | ASP | NH | Oak | RPP | NP | Row Total |
| Classified | Aspen (ASP) | 11 | 2 | 2 | 0 | 0 | 15 |
| | Northern Hardwoods (NH) | 4 | 8 | 1 | 0 | 0 | 13 |
| | Oak | 0 | 2 | 9 | 0 | 1 | 12 |
| | Red Pine Plantation (RPP) | 0 | 0 | 0 | 12 | 4 | 16 |
| | Natural Pine (NP) | 1 | 0 | 0 | 4 | 11 | 16 |
| | Column Total | 16 | 12 | 12 | 16 | 16 | 72 |

| | Accuracy (%) | | Errors (%) | |
|---|---|---|---|---|
| | Producer's | Consumer's | Commission | Omission |
| ASP | 68.75 | 73.33 | 31.25 | 25.00 |
| NH | 66.67 | 61.54 | 33.33 | 41.67 |
| Oak | 75.00 | 75.00 | 25.00 | 25.00 |
| RPP | 75.00 | 75.00 | 25.00 | 25.00 |
| NP | 68.75 | 68.75 | 31.25 | 31.25 |

| ML Probability Threshold | Classified Pixels (%) |
|---|---|
| 0.00 | 100.00 |
| 0.10 | 97.58 |
| 0.25 | 84.75 |
| 0.50 | 43.54 |
| 0.75 | 20.03 |

| Class | Conditional Kappa |
|---|---|
| ASP | 0.6571 |
| NH | 0.5385 |
| Oak | 0.7000 |
| RPP | 0.6786 |
| NP | 0.5982 |

| | |
|---|---|
| Overall Accuracy (%) | 0.7083 |
| Kappa Coefficient | 0.6341 |
| $s^2_k$ | 0.0030 |
| $Z_k$ | 11.5934* |

* Significant at $\alpha = 0.01$

**Table 3.7**
associated
developed
break met

| | | |
|---|---|---|
| Classified | Asp | |
| | Nort | |
| | Oak | |
| | Red | |
| | Natu | |
| | Colu | |

| | Pro |
|---|---|
| ASP | |
| NH | |
| Oak | |
| RPP | |
| NP | |

| Class |
|---|
| ASP |
| NH |
| Oak |
| RPP |
| NP |

**Table 3.7d.** Cross-validation-based Maximum Likelihood classification results and associated accuracy assessment parameters obtained by using spectral signatures developed from subplot pixels identified as representing apexes of individual trees (slope break method) in site II for subplots in site II and original DNs.

| | | Observed | | | | | |
|---|---|---|---|---|---|---|---|
| | | ASP | NH | Oak | RPP | NP | Row Total |
| Classified | Aspen (ASP) | 9 | 3 | 2 | 0 | 0 | 14 |
| | Northern Hardwoods (NH) | 0 | 10 | 1 | 0 | 0 | 11 |
| | Oak | 0 | 3 | 9 | 0 | 0 | 12 |
| | Red Pine Plantation (RPP) | 0 | 0 | 0 | 9 | 3 | 12 |
| | Natural Pine (NP) | 3 | 0 | 0 | 3 | 9 | 15 |
| | Column Total | 12 | 16 | 12 | 12 | 12 | 64 |

| | Accuracy (%) | | Errors (%) | |
|---|---|---|---|---|
| | Producer's | Consumer's | Commission | Omission |
| ASP | 75.00 | 64.29 | 25.00 | 41.67 |
| NH | 62.50 | 90.91 | 37.50 | 6.25 |
| Oak | 75.00 | 75.00 | 25.00 | 25.00 |
| RPP | 75.00 | 75.00 | 25.00 | 25.00 |
| NP | 75.00 | 60.00 | 25.00 | 50.00 |

| ML Probability Threshold | Classified Pixels (%) |
|---|---|
| 0.00 | 100.00 |
| 0.10 | 97.75 |
| 0.25 | 83.37 |
| 0.50 | 49.80 |
| 0.75 | 24.46 |

| Class | Conditional Kappa |
|---|---|
| ASP | 0.5604 |
| NH | 0.8788 |
| Oak | 0.6923 |
| RPP | 0.6923 |
| NP | 0.5077 |

| | |
|---|---|
| Overall Accuracy (%) | 0.7188 |
| Kappa Coefficient | 0.6492 |
| $s^2_k$ | 0.0033 |
| $Z_k$ | 11.3649* |

* Significant at $\alpha = 0.01$

**Table 3.7e.** Cross-validation-based Maximum Likelihood classification results and associated accuracy assessment parameters obtained by using spectral signatures developed from subplot pixels identified as representing apexes of individual trees (slope break method) in site I for subplots in site II and original DNs.

| | | Observed | | | | | |
|---|---|---|---|---|---|---|---|
| | | ASP | NH | Oak | RPP | NP | Row Total |
| Classified | Aspen (ASP) | 9 | 4 | 1 | 0 | 0 | 14 |
| | Northern Hardwoods (NH) | 1 | 10 | 3 | 0 | 0 | 14 |
| | Oak | 1 | 2 | 8 | 0 | 0 | 11 |
| | Red Pine Plantation (RPP) | 0 | 0 | 0 | 9 | 3 | 12 |
| | Natural Pine (NP) | 1 | 0 | 0 | 3 | 9 | 13 |
| | Column Total | 12 | 16 | 12 | 12 | 12 | 64 |

| | Accuracy (%) | | Errors (%) | |
|---|---|---|---|---|
| | Producer's | Consumer's | Commission | Omission |
| ASP | 75.00 | 64.29 | 25.00 | 41.67 |
| NH | 62.50 | 71.43 | 37.50 | 25.00 |
| Oak | 66.67 | 72.73 | 33.33 | 25.00 |
| RPP | 75.00 | 75.00 | 25.00 | 25.00 |
| NP | 75.00 | 69.23 | 25.00 | 33.33 |

| ML Probability Threshold | Classified Pixels (%) |
|---|---|
| 0.00 | 100.00 |
| 0.10 | 97.91 |
| 0.25 | 85.02 |
| 0.50 | 42.06 |
| 0.75 | 21.04 |

| Class | Conditional Kappa |
|---|---|
| ASP | 0.5604 |
| NH | 0.6190 |
| Oak | 0.6643 |
| RPP | 0.6923 |
| NP | 0.6213 |

| | |
|---|---|
| Overall Accuracy (%) | 0.7031 |
| Kappa Coefficient | 0.6284 |
| $s^2_k$ | 0.0034 |
| $Z_k$ | 10.7614* |

* Significant at $\alpha = 0.01$

**Table 3.7f.** Cross-validation-based Maximum Likelihood classification results and associated accuracy assessment parameters obtained by using spectral signatures developed from pixels identified as representing apexes of individual trees (slope break method) for subplots in sites I and II and brightness-normalized pixel DNs.

| | | Observed | | | | | |
|---|---|---|---|---|---|---|---|
| | | ASP | NH | Oak | RPP | NP | Row Total |
| Classified | Aspen (ASP) | 23 | 2 | 2 | 0 | 0 | 27 |
| | Northern Hardwoods (NH) | 4 | 25 | 2 | 0 | 0 | 31 |
| | Oak | 1 | 1 | 20 | 0 | 0 | 22 |
| | Red Pine Plantation (RPP) | 0 | 0 | 0 | 25 | 2 | 27 |
| | Natural Pine (NP) | 0 | 0 | 0 | 3 | 26 | 29 |
| | Column Total | 28 | 28 | 24 | 28 | 28 | 136 |

| | Accuracy (%) | | Errors (%) | |
|---|---|---|---|---|
| | Producer's | Consumer's | Commission | Omission |
| ASP | 82.14 | 85.19 | 17.86 | 14.29 |
| NH | 89.29 | 80.65 | 10.71 | 21.43 |
| Oak | 83.33 | 90.91 | 16.67 | 8.33 |
| RPP | 89.29 | 92.59 | 10.71 | 7.14 |
| NP | 92.86 | 89.66 | 7.14 | 10.71 |

| ML Probability Threshold | Classified Pixels (%) |
|---|---|
| 0.00 | 100.00 |
| 0.10 | 98.27 |
| 0.25 | 90.21 |
| 0.50 | 68.91 |
| 0.75 | 53.00 |

| Class | Conditional Kappa |
|---|---|
| ASP | 0.8134 |
| NH | 0.7563 |
| Oak | 0.8896 |
| RPP | 0.9067 |
| NP | 0.8697 |

| | |
|---|---|
| Overall Accuracy (%) | 0.8750 |
| Kappa Coefficient | 0.8435 |
| $s^2_k$ | 0.0008 |
| $Z_k$ | 29.1529* |

* Significant at $\alpha = 0.01$

**Table 3.7g.** Cross-validation-based Maximum Likelihood classification results and associated accuracy assessment parameters obtained by using spectral signatures developed from subplot pixels identified as representing apexes of individual trees (slope break method) in site I for subplots in site I and brightness-normalized pixel DNs.

| | | Observed | | | | | |
|---|---|---|---|---|---|---|---|
| | | ASP | NH | Oak | RPP | NP | Row Total |
| Classified | Aspen (ASP) | 13 | 1 | 1 | 0 | 0 | 15 |
| | Northern Hardwoods (NH) | 2 | 10 | 1 | 0 | 0 | 13 |
| | Oak | 1 | 1 | 10 | 0 | 0 | 12 |
| | Red Pine Plantation (RPP) | 0 | 0 | 0 | 14 | 1 | 15 |
| | Natural Pine (NP) | 0 | 0 | 0 | 2 | 15 | 17 |
| | Column Total | 16 | 12 | 12 | 16 | 16 | 72 |

| | Accuracy (%) | | Errors (%) | |
|---|---|---|---|---|
| | Producer's | Consumer's | Commission | Omission |
| ASP | 81.25 | 86.67 | 18.75 | 12.50 |
| NH | 83.33 | 76.92 | 16.67 | 25.00 |
| Oak | 83.33 | 83.33 | 16.67 | 16.67 |
| RPP | 87.50 | 93.33 | 12.50 | 6.25 |
| NP | 93.75 | 88.24 | 6.25 | 12.50 |

| ML Probability Threshold | Classified Pixels (%) |
|---|---|
| 0.00 | 100.00 |
| 0.10 | 98.28 |
| 0.25 | 90.73 |
| 0.50 | 68.96 |
| 0.75 | 50.39 |

| Class | Conditional Kappa |
|---|---|
| ASP | 0.8134 |
| NH | 0.7563 |
| Oak | 0.8896 |
| RPP | 0.9067 |
| NP | 0.8697 |

| | |
|---|---|
| Overall Accuracy (%) | 0.8611 |
| Kappa Coefficient | 0.8258 |
| $s^2_k$ | 0.0017 |
| $Z_k$ | 19.9145* |

* Significant at $\alpha = 0.01$

**Table 3.7h.** Cross-validation-based Maximum Likelihood classification results and associated accuracy assessment parameters obtained by using spectral signatures developed from subplot pixels identified as representing apexes of individual trees (slope break method) in site II for subplots in site I and brightness-normalized pixel DNs.

| | | Observed | | | | | |
|---|---|---|---|---|---|---|---|
| | | ASP | NH | Oak | RPP | NP | Row Total |
| Classified | Aspen (ASP) | 14 | 1 | 1 | 0 | 0 | 16 |
| | Northern Hardwoods (NH) | 2 | 10 | 1 | 0 | 0 | 13 |
| | Oak | 0 | 1 | 10 | 0 | 0 | 11 |
| | Red Pine Plantation (RPP) | 0 | 0 | 0 | 13 | 2 | 15 |
| | Natural Pine (NP) | 0 | 0 | 0 | 3 | 14 | 17 |
| | Column Total | 16 | 12 | 12 | 16 | 16 | 72 |

| | Accuracy (%) | | Errors (%) | |
|---|---|---|---|---|
| | Producer's | Consumer's | Commission | Omission |
| ASP | 87.50 | 87.50 | 12.50 | 12.50 |
| NH | 83.33 | 76.92 | 16.67 | 25.00 |
| Oak | 83.33 | 90.91 | 16.67 | 8.33 |
| RPP | 81.25 | 86.67 | 18.75 | 12.50 |
| NP | 87.50 | 82.35 | 12.50 | 18.75 |

| ML Probability Threshold | Classified Pixels (%) |
|---|---|
| 0.00 | 100.0 |
| 0.10 | 98.2 |
| 0.25 | 89.0 |
| 0.50 | 61.6 |
| 0.75 | 46.8 |

| Class | Conditional Kappa |
|---|---|
| ASP | 0.8393 |
| NH | 0.7231 |
| Oak | 0.8909 |
| RPP | 0.8286 |
| NP | 0.7731 |

| | |
|---|---|
| Overall Accuracy (%) | 0.8472 |
| Kappa Coefficient | 0.8081 |
| $s^2_k$ | 0.0019 |
| $Z_k$ | 18.6765* |

* Significant at $\alpha = 0.01$

**Table 3.7i.** Cross-validation-based Maximum Likelihood classification results and associated accuracy assessment parameters obtained by using spectral signatures developed from subplot pixels identified as representing apexes of individual trees (slope break method) in site II for subplots in site II and brightness-normalized pixel DNs.

| | | Observed | | | | | |
|---|---|---|---|---|---|---|---|
| | | ASP | NH | Oak | RPP | NP | Row Total |
| Classified | Aspen (ASP) | 11 | 1 | 1 | 0 | 0 | 13 |
| | Northern Hardwoods (NH) | 0 | 14 | 2 | 0 | 0 | 16 |
| | Oak | 0 | 1 | 9 | 0 | 0 | 10 |
| | Red Pine Plantation (RPP) | 0 | 0 | 0 | 11 | 1 | 12 |
| | Natural Pine (NP) | 1 | 0 | 0 | 1 | 11 | 13 |
| | Column Total | 12 | 16 | 12 | 12 | 12 | 64 |

| | Accuracy (%) | | Errors (%) | |
|---|---|---|---|---|
| | Producer's | Consumer's | Commission | Omission |
| ASP | 91.67 | 84.62 | 8.33 | 16.67 |
| NH | 87.50 | 87.50 | 12.50 | 12.50 |
| Oak | 75.00 | 90.00 | 25.00 | 8.33 |
| RPP | 91.67 | 91.67 | 8.33 | 8.33 |
| NP | 91.67 | 84.62 | 8.33 | 16.67 |

| ML Probability Threshold | Classified Pixels (%) |
|---|---|
| 0.00 | 100.00 |
| 0.10 | 98.44 |
| 0.25 | 89.85 |
| 0.50 | 66.80 |
| 0.75 | 54.76 |

| Class | Conditional Kappa |
|---|---|
| ASP | 0.8107 |
| NH | 0.8333 |
| Oak | 0.8769 |
| RPP | 0.8974 |
| NP | 0.8107 |

| | |
|---|---|
| Overall Accuracy (%) | 0.8750 |
| Kappa Coefficient | 0.8431 |
| $s^2_k$ | 0.0018 |
| $Z_k$ | 19.9988* |

* Significant at $\alpha = 0.01$

**Table 3.7j.** Cross-validation-based Maximum Likelihood classification results and associated accuracy assessment parameters obtained by using spectral signatures developed from subplot pixels identified as representing apexes of individual trees (slope break method) in site I for subplots in site II and brightness-normalized pixel DNs.

| | | Observed | | | | | |
|---|---|---|---|---|---|---|---|
| | | ASP | NH | Oak | RPP | NP | Row Total |
| Classified | Aspen (ASP) | 10 | 2 | 1 | 0 | 0 | 13 |
| | Northern Hardwoods (NH) | 1 | 13 | 1 | 0 | 0 | 15 |
| | Oak | 1 | 1 | 10 | 0 | 0 | 12 |
| | Red Pine Plantation (RPP) | 0 | 0 | 0 | 11 | 2 | 13 |
| | Natural Pine (NP) | 0 | 0 | 0 | 1 | 10 | 11 |
| | Column Total | 12 | 16 | 12 | 12 | 12 | 64 |

| | Accuracy (%) | | Errors (%) | |
|---|---|---|---|---|
| | Producer's | Consumer's | Commission | Omission |
| ASP | 83.33 | 76.92 | 16.67 | 25.00 |
| NH | 81.25 | 86.67 | 18.75 | 12.50 |
| Oak | 83.33 | 83.33 | 16.67 | 16.67 |
| RPP | 91.67 | 84.62 | 8.33 | 16.67 |
| NP | 83.33 | 90.91 | 16.67 | 8.33 |

| ML Probability Threshold | Classified Pixels (%) |
|---|---|
| 0.00 | 100.00 |
| 0.10 | 98.37 |
| 0.25 | 88.25 |
| 0.50 | 64.72 |
| 0.75 | 44.85 |

| Class | Conditional Kappa |
|---|---|
| ASP | 0.7160 |
| NH | 0.8222 |
| Oak | 0.7949 |
| RPP | 0.8107 |
| NP | 0.8881 |

| | |
|---|---|
| Overall Accuracy (%) | 0.8438 |
| Kappa Coefficient | 0.8042 |
| $s^2_k$ | 0.0021 |
| $Z_k$ | 17.3489* |

* Significant at $\alpha = 0.01$

**Table 3.8.** Z-scores of subplot classification result comparison for combinations of cross-validation-based classification scenarios computed as standardized differences of respective kappa coefficients. Parentheses denote p-values. Scores in bold and in italics indicate significance at $\alpha$=0.05. Scores in bold only indicate significance at $\alpha$=0.01. Classification signatures were developed using pixels identified as tree apexes via slope break-based imagery LMF processing.

| | | Site I & II, original DNs | Site I, signatures from Site I, original DNs | Site I, signatures from Site II, original DNs | Site II, signatures from Site II, original DNs | Site II, signatures from Site I, original DNs | Site I & II, with brightness normalization | Site I, signatures from Site I with brightness normalization | Site I, signatures from Site II with brightness normalization | Site II, signatures from Site II with brightness normalization |
|---|---|---|---|---|---|---|---|---|---|---|
| Z-score | Site I, signatures from Site I, original DNs | 0.0181 (0.9856) | | | | | | | | |
| | Site I, signatures from Site II, original DNs | -0.2415 (0.8092) | -0.2265 (0.8208) | | | | | | | |
| | Site II, signatures from Site II, original DNs | -0.0159 (0.9873) | -0.0292 (0.9767) | 0.1902 0.8492) | | | | | | |
| | Site II, signatures from Site I, original DNs | -0.2676 (0.7890) | -0.2910 (0.7711) | -0.0713 (0.9432) | -0.2541 (0.7994) | | | | | |
| | Site I & II, brightness normalization | **4.0285** (0.0001) | **3.1565** (0.0016) | **3.3969** (0.0007) | **3.0345** (0.0024) | **3.3191** (0.0009) | | | | |
| | Site I, signatures from Site I, brightness normalization | **3.1024** (0.0019) | ***2.5700*** (0.0102) | **2.7962** (0.0052) | ***2.4975*** (0.0125) | **2.7642** (0.0057) | -0.3540 (0.7233) | | | |
| | Site I, signatures form Site II, brightness normalization | **2.7062** (0.0068) | ***2.2603*** (0.0238) | ***2.4857*** (0.0129) | ***2.2035*** (0.0276) | ***2.4684*** (0.0136) | -0.6813 (0.4957) | -0.2950 (0.7680) | | |
| | Site II, signatures from Site II, brightness normalization | **3.3562** (0.0008) | **2.7948** (0.0052) | **3.0167** (0.0026) | **2.7151** (0.0066) | **2.9774** (0.0029) | -0.0141 (0.9888) | 0.2924 (0.7700) | 0.5754 (0.5650) | |
| | Site II, signatures form Site I, brightness normalization | ***2.5650*** (0.0103) | ***2.1595*** (0.0308) | ***2.3819*** (0.0172) | ***2.1093*** (0.0349) | ***2.3705*** (0.0178) | -0.7298 (0.4655) | -0.3504 (0.7260) | -0.0617 (0.9508) | -0.6229 (0.5334) |

**Table 3.9.** Classification error rates of subplots conditional upon cover types group (deciduous or coniferous) produced with maximum-likelihood based cross validation for all plots in the study area before and after brightness normalization using subplot pixels identified as tree crown apexes. Apex identification was performed using slope break-based imagery LMF processing.

| | | Aspen | Northern Hardwoods | Oak | Red Pine Plantation | Natural Pine |
|---|---|---|---|---|---|---|
| Original DNs | Deciduous | 7 (25%) | 8 (29%) | 6 (25%) | 1 (4%) | 8 (4%) |
| | Coniferous | 2 (7%) | 0 (0%) | 1 (4%) | 5 (18%) | 8 (25%) |
| Brightness normalization | Deciduous | 5 (18%) | 3 (11%) | 4 (17%) | 0 (0%) | 9 (0%) |
| | Coniferous | 0 (0%) | 0 (0%) | 0 (0%) | 3 (11%) | 7 (7%) |

**Table 3.10.** Change in class-conditional Kappa coefficients computed before and after brightness normalization using tree apex signatures.

| | Cover Type | Original DNs | Brightness Corrected | ΔKappa |
|---|---|---|---|---|
| All subplots using signatures from site I and II | ASP | 0.5952 | 0.8134 | 0.2182 |
| | NH | 0.6402 | 0.7563 | 0.1161 |
| | Oak | 0.6832 | 0.8896 | 0.2064 |
| | RPP | 0.6960 | 0.9067 | 0.2107 |
| | NP | 0.6402 | 0.8697 | 0.2295 |
| Site I subplots using site I signatures | ASP | 0.7429 | 0.8134 | 0.0705 |
| | NH | 0.5714 | 0.7563 | 0.1849 |
| | Oak | 0.7818 | 0.8896 | 0.1078 |
| | RPP | 0.6218 | 0.9067 | 0.2849 |
| | NP | 0.5714 | 0.8697 | 0.2983 |
| Site II subplots using site II signatures | ASP | 0.5604 | 0.8107 | 0.2503 |
| | NH | 0.8788 | 0.8333 | -0.0455 |
| | Oak | 0.6923 | 0.8769 | 0.1846 |
| | RPP | 0.6923 | 0.8974 | 0.2051 |
| | NP | 0.5077 | 0.8107 | 0.3030 |
| Site I subplots using site II signatures | ASP | 0.6571 | 0.8393 | 0.1822 |
| | NH | 0.5385 | 0.7231 | 0.1846 |
| | Oak | 0.7000 | 0.8909 | 0.1909 |
| | RPP | 0.6786 | 0.8286 | 0.1500 |
| | NP | 0.5982 | 0.7731 | 0.1749 |
| Site II subplots using site I signatures | ASP | 0.5604 | 0.7160 | 0.1556 |
| | NH | 0.6190 | 0.8222 | 0.2032 |
| | Oak | 0.6643 | 0.7949 | 0.1306 |
| | RPP | 0.6923 | 0.8107 | 0.1184 |
| | NP | 0.6213 | 0.8881 | 0.2668 |
| Average across all five classification scenarios | ASP | | | 0.1754 |
| | NH | | | 0.1287 |
| | Oak | | | 0.1641 |
| | RPP | | | 0.1938 |
| | NP | | | 0.2545 |

**Table 3.11.** Z-scores of subplot classification result comparison for combinations of cross-validation-based classification scenarios, computed as standardized differences of respective kappa coefficients. Associated p-values are in parentheses. Scores in bold indicate significance at $\alpha$=0.01. Classification scenarios entailed signature development using 1) all pixels in a subplot, and 2) pixels corresponding to subplot tree apexes identified via slope break-based imagery LMF processing.

| | All pixels, Original DNs | All pixels, Brightness normalization | Tree apex pixels, Original DNs |
|---|---|---|---|
| All pixels, Brightness normalization | 0.7511 (0.4576) | | |
| Tree apex pixels, Original DNs | **5.5137** (0.0000) | **4.7196** (0.0000) | |
| Tree apex pixels, Brightness normalization | **9.9054** (0.0000) | **9.0144** (0.0000) | **4.0285** (0.0001) |

# Figures

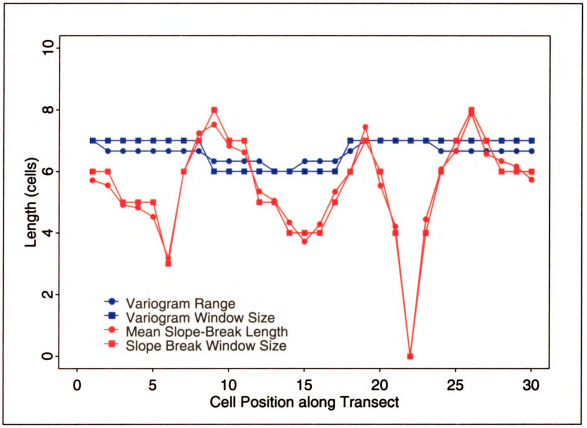


**Figure 3.1**. NIR band variogram ranges and mean slope-break lengths (circles) and corresponding window sizes (squares) computed along a transect dissecting a northern hardwoods subplot. Lines serve visualization purposes only.

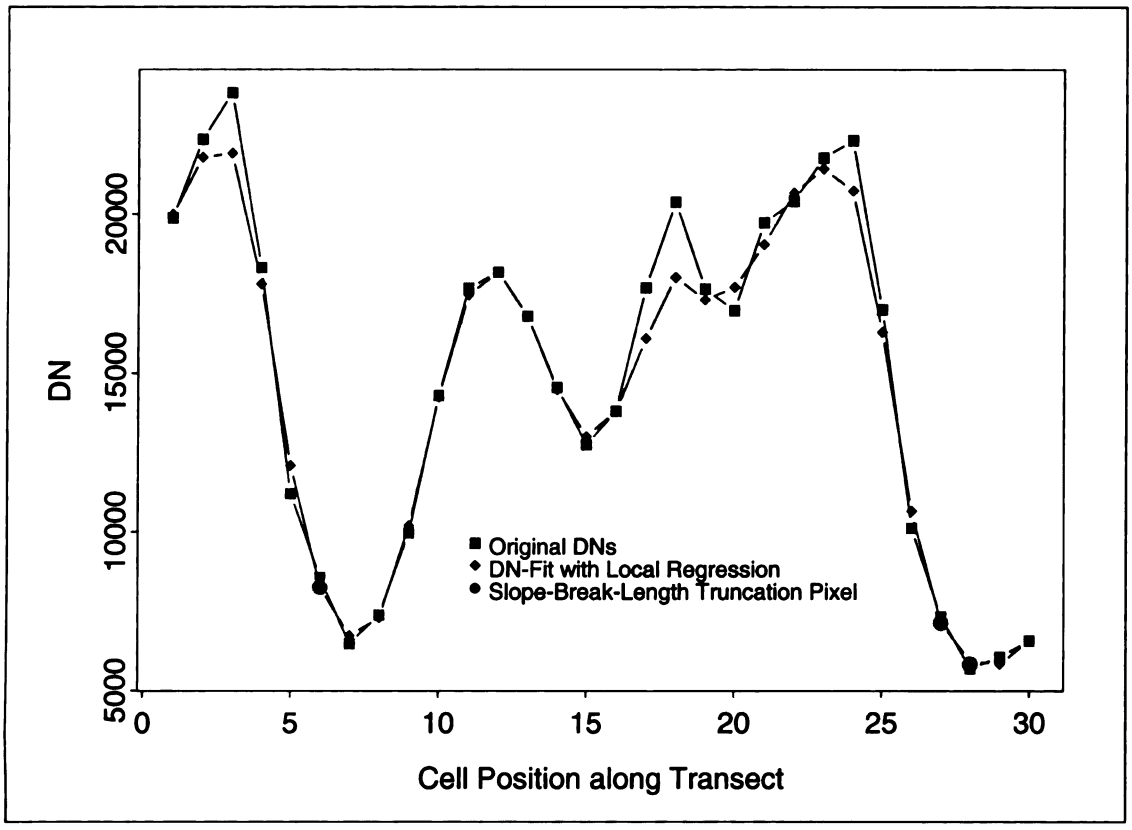


**Figure 3.2.** Original NIR band Digital Numbers (DN), DN-fit via local regression, and pixel identified as slope-break-length truncation locations, along a 30-pixel transect in a Natural Pine subplot.

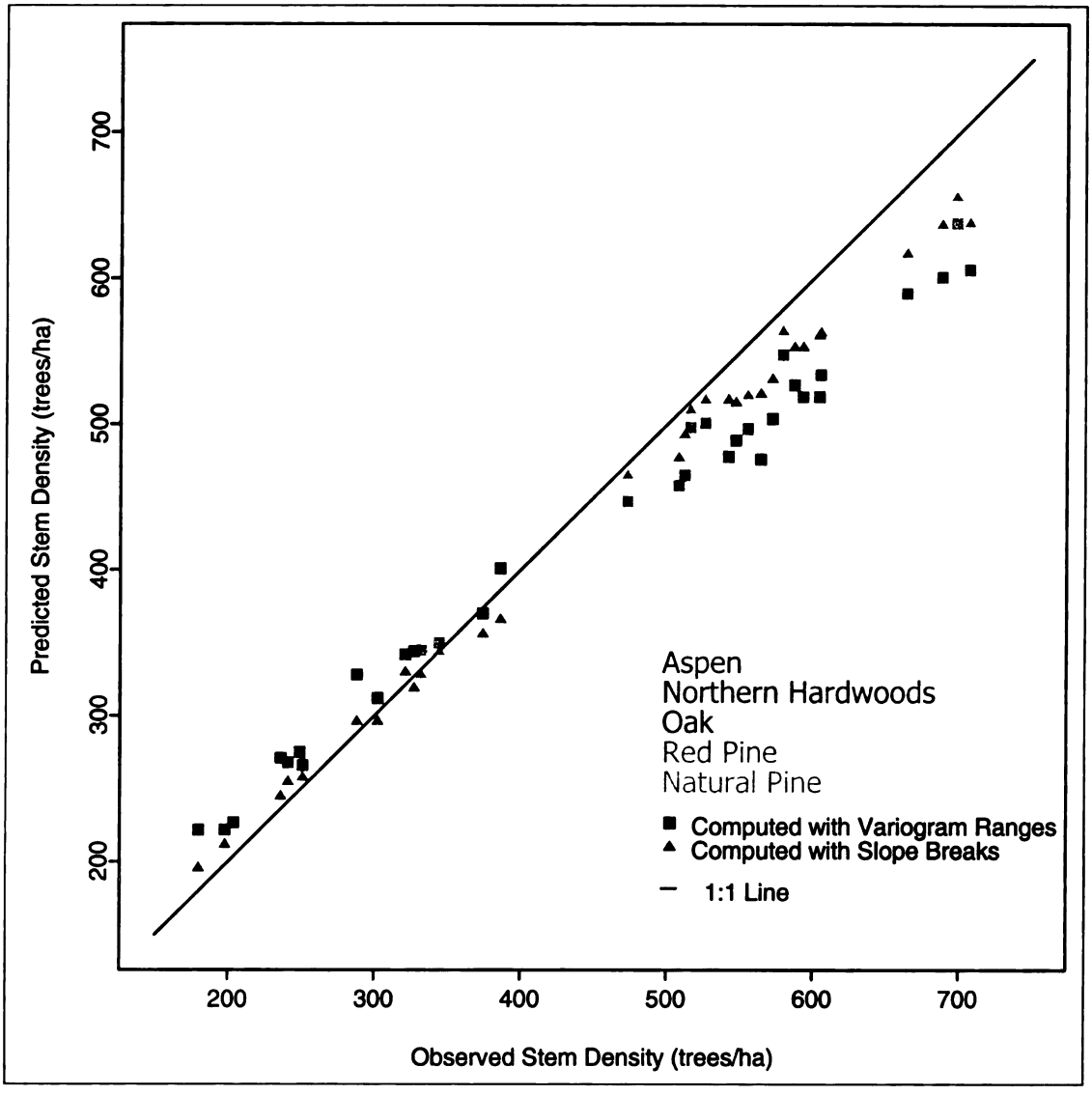


**Figure 3.3.** Observed vs. predicted stem density at the plot level for five forest cover types. Stem density estimates were obtained from tree apexes identified on NIR-band imagery via local maximum filtering (LMF) with window sizes conditioned upon (a) computed variogram ranges, and (b) mean slope break estimates. Plot cover types are color-coded while the LMF techniques employed are symbol-shape-coded.

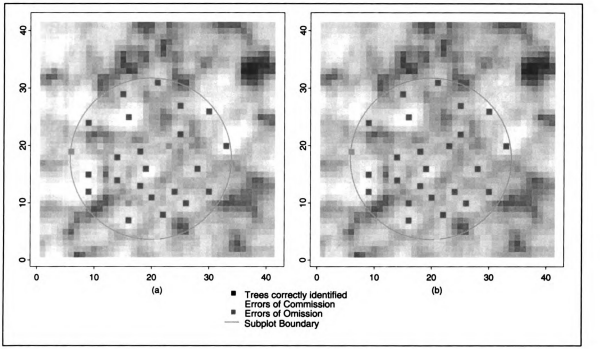


**Figure 3.4**. NIR band of an aspen subplot and tree apex locations identified by using local maximum filtering with window sizes conditioned upon (a) computed variogram ranges, and (b) mean slope break estimates.

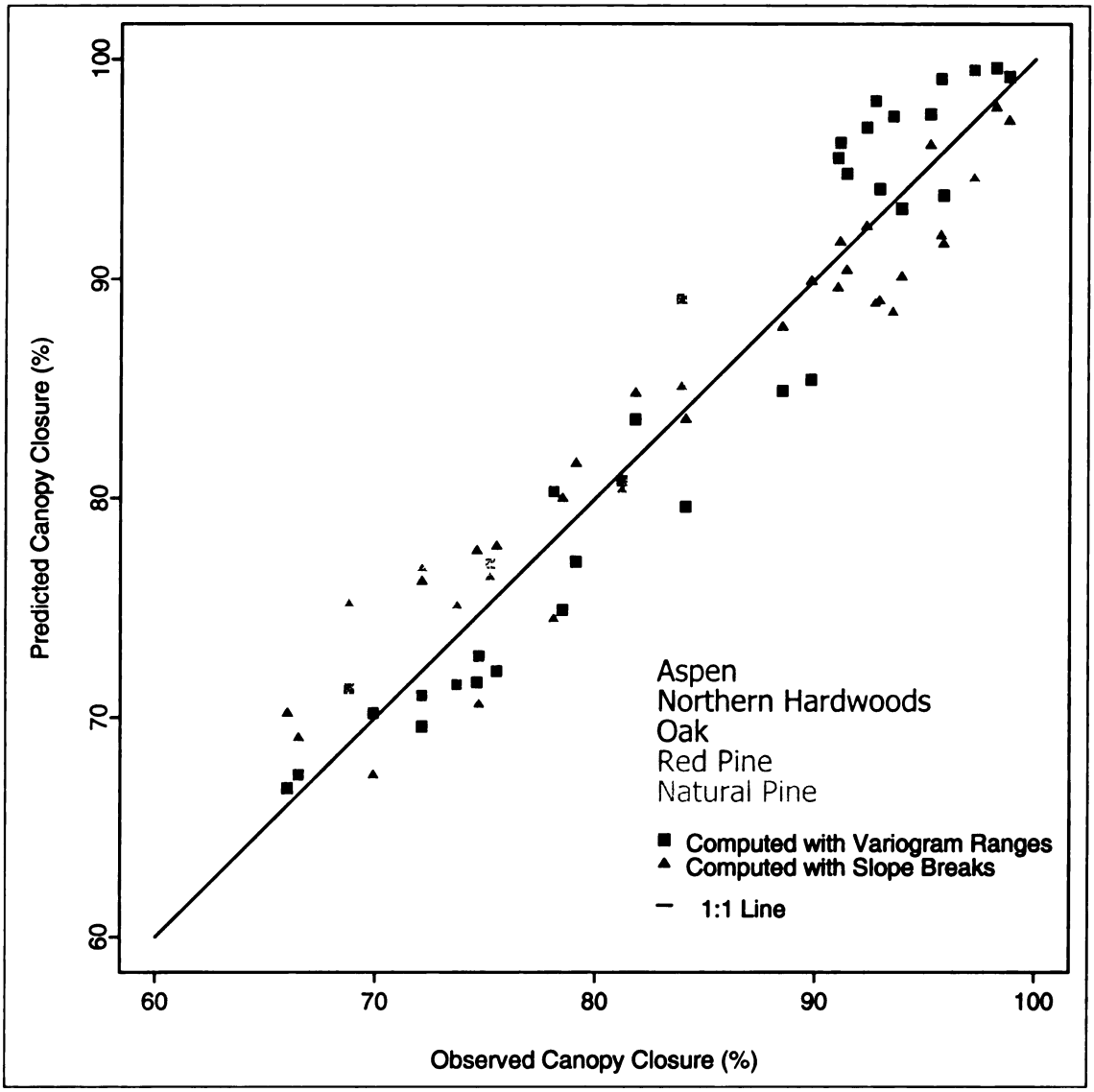


**Figure 3.5**. Observed vs. predicted canopy closure for plots in five forest cover types. Canopy closure estimates were obtained from crown delineation based on crown apexes identified on NIR-band imagery by using local maximum filtering (LMF) with window sizes conditioned upon (a) computed variogram ranges, and (b) mean slope break estimates. Cover types are color-coded while employed LMF techniques are symbol-shape-coded.

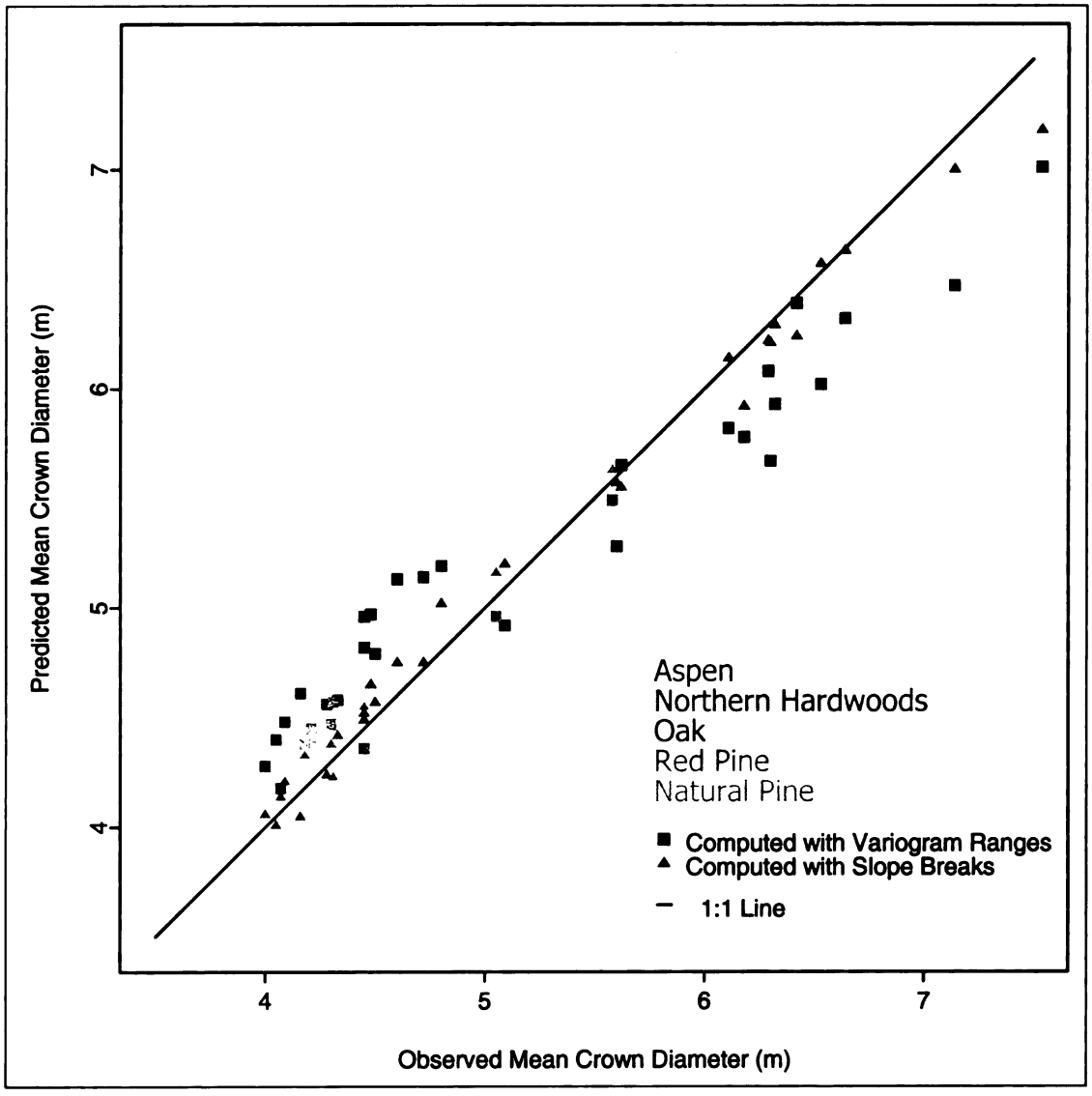


**Figure 3.6.** Observed vs. predicted mean crown diameter for plots situated in five forest cover types. Mean crown diameter estimates were obtained from crown delineation based on crown apexes identified on NIR-band imagery by using local maximum filtering (LMF) with window sizes conditioned upon (a) computed variogram ranges, and (b) mean slope break estimates. Cover types are color-coded while employed LMF techniques are symbol-shape-coded.

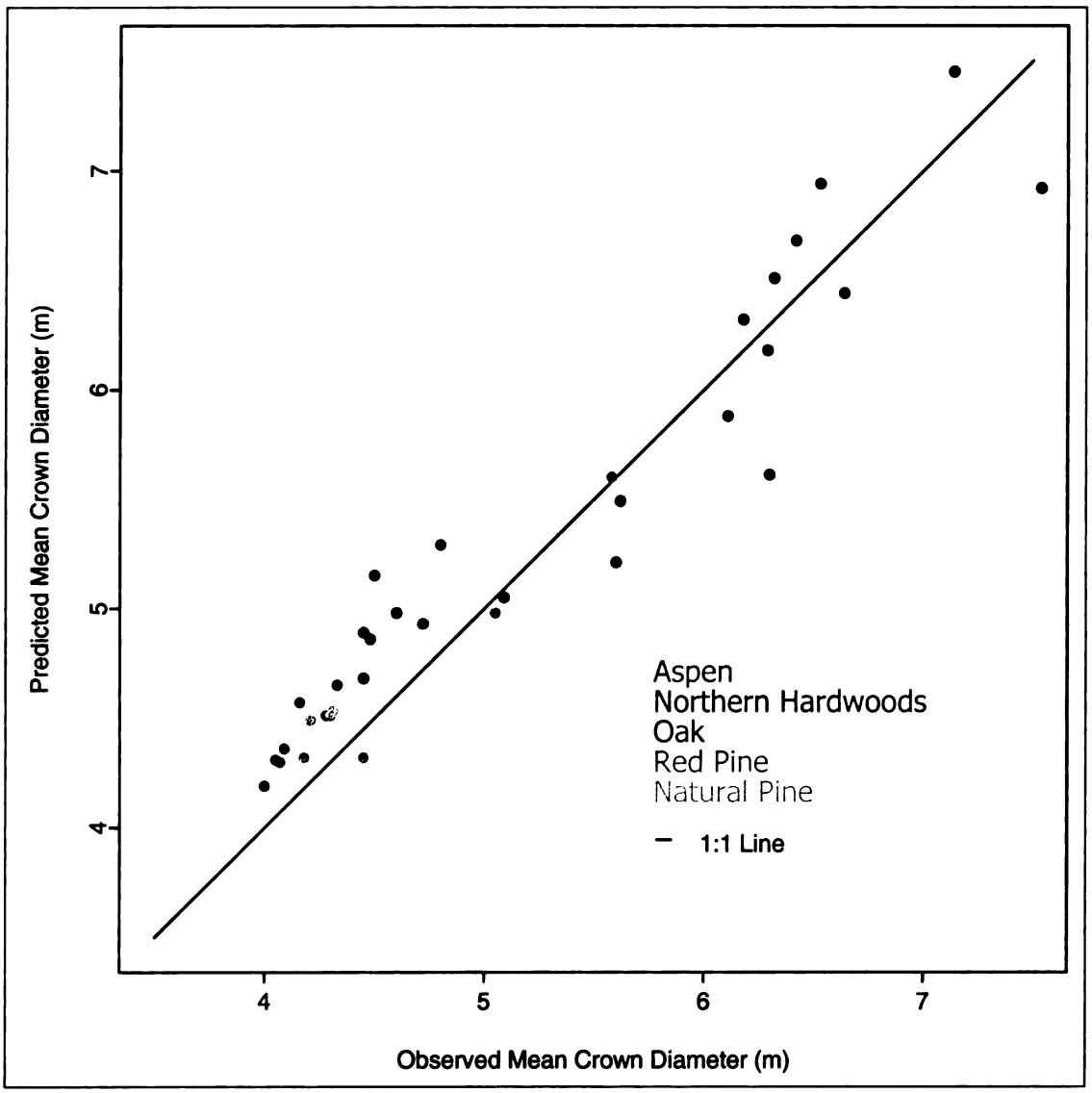


**Figure 3.7.** Observed vs. predicted mean crown diameter for plots situated in five forest cover types. Mean crown diameter estimates were calculated as the mean range of variograms computed using the NIR band Digital Numbers for every subplot in a plot. Cover types are color-coded.

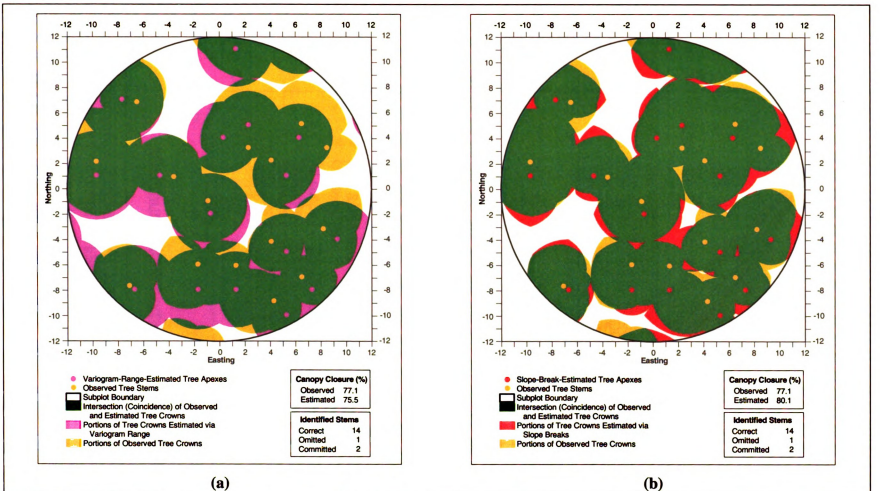


**Figure 3.8.** Observed and NIR-band-estimated individual tree crown extent of an oak subplot. Crown apex identification and subsequent crown delineation was performed by using (a) variogram ranges and (b) slope breaks. Coordinate system origin is at the subplot's center and its scale is measured in pixels.

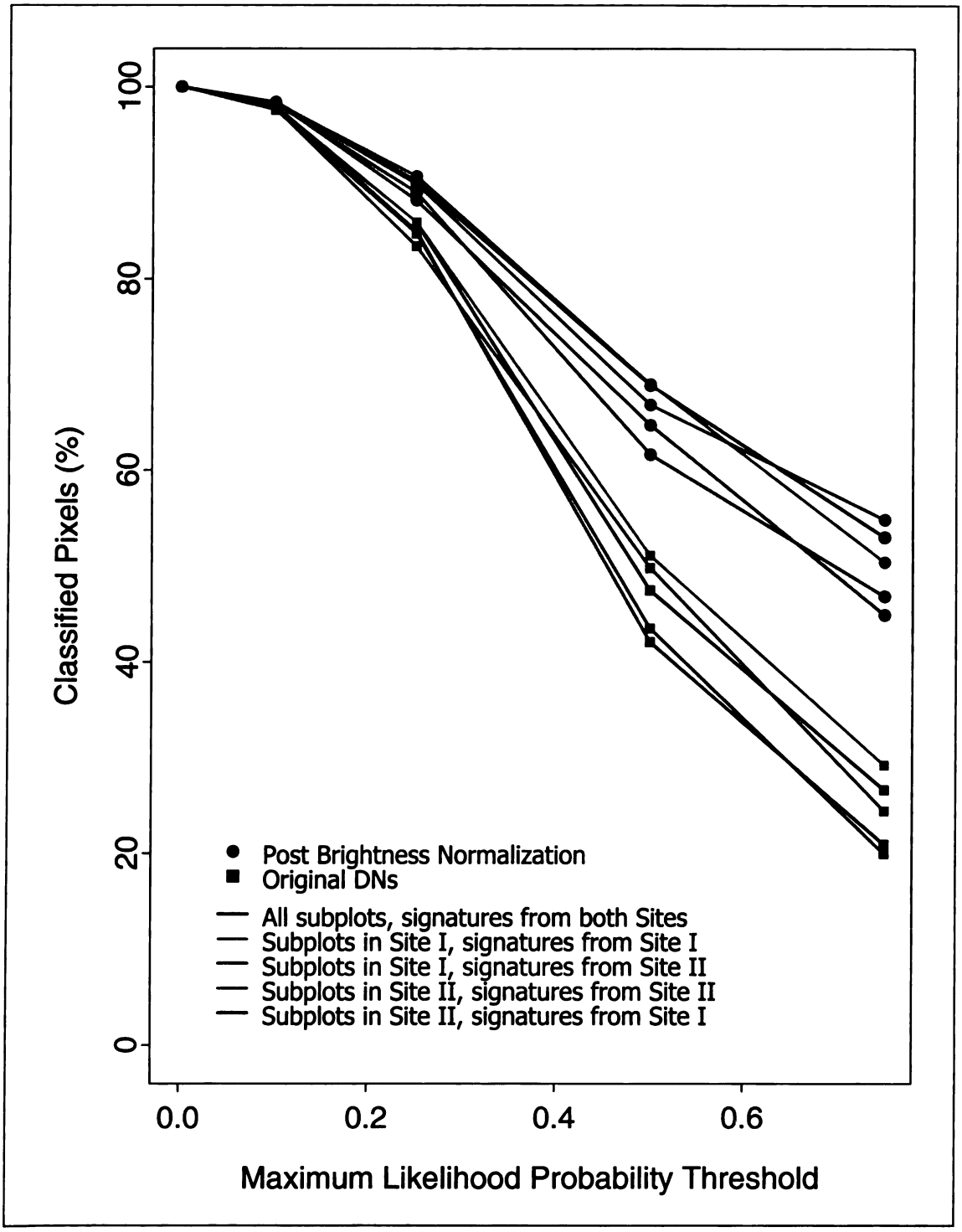


**Figure 3.9.** Percentage of classified pixels for various probability thresholds imposed on cross-validation-based maximum likelihood classification scenarios of cover types prior to and after imagery brightness normalization. Development of classification signatures was based on pixels identified as tree crown apexes via slope break-based imagery LMF processing. Lines serve visualization purposes only.

# CHAPTER 4

## AN INVESTIGATION OF THE UTILITY OF SECOND ORDER TEXTURE FEATURES FOR FOREST COVER TYPE CLASSIFICATION USING HIGH-SPATIAL-RESOLUTION AIRBORNE DIGITAL IMAGERY

## Abstract

*Image texture seldom has been used in forestry optical remote sensing applications, in part because of the complexity associated with its quantification and in part due to the absence of examples that substantiate its usefulness. In this chapter, a procedure based on image intensity co-occurrence is presented that provides with a quantitative evaluation of second order image texture features that carry discriminatory potential for forest cover type classification purposes. Procedure development and evaluation is based on two independent data sets and five common forest cover types present in the Midwest region. Analysis results indicate that classification accuracies exceeding 60% can be achieved by using only image texture information. In its current level of development, procedure applicability may be limited because of substantial computational cost, absence of computer software that could facilitate its automation, and the complexity of methodologies integral to feature selection process.*

## 4.1. Introduction

One of the better-known weaknesses of traditional remote sensing image classifications approaches, including those discussed in Chapters 2 and 3, is their sole reliance on the spectral response pattern at individual pixel locations (Chen, 1999). Many other types of information could become available for classification purposes if the methods for extracting that information from the imagery were not so fragmented and poorly developed (Franklin et al., 2000). One of the promising alternatives to pixel-based classification has been to consider classification of image data in a spatial context (Khazenie and Crawford, 1990). The latter translates into either using information on the

spatial variation of imagery tones independently or incorporating such information into an existing, spectrally-based classification process. The premise in the second case is that a pixel's assignment to a class when viewed in isolation may change when viewed in some context (Haralick and Joo, 1986). Imagery derivatives that contain such contextual information and describe spatial relationships between image entities are usually known as textural features. Spectral and textural features are interdependent because, as pointed out by Haralick et al. (1973), "... texture and tone have an inextricable relationship to one another ...".

An operational definition of image texture is challenging. It is generally regarded as a quantification of the spatial variation in image tone values. A more precise definition is complicated by the perceptual character of texture (Hay et al., 1996). Although investigations in the field of machine vision have revealed that the use of texture originates in the powerful, innate ability of humans to recognize textural differences, the complex neural and psychological processes by which this is accomplished have, so far, evaded detailed scientific explanation (Shapiro and Stockman, 2001).

Tone and texture are always present in an image, although one property can dominate the other at times, depending on the smoothness or roughness of the objects present, and on the image resolution relative to the surface roughness of each objects. If tonal variation inside a limited spatial extent is relative small, spectral information will dominate. Conversely, if tonal variation is large and presents meaningful structures, then texture will be dominant (Haralick et al., 1973). In H-resolution imagery (Strahler et al., 1986) depicting forested landscapes, the presence of pixels with smaller size than the image footprint of a single tree crown, together with the complex horizontal and vertical

structure of stand canopies, usually generate substantial tonal variability. In such cases, the analysis of texture might be well suited to detecting and quantifying canopy structure and cover-type variation across the landscape. One activity that routinely utilizes texture information is the interpretation of aerial photographs, which allows experienced operators to identify changes in the spatial distribution of forest vegetation (Hay and Niemann, 1994). With the increased availability of H-resolution digital imagery from airborne (Anger, 1999) and satellite platforms (Barnsley, 1999), it is expected that *digital* texture will become an important information source for many other forestry purposes (Green, 2000).

Insight into how texture might be analyzed digitally has focused on the structural and statistical properties of textures (Haralick, 1986). Those (outlined briefly in the next section) include first-order imagery statistics (e.g., standard deviation and variance), second-order statistics, frequency domain of Fourier power spectrum, spatial autocorrelation function (e.g., semivariance), and structural image features. In addition to their value for classification applications (Lark, 1996; Ryherd and Woodcock, 1997), structural and statistical texture properties of digital imagery have been used in forestry as stand-pattern predictors (Coops and Culvenor, 2000), and for the qualitative assessment of forest stand structure, age, density, and leaf area index (Cohen and Spies, 1992; Wulder et al., 1996, St-Onge and Cavayas, 1997; Franklin et al., 2001). A common characteristic among the aforementioned texture-based forestry applications is that they were developed using features defined *a-priori*. Because (as demonstrated below) most texture measures include a substantial number of associated features, those best suited for a particular investigation objective need to be identified using a systematic approach.

Unless there exists theoretical proof or experimental evidence that a particular feature, or set of features, is optimal for a particular application, limiting one's analysis to a selection of features found to perform well in other applications, or for that matter to those supported by a particular software package, will only fortuitously augment the chances for exploiting the full potential texture has to offer for that application (Conners and Harlow, 1980).

The objective of this chapter is to evaluate the utility of second-order texture features derived from spatial co-occurrence matrices for forest cover type classification of digital, high resolution imagery. More than 20 features were evaluated using established feature selection strategies. Feature selection and classification accuracy assessment was based on field observations within five forest cover types common in the Midwest region.

## 4.2. Digital imagery texture measures

The main texture recognition measures can be categorized into four groups. The first approach defines texture features that are derived from the Fourier power spectrum of the image via frequency domain filtering. Because different textures demonstrate different frequency patterns, it is reasonable to postulate that texture features are related to the distribution of spatial frequency components. The second approach is based on statistics that measure local properties that are thought to be related to texture, such as the mean or standard deviation of pixels values within a neighborhood. The third, and by far the most common, approach used in forest remote sensing applications, is the use of the joint gray level probability density (Haralick et al., 1973). The final approach is based on modeling the image using assumptions (e.g. that the image being processed possesses

fractal properties (Mandelbrot, 1982; Agterberg and Cheng, 1999)) or can be modeled using multiplicative, autoregressive random fields (Frankot and Chellapa, 1987).

### 4.2.1. Co-occurrence-based texture measures

The widely used co-occurrence methods attempt to characterize the second-order properties of an image. Co-occurrence can be regarded as the relative frequency, or joint probability, of image properties, occurring under predefined constraints. Pixel intensities, usually expressed in Digital Numbers (DNs), intensity variance, or intensity gradient are the image properties commonly used. These can be measured under such constraints as pixel spacing, both in magnitude and orientation, or other higher-order neighborhood definitions, for example windowing. Co-occurrence is typically represented in the form of a matrix. Gray Level Co-occurrence Matrices (GLCM) (Haralick, 1973) represent the probability of co-occurrence of image pixels intensities $i$ and $j$, under the spatial constraint of $d$ pixels separation between the pixels. Other forms of co-occurrence measures included the Gray Level Run Length Matrix (Galloway, 1975), the Statistical Feature Matrix (Wu and Chen, 1992), the Neighboring Gray Level Dependence Matrix (Sun and Wee, 1983), and the Generalized Co-occurrence Matrix (Davis et al., 1979).

The GLCM of an $N_g$ gray-level (i.e., single band) image on a domain $\boldsymbol{D} \subset Z^2$ models the image as a 2D function $I : \boldsymbol{D} \rightarrow \boldsymbol{G}$, where $\boldsymbol{G}=\{1, \ldots, N_g\}$. The GLCM element $P(i,j \mid d,\theta)$ is an estimate of the second-order joint probability density function of gray-level pairs within the image. Each matrix element is an estimate of the probability that two image pixels, separated by a displacement vector of magnitude $d$ and orientation angle $\theta$, have intensities $i$ and $j$, where $i$ and $j \in \boldsymbol{G}$ and

$$P(i,j \mid d,\theta) = \frac{\#\{k,l \in \boldsymbol{D} \mid I(k) = i, \quad I(l) = j, \quad \| k-l \|, \quad \angle(k-l) = \theta\}}{\#\{m,n \in \boldsymbol{D} \mid \quad \| m-n \| = d, \quad \angle(m-n) = \theta\}} \tag{4.1}$$

where # is read as 'number of (pixels)', $\angle$ is read as 'angle between two pixel centers', $\| \ \|$ denotes displacement vector magnitude or Euclidean distance between two pixel centers, and $k$, $l$, $m$, and $n$ are valid image pixel locations. Because of the discrete nature of digital image intensities, $P$ is, in fact, a discrete density rather than a continuous one. Therefore, for any given $d$ and $\theta$,

$$\sum_{i,j} P(i,j) \mid d,\theta) = 1 \tag{4.2}$$

and

$$\forall i,j \in \boldsymbol{G}, \quad 0 \le P(i,j \mid d,\theta) \le 1 \tag{4.3}$$

As an example, Figure 4.1a shows a gray-scale (or level) image with a range of intensities from 1 to 4 and, for simplicity, the pixel-pair counts (the numerator of equation (4.1)), rather than probability estimates. The upper left entry in the GLCM computed for $d$=1 and $\theta$=0° (Figure 4.1d), has a value of 2, which represents the number of times a pixel with intensity equal to 1 has an immediate neighbor to the right with intensity also equal to 1. Note that angular displacements are measured in a Cartesian, not geographic, coordinate system and that the distance measures are usually expressed in pixel increments in image row and column indices rather than true geometric quantities. In the later case and for adjacent pixels with angular displacement of 45° or 135°, $d$=1 is used although the true distance separating them is actually $\sqrt{2}$. This often necessitates proper scaling of the true distance between pixels to integer values, particularly when the length of the displacement vector is determined by spatial investigations (e.g., variogram

analysis). A comparison of Figures 4.1e and 4.1g shows that different $\theta$'s can produce markedly different GLCMs. Note also that GLCMs can be computed for multiple angles or ranges of angles (Figure 4.1h, 4.1i) and that simultaneous consideration of opposite angles ($\theta$ and $\theta+\pi$) does not, in general, produce the same matrix, i.e. $P(i,j \mid d,\theta) \neq P(j,i \mid d,\theta)$. In the latter case, isometric matrices (Figure 4.1i) are often formed by averaging the matrices calculated for opposite angles.

In addition to pixel displacement parameters $d$ and $\theta$, co-occurrence texture analysis procedures require the user to specify the level of requantization the original imagery has to undergo (3-bit, 4-bit, other), and, in the presence of multispectral imagery, the band(s) whose texture is to be evaluated. Most contemporary sensors offer 8-bit or higher radiometric (data) resolution, which is prohibitively fine for GLCM computations. Indeed, if an original imagery resolution of 8-bit ($N_g=2^8=256$) were to be used, the resulting GLCMs would contain $N_g^2$ (=65,536) elements. A radiometric resolution of 16-bit would necessitate a matrix with approximately $4.3*10^9$ elements. In addition to considerations related to computation load, such large matrix dimensionalities would seriously compromise the ability to derive meaningful and class-discriminatory texture features due to the large number of empty, or zero-value, matrix elements present (Conners and Harlow, 1980). Image requantization to a lower data resolution, sometimes known as image (radiometric) compression, can be performed either linearly or by using histogram equalization (Conners and Harlow, 1978). Other available techniques are less attractive because they require user intervention.

### 4.2.2. Gray Level Co-occurrence Matrix features

Information is extracted from GLCMs via secondary feature functions. Approximately 20 such features appear in the literature (Table 4.1) (Haralick et al., 1973; Conners et al., 1984). These can be grouped into four main types: 1) measures of an image's statistical properties; 2) measures of an image's visual characteristics; 3) measures based on information theory; and 4) measures of information based on correlation. Many of these secondary features are derived by weighting each of the co-occurrence matrix element values, and then summing these weighted values to form the feature value. The weighting applied to each element is based on a feature weighting function, so by varying this function, different texture information can be extracted from the matrix. Table 4.1 lists the weighting functions as coefficients of matrix element values $P(i,j)$ in the equations used to compute matrix features. Matrix element weighting functions fall into two main categories: 1) Weighting based on the element's value, and 2) weighting based on the spatial position of the element. A graphical representation of feature-specific weighting functions is provided in Figure 4.2.

Because matrix features are secondary image derivatives, their interpretation is occasionally somewhat less than intuitive. The value of feature inertia, often referred to as contrast, for example, increases with the frequency of adjacent bright and dark pixels and decreases when image intensity is strongly autocorrelated. Weighting is reversed in the Inverse Distance Moment feature weighting scheme which produces higher values for images that contain gradual DN changes. Feature energy, sometimes known as angular second moment, will be larger n non-zero matrix elements are concentrated in one or a few portions of the GLCM with a relatively large proportion of the total matrix being

either zero or near zero. The presence of patches of uniform intensity in the image would, therefore, produce larger energy values while images with a 'salt and pepper' appearance yield low energy values. These latter images, however, would be rich in entropy. It should be noted that texture feature values are strongly dependent on the relationship between pixel and object sizes. An image depicting a corn field just prior to harvesting, for example, would likely be of high entropy if acquired with 0.3m resolution, but of low entropy if acquired with 1.0m spatial resolution.

### 4.2.3. Image classification using GLCM features

It is evident from the discussion above that imagery classification using co-occurrence-based approaches tends to generate large amounts of intermediate texture information products. The analyst can often be confronted with as many as 50 pixel displacement vectors ($d$, $\theta$) used in GLCM construction, 5 or more spectral bands, 6 or more image band requantization and compression procedures, and more than 20 possible features extracted from each co-occurrence matrix. Exploring all these analysis choices would produce more than 10,000 variables, which would, most likely, overwhelm even the most sophisticated classifier. In addition, such an expansive set of choices would require a very large and expensive data set for classifier training. The term 'classifier' here is used to denote a rule, or set of rules, which assigns (or allocates) each unknown pixles to one and only one by using information from one or more attributes (features).

Visual analysis of texture displays has been used to understand the way in which class texture represents differences in the imagery (Franklin and Peddle, 1990) and thus to reduce the number of processed texture variables. Obviously, this approach is of limited utility in the presence of a large number of texture displays. The number of

GLCMs assumed to be capable of producing texture features useful for class discrimination can potentially be reduced via 1) investigations based on information theory; adoption of multi- rather than single-angular pixel displacement vectors (Sun and Wee, 1983), or 3) feature selection statistics to identify the optimal texture features for a particular classification application.

GLCM ranking in terms of information content can be used to select the displacement vector that has the potential of maximizing the discriminatory power of the derived texture features (i.e. texture features with similar values for objects of the same class membership, but with different values for objects of alternate classes). In that regard, each co-occurrence matrix can be treated as a contingency table formulated by two variables A and B, containing $a$ and $b$ classes respectively. If variables A and B are interpreted as pixel intensities at either end of the displacement vector ($d$, $\theta$), and the classes into which they fall as the $N_g$ gray levels, then the correspondence between a GLCM and a contingency table becomes clear. Texture information conveyed by co-occurrence matrices, is related to the strength of the statement that can be made about intensity level $i$ given observations about intensity level $j$ (and vice versa). If image texture is highly structured and the co-occurrence matrix is capable of capturing that structure, then observations $i$ should bias the probability of observing various $j$ intensity levels. If, on the other hand, structure is not captured, then observations about $i$ will not influence the probabilities of $j$, and $i$ and $j$ should be considered independent. Hence, the amount of image structure, or texture, conveyed by a co-occurrence matrix depends on the choice of $i$ and $j$, and therefore is a function of ($d$, $\theta$).

A quantitative measure of this structure can be obtained by hypothesizing that the variables $i$ and $j$ in a co-occurrence matrix are independent, and then using a chi-square goodness-of-fit test to determine the degree to which this hypothesis can be rejected by the image pixel intensities. In the presence of texture in an image, the statistic

$$\chi^2 = \sum_{i}^{N_g}\sum_{j}^{N_g} \frac{(x_{i,j} - r_i c_j / N)^2}{r_i c_j / N} \tag{4.4}$$

calculated for each GLCM computed from that image would follow a chi-square distribution with $(N_g\text{-}1)^2$ degrees of freedom, provided that the sum of matrix element values $N$ is sufficiently large (Zucker and Terzopoulos, 1980). In equation (4.4), $x$ represents the pre-normalized (numerator of equation (4.1)) matrix element values and $r$ and $c$ represent matrix row and column sums, respectively.

In images of forested landscapes, it is possible, although rare, that one or more gray levels is absent, especially for images with a small number of pixels, resulting in matrices with one or more columns and rows composed exclusively of zero-value elements. For such images, an adjustment of degrees of freedom for the $\chi^2$ statistic is necessary, so that p-values associated with the image intensity independence test mentioned above can be compared. Details on how such adjustment may be performed are provided by Zucker and Terzopoulos (1980). More often, different displacement vectors would result in a varying number of zero-value matrix elements. In the examples of Figure 4.1d-g, although no zero-valued columns or rows exist, 8 or 9 elements do have a zero value. In such circumstances, the influence of these elements on the ability to identify structure via co-occurrence computations can be accounted for by a $\chi^2$-statistic

normalization known as Cramer's V coefficient (Cramer, 1946). An illustration is provided in Figure 4.3a, which depicts a 100x100, 4-bit image with a regular (geometric) texture, exhibiting a repeated 10x10 pixel pattern, sometimes known as a 'texton'. For this image, 20 GLCMs were computed using incremental pixel displacement distances and, for simplicity, $0^{o}$ angular displacement. Cramer's V coefficients computed for these 20 matrices have an absolute maximum at $d = 10$ and local maxima at $d = \{5, 15, 20\}$ (Figure 4.3b), which indicates that the matrix information content quantified via the statistic in equation (4.4) is capable of detecting texton sizes and therefore can be useful in identifying the proper pixel displacement vector for co-occurrence-based investigations of texture.

Even when there is confidence that the proper displacement vector was used in co-occurrence matrix construction, the large number of features than can be extracted from the matrix for use in the classification process can compromise the classification accuracy achieved, were all features to be used by the classifier, unless a very large data set is available for classifier training (Silverman, 1986). This is known as the Hughes phenomenon (Hughes, 1968; Shahshahani and Landgrebe, 1994) or sometimes also referred to as the 'curse of [feature] dimensionality' (Bellman, 1961). The Hughes phenomenon can be shown by a simple example: Let $\mathbf{X}$ denote a two-dimensional, normally distributed vector and let the two-dimensional measurement vector $\mathbf{x}$, where $\mathbf{x} = [\underline{x}_1, \underline{x}_2]$ represent 100 realizations of random variable $\mathbf{X}$. The histogram of the first variate $\underline{x}_1 = [x_{1,1}, \ldots, x_{1,100}]^{\mathbf{T}}$, representing the extraction of one feature, is shown in Figure 4.4a. Note that the expected frequency for each of the 10 histogram bins is on the average 10 (=100/10), and that the histogram shape is an adequate approximation of the true

underlying distribution from which the realizations were extracted. The second variate $\underline{x}_2 = [x_{2,1}, \ldots, x_{2,100}]^T$, represents the extraction of a second feature. It is now necessary to estimate the new two-dimensional histogram containing 100 bins, with only the original number of (now 2-D) data points. The second histogram, shown in Figure 4.4b, contains many empty bins and all other bins have very low counts. On average, there is only 100/100 = 1 measure per bin. Therefore, the more features extracted, the more inaccurate the estimate of the underlying multivariate distribution becomes.

For classification purposes, where an unknown texture is to be allocated to one of several classes, it is important to accurately estimate the underlying class-conditioned feature distributions. While it would be desirable to extract only a minimal number of 'useful' secondary features (i.e. those whose class-conditional distributions exhibit statistical differences between classes), it is usually not known *a priori* which features will be useful. It is common practice to use all of the secondary features and subsequently reduce the resulting high-dimensional feature space using discriminant analysis and feature selection techniques. Such practice allows a more accurate estimation of the true distribution of features for each class based on the limited training data available. Reducing feature set dimensionality usually involves removing those features that provide little or no extra information to distinguish between texture classes either because they are correlated to other features or because their discriminatory power is very low. However, an increase in the number of features that need to be evaluated as candidates to participate in a classifier, results in an exponential increase in the number of possible feature combinations to be evaluated in the process. In the presence of 20 features, the number of possible combinations exceeds 1 million! Even if the optimal feature subset

dimensionality for classifier development is known *a priori*, say 4, there would still be 4,845 [= 20!/((20!-4!)4!] feature combinations to be evaluated.

While the performance of a classifier is best evaluated by computing its classification error rates (McLahlan, 1976; Habbema and Hermans, 1977), computational considerations necessitate alternative strategies. One such alternative is to use class-separability measures to estimate classification error rates. These measures attempt to assign a figure-of-merit to a feature, based on how 'dissimilar' the class-conditioned distributions of the feature are. One measure of dissimilarity is the amount of overlap between the class-conditioned distributions, with less overlap meaning more dissimilarity. Other measures quantify the separation between the distributions, normalized by the variance of each distribution. The second category of measures operate on the assumption that the greater the distance between class-conditional density functions, the less is the overlap among the density functions in feature space, and the smaller the probability of classification error becomes. Many probabilistic distance measures have been defined in the literature including the Mahalanobis (1936), Bhattasharyya (1943), Chernoff (1952), and Matusita (1956). Their use allows searching for an optimal subset of features from a pool of possible candidate features that are believed to maximize the discriminatory power of the feature set. Various strategies have been suggested for restricting the search to a smaller number of 'good' feature subsets. The three most popular are 'forward selection', 'backward elimination', and 'stepwise selection'. Details on their structure and implementation can be found in Kittler (1986). Although these procedures reduce the computation load significantly and provide viable feature selection schemes, they may not identify the globally optimum subset that would

be 'uncovered' by an 'all-subsets' search. Detection of the global optimum subset is guaranteed, albeit computationally costly to implement, by a procedure known as the branch-and-bound algorithm (Yu and Yuan, 1993).

The identification of the optimal feature subset is followed by the development of the classifier, which is used to assign previously unseen objects or observations to a class using the selected features. Most classifiers, including the popular linear and quadratic discriminant functions, are parametric mathematical rules with Bayesian structure. As such, they assume that the class-conditioned feature data are multi-variate normal. Quadratic discriminant functions are more sensitive than linear functions to departures from multi-variate Gaussian distributions in high-dimensional feature spaces (Lachenbruch, 1975; Seber, 1984). However, it is known that quadratic discriminant functions are robust against minor departures from normality (McLachlan, 1992). Also, because they are capable of exploring inequalities in the class-conditioned covariance matrices (linear functions assume equal covariance matrices among classes), they can improve the definition of decision boundaries compared to linear discriminant functions, thus leading to the possibility of lower classification error. Figure 4.5 presents an illustration of decision boundaries obtained by linear and quadratic discriminant functions fit in a two-class data set using two features.

## 4.3. Methods

### 4.3.1. Study Site Characteristics and Imagery Description

The study area comprises two sites, the one in the south-central part of Grand Traverse County (Site I) and the other in the northern part of Wexford County (Site II), Michigan (Figure 2.1). Note that figures in this dissertation often contain color. The sites

are separated by about 10km in the northwest-southeast direction and extend over 8,805 and 12,626 hectares of land, respectively. More than half (56%) of the study area is owned and managed by the Michigan Department of Natural Resource. Most of the study area consists of forests and wetlands (82%), while agricultural use, mainly row crops, represents 8%. Other land use classes include orchards (4%) and residential areas (4%). Residential development is concentrated in the northwestern part of site I. Geomorphic features include moraines and outwash. The average slope, calculated by using the finite differences algorithm on a 10m, 1:24,000 USGS Digital Elevation Model available for the area is 3.5% and 2.7% for sites I and II respectively. Relief is more prominent along the Manistee River, which crosses site II from northeast to southwest.

The study area is characterized by pronounced spatial heterogeneity of forest cover types. The majority of the forest cover types extant in the northern Lower Peninsula of Michigan are present in the forested part of the study sites. These include: 1. Aspen, consisting of Big Tooth (*Populus grandidentata*) and Quaking (*Populus tremuloides*) aspen; 2. Northern hardwoods, consisting primarily of Sugar Maple (*Acer saccharum*), Red Maple (*Acer rubrum*), American Beech (*Fagus americana*), Black Cherry (*Prunus serotina*), Basswood (*Tilia americana*) and White Ash (*Fraxinus americana*); 3. Oak, consisting of White (*Quercus alba*) and Red (*Quercus rubra*) oak; 4. Natural Pine, mainly White Pine (*Pinus strobus*); 5. Pine plantations consisting primarily of Red Pine (*Pinus resinosa*); and 6. Cedar swamps dominated by Northern White Cedar (*Thuja occidentalis*). The main forest management objectives of the MDNR include timber production, enhancement of wildlife habitat, recreation, preservation of aspen, and

riparian best management practices. Several private land owners offer a network of tracts used seasonally for horseback riding and snowmobiling.

The imagery data set used in this study was acquired on August 11, 1999, using the Digital Airborne Imaging System (DAIS [Space Imaging, 1999]). It contains four bands, three in the visible and one near infrared that were acquired by frame (digital array) cameras equipped with appropriate band-specific filters in a 2x2 arrangement. Appendix 1 contains detailed information on the technical specifications of the system (Table A.1), flight line orientation, and the spatial arrangement of frames in each study site (Figure A.1).

### 4.3.2. Field Measurements

Two sets of field measurements were obtained. In the first set a total of 34 plots, 16 in site I and 18 in site II, were installed in the study area stratified across the major forest cover types present with the exception of cedar swamps that were excluded due to accessibility issues. Plots were allocated on level land, within homogeneous stands, and away from cover type ecotone zones. Stand homogeneity was evaluated with field inspections. A minimum 60% canopy closure threshold was imposed by the MDNR as a selection criterion. All plots were situated within the inner quarter area of the associated image frame, resulting in plot-center view angles less than $10^{o}$. Field measurements were obtained in the summer of 2,000, exactly a year after the acquisition of imagery, following the FIA/FHM field protocols (Appendix 1, Figure A.2). Subsequent to their allocation, plot and subplot centers and subplot boundaries were precisely georefenced to image coordinate systems using field survey techniques. All spatial data were organized

as geographic information system (GIS) layers translated into the image coordinate system. Details on the methodologies employed are available in Chapter 2.

The second set of field observations was independent of the first and contained cover type and canopy closure data obtained by visual inspections for a total of 112 point-locations (60 in site I and 52 in site II), with no more than one location in a given forest stand, and no locations in stands with a plot from set one. Twenty two locations were in Aspen, 26 in Northern Hardwoods, 19 in Oak, 24 in Red Pine Plantations, and 21 in Natural Pine. As in the first set, all point locations were situated away from cover type ecotone zones and in homogeneous stands with canopy closure exceeding 60%. Locations were georeferenced using differential Global Positioning System technology. Their geographic coordinates were translated to image coordinates via manual image frame georeferencing using leaf-on and leaf-off, 1:12,000 scale Digital Ortho Quadrangles (DOQs) available for the study area (Michigan Department of Natural Resources, 2001) and nearest neighbor pixel interpolation.

### 4.3.3. Image Pre-processing

Image frame regions composed of pixels whose center was within a subplot's boundary were extracted from the frame and compressed to 4-bit data resolution using equation (4.5),

$$\forall(x,y), \qquad I'(x,y) = floor\{\frac{DN(x,y) - DN_{\min}}{DN_{\max} - DN_{\min}} 15.999\} + 1 \tag{4.5}$$

where the coordinate pair (x, y) is a valid image region pixel, $I'(x, y)$ is the requantised (or compressed) value of the DN of the pixel at (x,y), and the function floor() reduces a real-valued quantity to the largest integer lower than the function's argument. The

addition of 1 results in a requantised intensity range of $I'(x, y) \in \{1,...,16\}$ and allows intensity level '0' to indicate background pixels not to be processed. Linear requantisation was also used to compress circular, 30-pixel-diameter image regions centered on each of the 112 locations mentioned. Note that during image requantisation, any brightness discrepancies among frames or frame regions known to affect spectrally-based image analyses (Chapters 2 and 3) are eliminated, provided that any brightness variability originates from linear changes in sensor sensitivity or gain during image acquisition. Comparison of requantized imagery region histograms prior to and after correcting for brightness variations among frames revealed no differences.

A popular alternative to linear quantization, known as histogram equalization, was not considered here, because it produces a flat histogram. Maintaining histogram shape (guaranteed when using linear requantization), is important, because it ensures that the second-order probability statistics that are used subsequently in this study, and which are constrained by first-order probabilities, are not modified.

### 4.3.4. Band selection, co-occurrence matrix development, and texture feature selection

The large number of possible combinations of pixel displacement vectors than can be used in the construction of co-occurrence matrices and of the features that can subsequently be computed from these matrices, increases further in the presence of multispectal imagery. This necessitates an early evaluation of the potential each of the three factors (number of bands, texture features, and displacement vectors) possesses in supporting cover type classification endeavors. In this research, such an evaluation was performed using imagery texture information at the 112 locations with known forest

cover type. The same information was subsequently used for training a classifier operating on the derived texture features. The accuracy of the resulting classification procedure was estimated using information from the 134 subplots installed in the study area.

Early investigations, including visual and quantitative (Cramer's V) texture evaluations, revealed that the spectral collinearity known to exist among bands in the visible portion of the spectrum is also evident in the GLCMs computed from them. Paired T-tests of texture feature values obtained from matrices generated using various displacement vectors showed no significant differences among visible bands. Texture feature value differences between the visible bands and the NIR band were significant at $\alpha$=0.05 for approximately 1/3$^{rd}$ of the features tested. On this basis two of the visible bands (blue and red) were eliminated from further consideration.

Based on findings from experimentation with various single-direction displacement vectors, it was decided to proceed with multiple direction vectors of the form ($d$, $\{135+\pi, 0, 45, 90\}$) shown in Figure 4.1h. Although there are obvious differences in the structure of GLCMs computed using the same $d$, but different $\theta$ for small images or frame portions (Figure 4.1), these differences practically disappear in images depicting forested landscapes containing more than 300-350 pixels and they were found to persist among different $d$'s. Matrix information content was evaluated by computing corresponding Cramer's V coefficients for all $\theta \in [1,10]$. Texture feature evaluation was restricted to matrices that maximized information content.

A series of Hawkins (1981) tests performed using various combinations of texture features derived from the matrices that exhibited the highest information content showed

that, in general, the distribution function for each of these combinations could be considered multivariate normal. As a result, no feature value transformations towards normality were attempted. The optimal feature subset for cover type classification based on imagery co-occurrence derivatives was identified using the branch-and-bound algorithm by Yu and Yuan (1993). The algorithm was implemented using the Bhattacharyya metric to quantify distance between class-conditional densities. This metric was selected because of its ability to provide robust estimates when the feature distribution is Gaussian, or near-Gaussian, form. The metric is of non-parametric form and is computed as (Bhattacharyya, 1943)

$$D_B = -\log \int \sqrt{p(\mathbf{x} \mid \omega_1)...(p(\mathbf{x} \mid \omega_c)}d\mathbf{x} \tag{4.6}$$

where $\mathbf{x} = [\mathbf{x}_1, \ldots, \mathbf{x}_{N\upsilon}]$ represents a set of $N_\upsilon$ candidate feature vectors, $p(\mathbf{x}|\omega_i)$ is the class-conditional probability density of $\mathbf{x}$ for class $\omega_i$, and $c$ is the number of classes present. When the class-conditional distributions of the features are known and of Gaussian form, equation (6) can be expressed for two classes as

$$D_B = \frac{1}{4}(\boldsymbol{\mu}_1 - \boldsymbol{\mu}_2)^{\mathrm{T}}[\boldsymbol{\Sigma}_1 + \boldsymbol{\Sigma}_2]^{-1}(\boldsymbol{\mu}_1 - \boldsymbol{\mu}_2) + \frac{1}{2}\log\left[\frac{|\frac{1}{2}(\boldsymbol{\Sigma}_1 + \boldsymbol{\Sigma}_2)|}{\sqrt{|\boldsymbol{\Sigma}_1||\boldsymbol{\Sigma}_2|}}\right] \tag{4.7}$$

where $\mu_i$ and $\Sigma_i$ are the mean vector and covariance matrix of $\mathbf{x}$ for class $i$, and $|\Sigma|$ represents the determinant of $\Sigma$. In the presence of more than two classes (5 in this research), the metric value is estimated as the average of all pair-wise combinations. Following identification of the optimal feature space, the classification rule based on a quadratic discriminant function was developed. The decision boundaries imposed onto the feature space generated 5 multidimentional regions. Using the texture feature set

identified in the previous step, each of the 134 subplots was then assigned to the cover type class $k$ that maximized the quantity

$$-\frac{1}{2}\mathbf{x}^{\mathrm{T}}(\boldsymbol{\Sigma}_k^{-1}-\boldsymbol{\Sigma}_l^{-1})\mathbf{x}+(\boldsymbol{\mu}_k^{\mathrm{T}}\boldsymbol{\Sigma}_k^{-1}-\boldsymbol{\mu}_l^{\mathrm{T}}\boldsymbol{\Sigma}_l^{-1})\mathbf{x}-V \tag{4.8}$$

where

$$V=\frac{1}{2}\ln\left(\frac{|\Sigma_k|}{|\Sigma_l|}\right)+\frac{1}{2}(\boldsymbol{\mu}_k^{\mathrm{T}}\boldsymbol{\Sigma}_k^{-1}\boldsymbol{\mu}_k-\boldsymbol{\mu}_l^{\mathrm{T}}\boldsymbol{\Sigma}_l^{-1}\boldsymbol{\mu}_l) \tag{4.9}$$

and $l$ denotes any of the remaining $c$-1 classes. Note that equation (8) assumed that misclassification cost and prior probabilities were equal among classes. Classification accuracy estimates were derived from confusion matrices and associated indicators (percent of subplots correctly classified and kappa coefficients) (Congalton, 1991). Image compression, GLCM computations, feature extraction and optimal subset identification, and classifier training and testing were all implemented using scripts developed in C programming language, interfaced with Splus (Mathsoft, 2000) and Matlab (MathWorks, 1999) software in a Unix operating system.

## 4.4. Results and Discussion

As demonstrated already in Figure 4.3, co-occurrence matrices are capable of identifying the size of textons or patterns in digital images characterized by a regular texton arrangement. Assuming that the crowns of dominant and co-dominant trees in forested landscapes could be perceived as scene textons, it could be expected that co-occurrence matrices would capture scene texture characteristics and yield higher information content estimates when computed for pixel displacement vectors approximating in magnitude the size of tree crowns present. Contrary to expectations

though, analysis results indicated that, in imagery covering forested land, as the magnitude of pixel displacement distance increases, the information content of the resulting GLCMs, as quantified by Cramer's V statistic, decreases sharply for $d > 1$ (Figure 4.6), and fluctuates very little thereafter, even in stands where tree arrangement is regular (e.g. red pine plantations). Matrix elements with higher values were generally concentrated along the main matrix diagonal for $d = 1$, but formed a roughly circular cluster for larger distances. Figure 4.6 shows that $d = 1$ produces GLCMs with four times the information content of those produced with $d > 1$.

This somewhat unexpected finding prompted an investigation that involved construction of artificial surfaces in which either 1) a texton of set size was repeated randomly at varying spacing or 2) a texton of variable size was repeated at a set distance. Both cases produced GLCMs with information content patterns similar to those in Figure 4.6. As a result, it was concluded that the absence of strict regularity in tree-crown arrangement in forest stands causes a reduction in the ability of GLCMs produced using $d \geq 2$ to capture textural differences pertinent to stand structure conditions and cover type affiliation. Note that this result should not be perceived as contradicting earlier research findings (e.g., Franklin et al., 2000) which concluded that quantified imagery reflectance autocorrelation is useful in texture-based investigations. Those studies focused on the mean value and variance of image intensity which are first-order imagery properties while co-occurrence features explored here are second-order image properties.

The ability of multispectral, optical imagery to contribute in co-occurrence-based forest cover type classification endeavors can be seriously affected by the analysts' choices in the imagery requantisation process. When linear compression is employed

during imagery pre-processing, the presence of exposed soil in canopy openings or other spectrally bright targets within the forest stand, and the skewed-to-the-right intensity histograms they produce for the visible bands, confine vegetation related pixel intensity values $i$ and $j$ along the upper left $1/16^{th}$ ($i, j \leq 4$) of co-occurrence matrices computed for those stands. Under such circumstances, there is practically no variability in the structure of the matrices and texture features derived regardless of the cover type. Masking of non-vegetative scene components via Normalized Difference Vegetation Index (NDVI) or other band ratioing techniques prior to linear compression should be considered a necessary step in stands with medium or low canopy closure conditions or where presence of illuminated non-vegetation objects is suspected. Because the symmetry of NIR band intensity histogram is affected very little by reflectance regimes in and around canopy openings, co-occurrence matrices computed for that band are free from systematic bias in the distribution of intensity values present in them, thus rendering band pre-processing with NDVI filters redundant.

By observing the typical GLCMs computed for each cover type using pixel displacement distance $d = 1$ and multidirectional angular displacement (Figure 4.7), it appears that co-occurrence matrices can indeed be useful cover type discriminators, at least for the five types investigated. Visual matrix structure comparisons indicated that there might be some confusion between oak and red pine plantations, although the former exhibited a stronger intensity value concentration along the matrix diagonal. Northern hardwoods and natural pine stands showed higher probabilities for certain combinations of high (>12) intensity values, but for the latter cover type the percentage of darker tones was higher. This is probably due to the more extensive shadowing between adjacent

crowns. Aspen showed a concentration of matrix element values around mean intensity levels, characteristic of smooth canopies. However, the assessment of matrix structure separability among cover types must be substantiated in a quantitative form, such as the one offered by matrix-extracted feature values.

The brand-and-bound algorithm identified 4 features (energy, entropy, inertia, and homogeneity), all pertaining to the NIR band, as comprising the feature subset that provided the highest discrimination of cover type. When forced to identify only two features, the algorithm selected energy and inertia. When it was set to identify the three best features, it selected energy, inertia, and entropy. However, both of those smaller sets yielded a higher value for the mean Bhattacharyya metric, indicating that they are sub-optimal to the 4-feature set. Enforced feature set expansion resulted in the selection of shade and then second diagonal moment, both for the NIR band. It required a feature dimensionality of 8 for a green band feature to be included (as last) in the set. When NIR energy, entropy, inertia, and homogeneity were excluded, green energy was included as the 3$^{rd}$ feature, in a 3-dimensional feature set, behind NIR shade and NIR second diagonal moment. It is evident, therefore, that texture features computed using visible band imagery are inferior, in terms of cover type discriminatory power, compared to features computed using the NIR band. An important consideration here is that it might be inappropriate to label the discriminatory power of a feature as higher than that of another feature simply because it is present in a 5-feature optimal subset while the other feature is not. This is especially true when other features generated with the same type of value weighting mechanism are already included in the optimal subset. This is because co-occurrence matrix features are not orthogonal, and therefore feature correlation can

influence the membership of an optimal feature subset. In addition, relative to the number of features and classes considered, the small sample size may promote feature selection instability. The 112 observations used for feature selection are probably not a large sample, especially when 5 classes and 42 features (21 each for the NIR and green bands) participated in processes. However, the selection results obtained using many smaller feature sets indicated that the algorithm would have identified the same four optimal features even if a much large number of observations were available.

Two-dimensional representations of feature space depicting texture feature values and cover type class affiliation for each of the 112 observed locations (Figure 4.8) showed good seperability between most of the class pairs, when the appropriate feature pair combination was selected. The energy-inertia space for example, allowed discrimination between natural pine and red pine plantations, while the inertia-homogeneity space separated oak from most other classes. Oak and NH were better separated in entropy-inertia space, however, and a distinction between coniferous and deciduous cover types was better achieved using the energy-homogeneity space (Figure 4.8). Although impossible to visualize, class separability can be extended to four dimensional feature space. The only cover type that the identified features failed to discriminate effectively was aspen, which showed substantial and consistent overlap with all other cover types and particularly with oak in all two-dimensional feature space combinations. For the entropy-inertia space, aspen was present in all class regions identified by the quadratic discriminant function-based classifier (Figure 4.8). This finding is somewhat surprising considering that visual depictions of aspen co-occurrence matrices had revealed patterns in intensity arrangement that differed from those observed

for the other cover types. Apparently, the texture features derived from the matrices were not very effective in quantifying those differences. A possible explanation is that the absence of orthogonallity between texture features affects their discriminatory power for cover types whose GLCM exhibits a concentration of pixel intensity values at or around their center. This limitation can be potentially overcome by comparing class GLCMs directly for classification purposes, that is without using the extracted features. Preliminary investigations in that direction have yielded promising results.

The feature value arrangement shown in Figure 4.8 justified the use of the quadratic instead of the linear discriminant function, because it became apparent that class probability density functions, assumed by the linear function to be equal among classes, were markedly different. However, the use of the quadratic function sometimes generated 'strange-looking' feature space regions with instances of discontinuity. In the entropy-inertia space for example (Figure 4.8), the oak region had two disconnected components, one centered on coordinate location (inertia, entropy) = [8.5, 2.05] and the other around [5.0, 2.15]. In the entropy-homogeneity space, the oak region practically split the aspen region. In all two-dimensional feature space combinations (Figure 4.8), the means of aspen and oak were in close proximity. Aspen exhibited much higher feature value variability. The oak feature regions were approximately centered on the position occupied by the means, while the feature regions for aspen were 'pushed' away from the means.

Observations made in regard to class separability using the training data set were found to hold for classification rule testing using the 132 subplot data. The overall classification accuracy achieved was 65% with a kappa coefficient of 0.56, significant at

$\alpha$=0.01(Table 4.2). Only small discrepancies were observed between producer's and consumer's accuracies obtained for northern hardwoods, red pine plantations, and natural pine, but they varied substantially for aspen and oak. Only 2 out of 12 subplots were erroneously assigned to aspen (83% consumer's accuracy), but 18 aspen subplots were misclassified to other cover types (36% producer's accuracy). Consumer's accuracy was lowest for oak (50%), with 16 erroneously committed subplots. This classifier behavior was attributed to the positioning of oak feature values in the center of the four-dimensional feature space, where the tails of the northern hardwoods, red pine plantation and natural pine density distribution functions met. Small departures in oak feature values from the class mean resulted in class members being assigned to those other classes. The aspen feature space portion, being 'pushed' away from the feature space center, only minimally overlapped with the other classes, thus resulting in high consumer's accuracy. Substantial confusion rates were also observed between red pine plantations and natural pine, with 7 subplots of the former misclassified as the latter. It should be noted that these 7 subplots belonged to just 2 plots, a pattern also observed between northern hardwoods and aspen. Such a concentration of misclassification instances to particular plots indicated their smaller variability in texture, as opposed to spectral (Chapter 3), characteristics within these plots. The overall classification accuracy obtained via linear discriminant function-based classification yielded a kappa coefficient equal to 0.49, thus indicating that the flexibility of quadratic decision boundaries to adapt to class-conditioned feature densities rendered them superior to their linear counterparts.

A comparison between texture classification results to those obtained using spectrally-based methods is shown in Table 4.3. Texture-based classification was

statistically superior at $\alpha$=0.01 to spectral classification methods that used all pixels (Chapter 2). It was not statistically different at $\alpha$=0.10 to spectral classification that used only pixels identified as tree apexes on original DN imagery, and it was found to be inferior at $\alpha$=0.01 to classification methods that used only pixels identified as tree apexes on imagery corrected for brightness variations. Texture-based classification errors involving a particular cover type were found to be spatially correlated and often included all subplots in a plot, while errors of spectral classification were generally spatially random. It is likely that a hierarchical classification approach operating on both textural and spectral data might be capable of substantially increased classification accuracy compared to either classification method used independently. The ability of co-occurrence-based texture features to enhance cover type discrimination might be limited for stands characterized by smooth canopy surface.

Because image texture features operate in a spatial domain, their derivation necessitates images on which homogeneous textural regions are delineated. Such regions can often be obtained by overlaying imagery with digital versions of existing stand maps. In practice though, stand boundaries sometimes represent management units rather than homogeneous stands, or they encompass variable structural and textural stand attributes, especially for uneven aged stands, or they are outdated. In the absence of reliable stand boundary information, texturally homogeneous regions can be identified with visual imagery inspection. Investigations in the study area revealed that 300-350 contiguous pixels of approximately 0.9m ($\cong$ 3ft) that were representative of the textural stand structure suffice for a robust estimate of the stand texture features. As always, the analyst should exercise caution and avoid regions in which vegetation ecotones are suspected.

The accuracy of forest cover type classification via co-occurrence analysis of pixel intensity using imagery from the satellite platforms currently available may fall short of the accuracy obtained using multispectral airborne imagery, primarily because satellite platforms offer H-resolution imagery only for panchromatic bands. As indicated by the findings in this research, GLCMs computed using visible bands vary very little, thus compromising the ability of co-occurrence analysis to discriminate cover types effectively. Observations of forested landscapes in northern Michigan using 0.82m panchromatic IKONOS imagery has, however, demonstrated clearly identifiable texture differences among cover types, suggesting that alternative texture quantification techniques may be better suited to cover type classification efforts.

GLCM computations are efficient even for multidirectional pixel displacements. Currently available computer processors limit the time required to compute the matrix of a 20-hectare forest stand image with 1m pixels to a few ( < 10) seconds, while texture feature extraction is practically instantaneous. Texture-feature-based classifier training and testing is also expeditious. Optimal texture feature set identification, however, is a computationally intensive process, even for optimized search algorithms. Implementation of analytical texture-based approaches for forest classification is further complicated by the absence of software packages supporting the series of steps required by the process. Under such circumstances, information on features that possess discriminatory power for texture-based investigations, or at least on an approximate optimal feature space dimensionality, is important for operational methodology implementation.

Findings of the analysis presented in this chapter can provide a basis for the initiation of texture-based cover type classification efforts. In the presence of mature,

high canopy closure stands, a single pixel displacement vector length and an angular range of 180° (half a circle) are likely among the best choices for GLCM construction. NIR bands available in multispectral imagery should be given priority over visible bands. Results suggest that the optimal co-occurrence matrix feature subset would usually include at least one feature produced with element value weighting and one feature with positional weighting, and that the energy, entropy, inertia, and homogeneity features are likely to be optimal subset members.

It is important to remember that the formulation of this analysis strategy was based on incremental optimization. In that regard, the displacement vector used for GLCM construction was selected on the basis of matrix information content, and feature selection was based only on GLCMs that maximized information content and used a single distance metric among class-conditioned feature densities. Although those decisions are warranted by the need to reduce analysis extent to manageable levels, it is possible that the results obtained only constitute a local maximum in the domain of classification accuracy, and that other combinations of intermediate analysis choices could offer an improvement. On-going efforts aiming at procedure automation would allow a more detailed investigation on the ability of image texture to support stand-level forest cover type and structure classification.

## 4.5. Conclusion

Investigations on the utility of image texture for forest classification purposes have been sporadic and likely not well understood by the forestry community primarily due to the complexity associated with the quantification of texture. Classification accuracies obtained in those investigations have generally been too low to be useful and

were found to exhibit significant variability among geographic regions and stand structures.

This research explored one dimension of image texture depicting forested landscapes based on pixel intensity co-occurrence. Instead of relying on *a priori* selected sets of texture features derived from co-occurrence matrices, which is the usual practice, this study investigated all alternatives present in a sequence of steps used to compute feature values. The results indicated that understanding the influence that intermediate analysis choices have on the value of computed texture features can yield substantial improvements in the resulting classification accuracy. In addition, because co-occurrence texture features are derived using band-specific information, they are independent of distortions generated by band registration problems and brightness variability among frames (defects often present in H-resolution imagery). Potential limitations in using co-occurrence-based features for image classification occur 1) in the presence of stands with smooth canopies; 2) from the need for pre-existing, positionally accurate stand delineations; and 3) from the complexity associated with the procedures used to identify the optimal co-occurrence feature subset.

Outcomes of this research also indicate that texture-based classification is capable of detecting stand cover type differences missed by spectrally-based classification, given that the two techniques result is different spatial distributions of misclassifications. Identifying the causal factors that result in those misclassification differences should allow composite classification strategies that could substantially improve classification accuracies achieved by each technique independently.

To date, texture information in forestry applications of optical remote sensing applications has been regarded as only complimentary to that obtained via spectral analysis. The low appreciation for texture-based analyses might be due to the limited utility that texture-based past studies had revealed for forestry applications using coarse resolution imagery. Findings in this research indicated that the texture information content of digital, H-resolution imagery has the potential for significant contributions in support of forestry applications.

## Literature Cited


Anger, C.D. 1999. Airborne hyperspectral remote sensing in the future? In *Proc. Fourth International Symposium on Airborne Remote Sensing and 21st Canadian Symposium on Remote Sensing*, Canadian Aeronautics and Space Institute, Ottawa, p. 1-15.

Agterberg, F.P., and Q. Cheng. 1999. Introduction to special issue on "Fractals and Multifractals", *Comp. Geosci.*, 25:947-948.

Barnsley, M. 1999. Digital remotely-sensed data and their characteristics. In *Geographical Information Systems*, P.A. Longeley, M.F. Goodchild, D.J. Maguire, and D.W. Rhind [Eds], John Wiley, New York, p. 451-466.

Bhattacharyya, A. 1943. On a measure of divergence between two statistical populations defined by their probability distributions, *Bull. Calcutta Math. Soc.*, 35:99-109.

Bellman, R.E. 1961. *Adaptive Control Processes*, Princeton University Press.

Chen, J.M. 1999. Spatial scaling of a remotely sensed surface parameter by contexture, *Rem. Sensing Environ.*, 69:30-42.

Chernoff, H. 1952. A measure of asymptotic efficiency for tests of a hypothesis based on the sum of observations, *Ann. Math. Stat.*, 23:493-507.

Cohen, W.B., T.A. Spies. 1992. Estimating structural attributes of Douglas-fir/western hemlock forest stands from Landsat and SPOT imagery, *Rem. Sensing Environ.*, 41:1-17.

Congalton, R. 1991. A review of assessing the accuracy of classifications of remotely sensed data, *Rem. Sensing of Environ.*, 37, 35-46, 1991.

Conners, R.W., and C. Harlow. 1978. Equal probability quantizing and texture analysis of radiographic images, *Comp. Graph. Image Process.*, 8:447-463.

Conners, R.W., and C. Harlow. 1980. A theoretical comparison for texture algorithms, *IEEE Trans. Pattern Anal. Mach. Intel.*, 2:204-222.

Conners, R.W., M.M. Trivedi, and C.A. Harlow. 1984. Segmentation of a high-resolution urban scene using texture operators, *Comp. Vision Graph. Image Process.*, 25:273-310.

Coops, N.C., and D. Culvenor. 2000. Utilizing local variance of simulated high spatial detail imagery to predict spatial pattern of forests, *Rem. Sensing Environ.*, 71:208-260.

Cramer, H. 1946. Mathematical methods of statistics, Princeton University Press.

Davis, L.S., S.A. Johns, and J.K. Aggarwal. 1979. Texture analysis using generalized co-occurrence matrices, *IEEE Trans., Pattern Anal. Mach. Intel.*, 3:251-259.

Franklin, S.E., and D.R. Peddle. 1990. Classification of SPOT HRV imagery and texture features, *Int. J. Rem. Sensing*, 11:551-556.

Franklin, S.E., R.J. Hall, L.M. Moskal, A.J. Maudie, and M.B. Lavigne. 2000. Incorporating texture into classification of forest species composition from airborne multispectral images, *Int. J. Rem. Sensing*, 21:61-79.

Franklin, S.E., M.A. Wulder, and G.R. Gerylo. 2001. Texture analysis of IKONOS panchromatic data for Douglas-fir forest age class separability in British Columbia, *Int. J. Rem. Sensing*, 22:2627-2632.

Franklot, R.T., and R. Chellappa. 1987. Lognormal random-field models and their applications to radar image synthesis, *IEEE Trans. Geosci. Rem. Sensing*, 25:195-207.

Galloway, M.M. 1975. Texture analysis using gray level run lengths, *Comp. Graph. Image Process.*, 4:172-179.

Green, K. 2000. Selecting and interpreting high-resolution images, *J. Forestry*, 98:37-39.

Habbema, J.D.F., and J. Hermans. 1977. Selection of variables in discriminant analsysi by *F*-statistic and error rate, *Technometrics*, 19:487-493.

Haralick, R.M, K. Shanmugam, and I. Dinstein. 1973. Texture feature for image classification, *IEEE Trans. Systems Man Cyber.*, 3:610-621.

Haralick, R.M. 1986. Statistical image texture analysis. In *Handbook of Pattern Recognition and Image Processing*, T.Y. Young and K.S. Fu [Eds], Academic Press, New York, p. 247-249.

Haralick, R.M., and H. Joo. 1986. A context classifier, *IEEE Trans. Geosci. Rem. Sensing*, 24:997-1007.

Hay, G.J., K.O. Niemann. 1994. Visualizing 3-D texture: A three dimensional structural approach to model forest texture, *Can. J. Rem. Sensing*, 20:90-101.

Hay, G.J., K.O. Niemann, and G.F. McLean. 1996. An object-specific image texture analysis of H-resolution forest imagery. *Rem. Sensing Environ.*, 55:108-122.

Hawkins, D.M. 1981. A new test for multivariate normality and homoscedasticity, *Technometrics*, 23:105-110.

Hughes, G.F. 1968. On the mean accuracy of statistical pattern recognizers, *IEEE Trans. Inf. Theory*, 1:55-63.

Kittler, J. 1986. Feature selection and extraction, in *Handbook of Pattern Recognition and Image Processing*, T.Y. Young and K.S. Fu [Eds], Academic Press, San Diego, California.

Khazenie, N., and M.M. Crawford. 1990. Spatial-temporal autocorrelated model for contextual classification, *IEEE Trans. Geosci. Rem. Sensing*, 28:529-539.

Lark, R.M. 1996. Geostatistical description of texture on an aerial photography for discriminating classes of land cover, *Int. J. Rem. Sensing*, 17:2115-2133.

Mahalanobis, P.C. 1936. On the generalized distance in statistics, *Proc. Nat. Inst. Sciences India*, 2:49-55.

Mandelbront, B.B. 1982. *The fractal geometry of nature*, Freeman , San Francisco, California.

Mathsoft. 2000. S-plus 2000 professional release 3, Cambridge, Massachusetts.

MathWorks. 1999. MatLab ver. 5.0.3, Natick, Massachusetts.

Matusita, K. 1956.Decision rule, based on distance, for the classification problem. *Ann. Inst. Stat. Math.*, 8:67-77.

McLachlan, G.J. 1976. A criterion for selecting variables for the linear discriminant function, *Biometrics*, 32:515-529.

Michigan Department of Natural Resources. 2001. Forestry, Mineral and Fire Management Division, Resource Mapping and Aerial Photography; *1992 Series USGS Digital Orthophoto Quadrangles*, http://www.mcgi.state.mi.us/mgdl/doqs_zip/DOQQ92_Map.htm

Shapiro, L.G., and G.C. Stockman. 2001. *Computer Vision*, Prentice Hall, Upper Saddle River, New Jersey.

Silverman, B.W. 1986. *Density Estimation for Statistics and Data Analysis*, Chapman and Hall.

St-Onge, B.A., and F. Cavayas. 1997. Automated forest structure form high resolution imager based on directional semivariogram estimates. *Rem. Sensing Environ.*, 61:82-95.

Sun, C., and W.G. Wee. 1983. Neighboring gray level dependence matrix for texture classification, *Comp. Vision Graph. Image Process.*, 23:341-352.

Ryherd, S., and C.E. Woodcock. 1997. Combining spectral and texture data in the segmentation of remotely sensed images, *Photogramm. Eng. Rem. Sensing*, 62:181-194.

Shahshahani, B.M., and D.A. Landgrebe. 1994. The effect of unlabeled samples in reducing the small sample size problem and mitigating the Hughes phenomenon, *IEEE Trans. Geosci. Rem. Sensing*, 32:1087-1095.

Space Imaging Inc. 1999. DAIS: A Digital Airborne Imaging System. Space Imaging Corporation, Thornton, Colorado.

Strahler A.H., C.E. Woodcock, and J.A. Smith. 1986. On the nature of models in remote sensing, *Rem. Sensing Environ.*, 20:121-139.

Wu, C.M., and Y.C. Chen. 1992. Statistical feature matrix for texture analysis, *Comp. Vision Graph. Image Process.*, 54:407-419.

Wulder, M.A., S.E. Franklin, and M.B. Lavigne. 1996. High spatial resolution optical image texture for improved classification of forest stand leaf area index, *Can. J. Rem. Sensing*, 22:441-449.

Yu, B., and B. Yuan. 1993. A more efficient branch and bound algorithm for feature selection, *Pattern Recognition*, 26:883-889.

Zucker, S.W., and D. Terzopoulos. 1980. Finding structure in co-occurrence matrices for texture analysis, *Comp. Graph. Image Process.*, 12:286-308.

## Tables

**Table 4.1.** Commonly-used Gray Level Co-occurrence Matrix features.

| Features | | Equations |
|---|---|---|
| Energy: | $F1$ | $= \sum_{i,j} P(i,j)^2$ |
| Entropy: | $F2$ | $= -\sum_{i,j} P(i,j)\log P(i,j)$ |
| Homogeneity: | $F3$ | $= \sum_{i,j} [1/(1+(i-j)^2)]P(i,j)$ |
| Inertia: | $F4$ | $= \sum_{i,j} (i-j)^2 P(i,j)$ |
| Correlation: | $F5$ | $= -\sum_{i,j} [(i-\mu_x)(j-\mu_y)/\sqrt{\sigma_x \sigma_y}]P(i,j)$ |
| Shade: | $F6$ | $= \sum_{i,j} (i+j-\mu_x-\mu_y)^3 P(i,j)$ |
| Prominence: | $F7$ | $= \sum_{i,j} (i+j-\mu_x-\mu_y)^4 P(i,j)$ |
| Variance: | $F8$ | $= \sum_{i,j} (i-\mu_x)^2 P(i,j)$ |
| Sum Average | $F9$ | $= \sum_{i=3}^{2N_g} iP_{x+y}(i)$ |
| Sum Entropy: | $F10$ | $= -\sum_{i=3}^{2N_g} iP_{x+y}(i)\log P_{x+y}(i)$ |
| Sum Variance: | $F11$ | $= -\sum_{i=3}^{2N_g} (i-F9)^2 P_{x+y}(i)$ |
| Difference Average: | $F12$ | $= \sum_{i=0}^{N_g-1} iP_{x-y}(i)$ |
| Difference Entropy: | $F13$ | $= \sum_{i=0}^{N_g-1} -P_{x-y}(i)\log P_{x-y}(i)$ |
| Difference Variance: | $F14$ | $= \sum_{i=0}^{N_g-1} (i-F12)^2 P_{x-y}(i)$ |
| Information Measure: | $F15$ | $= [F2 - HXY1]/\max(HX, HY)$ |
| Coefficient of Variation: | $F16$ | $= \sigma(P(i,j))/\mu(P(i,j))$ |
| Peak Transition Probability: | $F17$ | $= \max(P(i,j))$ |
| Diagonal Variance: | $F18$ | $= \sigma^2(P(i,j))$ |
| Diagonal Moment: | $F19$ | $= \sum_{i,j} \sqrt{(0.5\|i-j\|P(i,j))}$ |
| Second Diagonal Moment: | $F20$ | $= \sum_{i,j} (0.5\|i-j\|P(i,j))$ |
| Triangular Symmetry: | $F21$ | $= \sum_{i,j} \|P(i,j) - P(j,i)\|$ |

$\mu_x = \sum_i i \sum_j jP(i,j)$ $\quad$ $\mu_y = \sum_j j \sum_i iP(i,j)$

$\sigma_x = \sum_i (i-\mu_x)^2 \sum_j P(i,j)$ $\quad$ $\sigma_y = \sum_j (j-\mu_y)^2 \sum_i P(i,j)$

$P_x(i) = \sum_j P(i,j)$ $\quad$ $P_y(j) = \sum_i P(i,j)$

$P_{x+y}(k) = \sum_{i,j \mid i+j=k} P(i,j)$ $\quad$ $P_{x-y}(k) = \sum_{i,j \mid i-j=k} P(i,j)$

HX and HY are the entropies of $P_x(i)$ and $P_y(j)$ respectively

$$HXY1 = -\sum_{i,j} P(i,j)\log(P_x(i)P_y(j))$$

**Table 4.2.** Forest cover type classification results and associated accuracy assessment parameters obtained by using a quadratic discriminant function-based classifier operating on four imagery texture feature (energy, entropy, inertia, and homogeneity) derived from Gray Level Co-occurrence matrices and trained with independent data (112 observations).

| | | Observed | | | | | |
|---|---|---|---|---|---|---|---|
| | | ASP | NH | Oak | RPP | NP | Row Total |
| Classified | Aspen (ASP) | 10 | 1 | 1 | 0 | 0 | 12 |
| | Northern Hardwoods (NH) | 6 | 22 | 3 | 0 | 0 | 29 |
| | Oak | 6 | 5 | 16 | 3 | 2 | 34 |
| | Red Pine Plantation (RPP) | 2 | 0 | 1 | 21 | 7 | 31 |
| | Natural Pine (NP) | 4 | 0 | 3 | 4 | 19 | 30 |
| | Column Total | 28 | 28 | 24 | 28 | 28 | 136 |

| | Accuracy (%) | | Errors (%) | |
|---|---|---|---|---|
| | Producer's | Consumer's | Commission | Omission |
| ASP | 35.71 | 83.33 | 64.29 | 7.14 |
| NH | 78.57 | 70.97 | 21.43 | 32.14 |
| Oak | 66.67 | 50.00 | 33.33 | 66.67 |
| RPP | 75.00 | 67.74 | 25.00 | 35.71 |
| NP | 67.86 | 63.33 | 32.14 | 39.29 |

| Class | Conditional Kappa |
|---|---|
| ASP | 0.7901 |
| NH | 0.6344 |
| Oak | 0.3929 |
| RPP | 0.5938 |
| NP | 0.5383 |

| | |
|---|---|
| Overall Accuracy (%) | 0.6471 |
| Kappa Coefficient | 0.5594 |
| $s^2_k$ | 0.0017 |
| $Z_k$ | 13.6023* |

* Significant at $\alpha = 0.01$

**Table 4.3.** Statistical comparison of texture-based forest cover type classification accuracy estimates with results obtained by using various spectrally-based, maximum likelihood classification schemes. Z-statistics correspond to standardized differences of corresponding kappa coefficient values.

| | | Texture Classification | | |
|---|---|---|---|---|
| | | $\Delta(k_{tex}-k_{spec})$ | Z-statistic | (p-value) |
| Spectral Classification | Tree Apexes, Original DNs | -0.0909 | -1.6069 | 0.1081 |
| | Tree Apexes, Brightness Correction | -0.2841 | -5.6820 | 0.0000 |
| | All Pixels, Original DNs | 0.2306 | 3.8433 | 0.0001 |
| | All Pixels, Brightness correction | 0.1843 | 3.0717 | 0.0021 |

## Figures

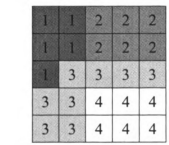

(a)

$d = 1$, $\theta = 0$

| $i$ \ $j$ | 1 | 2 | 3 | 4 |
|---|---|---|---|---|
| 1 | 2 | 2 | 1 | 0 |
| 2 | 0 | 4 | 0 | 0 |
| 3 | 0 | 0 | 5 | 2 |
| 4 | 0 | 0 | 0 | 4 |

(d)

$d = 1$, $\theta = 45$

| $i$ \ $j$ | 1 | 2 | 3 | 4 |
|---|---|---|---|---|
| 1 | 1 | 1 | 3 | 0 |
| 2 | 0 | 2 | 2 | 0 |
| 3 | 0 | 0 | 1 | 4 |
| 4 | 0 | 0 | 0 | 2 |

(e)

| Gray level $i$ \ Gray level $j$ | 1 | 2 | 3 | 4 |
|---|---|---|---|---|
| 1 | (1,1) | (1,2) | (1,3) | (1,4) |
| 2 | (2,1) | (2,2) | (2,3) | (2,4) |
| 3 | (3,1) | (3,2) | (3,3) | (3,4) |
| 4 | (4,1) | (4,2) | (4,3) | (4,4) |

(b)

$d = 1$, $\theta = 90$

| $i$ \ $j$ | 1 | 2 | 3 | 4 |
|---|---|---|---|---|
| 1 | 3 | 0 | 2 | 0 |
| 2 | 0 | 3 | 3 | 0 |
| 3 | 0 | 0 | 3 | 3 |
| 4 | 0 | 0 | 0 | 3 |

(f)

$d = 1$, $\theta = 135$

| $i$ \ $j$ | 1 | 2 | 3 | 4 |
|---|---|---|---|---|
| 1 | 2 | 0 | 0 | 0 |
| 2 | 1 | 2 | 3 | 0 |
| 3 | 0 | 0 | 3 | 2 |
| 4 | 0 | 0 | 1 | 2 |

(g)

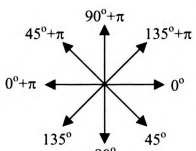


$d = 1$, $\theta \in \{135+\pi, 0, 45, 90\}$

| $i$ \ $j$ | 1 | 2 | 3 | 4 |
|---|---|---|---|---|
| 1 | 8 | 4 | 6 | 0 |
| 2 | 0 | 11 | 5 | 0 |
| 3 | 0 | 3 | 13 | 10 |
| 4 | 0 | 0 | 2 | 10 |

(h)

$d = 1$, $\theta \in \{135+\pi, 0, 45, 90, 135, 0+\pi, 45+\pi, 90+\pi\}$

| $i$ \ $j$ | 1 | 2 | 3 | 4 |
|---|---|---|---|---|
| 1 | 16 | 4 | 6 | 0 |
| 2 | 4 | 22 | 8 | 0 |
| 3 | 6 | 8 | 26 | 12 |
| 4 | 0 | 0 | 12 | 20 |

(i)

**Figure 4.1**. (a) A hypothetical 2-bit (4 gray levels) 5x5 image with, (b) Corresponding general (pre-normalized) GLCM form with gray levels 1-4. (c) Between-pixel angles used in the computation of GLCM, (d)-(i), GLCM structure for distance of 1 pixel and choices of angular displacements.

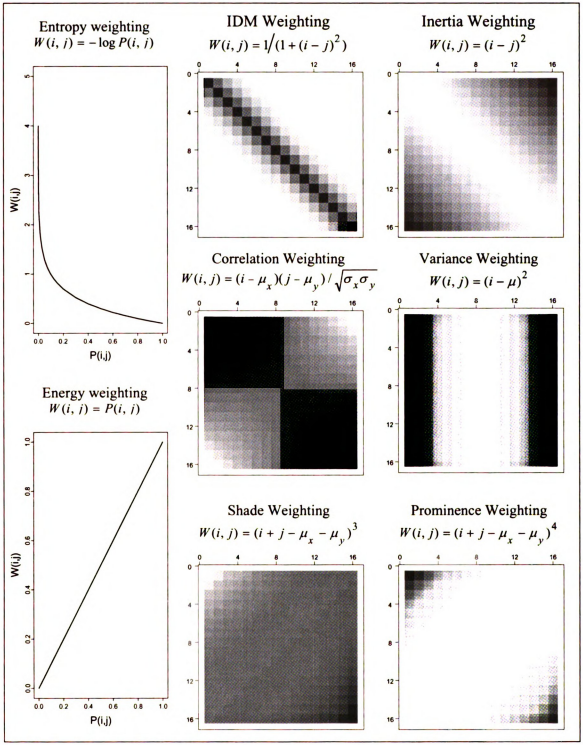


**Figure 4.2**. Pictorial representation of two classes of GLCM weighting functions: Weighting dependent on matrix element value (entropy and energy features), and weighting dependent on an element's spatial position (remaining features). Darker shades indicate larger element weighting.

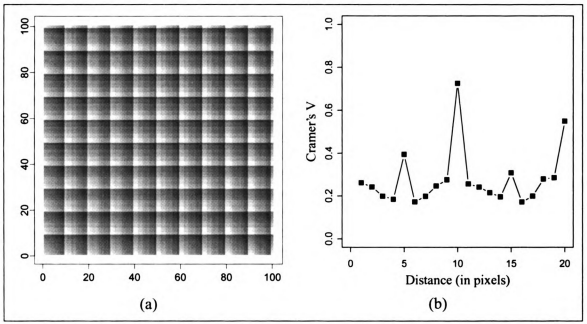


**Figure 4.3**. 4-bit image exhibiting geometric (regular) texture, and Cramer's V statistic calculated from image GLCMs as a function of displacement distance *d*. Angular pixel displacement ($\theta$) used was 0°).

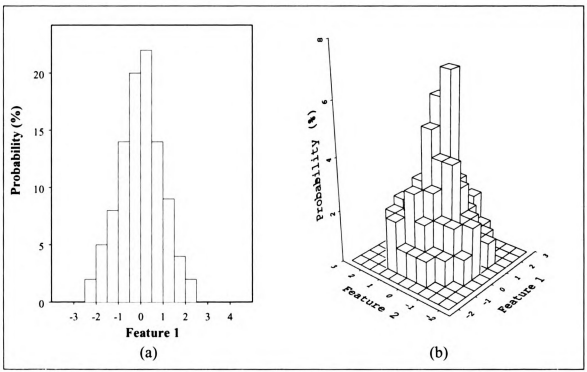


**Figure 4.4**. Pictorial representation of the Hughes phenomenon showing the decrease in expected feature class probability as data dimensionality increases from 1-D (**a**) to 2-D (**b**). 100 realizations were drawn for each feature class from Gaussian [~N(1,0)], independently and identically distributed data.

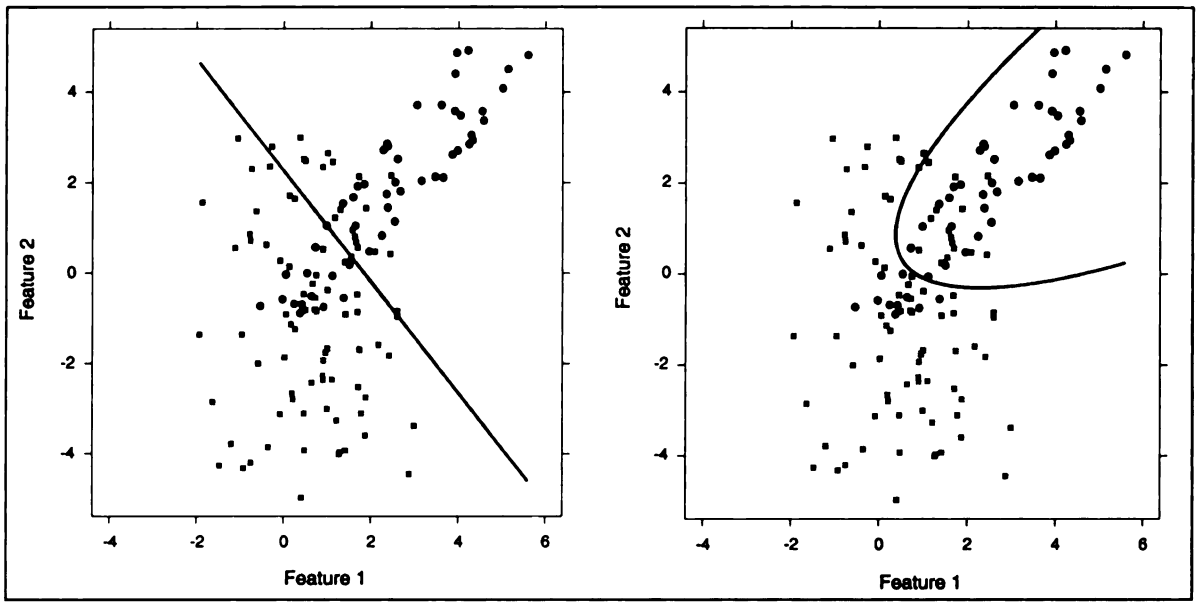


**Figure 4.5.** Decision boundaries for a two-class data set produced by a linear (a) and quadratic (b) discriminant function developed using two object features. Object class is color-coded.

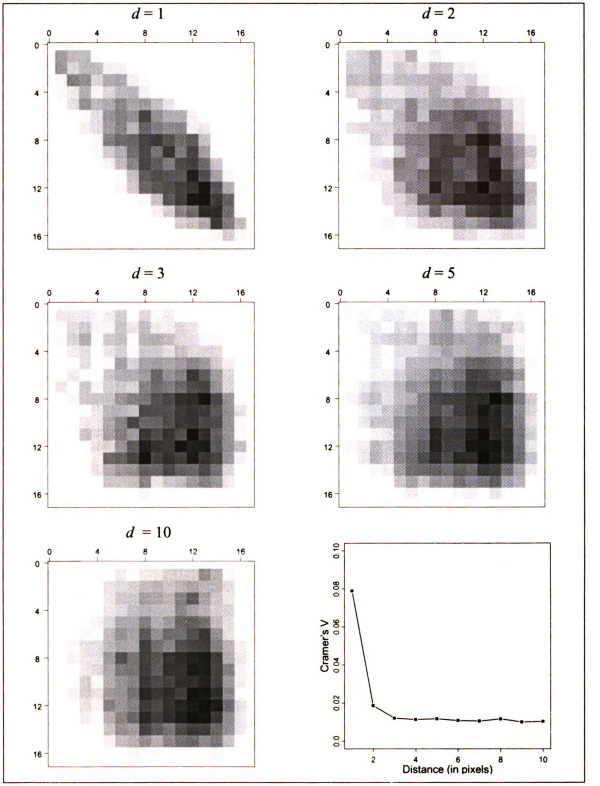


**Figure 4.6**. NIR-band Normalized Gray Level Co-occurrence Matrices of an aspen subplot produced $\theta=\{135+\pi, 0, 45, 90\}$ and various pixel displacement distances $d$, and values of corresponding Cramer's V statistic.

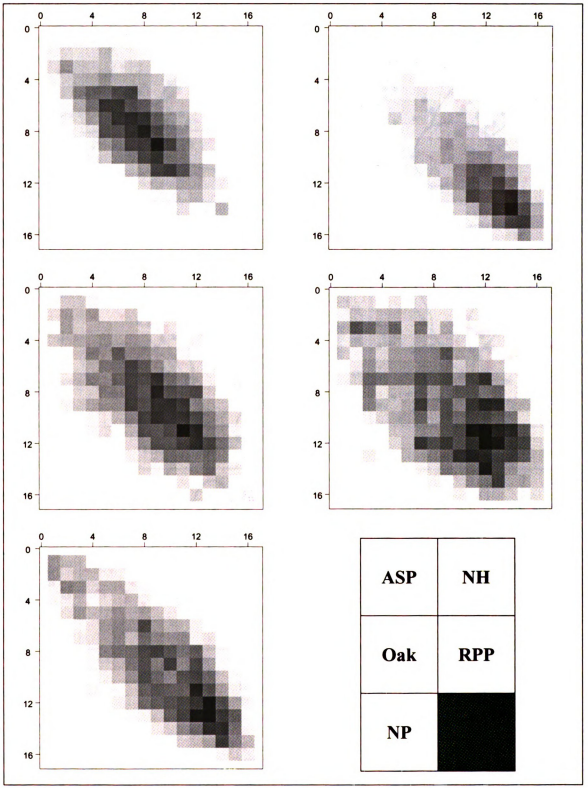


**Figure 4.7**. NIR-band Normalized Gray Level Co-occurrence Matrices produced for five subplot, each situated in one of the forest cover types present in the study area, using $d = 1$ and $\theta = \{135+\pi, 0, 45, 90\}$.

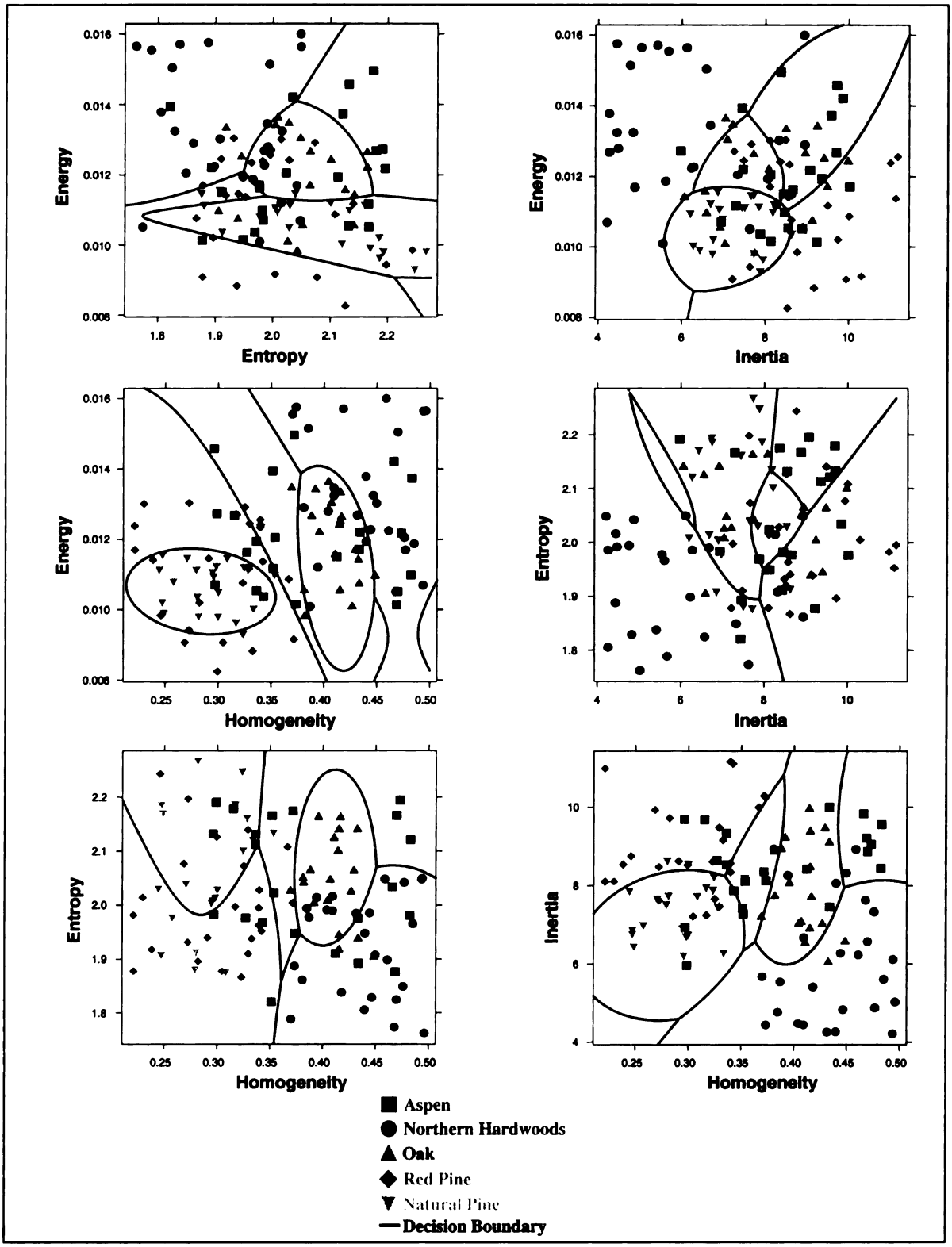


**Figure 4.8.** Forest cover type classification rules developed via quadratic discriminant functions for texture feature pairs derived from NIR-band Gray Level Co-occurrence Matrices calculated using [$d = 1$, $\theta = \{135+\pi, 0, 45, 90\}$] pixel displacement vectors.

# CHAPTER 5

## SUMMARY

## 5.1. A Critique of Analysis Methods

It is evident from the presentations in the previous chapters that the analysis of digital, airborne, high-resolution, imagery is an effort intensive process. This is because of the small footprint of such imagery, the frequent occurrence of geometric and radiometric imagery imperfections, and the absence of software packages that provide a complete suite of analytic capabilities needed. If the still substantial cost associated with imagery acquisition is also considered, it should not come as a surprise that examples of forestry applications using this type of remotely sensed data are rare. As shown in this dissertation, however, digital high-resolution imagery is a technology that can provide forest canopy attribute information with the accuracy required for forest management decision-making at the operational level. At the same time, this technology is compatible with classic uses of imagery in forestry, including cover type classification, and the potential was demonstrated to extend classification endeavors to the individual tree level.

It could be argued that the band registration problems present in the imagery were an isolated case originating from an unstable camera mounting and that, as imagery vendors accumulate experience, such problems will diminish. Unfortunately, this statement is probably only half-true. Personal communications with digital array camera manufacturers and users of digital airborne imagery revealed that band registration problems, although usually less pronounced than those found in the imagery used in this research, persist even after diligent camera mounting on the body of the aircraft. This is, in part, because the array detectors are aligned on a surface that is only approximately planar and, in part, because the orientation of the focal plane in relation to the body of the camera differs even among cameras of the same make and sequential serial numbers.

Precise alignment is possible, albeit very costly, for detector arrays mounted permanently on the same device, but practically unattainable for digital arrays belonging to individual cameras, such as those used for acquiring multispectral imagery from airborne platforms. Therefore, the need for misregistration detection and correction procedures, such as those developed in this study, would likely become a standard imagery pre-processing step.

Brightness variations among image frames should also be expected in airborne digital imagery for the foreseeable future. As mentioned in Chapter 1, cameras currently used for the acquisition of airborne imagery adjust the sensor's gain factor for each frame. Researchers investigating the sudden oak death problem in California acquired imagery using the Advanced Digital Airborne Spectrometer (ADAR) system, which has technical characteristics virtually identical to those of the DAIS system. They discovered that the gain factor quantification was accurate, but not precise. By employing targets of known reflectance in the study area, they found that their brightness-corrected imagery contained a near-infrared Digital Number (DN) RMSE of 6 for 8-bit NIR imagery. This corresponds to more than 2% of the theoretical DN range. Assuming that the gain factor quantification error is comparable between the two systems, the mean brightness variability among DAIS frames could exceed 1,500 DNs even after an adjustment based on spectral gain factors. Evidently, frame spectral brightness normalization would still be required even if the spectral gain factors were to be available. The methodology presented in Chapter 2 could be used to provide such normalization. It was shown to reduce the mean, among-frame brightness variability to 0.2% of the theoretical DN range.

The methodology to correct the Bidirectional Reflectance Distribution Function (BRDF) effect used in this study was developed in accordance with the imagery

acquisition protocol and the cover type distribution present in the study area. Visual comparisons of frame brightness prior to and after normalization suggested that the methodology performed well and quantitative evaluation of post-correction brightness variability along frame paths supported that assessment. It may, however, be difficult to extend this BRDF correction methodology to other imagery sets featuring a particular cover type, or cover type group. Fitting of a kernel-based BRDF model to the imagery data was implemented successfully (given that model coefficient convergence was achieved) for deciduous forests in the study area. There is no assurance that BRDF model parameter convergence could be achieved for other cover type groups or where the number of frames available is relatively small (<20). In addition to a non-linear increase in computational costs, a large number of frames would help model parameter convergence, but at the same time would decrease the probability of cover type presence in all overlapping areas between frames.

Reduction in computational cost and the less strict requirements for large number of frames and uniform spatial distribution of cover types can be achieved by substituting the brute-force BRDF effect normalization technique used in this study with techniques for which parameter estimation is analytical rather exhaustive-search-based. Mikkola and Pellikka (2002) describe such an analytical technique. The drawbacks of the analytical approaches are that they still require prior spatially explicit information of cover type distribution and also a minimum 66% overlap between adjacent frames along and between flight lines. Such high frame endlap rates are possible in the acquisition of aerial photographs, but not for digital array scanners. At least currently, the time required for information transfer from each detector to the on-board information storage system

precludes such a cycling rate. It was calculated that the maximum endlap rate that the DAIS camera system could sustain along the flight line 2,000m above ground altitude is about 40%. Obviously there are no technical restrictions for the amount of sidelap between flight lines. The 20% frame endlap rate present in the data set did not allow consideration of alternative BRDF effect normalization approaches.

A comparison of spectral classification accuracy results using all pixels in a stand or other image region (Chapter 2) to those obtained using only pixels identified as tree apexes (Chapter 3) leaves little doubt that the cost associated with tree apex identification is justified. It could be argued that substantial cost savings could be achieved by substituting pixels identified as tree apexes with those belonging to an upper, say $95^{th}$, spectral brightness percentile, which could be easily identified via spectral histogram computations. Those alternatives have been examined for several brightness percentiles and the results showed a reduction in classification accuracy in excess of 7% and sometimes as much as 15%. Classification accuracy discrepancies between the two alternatives should be expected to be even larger in mixed stands, and particularly in stands characterized by spectral brightness variability among dominant species. Using histogram information to identify tree apexes that are subsequently used for estimating canopy structure parameters was found to produce very poor results. This was because of excessive errors of omission due to bright pixel clustering around the apex of a single tree and the lower crown brightness of co-dominant trees that were partially in shadow.

The feature selection approach presented in Chapter 4 allowed a reduction in texture feature space dimensionality reduction from 42 to 4. This bypassed the Hughes phenomenon restrictions, and sustained a texture-based cover type classification accuracy

of about 65%. Obviously, feature selection can be used to serve objectives other than categorical classifications. Experimentation with co-occurrence feature subset optimization in support of stand classification based on canopy closure indicated that the two-dimensional space defined by the energy and variance features could provide very accurate canopy closure discrimination (< 10% error) in a 3-class formulation. There were no natural clusters in the distribution of canopy closure values for the 134 subplots used in the classification testing process. This indicates that image texture could be a useful discriminator for the continuous variables associated with canopy structure, at least for certain parameter value ranges. Hypotheses regarding of the utility of texture features for cover type discrimination could only be evaluated on a trial basis, given that cover type is a qualitative variable.

The need for computational efficiency has been mentioned more than once in this dissertation. Although efforts were made to optimize the scripts, there are still opportunities for improvement, particularly with the canopy parameter estimation via slope breaks. Those opportunities reside where C scripts "call" functions of supportive software packages, which are in turn executed via a software-package-specific language interpreter. One such example is the local regression fitted on the DNs of transects analyzed during the computation of window size in support of local maximum filtering. The magnitude of computational gain possible can be realized by considering that the processing via slope breaks of a one-hectare stand requires approximately 50,000 calls to the local regression function. The entire computation overhead cost associated with function interpretation external to the C scripts can be eliminated by including the function in the compiled C script. Experimentation with central processing units

operating at 3.0GHz showed that if all computations were to be performed via a stand-alone C script and by using the slope breaks approach, derivation of canopy attributes for an entire, average-sized (~1500 Ha) forest compartment could be completed in less than 36 hours.

In all previous chapters and the discussion presented above there is a frequent allusion to the link between spatially explicit cover type information and image-analysis information products. Identification of spectrally homogeneous image frame regions, such as those belonging to the same cover type, is important for the BRDF/brightness normalization efforts shown in Chapter 2 and they are a prerequisite for texture and canopy structure parameter estimation using DN autocorrelation presented in Chapters 3 and 4. Identification of such regions, or image segmentation as it is better known (Edwards, 1995), has been pursued. The current stage of image segmentation development, along with its implications on classification and canopy parameter estimation, is outlined below.

## 5.2. The Role of Image Segmentation

The purpose of image segmentation in forestry remote sensing is to partition forested land in regions of uniform reflectance patterns thought to correlate with spatial variables of interest. Image segmentation is usually accomplished via identification of boundaries or edges obtained using a series of filters or operators. Many of these operators, including those proposed by Prewitt (1970) and Roberts (1965) and the more sophisticated Laplacian of Gaussian and Canny operators, were used to segment a few image frames in the study area. Details on the theoretical foundation of such operators and how they can be computed are available in Pitas (1993). The results obtained by

these preliminary investigations were very poor with the number of identified boundaries rivaling the number of trees present. Apparently, those operators perceive the spatial variability of tones in high spatial resolution imagery as noise, even when imagery smoothing is performed prior to applying the operator. Poor segmentation quality results were also obtained by using the lattice-wobbling algorithm (Fortin and Drapeau, 1995).

It appears that the segmentation of high-spatial resolution imagery of forested landscapes should be redefined as the quest for imagery regions that are homogeneous in their tonal heterogeneity rather than comprising uniform tones, which implicitly introduces the concept of image texture in the image segmentation process. Very often, the regions on either side of a boundary that is easily identifiable by visual inspection have practically identical average tonal values over some area element comprising many pixels, but different arrangement of tones. This condition does not allow the gradient change seeking operators mention above to detect the boundary. So far, the best (visually assessed) image segmentation results over the study area have been obtained by modifying a technique introduced by Pekkarinen and Sarvi (2002), that combines region growing and tonal gradient seeking algorithms. Its merits include flexibility in band, or band combination, usage, the ability to restrict the size of delineated regions to be above a user-specified areal threshold, (i.e. the minimum mapping unit), and computational efficiency. This technique succeeded in consistently identifying boundaries among adjacent red pine plantations of different age, or thinning prescriptions and among adjacent stands characterized by differences in canopy closure and stem densities. It appeared to perform less than optimally in the presence of wide transition zones (ecotones) among cover types or canopy structure conditions.

In the absence of reliable, spatially explicit information delineating forest stands, image segmentation should be regarded as the first step in imagery analysis of forested areas. Until the boundary detection fidelity of segmentation methodologies improves sufficiently to allow automation, the identified forest regions would likely need to be examined manually and boundaries added where the segmentation process failed. Following this tessellation of forests into regions, tree apex identification could be obtained with the techniques of Chapter 3, and used for region assignment to a cover type, with an ensuing, independent allocation to a cover type using textural information. It is assumed that field observations or other forms of ancillary information, including manual forest cover type assessment from the imagery set, would have been used for prior development of spectral and textural signatures. Canopy structure parameter values, in addition to serving as an independent information product, could be used to assist in the development of cover type classification rules. If, for example, canopy structure analysis of an image region were to yield a mean crown diameter of 7m, while textural and spectral imagery derivatives suggested an allocation to the aspen cover type, the crown diameter information could be used to modify the cover type region assignment to the second texturally and spectrally most probable class (e.g. northern hardwoods), given that a 7m crown diameter value for aspen would be rather improbable in the study area. Using a regression tree approach could identify the exact form of such a hybrid classification rule. Details on the development and the merits of decision-tree-based classification can be found in Friedl et al. (1999) and Hansen et al. (2000). A preliminary investigation involving such a regression-tree-based classification rule has yielded a cover type classification accuracy of approximately 93%.

## 5.3. Evaluation of Analysis Results

Analysis findings indicated that extracting the information content of digital airborne imagery for forestry applications requires analysis methods specifically tuned to its characteristics. The ability to assign cover type affiliation to individual crowns, and thus determine species mixture and distribution for individual forest stands, cannot be paralleled by the coarser resolution imagery typically used today. However, technical problems associated with digital airborne imagery, including brightness variability among acquired imagery frames, and the, sometimes substantial, geometric distortions, potentially limit the opportunities for direct utilization of such technology for classification purposes. The series of techniques presented in Chapter 2 proved that the technical imperfections of such imagery could be corrected, in which case combinations of spectral (Chapter 3) and textural (Chapter 4) signatures could provide classification accuracies suitable for operational imagery utilization. Unfortunately, those developments are practically attainable only in the presence of experienced analysts and at considerable computational costs.

An area in which digital airborne imagery could become of unprecedented utility for forest inventory and management purposes is the retrieval of canopy structure parameters. As shown in Chapter 3, the presence of detailed field information allowed for a better understanding of the interaction between forest canopies and incident solar radiation as manifested in digital imagery, and supported the development of techniques capable of translating such knowledge into quantitative canopy parameter estimates. The sometimes impressively accurate canopy structure parameter estimation via image analysis, coupled with its independence from frame brightness and BRDF effects and

minimal requirements for user input, emphasize the importance of these findings, at least for high canopy closure stands. Although the computational cost associated with parameter estimation is currently substantial, continuous improvements in processing power and script optimization is expected to reduce the cost to manageable levels.

## 5.4. Evaluation of Field Data Collection Methods

It was mentioned in Chapter 3 that the availability of spatially precise data is an invaluable resource for methodology refinement that could determine the success or failure of the investigation. Because, at the same time, a field data collection campaign that involves survey-grade measurements is a very expensive endeavor, it is important to assure that the data collected meets the anticipated standards. Some of the lessons learned are outlined below for the benefit of the reader contemplating similar field data collection efforts.

Distance measurements obtained by electronic range devices are very reliable when taken using a line of sight free from any obstructions. However, measurements acquired under canopy may be prone to systematic biases, especially in the presence of dense understory vegetation. Up to 5% distance errors could be expected where portions of tree stems, branches, or leaves are contained in a 0.5m-radius virtual cylinder centered on the line of sight. Selection of sampling sites, and identification of reference objects used in plot georeferencing should be scheduled, if possible, after the acquisition of imagery for four reasons, presented here in decreasing order of importance: 1) On-site measurement accuracy evaluation is possible. 2) The availability of imagery allows plot allocation conditional upon frame boundaries. It might be desirable to avoid frame edges so that, for example, BRDF effects could be minimized. 3) Identification of suitable

reference objects used for plot referencing in image frame coordinates is much easier on digital or hard copies of the imagery and allows for an evaluation of contrast between a candidate reference object and the image background. 4) High-resolution imagery is an excellent navigation tool.

Dense forest canopies and a paucity of objects that can be used as positional reference often necessitate lengthy transects with many vertices for plot boundary determination in image coordinates. Regardless of how careful the instrument operator is, angular and distance measurement errors are bound to happen and can be corrected relatively easily when the personnel and equipment are still in the field. Unfortunately, it requires only one measurement error to convert the plot center from a point to a polygon of substantial size and thus deprive the analysts from the opportunity to use the plot information in a spatially explicit manner. The importance of the ability to verify measurement accuracy in the field is appreciated when expensive plot data becomes useless because it cannot be placed accurately on the image frame (M. Wulder, personal communication, 2000).

The use of the Forest Inventory and Analysis (FIA) field data collection protocol undoubtedly enhances the potential for a wider application of these study findings, but it also reduced plot allocation flexibility especially where stand homogeneity is a prerequisite for plot installation and in forests exhibiting intense fragmentation. In addition, the use of the FIA protocol often necessitates installation of a larger number of transect vertices, particularly in dense stands and inclined terrain.

## 5.5. Further Research Opportunities

Slope break computations were implemented using a set of heuristic rules whose mathematical description was presented in equations 33b-d in Chapter 3. It was stated that the appropriate value for the coefficient at the right side of equation 3.3c could be identified by examining the DNs of imagery transects for each of the cover types present. Such a requirement for user input could be relaxed by modifying Equation 3.3c to include an upper slope break length limit. It was observed that DN reduction along a transect connecting a pixel identified as a tree apex and a local DN minimum (corresponding to a canopy opening in shadow) is very often sigmoidal. The pixel along the transect at which the first decrease in the DN reduction rate occurs could be used to identify the proper upper slope break length limit aforementioned. Tentative implementation of a modified heuristic rule revealed that the proposed slope break length limits are cover type specific. Comparisons between heuristic-rule-estimated slope break lengths and field observations of crown extents showed that the former are unbiased and of similar variability to the one obtained by the current version of heuristic rule implementation.

Canopy closure estimates obtained in Chapter 3 treated tree crowns as opaque objects. Hence, these canopy closure estimates are likely exaggerated in comparison to the traditional definition of canopy closure (i.e. the percent of the sky sphere that can be observed from the ground). A link between the two canopy closure definitions can potentially be obtained by comparing the canopy closure estimates obtained in this study to canopy closure estimates obtained by digital hemispherical canopy photographs acquired at 4, equally-spaced points in each of the 134 subplots. Preliminary investigations have shown that the relationship between opaque and "transparent" canopy

closure definitions is cover type specific and of moderate strength. Estimate transformation, however, was found to improve estimate correlation.

It was shown in Chapter 4 that apparent differences in co-occurrence matrix structure sometimes remained elusive when matrix structure was quantified via computation of secondary features. Such observations raised skepticism as to whether the use of secondary features is the most powerful alternative for texture quantification and lead to the development of a matrix discrimination technique. The latter attempts to identify those matrix elements that contain maximum discrimination potential. The idea is particularly attractive given that it does not require feature extraction and thus is not sensitive to feature dimensionality problems.

## 5.6. Conclusion

To date, distributed forest attribute information is obtained via either stand cruising or aerial photo interpretation. Budget constraints, reductions in the number of experienced photointerpreters available, and the need for digital integration of information all necessitate solutions that can provide forest attribute information from digital means. High-resolution, digital, airborne imagery appears to be the most promising technology capable of delivering forest information products that meet current needs and expectations. The work compiled in this dissertation asserts the potential of airborne digital imagery to serve cover type classification purposes and the extraction of information related to forest canopy structure under high stand density conditions. Additional investigations would be needed to determine how, and if, the same technology can be used to deliver the same types of information in different stand density conditions or in other biotic regions.

## Literature Cited


Canny, J.F. 1986. A computational approach to edge detection, *IEEE Tran. Pattern Anal. Mach. Intel.*, 8:679-689.

Edwards, G. 1995. Methods for assessing local map accuracy in thematic classifications derived from remotely sensed imagery, *Proc. 17th International Cartographic Conf.*, Barcelona, Spain, p. 1521-1530.

Fortin, M.-J., and P. Drapeau. 1995. Delineation of ecological boundaries: comparison of approaches and significance tests, *Oikos*, 72:323-332.

Friedl, M.A., C.E. Brodley, and A.H. Strahler. 1999. Maximizing land cover classification accuracies produced by decision trees at continental to global scales, *IEEE, Trans. Geosci. Rem. Sensing*, 37:969-977.

Hansen, M.C., R.S. Defries, J.R.G. Townsend, and R. Sohlberg. 2000. Global land cover classification at 1km resolution using a classification tree approach, *Int. J. Rem. Sensing*, 21:1331-1364.

Mikkola, J, and P. Pellikka. 2002. Normalization of bi-directional effects in aerial CIR photographs to improve classification accuracy of boreal and subarctic vegetation for pollen-landscape calibration. *Int. J. Rem. Sensing*, 23:4719–4742.

Pekkarinen, A., and V. Sarvi, V. 2002. Detection of clearcuttings with help of high-altitude panchromatic aerial photographs and image segmentation, *Proc. Operational Tools in Forestry using Remote Sensing Techniques*, Forest SAT Symposium, Edinburgh, Scotland (CDROM).

Pitas, I. 1993. *Parallel Algorithms for Digital Image Processing, Computer Vision, and Neural Networks*, John Wiley, New York.

Prewitt, J. 1970. Object enhancement and extraction. In *Picture Processing and Psychopictorics*, B. Lipkin and A. Rosenfeld [Eds], Academic Press, New York.

Roberts, L.G. 1965. Machine perception of three dimensional solid, *Optical and Electro-optical Information Processing*, J.T. Tippell (Ed), MIT Press, Massachusetts.

# APPENDIX 1

## A.1. Crown delineation

Let $[V_1\ V_2\ \ldots\ V_n]^T$ an n-element vector of distance and azimuth offsets from tree stems in the subplot coordinate system. Each vector element represents field measurements of vertices on the crown periphery as the latter is defined when viewed from above. Hence, the term 'crown' in this application corresponds to the projected-to-the-ground portion of tree foliage that is unobstructed by the foliage of adjacent trees when viewed from directly above. For simplicity in the example presented here it is assumed that the stem is dimensionless (a point), it is positioned at the origin of the coordinate system, and the first vector element belongs on the Y-axis (Figure A.5). Note that figures in this dissertation, including the Appendices often contain color. The objective is to link the planar representation of vector elements (points A to D in Figure A.5), by using a closed convex spline. The spline is assumed to depict the periphery of the crown. It should pass through all the field-measured points (exact representation) and, preferably, maintain a derivative everywhere along its length (absence of discontinuities). The last criterion provides the spline with an aesthetically appealing, smooth form characteristic of objects in natural settings. The objective is stochastic in nature since there is an infinite number of splines that meet the convexity, point exactness, and continuity criteria.

One possible spline realization is produced as a linear combination of circular arcs and projected arc components. The algorithm that generates the crown realization rotates each vector element $V_i$ until the azimuth of its rotated version coincides with the azimuth of the next-in-sequence vector element $V_{i+1}$. $V_i$ rotation around the origin (tree stem) draws a circular arc segment, which in the illustrative example of Figure A.5 is

represented by a dashed line. Generally, sequential vectors have different lengths ($|V_i| \neq |V_{i+1}|$), so the arc segment produced by rotation of $V_i$ would miss the vertex of $V_{i+1}$. In such cases, the difference $|V_i|-|V_{i+1}|$, measured along $V_{i+1}$, is bridged by shifting the projection of the arc segment on the X axis proportionally to the $(|V_i|-|V_{i+1}|)/|V_i|$ ratio. Arc shifting along the X-axis ensures that sequential arc segments, represented with solid, colored lines in Figure A.5, would form a closed convex spline. Because the derivative is meaningful everywhere on a circle or forms of circle translation, every spline derived with this algorithm is free of discontinuities.

Spline coordinates for each quadrant can be calculated using the following formulae:

$$S_y = (\pm)\sqrt{(R_{y(i+1)} - R_{yi})^2 - X^2}\,, \tag{A.1}$$

$$S_x = (\pm)\left[\sqrt{(R_{y(i+1)} - R_{yi})^2} + \frac{(R_{x(i+1)} - R_{xi}) - (R_{y(i+1)} - R_{yi})}{(R_{y(i+1)} - R_{yi})} X\right], \quad \forall X \in [R_{xi}, R_{x(i+1)} - R_{xi}] \tag{A.2}$$

where $R_{xi}$ and $R_{x(i+1)}$ are the vertex coordinates of elements $V_i$ and $V_{i+1}$ on the X-axis, and $R_{yi}$ and $R_{y(i+1)}$ are the vertex coordinates of $V_i$ and $V_{i+1}$ on the Y-axis. Note that the signs of $S_x$ and $S_y$ are quadrant specific, with $S_y$ taking positive values in quadrants 1 and 4 and negative values in quadrants 2 and 3. $S_x$ takes positive values in quadrants 1 and 2 and negative values in quadrants 3 and 4.

Crown representation fidelity is a function of crown shape, number of offset measurements, and the number of spline vertices calculated. Trees in even-aged coniferous stands have crown projections to the ground that approximate circles. Four to five offset measurements would, in general, suffice for delineating regularly shaped crowns. In uneven aged deciduous stands, tree competition for light and nutrients,

management practices, and disturbances, among other factors, often result in polymorphic, irregular crowns. In such circumstances, adequate crown delineation may require more than 15 crown-offset measurements. Spline segment vertices were calculated for 3cm increments along the X and Y axes.

The spline-based crown delineation approach outlined above, produces small overlapping regions between adjacent trees. In GIS terminology these small regions are known as "sliver polygons" and need to be eliminated prior to GIS-based analysis operations. Maintaining sliver polygons would, for example, result in a positive bias of average subplot crown diameter estimates. A sliver polygon between two adjacent touching crowns could be eliminated by merging it with the largest adjacent crown, or with the crown of the taller tree. Or it could be dissected using a line perpendicular to the line that joins the stems of the two trees, with each of the two new polygons produced by the dissection subsequently merged to the corresponding crown. The proper sliver polygon elimination approach was selected in each case after consulting field notes with information on the vertical arrangement and the relative crown height between adjacent trees. Crown polygons were organized as ArcInfo GIS vector layers in subplot coordinate system.

## A.2. Crown centroid calculation

All GIS software packages automatically calculate the area of polygons in vector layers. Centroid calculation is usually offered as an option. However, most packages, including ArcInfo, calculate a pseudo rather than the true centoid. The pseudo-centroid is calculated as the center of the bounding rectangle around a polygon. Note that coordinate system rotation would affect the location of pseudo-centroids. Depending on polygon

shape, there might be a significant discrepancy between the true and the pseudo centroid. The area $A$ of a polygon and coordinates ($C_x$, $C_y$) of its true centroid can be calculated as:

$$A = \frac{1}{2}\sum_{i=1}^{n}[(X_i Y_{i+1} - X_{i+1}Y_{i)}], \tag{A.3}$$

$$C_x = \frac{1}{6A}\sum_{i=1}^{n}[(X_i + X_{i+1})(X_i Y_{i+1} - X_{i+1}Y_{i)}], \tag{A.4}$$

$$C_y = \frac{1}{6A}\sum_{i=1}^{n}[(Y_i + Y_{i+1})(X_i Y_{i+1} - X_{i+1}Y_{i)}], \tag{A.5}$$

Compared to crown centroids, tree stems are more frequently located close to the visible crown periphery, or even outside of it, particularly in uneven aged deciduous stands (Figure A.3). Although it is theoretically possible for either the true or pseudo centroids to lay outside the crown, in practice this is very rarely the case, especially for true centroids, because visible-from-above crown portions tend to have convex peripheries (Figure A.6). Increasingly irregular crowns exhibit larger discrepancies between their true and pseudo centroids (Figure A.6). Therefore, true crown centroids are a reasonable choice when there is a need for point representations of crowns.

## A.3. Crown diameter calculation

Crown diameter is perhaps an awkward term because of its implicit reference to a circular tree crown shape is often unrealistic. However, it is frequently used as input in green biomass, wood volume, crown closure, and wildlife habitat models. A crown diameter estimate can be calculated efficiently as the diameter of a circle of the same area. An alternative estimate can be obtained by measuring the within-crown length of linear segments that pass through the crown's centroid. The second approach is

potentially superior to the first because it accounts for crown shape. Diameter estimate bias can be introduced when only a small number of linear segments is employed. Experimentation with many crown shapes and sizes revealed that for regularly shaped, nearly circular crowns the linear-line-segment-derived estimate is equivalent to the diameter of a circle occupying the same area with the crown, provided that an adequate number of line segments has been utilized (Figure A.7). For significantly non-circular crown shapes, the circle-area-based estimates are consistently larger that those calculated with the line segment approach (Figure A.7).

## A.4. Bidirectional Reflectance Distribution Function Model

The linear, kernel-driven, three-parameter model developed by Roujean et al. (1992) is a semi-empirical approach designed to correct BRDF effects for heterogeneous surfaces. The model considers the surface reflectance of an object to be the synergistic effect of two processes: a diffuse reflection component that accounts for the geometrical structure of opaque reflectors located at the surface of the object and a scattering contribution from the volume of the object. The model in a generic form can be expressed as

$$\rho = \alpha\rho_{geom} + (1-\alpha)\rho_{vol} \tag{A.6}$$

where $\rho$ is the object's spectral reflectance, and $\alpha$ is an empirical coefficient that characterizes the relative weight of the geometric and volume components $\rho_{geom}$ and $\rho_{vol}$ respectively. The model can be explicitly written as

$$\rho(\theta_s,\theta_v,\varphi) = k_0 + k_1 f_1(\theta_s,\theta_v,\varphi) + k_2 f_2(\theta_s,\theta_v,\varphi) \tag{A.7}$$

where $\theta_s$ is the solar zenith angle, $\theta_v$ is the view zenith angle, and $\varphi$ is the relative azimuth angle. $k_0$ is the bi-directional reflectance for $\theta_s = \theta_v = 0$, $k_1$ is the weight for the geometric scattering function $f_1$ and $k_2$ is the weight for volume scattering kernel function $f_2$. The physical meaning of the angular parameters $\theta_s$, $\theta_v$, and $\phi$ is shown in Figure A.4. Coefficients $k_0$, $k_1$, and $k_2$ are determined empirically. Functions $f_1$ and $f_2$ are defined as

$$f_1(\theta_s, \theta_v, \varphi) = \frac{1}{2\pi}[(\pi - \varphi)\cos\varphi + \sin\varphi]\tan\theta_s \tan\theta_v - \frac{\tan\theta_s + \tan\theta_v + G}{\pi} \tag{A.8}$$

$$f_2(\theta_s, \theta_v, \varphi) = \frac{4}{3\pi} \frac{1}{\cos\theta_s + \cos\theta_v}\left[\left(\frac{\pi}{2} - \xi\right)\cos\xi + \sin\xi\right] - \frac{1}{3} \tag{A.9}$$

where $\xi$ is derived from

$$\cos\xi = \cos\theta_s \cos\theta_v + \sin\theta_s \sin\theta_v \cos\varphi \tag{A.10}$$

and $G$ from

$$G = \sqrt{\tan^2\theta_s + \tan^2\theta_v - 2\tan\theta_s \tan\theta_v \cos\varphi} \tag{A.11}$$

Typical BRDF correction implementation entails multiplying pixel values with the $\rho_0(\theta_{s_0}, \theta_{v_0}, \varphi_0)/\rho(\theta_s, \theta_v, \varphi)$ ratio, also known as the BRDF coefficient, where $\rho_0(\theta_{s_0}, \theta_{v_0}, \varphi_0)$ is pixel reflectance for standard viewing and illumination geometry and $\rho(\theta_s, \theta_v, \varphi)$ for actual geometry. Table A.3 shows the geometry parameter values for standard and actual BRDF corrections used in this study.

The empirical component of the model, is demonstrated by the fact that model intercept and function weighting coefficients are surface or, for the purposes of this study, cover type dependent. In practice, their values are determined by using radiometric

measurements of cover type reflectance either *in situ*, in lab settings (Loechel et al., 1997, Deering et al., 1999, Weiss et al., 1999), or alternatively by examining correlations between DNs and scattering angles of reference sample areas on overlapping images (Mikkola and Pellikka, 2002). In the absence of known coefficient values appropriate for the biome present in the study area, coefficient values were determined via the optimization exercise outlined in Chapter 2. In the interest of limiting the number of coefficient value combinations needed to be evaluated, a set of values found to perform well in a warm temperate forest were used for the initiation of the optimization process (Table A.2). Given that the imagery set was acquired with a nadir looking sensor and a maximum view angle of $12.36^0$ (Table A.3) over gentle terrain, combinations of $k_0$, $k_1$, and $k_2$ values that yielded correction coefficients outside the 0.7-1.3 range were rejected as invalid.

## A.5. Maximum likelihood classification

Maximum likelihood (ML) is a supervised classification method. The probability of a pixel belonging to each of a predefined set of classes is calculated, and the pixel is assigned to the class for which the probability is highest. ML is based on the Bayesian probability formula:

$$P(q,r) = P(r \mid q)P(q) = P(q \mid r)P(r) \tag{A.12}$$

where $q$ and $r$ are generally called 'events'. $P(q,r)$ is the probability of coexistence of events $q$ and $r$, $P(q)$ and $P(r)$ are the prior probabilities (of occurrence) of events $q$ and $r$, and $P(q \mid r)$ is the conditional probability of event $q$ given (the presence of) event $r$. $P(r \mid q)$ is defined in the same manner. In remote sensing applications, an event is

equivalent to a pixel for which a size $k$ vector is defined ($k$ represents the pixel's spectral dimension or the number of bands present). If $q_i$ is the vector of $k$ spectral values (DN, radiance or reflectance) for the i$^{th}$ pixel and $r_j$ is information class $j$ then (A.12) can be rewritten as:

$$P(r_j \mid q_i) = \frac{P(q_i \mid r_j)P(r_j)}{P(q_i)} \tag{A.13}$$

It is commonly assumed that $P(q)$ is uniformly distributed, and therefore its function in (A.13) is to standardize the fraction on the equation's right hand side. Hence, (A.13) can be rewritten as:

$$P(r_j \mid q_i) \propto P(q_i \mid r_j)P(r_j) \tag{A.14}$$

Pixel $i$ can thus be allocated to class $\tau$ that maximizes $P(w_k \mid x_i)$ in (A.14). The classification criterion is then expressed as:

$$W_k = \max[P(q_i \mid r_j)P(r_j)] \quad \forall w_j \tag{A.15}$$

Equation (A.15) offers the maximum a posteriori solution, which maximizes the product of conditional probability and prior probability. In most remote sensing classification applications, the prior probability $P(r)$ is also set to be uniformly distributed primarily because often there is no information on class distribution in the area of interest, which further reduces (A.15) to:

$$P(r_j \mid q_i) \propto P(q_i \mid r_j) \tag{A.16}$$

Allocating pixel $i$ to class $\tau$ that maximizes (A.16) provides the maximum likelihood solution.

Normally, the conditional probability $P(q_i \mid r_j)$ is assumed to follow a Gaussian distribution. $P(q_i \mid r_j)$ can then be expressed as:

$$P(q_i \mid r_j) = \frac{1}{\sqrt{2\pi^k \mid C_j \mid}} \exp(-\frac{1}{2}(\boldsymbol{q}_i - \boldsymbol{\mu}_j)^{\mathrm{T}} \boldsymbol{C}_j^{-1}(\boldsymbol{q}_i - \boldsymbol{\mu}_j) \tag{A.17}$$

where $\boldsymbol{C}_j$ is the covariance matrix of class $r_j$ with dimension $k$, $\mu_j$ is the mean vector of class $r_j$, and $|\cdot|$ denotes the determinant.

In practical applications, equation (A.17) can be reduced to the following expression by taking the natural logarithm:

$$\ln[P(q_i \mid r_j)] = \frac{-1}{2} k \ln(2\pi)(\frac{-1}{2}) \ln \mid \boldsymbol{C}_j \mid -\frac{1}{2}(\boldsymbol{q}_i - \boldsymbol{\mu}_j)^{\mathrm{T}} \boldsymbol{C}_j^{-1}(\boldsymbol{q}_i - \boldsymbol{\mu}_j) \tag{A.18}$$

which is computationally advantageous to (A.17) because it avoids the exponential term. Because the term $k\ln(2\pi)$ is the same for all classes, it can be regarded as a constant and be eliminated from equation (A.18) without affecting the ranking of the $\ln[P(q_i \mid r_j)]$ values. Equation (A.18) is finally multiplied by –2 to give:

$$-\ln[P(q_i \mid r_j)] = \mid \boldsymbol{C}_j \mid + (\boldsymbol{q}_i - \boldsymbol{\mu}_j)^{\mathrm{T}} \boldsymbol{C}_j^{-1}(\boldsymbol{q}_i - \boldsymbol{\mu}_j) \tag{A.19}$$

Obviously, maximizing equation (A.17) is equivalent to minimizing equation (A.19). It should be noted that the second term in the right hand side of equation (A.19) is the Mahalanobis distance, and therefore the geometrical shape of the cloud of points in $k$-dimensional spectral space formed by a set of pixels belonging to a given class can be described by an ellipsoid. The shape of the ellipsoid depends on the covariance among the features in the spectral space. In the presence of only two bands (two dimensional

spectral space), the maximum likelihood function delineates ellipsoidal, equally-probable contours, which can be regarded as decision boundaries. A careful examination of equation (A.19) reveals that an inadequate number of pixels in a class and/or a large number of bands involved can produce considerable biases in the computation of the class statistics, including the mean vector and covariance matrix, which is ultimately translated into biases in the classification results. Hence, there is a need for an accurate estimate of class statistics if maximum likelihood classification is to perform in a satisfactory way (Landgrebe, 1998). Accurate estimates of such statistics, sometimes known as distribution moments, representative of a class can be computed when pixel membership in the class spectral signature is adequate.

## A.6. Cross-validation and classification accuracy assessment

An important part of every classification is the assessment of its accuracy. The term 'accuracy' denotes the level of agreement between class labels assigned by the image processing method and class allocations based on ground data. Often, ground data do not necessarily represent reality, due to observation and recording errors, or because of the time elapsed between observations and the acquisition of imagery. If a separate set of ground observations is not available, accuracy can be evaluated relative to the data set used to train the classifier, but the degree of accuracy will be overstated. In these circumstances, the use of cross-validations is preferable. In cross validation, ground observations are subdivided into $n$ subsets of approximately equal size. The majority ($n$-$1$) of these subsets are used for training the classifier. The remaining $n^{th}$ subset is used for classification error estimation. Each of the $n$ subsets is used in turn for testing, with the

remaining ($n$-$1$) subsets being used for training. Once this cycle of training and testing is completed, the error estimates are combined (Schaffer, 1993).

The most common measures of classification accuracy assessment in remote sensing are based on the computation of the confusion or contingency matrix, a $v$ x $v$ square matrix, where $v$ is the number of classes. The matrix shows the relationship between the class labels assigned by the classifier and the class labels assigned by ground observations. The diagonal elements represent correctly classified entries while off-diagonal elements correspond to classification errors. An index of overall classification accuracy can be obtained by dividing the sum of the diagonal entries of the confusion matrix by the total number of samples. Overall accuracy estimates can be misleading, however, as they do not provide any class-specific accuracy estimate nor do they account for the relative proportion of samples tested. Accuracy estimates for individual classes are embedded in the concepts of producer's accuracy and user's accuracy. For each information class $i$ in a confusion matrix, the producer's accuracy is calculated by dividing the entry ($i$,$i$) by the sum of column $I$ (the total number of class $i$ pixels in the ground data), while the user's accuracy is obtained by dividing the entry ($i$,$i$) by the sum of row $i$ (the total number of class $i$ pixels labeled by the classifier). Thus the producer's accuracy indicates the proportion of samples in the testing data set that are correctly recognized by the classifier. The user's accuracy measures the proportion of samples identified by the classifier as belonging to class $i$ that agree with the testing data. It is evident that all these indices utilize only a small portion of the information in the confusion matrix. A multivariate index, known as the kappa coefficient (Cohen, 1960), that largely overcomes the limitation of the indices mentioned previously, is favored by

many analysts. The kappa coefficient quantifies the probability of chance agreement of class labels assigned by the classifier and those present in the testing data set. It should be noted that a number of authors (e.g. Foody, 2000) argue that the kappa coefficient overestimates chance agreement and underestimates accuracy and they suggest alternative formulations. In any case, the standard kappa coefficient is defined as:

$$\hat{k} = \frac{N\sum_{i=1}^{v} x_{ii} - \sum_{i=1}^{v} x_{i+}x_{+i}}{N^2 - \sum_{i=1}^{v} x_{i+}x_{+i}} \tag{A.20}$$

where $\hat{k}$ (k-hat) is the estimated kappa coefficient, $v$ is the number of rows and columns in the matrix, $x_{ii}$ is the matrix element at row and column $i$, + represents row and column summation over the index, and $N$ is the total number of samples in the testing data set.

An important property of this index is that its ratio to the square root of its variance follows a Gaussian distribution, provided that the number of samples in the confusion matrix is sufficiently large. Hence, the ratio $\hat{k}/\sqrt{\hat{\sigma}_{[\hat{k}]}}$ can be used for parametric comparison of kappas obtained by using different classifiers, and variable testing sample sizes. The large sample variance of kappa (Rosenfield and Fitzpatrick-Lins, 1986; Hudson and Ramm, 1987) is computed as:

$$\hat{\sigma}_{[\hat{k}]} = \frac{1}{N}\left[\frac{\theta_1(1-\theta_1)}{(1-\theta_2)^2} + \frac{2(1-\theta_1)(2\theta_1\theta_2 - \theta_3}{(1-\theta_2)^3} + \frac{(1-\theta_1)^2(\theta_4 - 4\theta_2{}^2}{(1-\theta_2)^4}\right] \tag{A.21}$$

where

$$\theta_1 = \sum_{i=1}^{v} \frac{x_{ii}}{N}, \tag{A.22}$$

$$\theta_2 = \sum_{i=1}^{v} \frac{x_{i+} x_{+i}}{N^2}, \tag{A.23}$$

$$\theta_3 = \sum_{i=1}^{v} \frac{x_{ii}(x_{i+} x_{+i})}{N^2}, \text{ and} \tag{A.24}$$

$$\theta_4 = \sum_{i=1}^{v} \sum_{i=1}^{v} \frac{x_{ii}(x_{i+} x_{+i})^2}{N^3} \tag{A.25}$$

The test of significance between two independent kappas is formulated as (Rosenfield and Fitzpatrick-Lins, 1986):

$$Z = \frac{\hat{k}_1 - \hat{k}_2}{\sqrt{\hat{\sigma}_{[\hat{k}_1]} + \hat{\sigma}_{[\hat{k}_2]}}} \tag{A.26}$$

where Z is the standard normal deviate. A Z score larger than 1.645, 1.960, or 2.576 would indicate significant differences between the two kappas at the 90, 95, and 99 percent probability level, respectively.

## Literature Cited


Cohen, J. 1960. A coefficient of agreement for nominal scales, *Educational and Psychological Measurement*, 20:37-46.

Deering, D.W., T.F. Eck, and B. Banerjee. 1999. Characterization of the reflectance anisotropy of three boreal forest canopies in spring-summer. *Rem. Sensing Environ.*, 67:205-229.

Foody, G.M., 2000. Accuracy of thematic maps derived by remote sensing, In *Proc. of the Accuracy 2000 Conference*, G.B.M. Heuvelink, and M.J.P.M. Lemmens [Eds], Delft University Press, Amsterdam, pp217-224.

Hudson, W.D., and C.W. Ramm. 1987. Correct formulation of the kappa coefficient of agreement, *Photogramm. Eng. Rem. Sensing*, 53:421-422.

Landgrebe, D. 1998. Information extraction principles and methods of multispectral and hyperspectral image data. In *Information Processing for Remote Sensing*, C.H. Chen [Ed], World Scientific Publishing, River Edge, New Jersey.

Loechel, S.E., C.L. Walthall, E. Brown de Coulston, J. Chen, B.M. Markham, and J. Miller. 1997. Variability of boreal forest reflectances as measured from a helicopter platform. *J. Geophys. Res.*, 102:495-503.

Mikkola, J, and P. Pellikka. 2002. Normalization of bi-directional effects in aerial CIR photographs to improve classification accuracy of boreal and subarctic vegetation for pollen-landscape calibration. *Int. J. Rem. Sensing*, 23:4719–4742.

Rosenfield, G.H., and K. Fitzpatrick-Lins. 1986. A coefficient of agreement as a measure of thematic classification accuracy, *Photogramm. Eng. Rem. Sensing*, 52:223-227.

Roujean, J.L., M. Leroy, and P.Y. Deschamps. 1992. A bi-directional reflectance model on earth's surface for the correction of remote sensing data, *J. Geophys. Res.*, 97:455-468.

Schaffer, C. 1993. Selecting a classification method by cross validation. *Mach. Learning*, 13:135-143.

Weiss, M., F. Baret, M. Leroy, A. Bégué, O. Hautecoeur, and R. Santer. 1999. Hemispherical reflectance and albedo estimate from accumulation of across-track sun-syncronous data, *J. Geophys. Res.*, 104:122-132.

# Tables

**Table A.1.** DAIS technical specifications

| | | |
|---|---|---|
| **Camera** | | |
| Manufacturer/model | DALSA CA-D7-1024T digital frame camera | |
| Array size | 1024 x 1024 pixels | |
| Pixel size | 12 x 12 micrometers (100% fill factor) | |
| Spectral resolution | 16 bits per pixel | |
| **Lenses** | | |
| Nominal focal length | 28mm | |
| Aperture range | F2.8 to F16 | |
| Angular field of view | 24.6 degrees | |
| **Interference filters** | | |
| Filter bandpasses | Blue | 450-530nm |
| | Green | 520-610nm |
| | Red | 640-720nm |
| | Near Infrared | 770-880nm |
| **Camera mount** | | |
| Model | Zeiss T-AS Gyro Stabilizer | |
| Roll/Pitch compensation range | ±5 degrees | |
| Yaw compensation | ±6.5 degrees | |
| Degree of stabilization | 1:10 to 1:30 | |
| **Camera control unit** | | |
| Maximum frame capture rate | 1 frame every 3.5 seconds | |
| Storage capacity | Sufficient for 8 hours continuous imaging at maximum frame capture rate | |
| **Sensor orientation** | | |
| Position | Post-processed kinematic GPS | |
| | $\sigma_x$: | 0.3m |
| | $\sigma_y$: | 0.3m |
| | $\sigma_z$: | 0.3m |
| Attitude | Applanix POS/AV 510 post-processed with GPS | |
| | $\sigma_{roll}$: | 20 arcsecs |
| | $\sigma_{pitch}$: | 20 arcsecs |
| | $\sigma_{yaw}$: | 60 arcsecs |

**Table A.2.** Coefficient values used in the Roujean et al. (1992) BRDF model for deciduous forest and those derived with the brightness normalization process.

| | | Coefficient | | | | | |
|---|---|---|---|---|---|---|---|
| | | Initial | | | Optimized | | |
| | | $k_0$ | $k_1$ | $k_2$ | $k_0$ | $k_1$ | $k_2$ |
| Band | Blue | 0.030 | 0.000 | 0.087 | 0.153 | 0.115 | 0.036 |
| | Green | 0.030 | 0.000 | 0.087 | 0.183 | 0.147 | 0.052 |
| | Red | 0.030 | 0.000 | 0.087 | 0.147 | 0.099 | 0.058 |
| | NIR | 0.400 | 0.040 | 0.295 | 0.281 | 0.058 | 0.301 |

**Table A.3.** Standard and actual BRDF viewing and illumination geometry parameter values used in brightness normalization.

| | | Standard Geometry | Actual Geometry | |
|---|---|---|---|---|
| Solar zenith angle[1] | $\theta_s$ | $35^0$ | Site II: $31.19^0 - 38.94^0$, Site I: $28.46^0 - 29.12^0$ | [2] |
| Solar azimuth angle[1] | $\varphi_s$ | $180^0$ | Site II: $127.09^0 - 154.58^0$, Site I: $169.12^0 - 195.48^0$ | [2] |
| View zenith angle | $\theta_v$ | $0^0$ | $0^0 - 12.36^0$ | [3] |
| View azimuth angle | $\varphi_v$ | NA[4] | $0^0 - 360^0$ | [3] |
| Relative view angle | $\varphi$[5] | NA[4] | $0^0 - 360^0$ | [3] |

[1] Computed using software available at http://www.susdesign.com/sunangle/, maintained by C. Gronbeck, Sustainable By Design, Seattle, Washington.
[2] Overlapping frame region specific, calculated for the region's center.
[3] Pixel specific.
[4] Nadir looking sensor.
[5] $\varphi = \varphi_s - \varphi_v$.

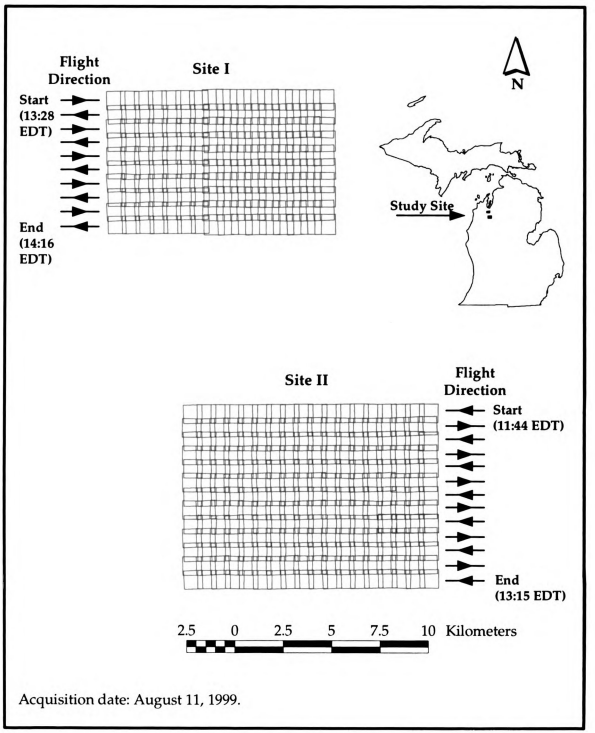


**Figure A.1.** Spatial arrangement of DAIS image frames for Sites I and II.

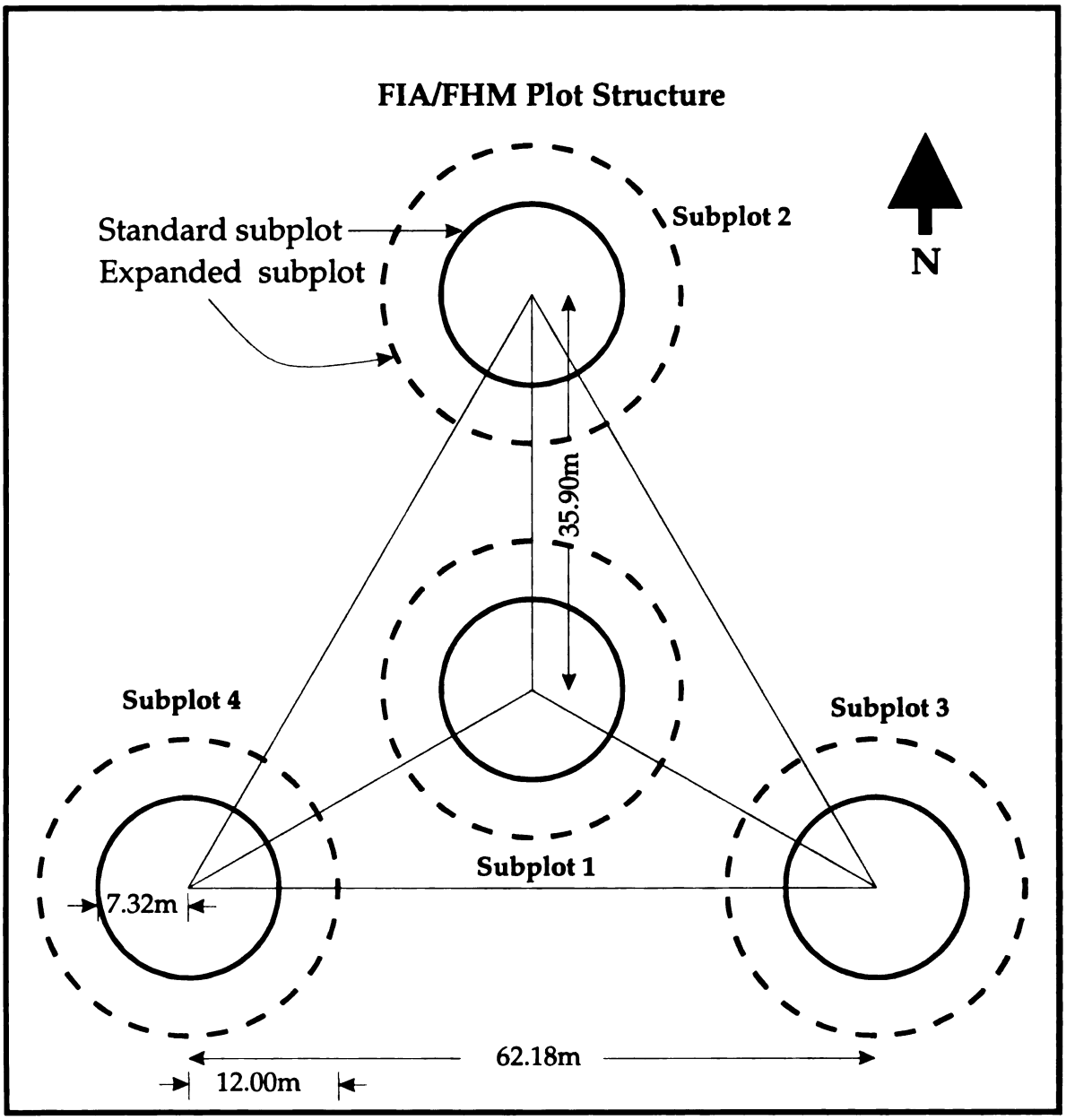


**Figure A.2.** Plot design according to the FIA/FHM protocol.

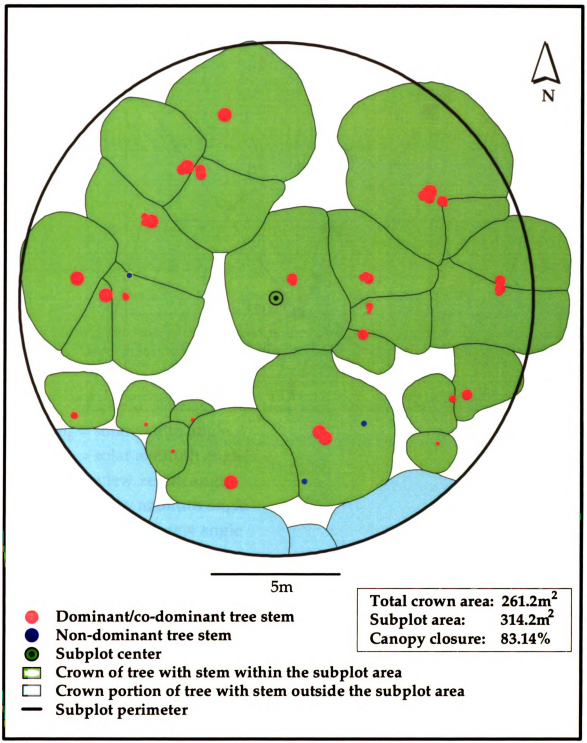


**Figure A.3.** Vertical tree crown projection map for a northern hardwood subplot (24B). Crowns correspond to the portion of tree foliage visible from above. Dots represent tree stems and are of size proportional to stem DBH.

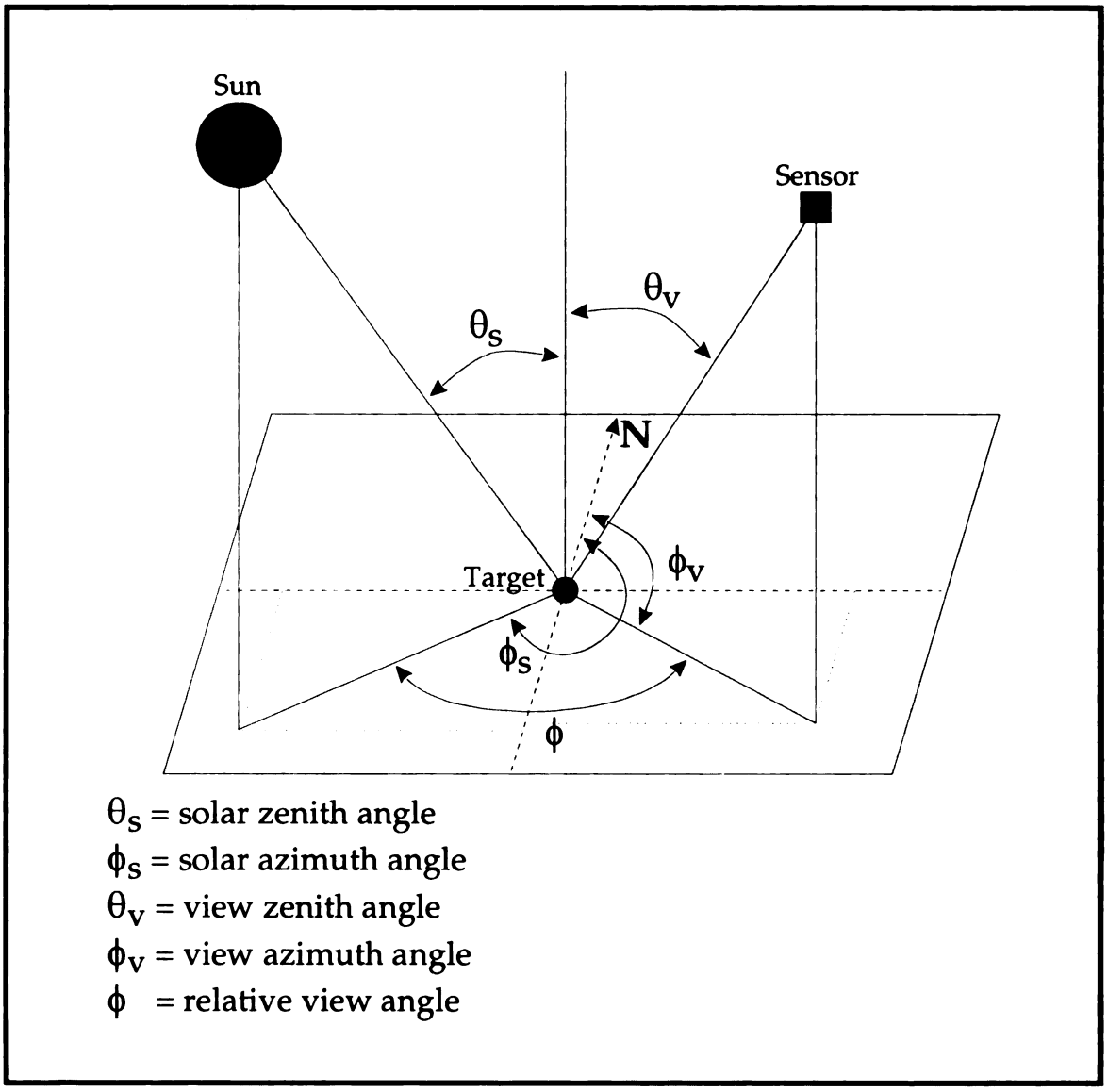


**Figure A.4**. Illustration of target viewing and illumination geometry, and associated angular parameters used in BRDF models. The figure, drawn in perspective, preserves angles but not distances.

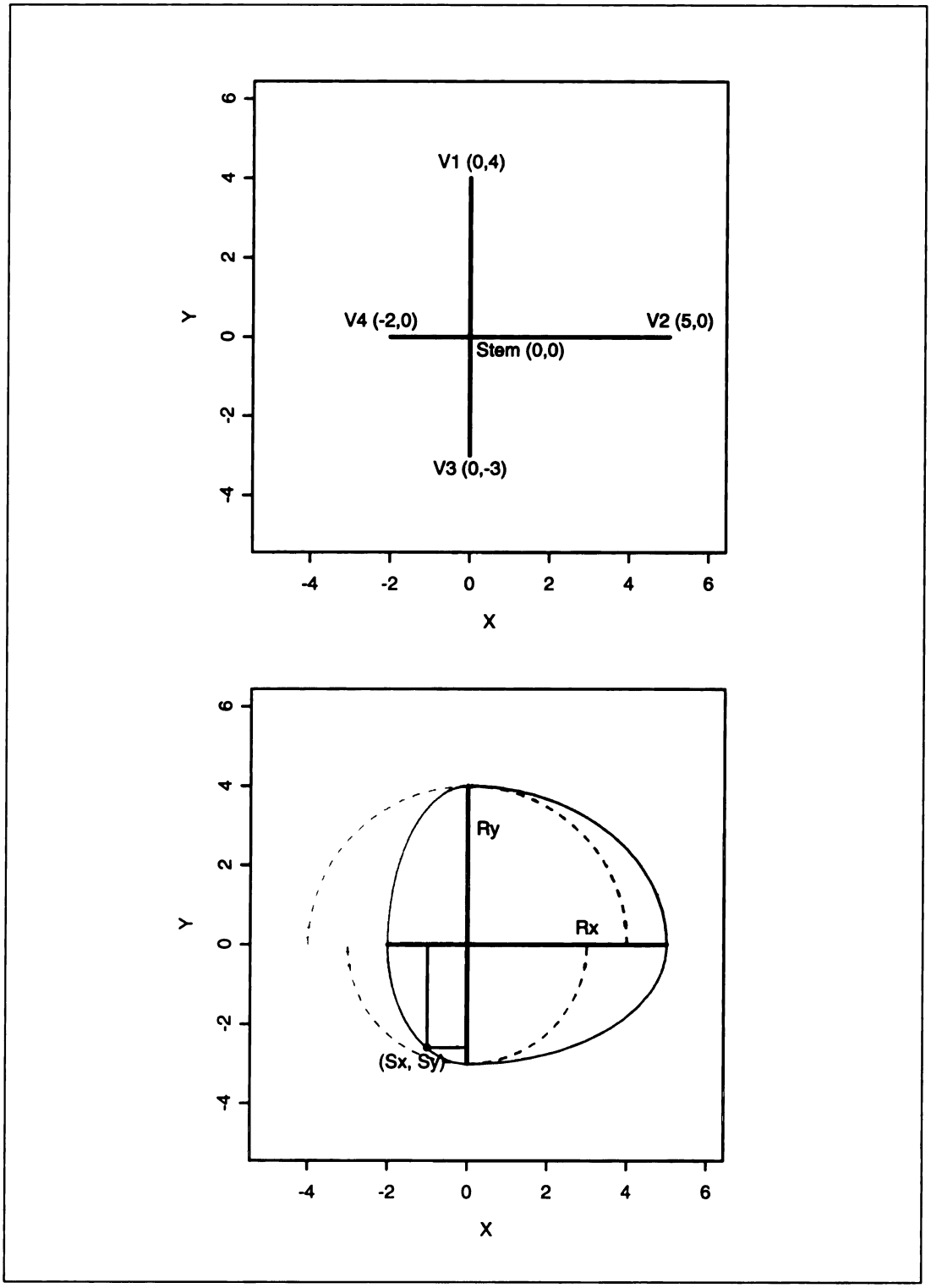


**Figure A.5.** Spline-based tree crown delineation using four, projected-to-the-ground offsets of crown periphery. Offsets are expressed as vectors $V_1$ to $V_4$. Dashed lines in the bottom part denote circular arc segments for each of the four quadrants defined by pairs of clockwise adjacent vectors. Solid line spline segments $S(S_x, S_y)$ represent the derived horizontal extent of the crown and are produced by circular arc shifting along the X-axis, proportional to the $(R_x-R_y)/R_x$ ratio. $R_x = |V_i|$ and $R_y = |V_{i+1}|$.

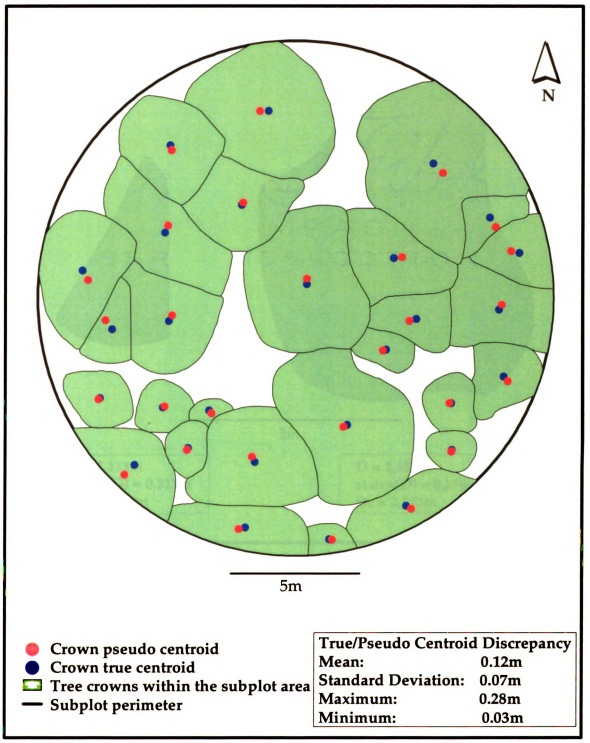


**Figure A.6.** Vertical tree crown projection map for a northern hardwood subplot (24B). Crowns correspond to the portion of tree foliage visible from above. Dots represent true and pseudo crown centroids.

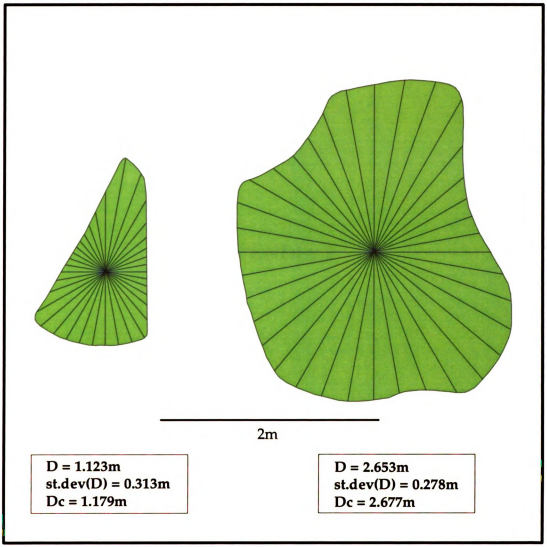


**Figure A.7.** Calculation of crown diameter D as the mean length of lines revolving at 10° increments around the crown's centroid. Dc denotes the diameter of a circle occupying the same area with the crown.

# APPENDIX 2

## B.1. Effects of Brightness/BRDF Normalization on Semivariogram Range Computation.

Let $Z(x_{i,j})$ be the digital numbers (DNs) of pixels in the 51 rows by 51 columns image depicted in Figure B.1a and corresponding to a portion of a coniferous forest stand in the near infrared band, where $i$ and $j$ represent image row and column indices respectively. An omnidirectional empirical variogram (Figure B.1b) computed for the image carries a range of approximately 5 distance (pixel width) units. Note that figures in this dissertation, including the Appendices often contain color. A linear translation $[(Z(x_{i,j})*1.5)-5000]$ of the image (Figure B.1c), similar to the one performed during brightness normalization has no effect on the form of the empirical variogram or its range, but it does alter the variogram's sill (Figure B.1d). Such variogram behavior is expected since addition or subtraction of a DN amount from all pixels does not affect the square difference of DNs in pixel pairs separated by distance $h$ (Chapter 3, Equation 3.2). At the same time multiplication of DNs with a constant is a monotonic operation that preserves the relative ordering of square difference sums for different lag increments. When however, the original DNs are processed with a non-monotonic or anisotropic function, such as the one depicted as a surface in Figure B.1f, the square difference of DNs for pixel pairs separated by distance $h$ and situated at or close to surface locations with high autocorrelation gradient will be smaller than the square differences of DNs for pixel pairs separated by the same distance $h$, but situated at surface locations characterized by weaker a anisotropy gradient, thus altering the variogram form and hence its range and sill. Because H-resolution images of forested landscapes contain intrinsic autocorrelation gradients, the effects of image DN processing with non-

monotonic, anisotropic operators on the image variogram would be detectable only when the autocorrelation gradient introduced by those operators would be weaker than the intrinsic autocorrelation gradient. Kernel-based BRDF models such as that by Roujean et al., (1992) involve image processing with functions that exhibit strong autocorrelation and bi-directional distribution factors (BRFs) usually within the 0.7 to 1.3 range. Therefore, under most circumstances, BRDF correction operations would only minimally, if at all, affect computed variogram parameters. In the example of Figure B.1, the image processing function represented as a surface, is bounded within the range aforementioned and, as expected, it does not modify the range of the corresponding variogram although it appears to influence its form, at least for the larger lag distances.

## B.2. Trend Surface Analysis

Let Z be a single band image with $Z(\boldsymbol{s})$ representing the value (DN, radiance, reflectance, etc.) of an image pixel at location $\boldsymbol{s}$ with spatial coordinates $(s_i,s_j)$, where $i$ and $j$ represent image row and column indices. Z, as any other image, can be modeled as a spatially continuous random surface of large-scale variations around a mean value. The model involves the fitting of polynomial functions of the spatial coordinates $\boldsymbol{s}(s_i,s_j)$ of each pixel, to corresponding image pixel values. The multiple regression model employed, known as ordinary least squares regression, may be written as

$$Z(\boldsymbol{s}) = x^T(\boldsymbol{s})\boldsymbol{\beta} + \varepsilon(\boldsymbol{s}) \qquad \text{(B.1)}$$

where $Z(\boldsymbol{s})$ is the image value at location $\boldsymbol{s}$, $x^T(\boldsymbol{s})\beta$ represents the trend or mean value of the surface at $\boldsymbol{s}$, and $\varepsilon(\boldsymbol{s})$ is a zero-mean random variable representing fluctuations from the trend. The $(\rho \times 1)$ vector of $x(\boldsymbol{s})$ consists of $\rho$ functions of the spatial coordinates $(s_i,s_j)$

of point $\boldsymbol{s}$. For a linear trend model $x(\boldsymbol{s}) = (1, s_i, s_j)^T$, for a quadratic model $x(\boldsymbol{s}) = (1, s_i, s_j, s^2_i, s^2_j, s_i s_j,)^T$, and accordingly for higher-order models. $\beta$ is a ($\rho$ x 1) vector of parameters to be estimated when the model is fitted to the pixel values. Ordinary least squares estimates $\hat{\beta}$ as

$$\hat{\beta} = (\boldsymbol{X}^T \boldsymbol{X})^{-1} \boldsymbol{X}^T Z \tag{B.2}$$

where $Z$ is the vector of pixel values and $\boldsymbol{X}$ is an ($n$ x $\rho$) matrix with row vectors $x^T(s_{ij})$, $i = 1, \ldots, n$, and j = 1, ... , $m$, with $n$ and $m$ representing the number of image rows and columns respectively.

In imagery of forested landscapes, $x^T(\boldsymbol{s})\beta$ can be thought of as the broad-scale DN variation due to, for example, topographic effects, vegetation ecotones, etc., and $\varepsilon(\boldsymbol{s})$ as the local DN variation due to the structural characteristics of forest canopy. In variogram analysis of forest stands depicted in high-spatial-resolution digital imagery and aiming at identifying the proper window size for subsequent local maximum filter (LMF) imagery processing (Chapter 3), the presence of a non-zero $x^T(\boldsymbol{s})\beta$ imagery component would introduce systematic biases in computed variogram ranges (Figure B.2) (Cressie, 1991), thus necessitating its elimination. The latter could be accomplished by estimating the value of vector $\beta$ elements in equation (B.1) so that $\varepsilon(\boldsymbol{s})$ could be isolated from $Z(\boldsymbol{s})$. Variogram analysis could then proceed using the $\varepsilon(\boldsymbol{s})$ image component only.

Unfortunately, equation (B.1) assumes that $\varepsilon(\boldsymbol{s})$ is independent among locations and has constant variance; thus in its equation (B.1) form $\varepsilon(\boldsymbol{s})$ cannot be thought of as representing the structural characteristics of forest canopy. One way to avoid the implausibility of the assumption in the basic form of the trend surface regression model is

to relax the assumption of $\varepsilon(s)$ independence by the use of the generalized least squares approach. The model then becomes

$$Z(s) = x^T(s)\boldsymbol{\beta} + U(s) \tag{B.3}$$

where $U(s)$ is again a zero-mean random variable representing fluctuation from the trend exhibiting a covariance function $C()$. In this formulation, the previous least squares estimates for $\beta$ is replaced by its generalized least squares equivalent

$$\hat{\beta} = (\boldsymbol{X}^T\boldsymbol{C}^{-1}\boldsymbol{X})^{-1}\boldsymbol{X}^T\boldsymbol{C}^{-1}Z \tag{B.4}$$

where $\boldsymbol{C}$ is an ($m*n$ x $m*n$) matrix of covariances between all possible $U(s_{ij})$ pairs in the image. Generalized least squares provide a way of including both first- and second-order variation in the model while assuring that parameter estimates allow for spatial dependence. The only remaining difficulty is that the covariance matrix $\boldsymbol{C}$ is unknown. In practice, the model described by equation (B.1) is fit to the pixel values initially using ordinary least squares regression. Regression residuals are used to estimate a variogram model $\hat{\gamma}()$, giving rise to an equivalent covariogram model $\hat{C}()$. The latter allows the construction of an estimated covariance matrix $\hat{\boldsymbol{C}}$ between pixel locations. Subsequently, the model described by equation (B.3) is fit to the pixel values using generalized least squares with the estimated covariance matrix $\hat{\boldsymbol{C}}$. This process adjusts both the model parameter estimates and the standard errors of the ordinary least squares regression for second-order autocorrelation. If necessary, the process can be iterative until estimates of $\hat{\boldsymbol{\beta}}$ and $\hat{C}()$ are obtained. The validity of the final model depends upon 1) the choice of an appropriate form of trend surface, and 2) the choice of an appropriate variogram model. The decomposition of the image into first- and second-order components in the

methodology described above is, to some extent, arbitrary. In reality, the two components are confounded; certain types of second-order variation can lead to trend-like effects making it impossible to objectively distinguish between the two components. Additional obstacles for the application of the generalized least squares approach appear when process automation is contemplated, primarily because appropriate covariogram model specification necessitates analyst intervention.

In this study, the effect of trend on variogram range was investigated. Variogram ranges were computed (*i*) using the original DNs, (*ii*) after DN processing with ordinary least squares, and (*iii*) after DN processing with five-iteration, generalized least squares. More than two hundred 50-pixel-wide, circular imagery regions with centers within a subplot, and equally distributed among cover types were analyzed in the process. The range of empirical variograms was determined automatically as the shorter lag distance for which the slope of line segments connecting vertices of a spline (Hastie and Tibshirani, 1990) fitted to the empirical variogram was lower than 5%. The lag increment was set to one third of a pixel.

Fitting of the spline to the empirical variogram was a step necessary towards process automation. Attempts to determine the range of empirical variograms as the lag distance for which the corresponding semivariance estimate declines for the first time (Franklin et al., 1996) proved inappropriate because they were susceptible to sporadic semivariance underestimation for short lags. Such a circumstance can be observed at the post-trend-processed semivariance estimates in Figure B.2 between lag = 2.66 and lag = 3.00. Using the spline in that case allowed restoring the automatically computed

range from 3.00 distance units (pixels) to 5.00, which coincides with the range determined with visual inspection of the variogram.

Analysis revealed that the instances of unbounded variograms calculated using the original DNs, were eliminated when either ordinary or generalized lease squares trend removal was used. In 83% of the total number of imagery regions processed, both regression models produced identical variogram ranges and in 13% the difference of computed range was 1 lag increment (i.e. $1/3^{rd}$ of a pixel). For 4% of the regions, the use of ordinary and generalized least squares regression on region DNs produced variogram ranges that differed in magnitude between 2 and 5 lag increments ($2/3^{rds}$ and $5/3^{rds}$ of a pixel respectively). However, no patterns in the spatial distribution of regions for which discrepancies in the range of DN variograms calculated after processing with ordinary and least squares regression could be established. Thus was decided to use ordinary least squares regression for the first-order DN autocorrelation removal. Variogram ranges computed automatically on the trend-processed imagery were used to determine appropriate window sizes for subsequent LMF imagery processing.

## Literature Cited

Cressie, N. 1991. *Statistics for Spatial Data*. John Wiley, Chichester, U.K.

Franklin, S.E., M. Wulder, and M. Lavigne. 1996. Automated derivation of geographic windows for use in remote sensing digital analysis. *Comp. Geosci.*, 22:665-673.

Hastie, T.J., and R.J. Tibshirani. 1990. *Generalized Additive Models*. Chapman and Hall, London, U.K.

Roujean, J.L., M. Leroy, and P.Y. Deschamps. 1992. A bi-directional reflectance model on earth's surface for the correction of remote sensing data, *J. Geophys. Res.*, 97:455-468.

## Figures

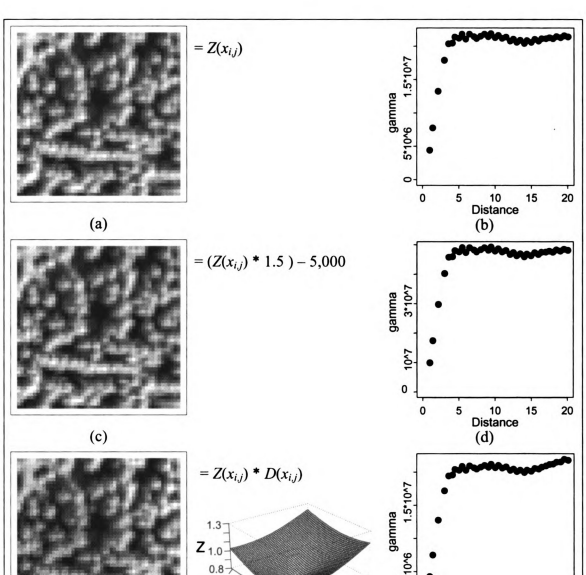


**Figure B.1**. (a,b) Portrayal of original digital numbers $Z(x_{i,j})$ for row $i$ and column $j$ indices of the NIR band for a coniferous stand and corresponding omnidirectional empirical variogram.(c, b) Portrayal of digital numbers after image linear translation and corresponding empirical variogram. (e, f, g). Portrayal of digital numbers after processing original imagery with surface $D(x_{i,j})$ approximating an imaginary anisotropic kernel similar to those typically embedded within BRDF normalization models, and corresponding empirical variogram.

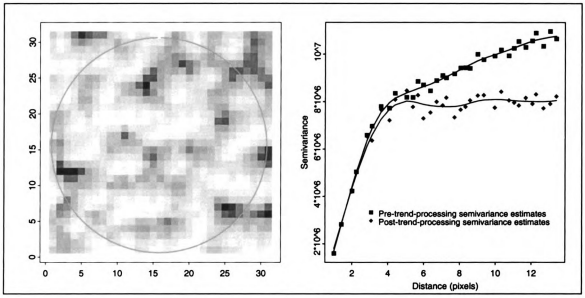


**Figure B.2**. NIR band image of a Red Pine subplot and empirical variograms computed by using the DNs of pixels within the subplot prior to and after processing for removal of first order autocorrelation. Circle in orange superimposed on the image denotes the subplot boundary. Lines in the variogram plot denote a spline fit on the estimates of semivariance.

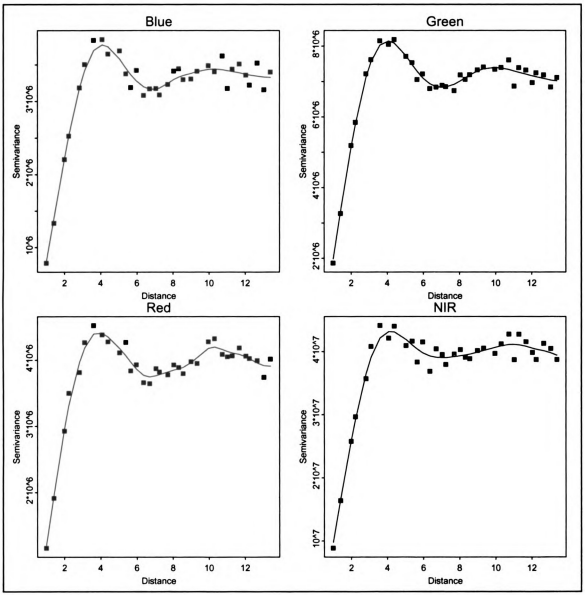


**Figure B.3.** Empirical variograms and fitted splines of post-trend-processed imagery depicting a Red Pine subplot.